Novel approaches for quantitative electrogram analysis for rotor identification:

Implications for ablation in patients with atrial fibrillation

A DISSERTATION
SUBMITTED TO THE FACULTY OF
UNIVERSITY OF MINNESOTA
BY

Shivaram Poigai Arunachalam

IN PARTIAL FULFILLMENT OF THE REQUIREMENTS
FOR THE DEGREE OF
DOCTOR OF PHILOSOPHY

Advisor: Dr.Alena Talkachova
University of Minnesota- Twin Cities
Major: Biomedical Engineering
Minor: Product Design

May, 2017

Acknowledgements

I am extremely indebted to my thesis advisor Dr. Alena Talkachova for her ultimate support and confidence in me all through this work. Her invaluable knowledge, experience, guidance, patience and timely advice are ineffable which was conducive towards successful completion of this work which otherwise wouldn't have been possible.

I would like to thank my committee members Dr.Robert Tranquillo, Dr.Hubert Lim and Dr.Barry Kudrowitz for their advice, support, and contributions to this thesis. My work has greatly benefited from their expertise and assistance. I would also like to thank Dr.Paul Iaizzo and Dr.Bin He for their invaluable comments and suggestions during the written preliminary exam as an evaluator.

I would like to thank my physician collaborators in the Department of Cardiovascular Medicine, Mayo Clinic, Rochester, MN namely Dr.Paul Friedman, Dr. Siva Mulpuru and Dr.Suraj Kapa for their invaluable clinical guidance, suggestions and support throughout this research work. Special thanks to Dr.Tobias Oesterlein, Karlsruhe Institute of Technology (KIT), Karlsruhe, Germany, for assisting with 3D visualizations.

I would like to extend my sincere thanks to Dr.Philip Araoz (and his family), my PI at the Radiology department in Mayo Clinic, Rochester MN for his immense support and encouragement to pursue my doctoral degree. Without his ineffable belief and confidence in me, accomplishing this doctoral degree would have just been a dream.

I am always indebted to Dr.Lewis F. Brown, Professor and Dean of Engineering, South Dakota State University, for his mentorship and professional guidance in the field of

digital signal and image processing and have been instrumental in shaping my career in medicine and biomedical engineering.

I am extremely thankful to the faculty, colleagues and staff of the biomedical engineering department at the University of Minnesota as well as the department of Radiology in Mayo Clinic and fellow graduate and under graduate students in Dr.Alena's lab for all their support and encouragement during my tenure as a doctoral candidate.

My heartfelt thanks to my wife Dr.Suganti Shivaram without whom this wouldn't have been possible by any means. Her ultimate love, faith and confidence in me, and her innumerable sacrifices throughout this work are ineffable which was significant towards successful completion of this work. My sweet thanks to my sons Srishiwin Shivaram and Kriszwin Shivaram for making my doctoral pathway extremely memorable and enjoyable.

I would like to express my gratitude to my father Mr. P.S. Arunachalam and mother Mrs. A. Malarkodi who has always been my backbone for my personal and professional career with their boundless love, faith and confidence in me and their continued support. My heartfelt thanks to my sister B. Gomathi Priya, brother-in law S.M. Balasubramanian, and my nieces B. Aarthi Devi, B. Renuga Sri, my brother Mr.A Chokkalingam, sister-in-law Mr. A.Raja Rajeswari and all my in-laws from my wife's end for their invaluable support and encouragement from overseas (India) for pursuing my doctoral degree. Without them I would have not accomplished this work.

Shivaram P. Arunachalam

May 10th 2017

Dedicated

To

My wife Dr.Suganti Shivaram, my sons Srishiwin Shivaram and Kriszwin Shivaram, my father Mr.Arunachalam Poigai Sivaraman and my mother Mrs. Malarkodi Arunachalam

Abstract

Atrial fibrillation (AF) is the most common sustained cardiac arrhythmia that causes stroke affecting more than 2.3 million people in the US. Catheter ablation with pulmonary vein isolation (PVI) to terminate AF is successful for paroxysmal AF but suffers limitations with persistent AF patients as current mapping methods cannot identify AF active substrates outside of PVI region. Recent evidences in the mechanistic understating of AF pathophysiology suggest that ectopic activity, localized re-entrant circuit with fibrillatory propagation and multiple circuit re-entries may all be involved in human AF. Accordingly, the hypothesis that rotor is an underlying AF mechanism is compatible with both the presence of focal discharges and multiple wavelets. Rotors are stable electrical sources which have characteristic spiral waves like appearance with a pivot point surrounded by peripheral region. Targeted ablation at the rotor pivot points in several animal studies have demonstrated efficacy in terminating AF. The objective of this dissertation was to develop robust spatiotemporal mapping techniques that can fully capture the intrinsic dynamics of the non-stationary time series intracardiac electrogram signal to accurately identify the rotor pivot zones that may cause and maintain AF.

In this thesis, four time domain approaches namely multiscale entropy (MSE) recurrence period density entropy (RPDE), kurtosis and intrinsic mode function (IMF) complexity index and one frequency domain approach namely multiscale frequency (MSF) was proposed and developed for accurate identification of rotor pivot points. The novel approaches were validated using optical mapping data with induced ventricular arrhythmia in ex-vivo isolated rabbit heart with single, double and meandering rotors

(including numerically simulated data). The results demonstrated the efficacy of the novel approaches in accurate identification of rotor pivot point. The chaotic nature of rotor pivot point resulted in higher complexity measured by MSE, RPDE, kurtosis, IMF and MSF compared to the stable rotor periphery that enabled its accurate identification. Additionally, the feasibility of using conventional catheter mapping system to generate patient specific 3D maps for intraprocedural guidance for catheter ablation using these novel approaches was demonstrated with 1055 intracardiac electrograms obtained from both atria's in a persistent AF patient. Notably, the 3D maps did not provide any clinically significant information on rotor pivot point identification or the presence of rotors themselves. Validation of these novel approaches is required in large datasets with paroxysmal and persistent AF patients to evaluate their clinical utility in rotor identification as potential targets for AF ablation.

Table of Contents

List of Tables

List of Figures

CHAPTER 1: INTRODUCTION

1.1 Motivation and problem statement

Atrial Fibrillation (AF) or irregular activation of the atria is an electrical derangement of cardiac excitation and propagation whose initiation depends on the presence of triggers and its maintenance requires an appropriate arrhythmogenic substrate. AF is one of the most common cardiac arrhythmia affecting more than 2.3 million people and is one of the leading sources of health care expenditure in the United States [1]. AF serves as an adverse prognostic marker and is associated with increased rates of the death, stroke and heart failure events [2]. Several mechanisms of AF have been described so far, with the most accepted mechanism being the complex interplay between various triggers that induce arrhythmia via reentry or triggered activity, and myocardial substrates that maintain them [3-5]. Recent animal research shows that AF may also be maintained by rapid localized sources called a 'rotor' that applies to the organizing source (driver) of functional reentrant activity [6]. The recent development of patient-specific computational mapping has revealed that the substrates for human AF are not necessarily 'random', but also comprised of stable electrical rotors and focal sources at diverse locations within either atrium [7].

Maintenance of sinus rhythm with anti-arrhythmic drugs and cardioversions is associated with increased quality of life in patients with symptomatic AF. However, efficacy of anti-arrhythmic drugs is only marginal in maintenance of sinus rhythm [8]. For the past years, there is a rise in popularity of catheter ablation, which is an invasive non-pharmacological therapy that aims to restore normal sinus rhythm in the atria by

eliminating triggers arising from the pulmonary veins (PV) that maintain AF through pulmonary vein isolation (PVI) [9]. Although more successful, recurrence rates are high, particularly in patients with persistent or long-standing AF [10]. In these patients, AF is mostly maintained by the rotors that are located outside of pulmonary veins (PV) region [11]. A major challenge in these patients is accurate identification of the arrhythmogenic substrates, so that ablative therapy can be successfully applied. Current processing methods that are used to identify AF vulnerable regions in a clinical setting include analysis of the dominant frequency (DF), complex fractionated electrograms (CFAE), phase analysis and local activation time (LAT) maps [12]. All these techniques are based on temporal analysis of electrograms from different spatial locations of atria. However, the high frequency of recurrence of arrhythmias in patients with persistent AF after PV isolation and linear ablation, show that these current techniques of AF analysis are not adequate to predict critical areas of AF maintenance. As a result, none of the currently available commercial mapping systems can predict the rotor location outside of PVs in patients with persistent AF. Therefore, there is a clear need for more robust spatio-temporal mapping techniques to precisely identify rotor pivot point locations for human AF to generate patient specific 3D maps that can guide catheter ablation to permanently terminate AF.

1.2 Objectives

The aim of this PhD thesis is to develop novel time and frequency domain techniques that can identify pivotal (self-sustaining) regions of chaotic rhythms like human AF. The basic tenet behind developing variety of approaches is that different properties of the

intracardiac electrograms can be exploited with different techniques to precisely identify the rotor pivot point as suitable ablation targets that can guide faithful ablation. In this thesis, I will evaluate the utility of these tools in animal models, where high-resolution optical mapping data allows for direct visualization and identification of rotor location in the heart. The efficacy of these novel techniques will be demonstrated with their ability to precisely locate the known rotor pivot locations with optical mapping data from a single rotor, figure-of-eight double rotor and meandering rotors. Finally, in this research, I propose to apply these novel techniques to clinical intracardiac electrograms from patients who underwent electroanatomical mapping for AF ablation procedure at the Mayo Clinic Department of Cardiovascular Medicine, Rochester, MN, to demonstrate the feasibility of using current catheter mapping systems to generate patient specific 3D maps that the physicians can infer along with conventionally available LAT maps and CFAE in a clinical setting. The objectives of the thesis will be realized through the following three specific aims:

Specific Aim 1: To develop novel quantitative electrogram analysis methods to identify rotor pivot point that is translatable to intra-atrial electrogram analysis for identifying potential targets for AF ablation

It is known that the complexity of intracardiac electrogram is larger in the vicinity of the core of the rotor, when compared at distant locations with varying temporal characteristics. Time domain approaches will exploit these temporal complexities between the rotor core and the peripheral regions thus enabling precise identification of rotor core area. Several novel time domain methods are developed and used in this thesis

such as multiscale entropy (MSE), kurtosis, recurrence period density entropy (RPDE), and empirical model decomposition (EMD). Commonly used frequency domain based processing methods is the DF approach which is known to have uniform DF values throughout the atrial regions during AF, and cannot precisely identify the rotor pivot point compared to the periphery region. The chaotic nature of AF yields various frequency components at the rotor core compared to the periphery which can be exploited for its precise identification. In this thesis, a novel frequency domain based approach namely multiscale frequency (MSF) technique is developed to correctly predict pivotal regions, especially outside of PV zone. I will also calculate DF, Shannon entropy (SE) and Renyi entropy (RE), for comparison purposes. I hypothesize that these novel techniques will demonstrate higher complexity at the core of the rotor compared to the periphery using optical mapping data, and therefore can be used to predict its location outside of PV during persistent AF.

Specific Aim 2: To demonstrate the robustness of the novel electrogram analysis approaches with noise and validate their efficacy using short time series data using simulated sinusoidal wave and flat baseline ECG.

Electrograms and ECG's obtained in a real-time clinical setting is often contaminated with most common types of noise such as white, pink and brown noise apart from other high frequency noises which can be robustly removed with preprocessing steps. However, it is important that the newly developed methods demonstrate robustness with white, pink and brown noise due to their complexity in separating them from time series data for reliable identification of rotor pivot points in actual clinical setting. This specific

aim will demonstrate the efficacy of each of the newly developed approach to estimate complexity of short time series data in its raw form and with noise using simulated single and multi-frequency sinusoidal waveform and flat baseline ECG.

Specific Aim 3: To demonstrate the efficacy of MSE and MSF technique to robustly discriminate normal sinus rhythm and AF on a single lead ECG.

This specific aim will demonstrate the efficacy of MSE and MSF technique to robustly discriminate normal sinus rhythm and AF on a single lead ECG without any preprocessing steps. Since, the efficacy of EMD, RPDE and kurtosis approaches has already been demonstrated with ECG analysis; these approaches were not used for the discrimination analysis in this section of the thesis.

Specific Aim 4: To validate the efficacy of the novel electrogram analysis approaches using numerically simulated and optical mapping rotor data with known pivot point locations.

This specific aim will demonstrate the efficacy of these novel techniques with their ability to precisely locate the known rotor pivot locations with optical mapping data from a single rotor, figure-of-eight double rotor and meandering rotors. Additionally, these approaches will also be validated using meandering rotor data sets from numerical simulation.

Specific Aim 5: To assess the feasibility of using current catheter mapping system to generate patient specific 3D maps by implementing the novel approaches for rotor mapping using bipolar intra-atrial electrograms from human Atrial Fibrillation patients to guide catheter ablation.

The utility of novel mapping techniques in a clinical setting demands the feasibility of translating these approaches to produce patient specific 3D maps that can guide catheter ablation by the cardiac electrophysiologist. The objective of this section is to assess the feasibility of collecting, exporting and analyzing intracardiac electrograms from human AF patients with the techniques developed in Specific Aims 1 and 2, from the CARTO electroanatomic mapping software in Mayo Clinic, Catheter Lab Department of Cardiovascular Medicine to generate 3D patient specific maps that can inferred along with conventionally available LAT maps. I hypothesize that it is feasible to generate near-real time patient specific 3D maps from human AF patients that can potentially guide cardiac electrophysiologists for catheter ablation to terminate AF.

1.3 Thesis organization

This thesis first presents some background information on the structure and function of the heart, its electrical activity, features and characteristics of the electrocardiogram (ECG), intracardiac electrogram and its measurement in Chapter II. This chapter also provides background information on AF; its epidemiology, types, and the pathophysiological mechanisms that causes and maintains AF. Current therapies to terminate AF and their limitations are discussed. Review of catheter ablation strategies that are clinically used are presented. The chapter then provides thorough literature review on the several electrogram analysis techniques that are currently being explored and their limitations leading to the motivation of this thesis. The need for a more robust spatio-temporal mapping system to guide AF ablation will be well illustrated in this chapter based on the background information provided.

Chapter III discusses in detail each of the newly developed mapping technique in this thesis namely multiscale entropy, recurrence period density entropy, kurtosis, empirical mode decomposition and multiscale frequency. The theoretical framework and the rationale behind their ability to precisely identify rotor core regions compared to the periphery will be clearly illustrated.

Chapter IV discusses in detail the approach taken to demonstrate the robustness of the novel approaches with various noises such as white, pink and brown noise. Efficacy of these approaches with short time series data using simulated single frequency, multi-frequency and flat baseline ECG are demonstrated by comparing it with SE which is considered as 'gold standard' for the purposes of this work.

Chapter V will demonstrate the efficacy of the MSE and MSF technique in robustly discriminating ECG with Normal sinus rhythm and AF on a single lead ECG obtained from the Physionet/Physiobank database. Chapter VI provides the description of the optical mapping data from isolated rabbit hearts for the single, figure-of-eight and meandering rotors as well as meandering rotors from numerical simulation. Efficacy of each of the newly developed mapping technique will be demonstrated in precisely identifying the rotor core region using each of these data sets. SE, RE and DF maps will be generated for each data set for comparison purposes.

Chapter VII will then describe the Institutional Review Board (IRB) approvals from Mayo Clinic and University of Minnesota, clinical setting to obtain intracardiac electrograms from AF patients, description of the electroanatomic mapping system, and the process involved in acquiring and exporting the data for offline analysis to generate

patient specific 3D maps. The chapter also presents the various 3D maps obtained from intracardiac electrogram analysis from AF patient data. Critical evaluation and discussion of these results are presented for each of these techniques and their limitations.

Justifications of how the newly developed rotor mapping techniques overcomes the current problem and challenges with identifying active substrates in AF patients are presented in the conclusions part in Chapter VIII. Future recommendations for this research are also provided based on some shortcomings that might be encountered with these techniques as a potential next step to fully integrate these approaches in the clinical setting to obtain near-real time patient specific 3D maps that can guide the electrophysiologists during catheter ablation to terminate AF and possibly other cardiac arrhythmias. Outcomes of this dissertation research are shown in APPENDIX A.

CHAPTER 2: REVIEW OF CARDIAC ANATOMY, ELECTROPHYSIOLOGY AND ATRIAL FIBRILLATION

2.1 Introduction

This section of the thesis is devoted to the discussion of the basic fundamentals of cardiac anatomy and electrophysiology including generation of electrocardiogram and intracardiac electrogram signals, their features and characteristics. Review of atrial fibrillation (AF) is provided covering several aspects such as disease epidemiology, pathophysiology, and treatment procedures. Specifically, detailed discussion is provided on the various theories on the electro-mechanistic features that initiate and maintain AF including rotor formation. Review of catheter ablation strategies and current clinical challenges are discussed that motivate novel research in this field. A brief review of the optical mapping procedure is presented which is used to obtain single, figure-of-eight double and meandering rotor data from *ex vivo* rabbit heart. This chapter also provides a brief review of the MIT-BIH PhysioBank/Physionet database from which ECG traces are used for testing newly developed approaches in this thesis.

Literature review on existing methods for intracardiac electrogram analysis including preprocessing steps is provided with brief description of each of these approaches followed by a discussion of the limitations of these approaches that challenges their clinical use for rotor identification. These discussions will provide the rationale behind the need for novel quantitative electrogram analysis approaches for reliable and accurate identification of rotor pivot points as suitable targets for ablation for AF and other

complex arrhythmias. Therefore, the central idea and purpose of this thesis will be understood at the end of this chapter.

2.2 Review of the structure and function of the heart

2.2.1 The heart and its physiology

2.2.1.1 Location of the heart in the thorax

The heart is located in the chest between the lungs behind the sternum and above the diaphragm surrounded by the pericardium [13]. It weighs about 250-300 g and about the size of a fist. The center of the heart is about 1.5 cm to the left of the midsagittal plane, and great vessels namely the superior and inferior vena cava, the pulmonary artery and vein, as well as the aorta are located above the heart. The esophagus and the spine lie further behind the heart. Figure 2-1 gives an idea on the location of the heart in the thorax.

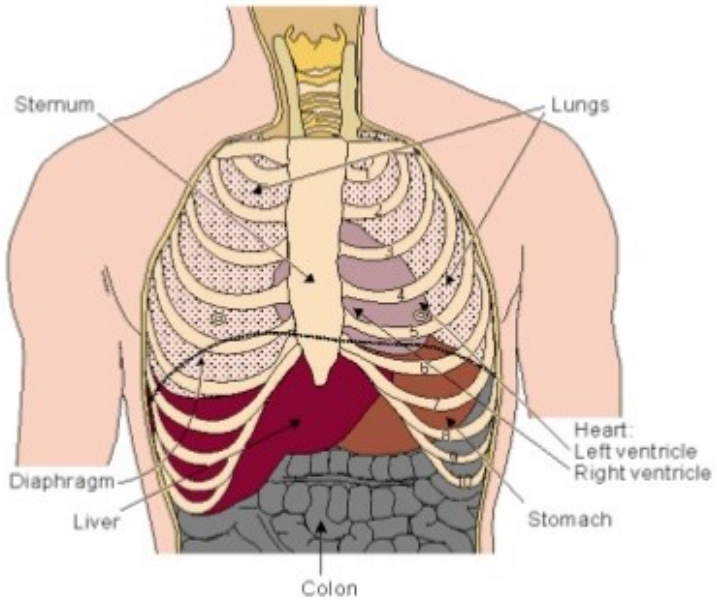

Figure 2-1: Location of the heart in the thorax *(Adapted from [13])*

2.2.1.2 Anatomy of the heart and cardiovascular system

Figure 2-2 shows the cross section of the heart. Heart muscle is known as the myocardium with similar striations like skeletal muscle. There are four chambers namely the right and left atria and ventricles. Cardiac muscle cells are oriented more tangentially than radially, and that the resistivity of the muscle is lower in the direction of the fiber has importance in electrocardiography and magnetocardiography [13].

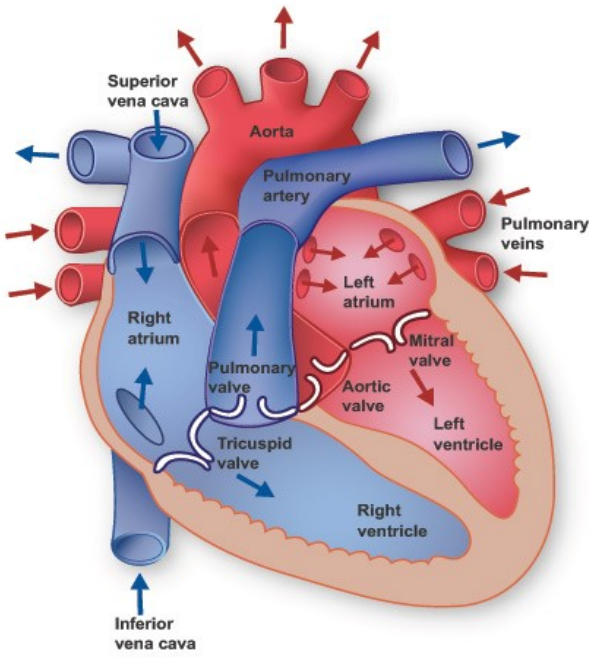

Figure 2-2: Cross Section of the heart *(Adapted from [14])*

The heart has four valves: tricuspid valve is between the right atrium and ventricle; mitral valve between the left atrium and ventricle [14]. Two semilunar valves namely the pulmonary valve lies between the right ventricle and the pulmonary artery and the aortic valve lies in the outflow tract of the left ventricle controlling flow to the aorta. Deoxygenated blood returns from the systemic circulation to the right atrium and from there goes through the tricuspid valve to the right ventricle. It is ejected from the right

ventricle through the pulmonary valve to the lungs. Oxygenated blood returns from the lungs to the left atrium and from there through the mitral valve to the left ventricle. Finally, oxygenated blood is pumped through the aortic valve to the aorta and the systemic circulation. The left ventricular wall and the septum are much thicker than the right ventricular wall because the left side has greater work to do while circulating blood through all of the body's tissues.

2.2.1.3 The cardiac cycle

The successive mechanical events characterizing the contractile function of the heart during the cardiac cycle can be divided into two general events namely diastole which refers to the filling of the blood in the chambers and systole refers to the ejection of blood from the chambers [14] shown in Figure 2-3.

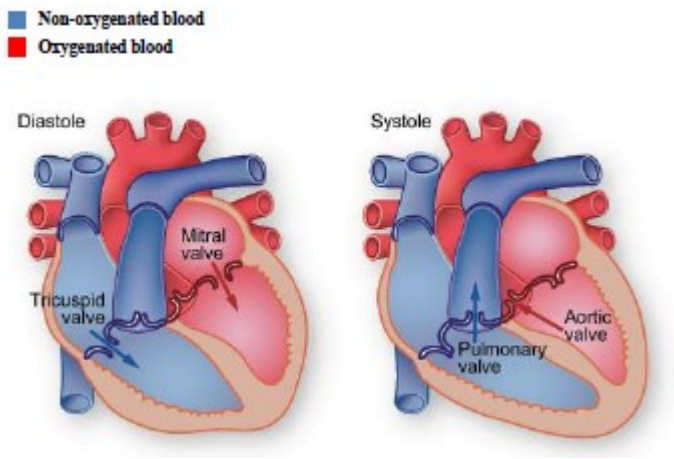

Figure 2-3: Cardiac cycle demonstrating blood flow pathways during diastole and systole *(Adapted from [14])*

The cardiac cycle is further divided into seven phases' namely atrial systole, isovolumetric contraction, rapid ejection, reduced ejection, isovolumetric relaxation, rapid filling, and reduced filling.

2.2.1.4 Cardiac myocytes electrical activity

The primary function of cardiac myocytes is to 'contract' which are initiated by electrical changes that allows for a coordinated contraction of the heart that constitutes the cardiac cycle. The transmembrane potential (TMP) is defined by the difference in voltage between the interior and exterior of a cell, and in the resting state, the membrane potential of a myocardial cell is around -80 to -90 mV [15]. Several ions are present inside and outside of the cells, of which sodium (Na^{+}), potassium (K^{+}), chloride (Cl^{-}), and calcium (Ca^{++}) are important in determining the membrane potentials. The electrical polarity is maintained by transmembrane pumps that ensure the appropriate distribution of ions to keep the insides of the cardiac cells relatively electronegative compared to the extracellular space. Cardiac cells can reverse their internal negativity in a process called '*depolarization'* which happens when a normal depolarization current spreads from one cardiac cell to another during electrical activation of the heart. After depolarization is complete, the cardiac cells are able to restore their resting polarity through a process called '*repolarization'*. The electrical cycle from a single cell of depolarization and repolarization is called an *'action potential'* (AP) [15]. By convention, the action potential for non-pacemaker cell has five phases numbered from 0 to 4 shown in Figure 2-4. Non-pacemaker action potentials are typically found in cells such as atrial and ventricular myocytes and Purkinje cells. Following are the events during the 5 phases of non-pacemaker AP [15] shown in Fig. 2-4:

Phase 4 – represents the resting phase at TMP

Phase 0 – represents depolarization caused by rapid influx of Na^{+} ions.

Phase 1 – represents early repolarization caused by efflux of K^+ ions.

Phase 2 – represents the plateau phase through influx of Ca^{++} ions.

Phase 3 – represents repolarization caused by efflux of K^+ ions.

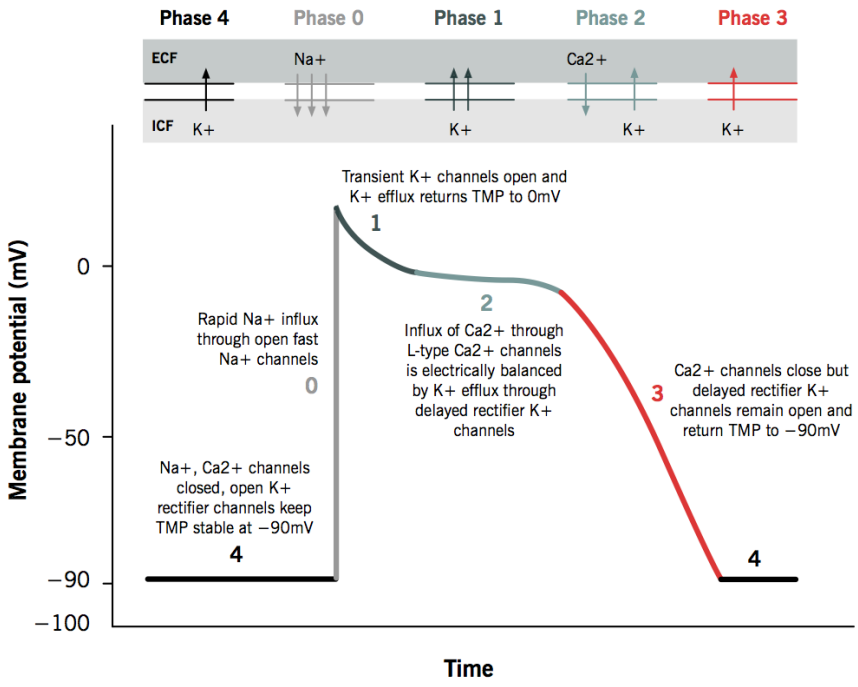

Figure 2-4: Phases of non-pacemaker action potential *(Adapted from [15])*

During phases 0, 1, 2, and part of phase 3, the cell is *'refractory'* (i.e., unexcitable) to the initiation of a new action potential. During absolute refractory period (ARP), the cell is completely unexcitable to a new stimulus. Effective refractory period (ERP) is the period including ARP and a short segment of phase 3 during which a stimulus may cause the cell to depolarize minimally but will not result in a propagated action potential i.e. neighboring cells will not depolarize. During relative refractory period (RRP) a greater than normal stimulus will depolarize the cell and cause an action potential. Finally, supranormal period is a hyper excitable period during which a weaker than normal stimulus will depolarize the cells and cause an action potential [15].

Pacemaker cells found in the SA and AV node have no true resting potential, but instead generate regular, spontaneous action potentials and possess the property of automaticity i.e. they have the ability to spontaneously depolarize [16]. The depolarization current of the action potential is carried primarily by relatively slow, inward Ca^{++} currents instead of fast Na^{+} currents. Pacemaker cell nodal action potentials are divided into three phases. Phase 4 is the spontaneous depolarization which constitutes the pacemaker potential that triggers the action potential once the membrane potential reaches threshold between -40 and -30 mV. Phase 0 is the depolarization phase of the action potential which is followed by phase 3 repolarization. Once the cell is completely repolarized at about -60 mV, the cycle is spontaneously repeated as shown in Figure 2-5.

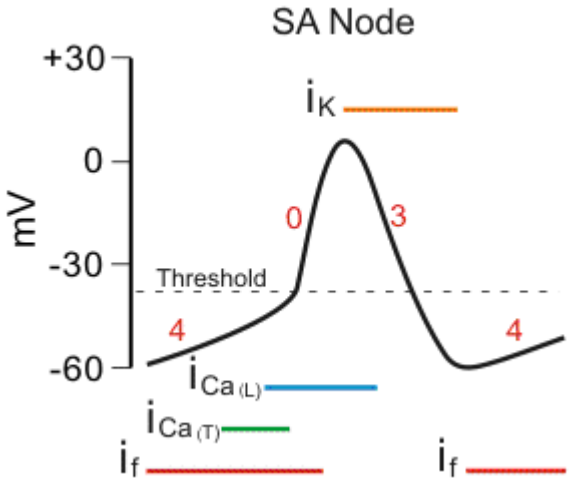

Figure 2-5: Phases of pacemaker action potential *(Adapted from [16])*

Phase 4 undergoes a spontaneous depolarization from -65 mV to a threshold voltage of about -40 mV due to special pacemaker currents called "funny" currents i_f. As the depolarization reaches the threshold voltage, the slow calcium channels begin to open through transient or T-type Ca^{++} channel (current $i_{Ca(T)}$) and long-lasting, or L-type

Ca^{++} channels (current $i_{Ca(L)}$) causing an increase in calcium conductance and phase 0 is initiated [16]. Phase 0 corresponds to the upstroke of the action potential. When the membrane is depolarized to a threshold value of about -40 mV, specific slow calcium channels open, causes a slow inward movement of Ca^{++} ions. For pacemaker cells, the slope of phase 0, which corresponds to the rate of depolarization, is much slower than that of non-pacemaker cells. Phase 3 corresponds to the repolarization. The depolarization in phase 0 causes the potassium channels to open repolarizing the cell toward the equilibrium potential for K^+ ions (current i_K). At the same time, the slow inward Ca^{++} channels that opened during Phase 0 become inactivated, which also contributes to the repolarization process. When the membrane potential reaches -65 mV, phase 3 ends.

2.2.1.5 Electrical conduction system of the heart

Located in the right atrium at the superior vena cava is the sinus node (sinoatrial or SA node) which consists of specialized muscle cells as seen in Figure 2-6. The SA nodal cells are self-excitatory, pacemaker cells which spontaneously generate an electrical action potential at the rate of about 70 per minute [17]. From the sinus node, activation propagates throughout the atria muscles causing contraction, but cannot propagate directly across the boundary between the atria and ventricles.

The atrioventricular node (AV node) is located at the boundary between the atria and ventricles which simultaneously fires action potentials at an intrinsic frequency of about 30-40 pulses/min [17]. In a normal heart, the AV node provides the only conducting path from the atria to the ventricles. Propagation from the AV node to the ventricles is

provided by a specialized conduction system called the bundle of His separating into two bundle branches propagating along each side of the septum, constituting the right and left bundle branches. Even more distally the bundles divide into Purkinje fibers that diverge to the muscles of the inner sides of the ventricular walls. From the inner side of the ventricular wall, the many activation sites cause the formation of a contraction wave front which propagates through the ventricular mass toward the outer wall which results from cell-to-cell activation [17].

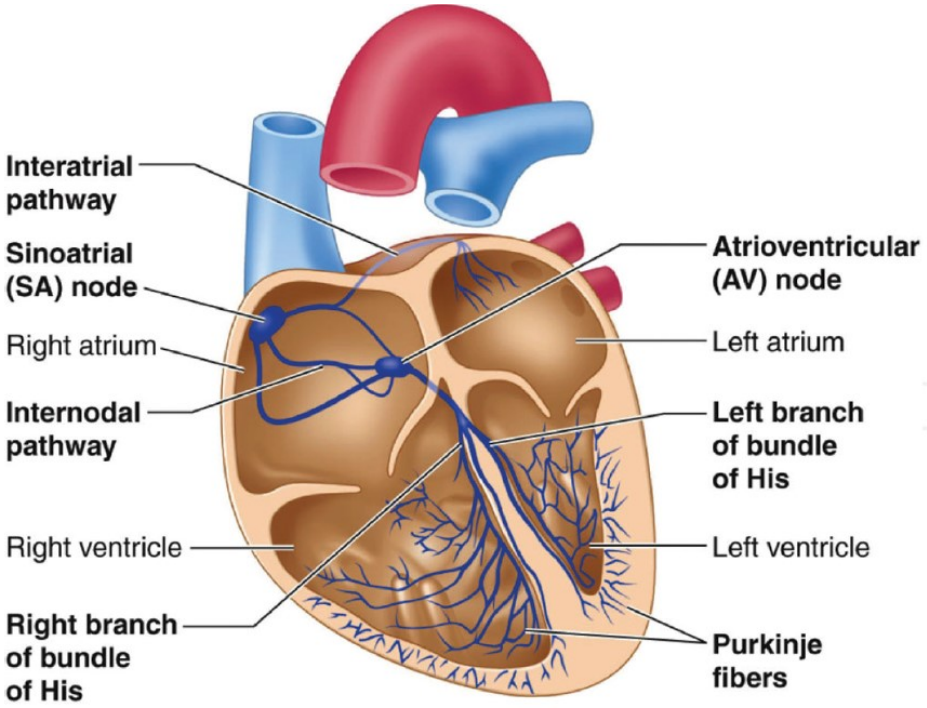

Figure 2-6: Electrical conduction system of the heart. *Figure illustrates the different electrical nodes and muscle fibers that play a role in the electrical conduction system (Adapted from [18])*

After each ventricular muscle region has depolarized, repolarization occurs. Repolarization is not a propagating phenomenon, and because the duration of the action impulse is much shorter at the epicardium (the outer side of the cardiac muscle) than at

the endocardium (the inner side of the cardiac muscle), the termination of activity appears as if it were propagating from the epicardium toward the endocardium. Because the intrinsic rate of the sinus node is the greatest, it sets the activation frequency of the whole heart. If the connection from the atria to the AV node fails, the AV node adopts its lower intrinsic frequency and maintains a beating heart. If the conduction system fails at the bundle of His, the ventricles will beat at the rate determined by their own region that has the highest intrinsic frequency. Such electric signals generated may be recorded with a microelectrode, which is inserted inside a cardiac muscle cell. However, the electrocardiogram (ECG) is a recording of the electric potential on the outer surface of the thorax generated by the electric activity of the heart. The ECG thus represents the extracellular electric behavior of the cardiac muscle tissues [17].

2.2.2 Cardiac Electrocardiography

2.2.2.1 The limb leads and Einthoven's triangle

Willem Einthoven introduced the first clinically significant ECG measuring system in 1908 and suggested the use of three electrical limb lead connections to construct what would become known as "Einthoven's triangle" [17] as shown in Figure 2-7. Einthoven discovered that an electric signal was produced by the heart during each heartbeat, and this signal can be measured on the outer surface of the body. He was the first to standardize electrical connections to the body at the three limbs: left arm, right arm and left leg. Einthoven's limb lead I is defined as the difference between the potential at the left arm and the potential at the right arm. Limb lead II is the difference

between the potential at the left leg and the potential at the right arm, and limb lead III is the difference between the potential at the left leg and the potential at the left arm [17].

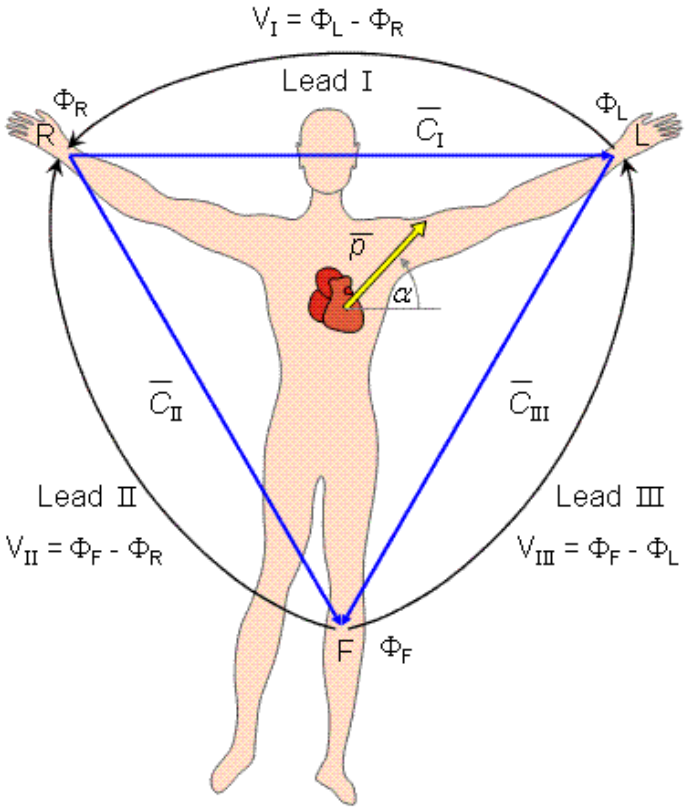

Figure 2-7: Limb Leads and Einthoven's Triangle *(Adapted from [17])*

V_I, V_{II}, and V_{III} denote these difference voltages for lead I, lead II, and lead III respectively. By applying Kirchhoff's Voltage Law, Einthoven showed the following relationship can be derived:

$$V_I + V_{III} = V_{II} \tag{2.1}$$

From the relationship in (2.1), it can be noted that any two of the three leads are independent.

2.2.2.2 Augmented leads and its placement

Each configuration of lead connections to the limbs produces a different perspective of the ECG signal, which provides unique information for the cardiologist. Measurement of the potential between each limb electrode and the so called Wilson central terminal (WCT) gives three additional limb leads of interest to physicians [17]. These resulting new views of the ECG signal are easily derived from the three standard limb connections to the body and augment the standard lead I, lead II and lead III signals. These new lead configurations were adopted by the medical community and given the names "augmented leads", designated aV_F, aV_L and aV_F.

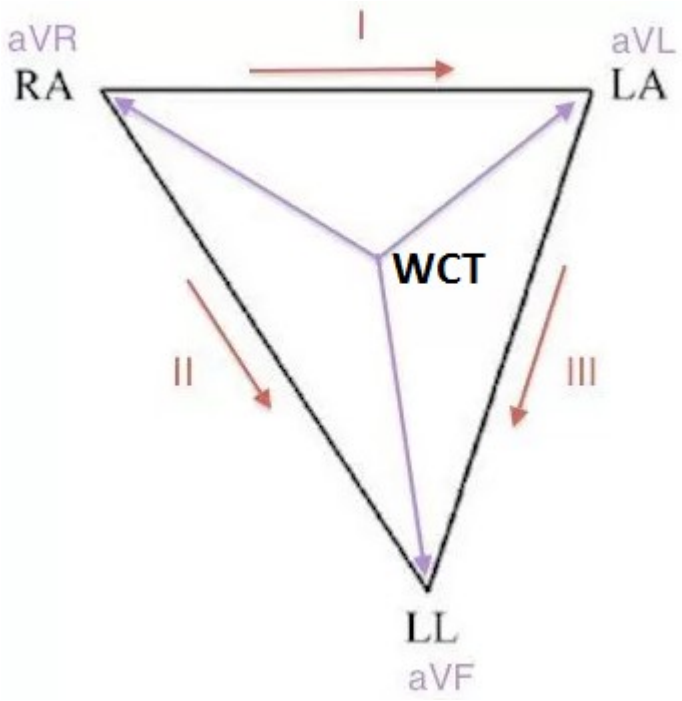

Figure 2-8: Augmented lead configuration *(Adapted from [17])*

Figure 2-8 shows the connections for each of the augmented leads: It can be shown that the mathematical relationship between the standard and augmented leads is given by:

$$aV_R = -\frac{V_I + V_{II}}{2},\ aV_L = \frac{V_I - V_{III}}{2} \text{ and } aV_F = \frac{V_{II} + V_{III}}{2} \quad (2.2)$$

With the augmented leads, there are six standard ECG leads, I, II, III, aV_R, aV_L and aV_F which provide a moderately complete representation of the depolarization activity in the frontal plane [17].

2.2.2.3 Precordial leads and its placement

The medical community eventually proposed six new lead connections to the body that provide additional electrical perspectives of the heart. These are called precordial or chest leads [17, 19]. These connections, designated V_1 - V_6, require placement of electrodes across the chest as shown in Figure 2-9.

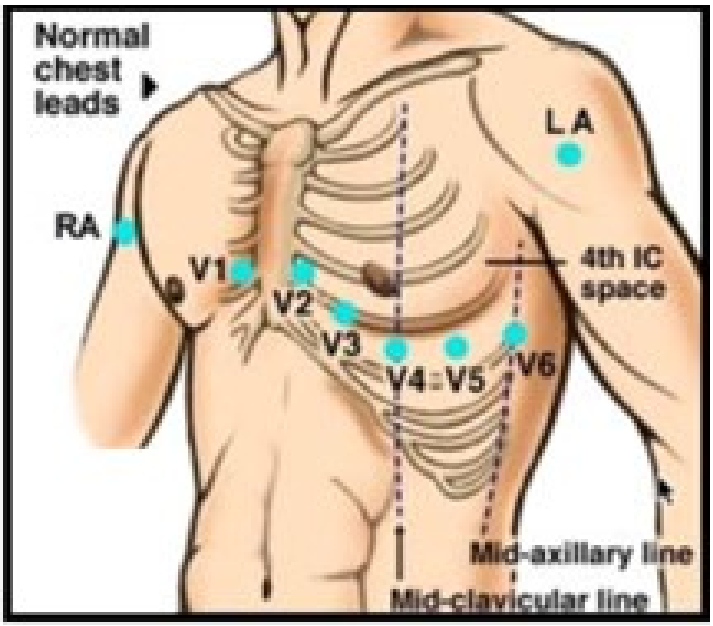

Figure 2-9: Precordial lead configuration *(Adapted from [19])*

As with the previously discussed augmented leads, the precordial leads are unipolar leads measured with respect to the same common terminal. The points V_1 and V_2 are located at

the fourth intercostal space on the right and left side of the sternum; V_4 is located in the fifth intercostal space at the mid-clavicular line; V_3 is located between the points V_2 and V_4; V_5 is at the same horizontal level as V_4 but on the anterior axillary line; V_6 is at the same horizontal level as V_4 but at the midline. The location of the precordial leads is illustrated in Figure 2-9.

2.2.2.4 Formation of the electrocardiogram (ECG) signal

Figure 2-10 illustrates the sequence of events involved in the formation of the ECG [20]. The yellow color denotes areas that are excited. Impulse spreads from right atrium to left atrium via the atrial muscle cells where the atria share a wall. The ECG monitors the spread of the signal as seen in Figure 2-10. The electrochemical current flow through the cardiac muscle produces a resulting voltage potential throughout the body and on the surface of the skin which can be measured. The ECG is the most important and definitive noninvasive diagnostic test for cardiac arrhythmias. The normal lead II ECG signal is depicted in Figure 2-11. The ECG signal consists of a small P-wave which is the result of atrial contraction (depolarization), the ventricular contraction which produces a rapid and angular QRS complex, while ventricular repolarization (returning to the resting state) produces the T-wave. The U wave is a very small deflection following the T wave and has the same polarity as T wave. It is often not observed on the healthy ECG waveform.

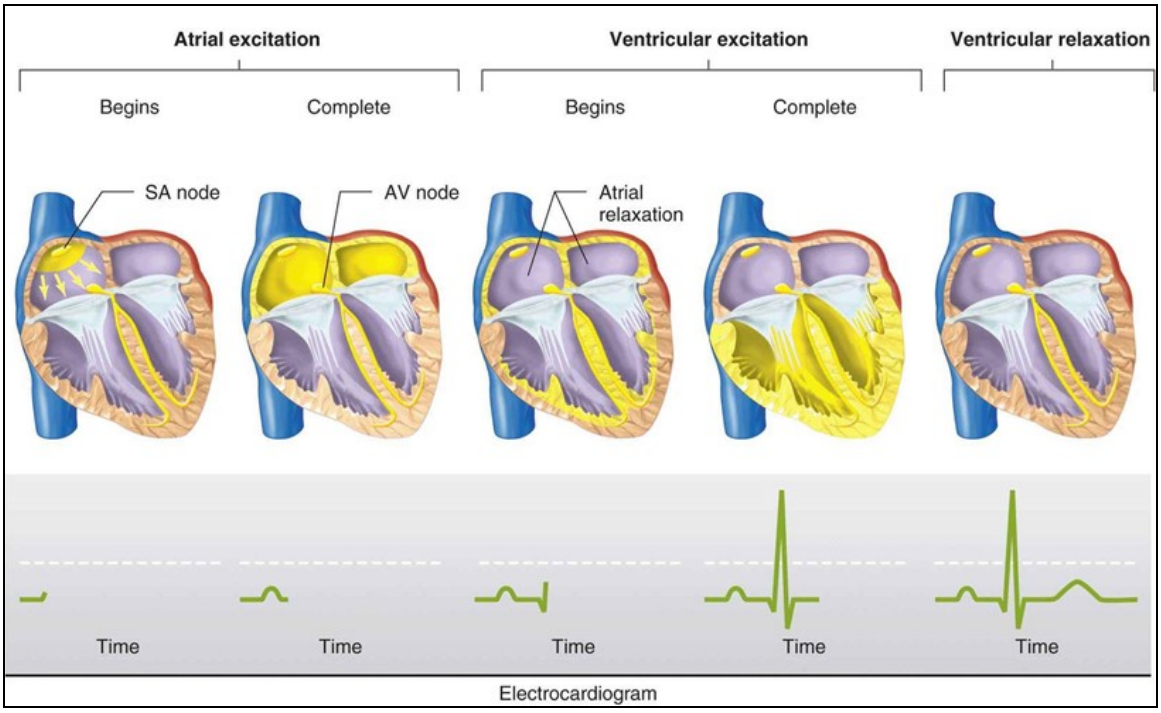

Figure 2-10: Sequence of cardiac excitation that result in the formation of the ECG *(Adapted from [20])*

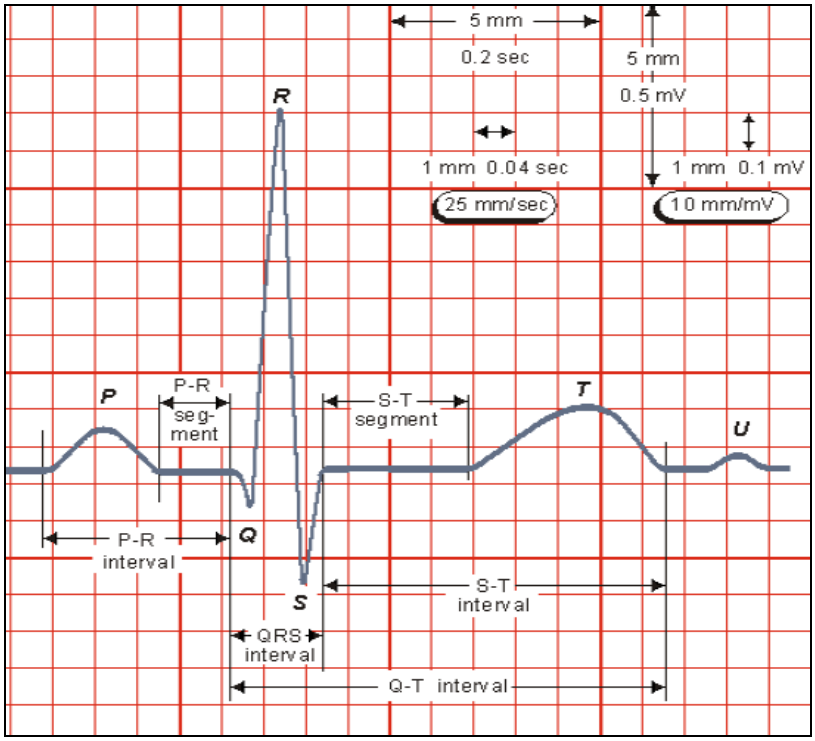

Figure 2-11: Normal lead II ECG signal *(Adapted from [13])*

2.2.2.5 Segments of the ECG signal and their characteristics

The ECG waveform consists of the P-wave, the QRS complex, the T-wave and the U-wave as seen in Fig. 2-11. Each component has its own characteristics distinguished from others, in terms of the duration, polarity, voltage level, shape and axis. In the normal healthy heart, the duration of the P-wave is not greater than 0.11 seconds, which implies the time it takes for the depolarization current to flow through the two atria. An increased width usually indicates left atrial abnormality or right atrial muscle damage (hypertrophy) [17]. If the amplitude of the P-wave is greater than 0.3 mV, atrial enlargement is suspected and indicates AV valvular problems, hypertension, cor pulmonale, or congenital heart disease [17]. The P-wave is normally positive in leads I, II, aV_F and V_4 to V_6, positive, negative, or biphasic in leads III, aV_L, and V_1 to V_3, and always negative in lead aV_R. An intensively negative and elongated duration in the P wave of V_1 may be a sign of left atrial abnormality. The normal P-wave is not notched or peaked.

The duration of the QRS complex in a healthy adult is 0.05 to 0.1 seconds, which indicates the intraventricular conduction time. The amplitude of the QRS complex varies with age and the placement of the electrodes; however it should not be less than 0.6 mV in V_1 and V_6, 0.8 mV in V_2 and V_5, and 1 mV in V_3 and V_4. The low amplitude in the QRS complex indicates diffuse coronary disease, pericardial effusion, emphysema, myxedema, primary amyloidosis, and cardiac failure [17]. The QRS complex is normally positive to equiphasic in leads I, II, and V_3 to V_6, positive, negative, or equiphasic in leads aV_L and aV_F, and finally negative in lead aV_R.

The T-wave is the representation of current generated during rapid repolarization of the heart. The amplitude of the normal T-wave does not surpass 0.5 mV in leads I, II, and III, or 0.1 mV in the precordial leads. A sharp and elevated T-wave is a sign of hyperkalemia or myocardial ischemia. It is positive in leads I, II and V_2 to V_6, inverted in lead aV_R, positive or inverted if the QRS complex is less than 0.6 mV in amplitude in leads aV_L and aV_F, finally various polarity in leads III and V_1. The normal T-wave has rounded and asymmetric shape. Abnormalities involved in the T-wave are sign of hyperkalemia, hyperventilation, metabolic diseases, and acid-base imbalance [5]. The U-wave is not normally perceived due to its low amplitude. The mechanism of the U-wave is still not fully known; however its high amplitude indicates hypokalemia; the inversion after the positive deflection in the U-wave is a sign of ischemia, and the negative initial part of the U-wave is the most common cause of hypertension.

The duration of the normal PR interval is 0.12 to 0.20 seconds, which represents the time for the pulse to pass through from the atria to the ventricles. A PR interval that is outside these boundaries may be normal for an individual; however the prolonged PR interval could also be a sign of AV block or hypothyroidism, and a shortened PR interval could be a sign of pre-excitation syndrome, AV junctional rhythms, glycogen storage disease, or hypertension [17]. The PR interval is clinically significant since it is involved in four processes; atrial depolarization, the AV node activation, conduction from the AV node to the ventricle, and conduction from the ventricle to the endocardium.

The QT interval corresponds to the sum of depolarization and repolarization periods of the heart, and it is useful as a measure of repolarization. The normal QT interval is less

than 0.48 seconds. Heart rate significantly affects the QT interval; as the heart rate increases, the QT interval shortens and vice versa. The QT interval is influenced by drugs, notably quinidine, procainamide, disopyramide, bradycardia, hypokalemia, or hypomagnesemia. Table 2-1 lists the characteristics of normal ECG waves in terms of duration, amplitude, polarity and shape.

Table 2-1 Characteristics of the normal ECG waves (Adapted from [17])

	P wave	QRS complex	T wave
Duration	≤ 0.11 sec	0.05 to 0.10 sec	0.18 sec
Amplitude	≤ 0.3 mV	0.6 mV in V_1 and V_6 0.8 mV in V_2 and V_5 1.0 mV in V_3 and V_4	≤ 0.5mV in I, II, III ≤ 0.1 mV in precordial
Polarity	Positive I, II, aV_F, V_4 to V_6 Negative aV_R	Positive or equiphasic I, II, V_3 to V_6 Negative in aV_R	Positive I, II, V_2 to V_6 Varied III and V_1 Inverted aV_R
Shape	Upright I, II, aV_F, V_4 to V_6 Inverted aV_R Not notched or peaked	Peaked	Rounded and asymmetric

2.2.2.6 The 12-Lead ECG system

The most commonly used diagnostic ECG systems in modern health care centers use a standard 12-lead ECG system, consisting of three limb leads (I, II, III), three augmented leads (aV_R, aV_L, aV_F), and six precordial leads V_1, V_2, V_3, V_4, V_5, and V_6 [17]. Among the twelve leads, the first six leads: I, II, III, aV_R, aV_L, aV_F originate from the same three measurement locations. This fact leads to the important point that any two of these six leads contain the exact information as the other four leads, as already seen in equation (2.1). However, the 12-lead ECG recording is required for enhanced pattern recognition, which may provide physicians with the opportunity to distinguish the projections of the resultant cardiac vector at different angles and more accurately diagnose problems [6].

Recently, with the growing need for remote monitoring of ambulatory patients and the rise of many hand held ECG monitors, fewer EGC leads are being used to get the maximum information possible. However, clinically the 12-lead ECG system remains the standard to get a comprehensive view of the electrical activity of the heart.

2.2.2.7 Review of intracardiac electrograms

Intracardiac electrogram (EGM) are obtained from the recording of cardiac potentials from electrodes directly in contact with the heart. Intracardiac EGMs record therefore the local electrical activity of the heart i.e. the cardiac tissue surrounding the electrode in contact. All electrical potentials measured by any device are actually measuring difference in potentials between two electrodes. By convention, all clinical EGMs are differential recordings from one source connected to the anodal (positive) input of the recording amplifier and a second source connected to the cathodal (negative) input. Unipolar EGMs represent the potential difference between the electrode in contact with the heart which is also called the exploring electrode and a reference electrode distant from the heart referred as an indifferent electrode and in theory placed at and infinite distance. In practice, the Wilson central terminal is used to approximate the indifferent electrode [21]. Bipolar EGMs represent the potential difference between two electrodes and are calculated as the algebraic difference between the two unipolar EGMs at the two sites using the same reference.

Main characteristic features that distinguish between unipolar bipolar EGM's are based on the spatial resolution, temporal resolution and directionality. Spatial resolution is the ability to locate the discrete area of excited tissue generating the recorded potentials

[22]. Temporal resolution: ability to identify the local activation time which coincides best with the arrival of the depolarization wave front. Directionality is the ability to provide information regarding the direction and the origin of wave fronts [22]. Figure 2-12 shows the relationship between body surface, unipolar and bipolar electrograms. Table 2-2 shows the characteristic features of unipolar bipolar electrograms discussed below.

Unipolar EGM

Spatial resolution: Unipolar EGMs record the activity occurring between the exploring electrode and the reference electrode and, therefore, contain substantial far-field signal generated by the depolarization of remote tissue. Typically, the far-field activity is of much higher amplitude than the local signal occurring at the exploring electrode, and therefore, distant activity can be difficult to separate from local activity [22-23]. Unipolar EGMs have also poor signal-to-noise ratio. Filtering may improve the signal quality by eliminating noise, but it may also alter the signal. Unipolar EGMs reflect the potential generated by the tissue in direct contact with the exploring electrode as well as far field activity.

Temporal resolution: In unipolar recording, the local activation time is positioned at the point of maximum downslope (i.e., maximum negative dV/dt), which corresponds to the maximum sodium channel conductance. It has been shown that using this fiducial point, the error in determining the local activation time is less than 1 millisecond [23].

Directionality: The morphology of unipolar recordings indicates the direction of wavefront propagation and therefore its origin. When the depolarization wavefront is moving towards the recording electrode, a positive deflection is produced. When the

depolarization wavefront is moving away from the recording electrode, a negative deflection is produced.

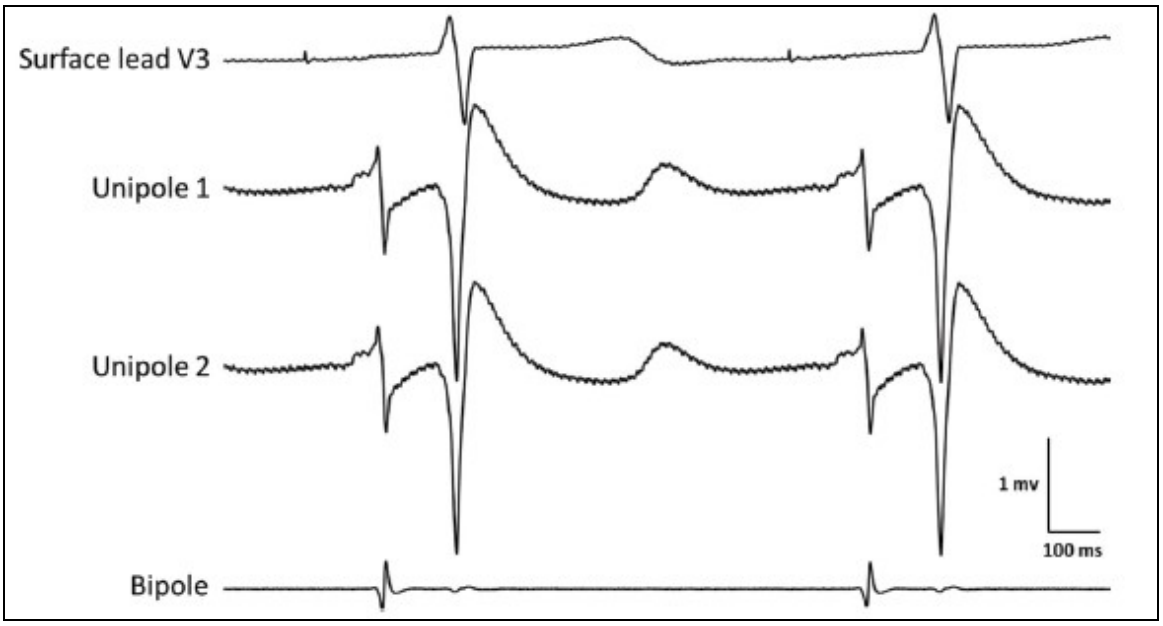

Figure 2-12: Relationship between different types of electrograms; *The top-most plot is the surface lead which illustrates the QRS complex. The next two signals are two closely spaced unipoles; the far-field ventricular activations can be clearly seen in them. The last signal is the resultant bipole of the two unipoles in the figure. It can be clearly seen that the ventricular activations gets canceled giving rise to atrial activations alone. Also, the baseline noise present in unipoles is removed in the bipole signal. (Adapted from [18])*

Bipolar EGM

Spatial resolution: Bipolar EGMs by virtue of subtraction of closely spaced electrodes, eliminate noise and far-field activity, hence improving the signal-to-noise ratio [23]. As a byproduct, high frequency components are more accurately seen. The neat feature of bipolar EGM is that, when the distance from a signal or noise source to the electrodes is larger than the distance between the two electrodes, the noise is recorded quasi-identically by the two electrodes, and efficiently eliminated by subtraction. Moreover, as

the distance from the recording site increases, amplitude and frequency of the recorded signal decrease depending on the inter-electrode distance. Bipolar EGMs reflect the local electrical activity produced by the area of tissue in contact with and between the two electrodes [23]. As the distance between the two electrodes of bipolar recording decreases, the spatial resolution increases.

Temporal resolution: For bipolar EGMs, the detection of local activation times is more difficult due to the generation of the bipolar recordings. Most commonly, the absolute maximum electrogram amplitude is chosen, which correlates with the local activation time that corresponds to the maximal negative downslope (dV/dt) of the unipolar recording. However, in the case of complex fractionated EGMs, this fiducial point cannot be reliably used for determining the local activation time [23].

Directionality: The orientation of the bipolar recording axis with respect to the direction of propagation of the activation wavefront has a direct influence on the morphology and amplitude of bipolar EGMs [23]. When the depolarization wavefront is propagating in the direction exactly perpendicular to the bipolar recording axis, no difference in potential between the recording electrodes is produced, and hence no resulting signal is recorded. As opposed to unipolar EGMs, the direction of wavefront propagation cannot be reliably inferred from the morphology of the bipolar signal, although a change in morphology can be a useful finding [23].

Table 2-2 Summary of unipolar and bipolar EGMs properties in terms of directionality, spatial and temporal resolution (Adapted from [23])

		Unipolar		Bipolar
Spatial resolution	+	Good spatial resolution	+	Reflect the local electrical activity
	–	Contain far-field activity	+	Far-field activity is removed
	–	Poor signal-to-noise ratio	+	High frequency components more accurately seen
			–	Loss of spatial resolution depending on electrode distance
Temporal resolution	+	Precise measure for estimating the local activation time	+	Good for visual or manual assessment of local activation time
	–	Visually difficult to assess the local activation time	–	Less precise for estimating the local activation time
Directionality	+/–	Morphology indicates the direction of wavefront propagation	+/–	Morphology dependent on wavefront direction

2.3 Review of Atrial Fibrillation (AF)

2.3.1 What is AF?

The American Heart Association/ American College of Cardiology/ European Society of Cardiology (AHA/ACC/ESC) guidelines [24] define AF as an uncoordinated electrical atrial activation with consequent mechanical deterioration, associated fibrosis and loss of atrial muscle mass affecting the ability of the atria to pump blood effectively [24-25]. In more general terms, AF or irregular activation of the atria is a spatio-temporal event of an electrical derangement of cardiac excitation and propagation whose

initiation depends on the presence of triggers and its maintenance requires an appropriate arrhythmogenic substrate subsequently leading to a consequent deterioration of atrial mechanical functions. The most common clinical complications for patients whose AF persists are stroke, hypertension, heart failure, coronary artery and valvular heart diseases [26].

On the ECG, AF is distinguishable by the replacement of the P wave with rapid oscillations called atrial fibrillatory waves (f-waves) or a total absence of P-wave without f-waves as seen in Figure 2-13 compared to normal ECG. Generally atrial fibrillatory activity is best seen in lead V1 and its rate is between 300 and 600 bpm. The f-waves vary in amplitude, morphology and period, which may be reflective of various simultaneous atrial activations present at different locations and time within the atria [24].

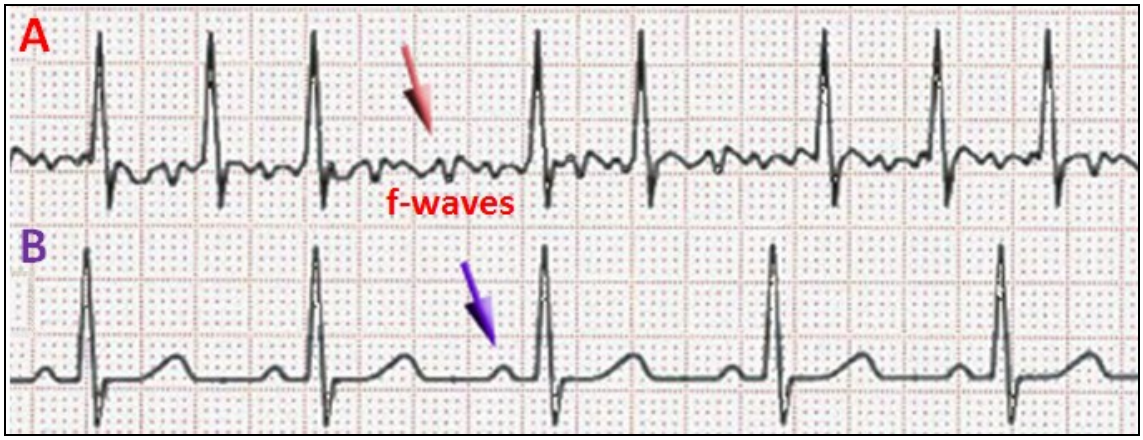

Figure 2-13: Representative example of an ECG with AF (A) showing f-waves and a normal ECG trace (B) *(Adapted from [24])*

2.3.2 Clinical implications of AF

2.3.2.1 AF epidemiology

AF is the most commonly encountered sustained cardiac arrhythmia in clinical practice. Of all type of cardiac arrhythmias related hospitalizations, AF accounts for over one third. Epidemiological studies suggest that, independently of other known predictors of mortality, AF is the cause for doubling death rates [27]. It is estimated that 20% of all strokes are caused by AF and that AF-related events are more severe than strokes of other origin [28]. AF is complicated by hemodynamic impairment such as loss of atrial contractile function, irregular and fast ventricular rate which may lead to a decrease in quality of life for affected patients. Over 33.5 million individuals suffered from AF worldwide in 2010 with 5 million new cases occurring each year and that over the last two decades both the prevalence and incidence of AF have increased drastically [1]. As life expectancy increases, AF prevalence is estimated to double in the next fifty years.

Recent center for disease control (CDC) report suggests an estimated 2.7–6.1 million people in the United States have AF [29]. With the aging of the U.S. population, this number is expected to increase. Approximately 2% of people younger than age 65 have AF, while about 9% of people aged 65 years or older have AF [29]. More than 750,000 hospitalizations occur each year because of AF in the US which contributes to an estimated 130,000 deaths each year. The death rate from AF as the primary or a contributing cause of death has been rising for more than two decades and AF costs the US about $6 billion each year. Medical costs for people who have AF are about $8,705 higher per year than for people who do not have AF [29].

Worldwide epidemiological data on AF suggest that AF can be considered as an emergent global epidemic [1]. It is important to mention that AF may be undiagnosed, and that many patients with AF will never present to hospital [30]. The prevalence of AF increases with age from < 0.5% at 40 - 50 years, to 5 - 15% at 80 years and AF incidence rates are higher in males compared to females [28]. Lifetime risks for developing AF are approximately 25% in subjects older than 40 years, independently of gender [31]. AF is associated with different cardiovascular events the prevention of which is the main goal of therapeutic strategies.

2.3.2.2 Risk factors associated with AF

AF is related to numerous other clinical conditions or risk factors. Most of them contribute to a progressive process in the development of the disease by favoring either the occurrence of AF "triggers" which are responsible for the initiation and/or the formation of "substrate" for AF that is responsible for its perpetuation. Several risk factors are listed below [28]:

- Age increases the risk of developing AF.
- Hypertension is found in most of AF patients. It is an independent predictor of AF and contributes to its progression.
- Thyroid dysfunction in particular hyperthyroidism is associated with AF and may be the only cause for its development.
- Obesity is found in more than a quarter of AF patients.
- Sleep apnea may be a pathophysiological factor for AF especially in association with hypertension or diabetes.

Other conditions are also a risk factor for AF such as coronary artery disease, valvular heart disease, obstructive lung disease, symptomatic heart failure, cardiomyopathies, diabetes and chronic renal diseases [28].

2.3.2.3 Types of AF

In clinical practice, classification of AF is useful for the management of AF patients to characterize the arrhythmia at a given moment based on the clinical presentation and duration of the arrhythmia. According to a recent classification published by the Task Force for the Management of Atrial Fibrillation of the European Society of Cardiology [28] the types of AF are as follows illustrated in Figure 2-14:

First diagnosed AF - a patient presents an AF for the first time, independently of the severity of AF-related symptoms.

Paroxysmal AF- the arrhythmia self-terminates, usually within 48 hours.

Persistent AF - the arrhythmia becomes sustained for a duration longer than 7 days or requires termination by cardioversion

Long-standing persistent AF - the arrhythmia becomes sustained for duration greater than one year.

Permanent AF- when the presence of the arrhythmia is accepted by the physician and the patient. In this category, the cardioversion has failed and if a rhythm control strategy is chosen, the arrhythmia is reclassified in long-standing persistent.

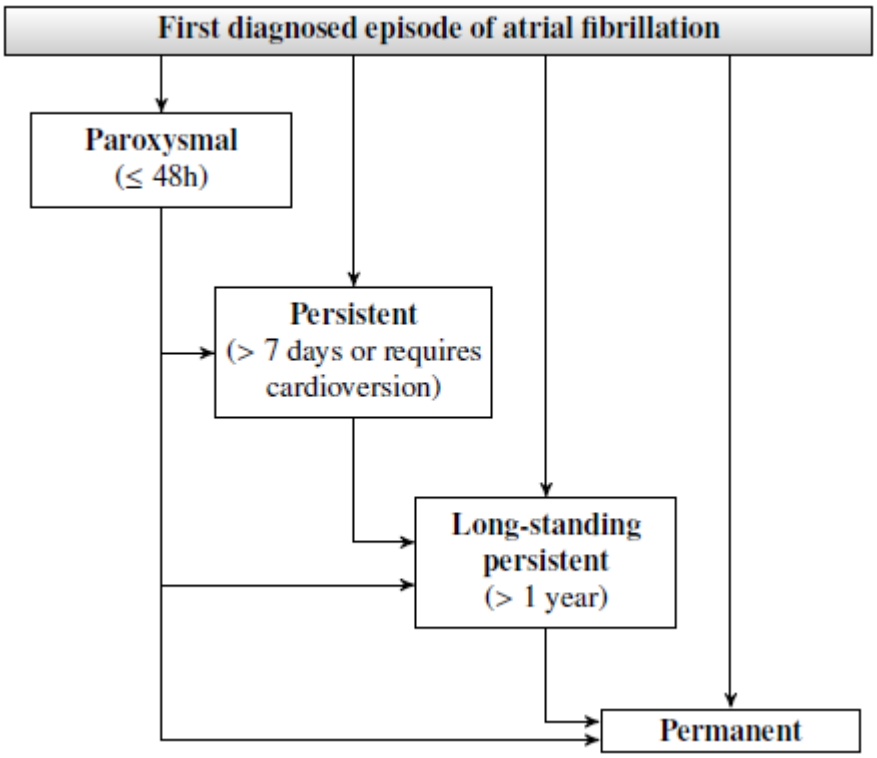

Figure 2-14: Demonstration of the classification of various types of AF *(Adapted from [28])*

2.3.2.4 Symptoms of AF

Patients can experience periods of both symptomatic and asymptomatic AF. Most commonly, AF can be recognized by a sensation of palpitations which are sensations of a racing, uncomfortable, irregular heartbeat or a flip-flopping in one's chest. In patients in whom the arrhythmia has become permanent, palpitations may decrease with time. Other symptoms of AF are weakness, reduced ability to exercise, fatigue, lightheadedness, dizziness, confusion, shortness of breath, chest pain or dyspnea such as respiratory distress [32].

2.3.3 Pathophysiological mechanisms of AF

As discussed in the previous section, AF is an electrical derangement of cardiac excitation and propagation whose '*initiation'* depends on the presence of triggers and its '*maintenance'* requires an appropriate arrhythmogenic substrate. Several mechanisms of AF have been described so far, with the most accepted mechanism being the complex interplay between various triggers that induce arrhythmia via reentry or triggered activity, and myocardial substrates that maintain them. The following section will discuss in detail the mechanisms underlying the initiation and maintenance of AF and the current trend towards a comprehensive understanding on the pathophysiological mechanisms of AF.

2.3.3.1 Focal mechanisms of AF initiation

The hypothesis that AF is initiated by multiple rapid firing ectopic foci that spread across the atria was first introduced in the beginning of the 20th century, highlighted in [33] and later evidenced in an AF modelling experiment [34]. Recently, several researchers have suggested and shown that in most cases AF begins with a rapid focal activity in the pulmonary veins (PVs), and less commonly in the superior vena cava, the coronary sinus (CS), or the left atrial posterior wall [24, 28]. Figure 2-15 shows a posterior view of the atria, and the corresponding locations of the common triggers that may initiate AF. The identification of these triggers is of major clinical importance because any treatment that may eliminate them may be successful in terminating AF. Haisseguerre et al. have shown that the ablation of focal triggers around the PVs could terminate paroxysmal AF [4-5]. It is now well established and accepted by the medical

community that the PVs are a crucial source of triggers in the initiation of AF. The underlying mechanism responsible of focal firing still remains unclear.

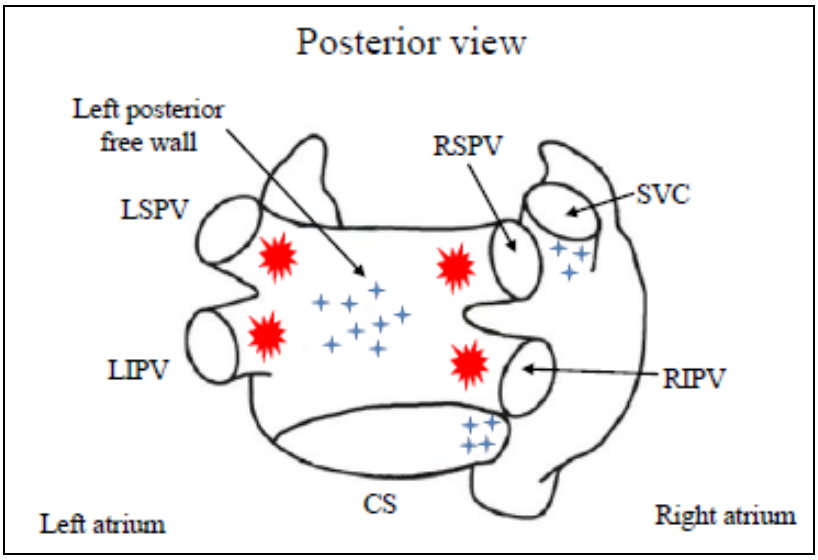

Figure 2-15: Common locations of focal triggers responsible for initiating AF; *The four pulmonary veins (PVs, in red) are the most common source of foci. The four PVs are: left superior PV (LSPV), left inferior PV (LIPV), right superior PV (RSPV), right inferior PV (RIPV). Other sites of AF sources (blue) are the coronary sinus (CS), the superior vena cava (SVC), and the left posterior free wall (Adapted from [8])*

2.3.3.2 Mechanisms for AF maintenance

Once the trigger is set to initiate AF, active substrates are required to maintain AF activity and there are two prominent theories that support the mechanisms behind AF maintenance as below:

2.3.3.2.1 Multiple wavelet theory for AF

For many years, the multiple wavelet hypotheses for AF maintenance were widely accepted as the dominant AF mechanism. The hypothesis was advanced by Moe et al., who proposed a model in which AF is sustained by multiple randomly wandering wavelets colliding with each other and extinguish [35-36]. These wavelets occur

simultaneously throughout the left and right atria and continuously undergo either self-extinction or self-perpetuation such as wave breaks into "daughter" wavelets. Figure 2-16 shows a schematic drawing of the large and small reentrant wavelets.

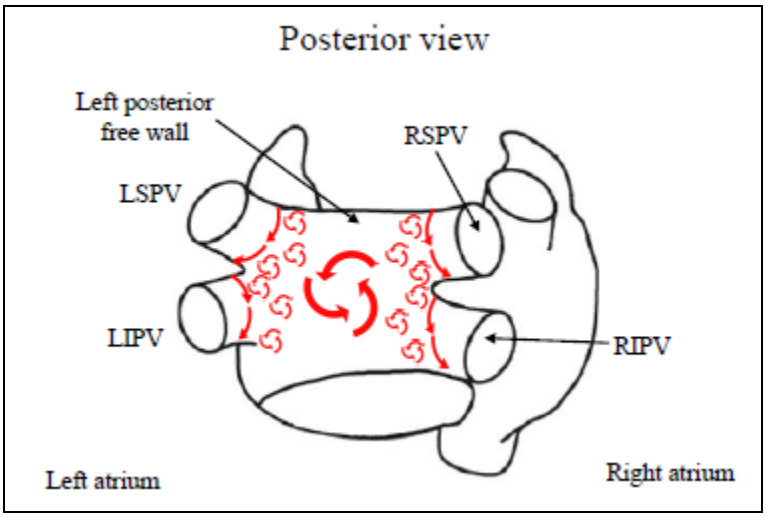

Figure 2-16: Schematic drawing of the large and small reentrant multiple wavelets favoring AF initiation and maintenance *(Adapted from [8])*

Typically, these wavelet circuits have a variable and short cycle length and AF requires the presence of at least four to six independent wavelets to perpetuate [37]. In this model, the number of wavelets depends at any time on the excitable mass, atrial conduction velocity and refractory period in different parts of the atria. The presence of anatomical obstacles such as the PVs also favors the creation of daughter wavelets. The number of wavelets increases with a larger atrial mass, shorter refractory period and delayed conduction. It is more likely that AF is sustained when the number of wandering wavelets increases. The multiple wavelet hypotheses have been subsequently confirmed by experimental work [38-39]. However, in recent mapping studies of small atrial regions, this model has recently been challenged and does not easily explain clinical

observations of AF termination by limited ablation at PVs [40-42] or other sites [43,44], or the above evidence for spatiotemporal stability in AF.

2.3.3.2.2 Reentrant mechanism theory for AF

Another popular theory for AF maintenance is the reentrant mechanism where some authors have shown in isolated sheep hearts that, in the presence of an appropriate heterogeneous AF substrate, a focal trigger usually localized in one PV can result in a single meandering functional reentrant stable electrical driver called as *'rotor'* [45]. Now substantial data support rotors as localized sources for AF, first postulated by Mines and Lewis, then reported in seminal studies by Schuessler, Cox and Boineau [39, 46] who showed that AF may be sustained by stable drivers and by Jalife et al [6, 47] who demonstrated electrical spiral waves or rotors that perpetuate AF in various models. The term rotor applies to the organizing source of functional reentrant activity which is the structure immediately surrounding the pivot of a rotating wave in two or three dimensions. This model is illustrated in Figure 2-17 which shows the presence of a single source of stable reentrant activity, i.e., the mother circuit, with high frequency wave fronts emanating from a focal trigger located within the left superior PV (LSPV).

When conditions of heterogeneity are adequate, the wave fronts break and initiate two counter-clocking vortices. Alternatively, only one of the vortices remains shown in red plain line in Fig. 2-17 and are responsible for maintaining AF. The reentrant mechanism can occur as anatomic reentry or functional reentry [48] as shown in Figure 2-18. In anatomical re-entry, circuit size is determined by fixed anatomic obstacles (Fig 2-18 left). In functional re-entry (Fig 2-18 middle), circuit size = conduction velocity x refractory

period which is the length of the refractory tail. If the wavefront travels too quickly, or its refractory period is too long, its leading end would “bite its tail” and extinguish itself (Fig 2-18 right) the properties of which determine the smallest possible circuit size [48].

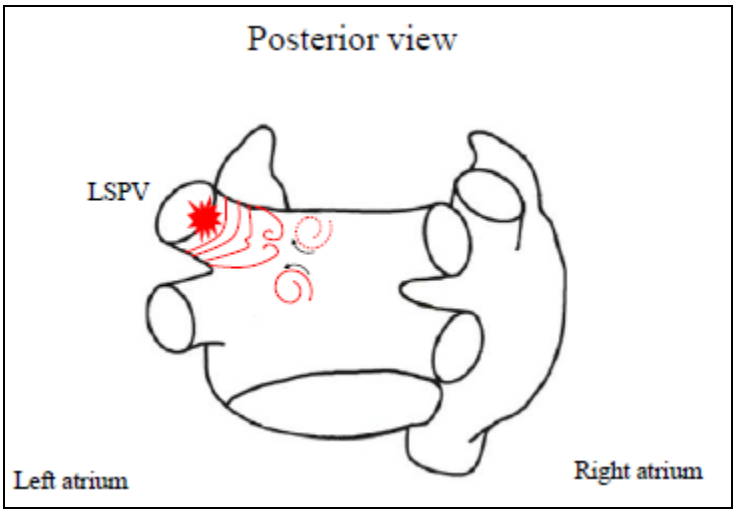

Figure 2-17: Schematic drawing of the mother circuit reentrant mechanism resulting in rotors *(Adapted from [8]).*

The waves emerging from the rotor may undergo spatial fragmentation upon anatomical obstacles such as PVs or scars leading to the formation of multiple wavelets spreading out in multiple directions at varying conduction velocity with fibrillatory conduction. The dominant rotors responsible for driving AF generally originate and anchor within the LA while the RA is being activated passively [50]. Indeed, ablation at AF rotor pivot point was recently shown to suppress AF in a canine model [50]. Indirectly, stable sources for human AF explain localized regions of stable high dominant frequency [51-54] and consistent activation vectors over time [55]. Reentrant approach shows more organization and stability in its pattern of wave propagation. Although, rotors or spiral waves has been shown to underlie various types of ventricular and atrial

arrhythmias, there is an ongoing debate on the precise nature, location and mode of initiation of those reentrant sources.

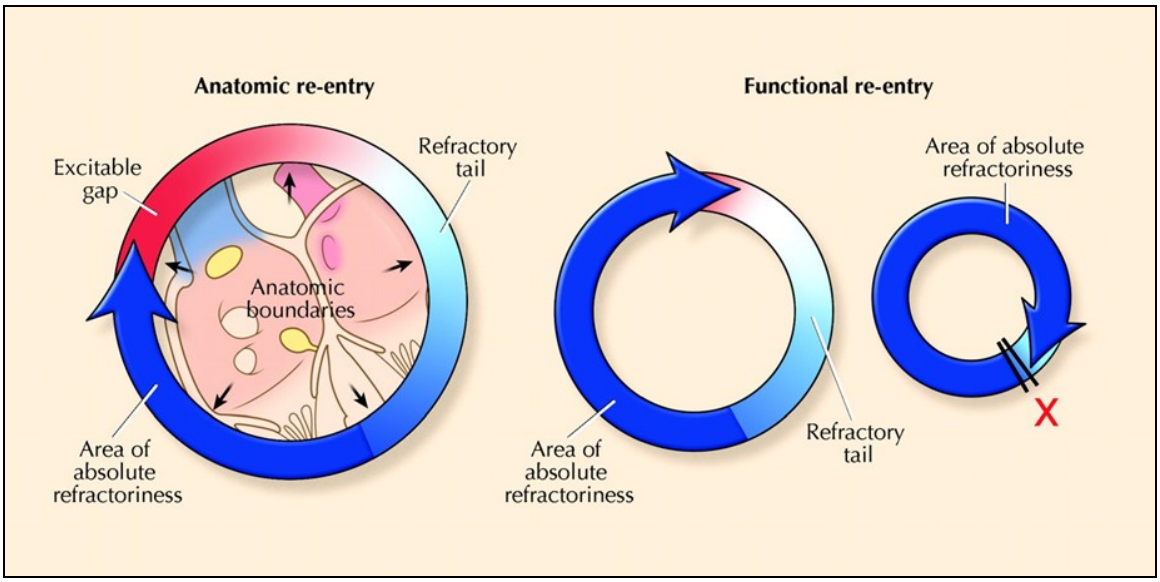

Figure 2-18: Schematic of anatomic versus functional re-entry. *(Adapted from [48])*

Multiple wavelet theory faces a growing challenge as it does not explain how certain anti-arrhythmic drugs work. Example, antiarrhythmic drugs that block Na^+ channels are effective in terminating AF, but should promote AF because they decrease conduction velocity and consequently decrease the AF path wavelength. Recent evidences have brought the scientists back to the beginning of the twentieth century debates suggesting that ectopic activity, localized re-entrant circuit with fibrillatory propagation and multiple circuit re-entries may all be involved in human AF [56] as seen in Figure 2-19.

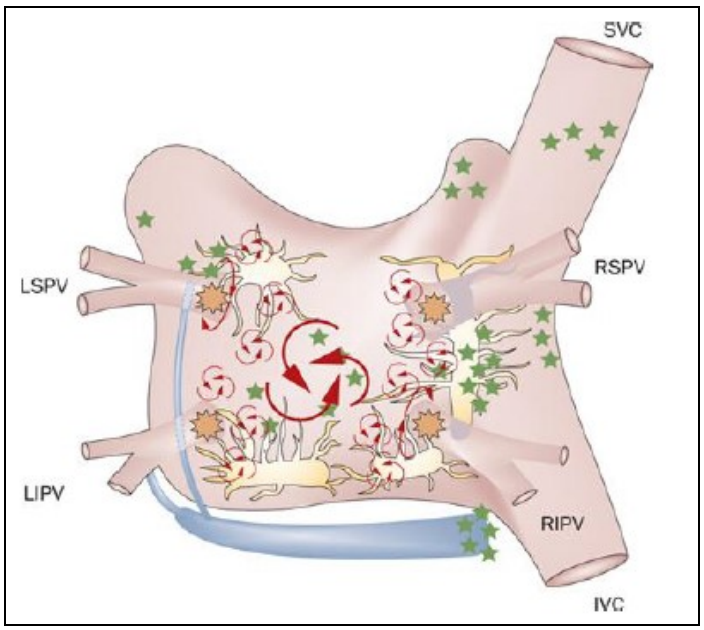

Figure 2-19: The anatomical and arrhythmic mechanisms of AF *(Adapted from [56])*

2.3.3.3 Review of the presence and stability of rotors in AF

Recent research supports strong evidence for the presence of hierarchical spatiotemporal organization in AF both in animal models and in humans [49, 54-60] that is inconsistent with the multiple wavelet hypotheses and suggests AF maintenance by localized sources or rotors. Figure 2-20 highlights the current hypothesis for AF maintenance where Fig. 2-20 A shows the diagram of AF maintenance near a PV that has been hypothesized to be driven by ectopic focus (Fig. 2-20 A-left), rotors (Fig. 2-20 A-middle) or multiple wavelets (Fig. 2-20 A-right) and different wave fronts are represented in purple [61]. Fig. 2-20 B shows a representation of the compatibility of rotor maintenance with other mechanisms. Rotors can be initiated by wave breaks near an ectopic focus (Fig. 2-20 B-left) and underlie endocardial or epicardial breakthroughs (Fig. 2-20 B-middle). A drifting rotor, whose trajectory is depicted in blue, can be the driver of multiple and apparently disorganized atrial wavelets (Fig. 2-20 B-right) [61].

Discrete atrial fibrillatory sources have been hypothesized to be either ectopic foci [11, 62] or rotors [45]. Rotors are formed through functional reentry as its action potential circulates around an excitable but unexcited core [63-65]. Rotors can be initiated by a focal discharge including a sinus wave due to a wavefront break, as illustrated in Fig. 2-20 B implying that the focal and rotor hypotheses as AF drivers are not mutually exclusive. In addition, repetitive surface breakthroughs of activations may actually be the consequence of hidden intramural reentry [66-67] and the presence of drifting and fast rotors anywhere can explain the presence of multiple wavelets in their periphery. Therefore, the hypothesis that rotor is an underlying AF mechanism is compatible with both the presence of focal discharges and multiple wavelets [61].

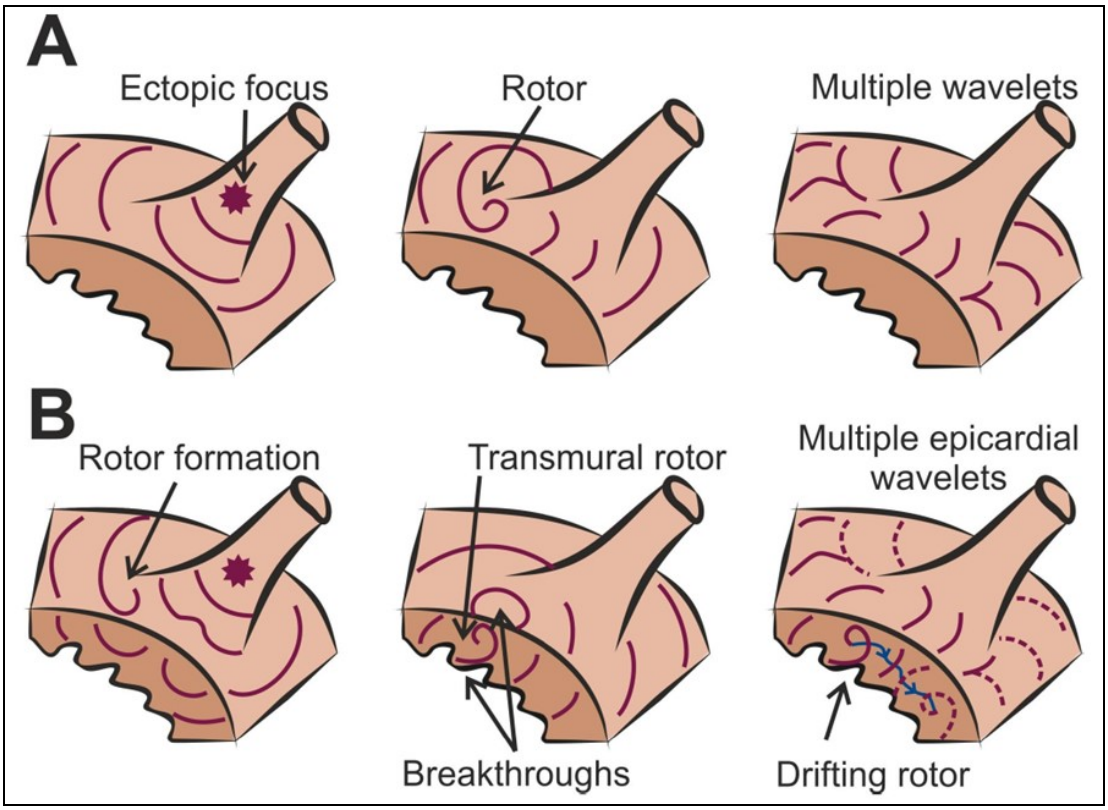

Figure 2-20: Schematic of current hypotheses for AF maintenance *(Adapted from [61])*

Ex vivo animal experimentation using Langendorff-perfused isolated hearts models using optical mapping technology (discussed in section 2.5) has shed light into deeper understanding and growing knowledge on rotors and their role in AF [59, 68]. Several experimental, numerical and theoretical studies have looked at the various factors that contribute to rotor drift causing meandering rotors [69-83]. Rotors consist of a wavefront and a wave tail, and they may rotate about a functional center called the rotor core or pivot point shown in Figure 2-21. The region away from the core is the rotor periphery. The gap between the front and the tail is the wavelength of the rotor. A rotor propagates with a conduction velocity, and rotates following a periodic cycle length [18]. The velocity vectors at the wavefront of a rotor are also illustrated in Figure 2-21. Ablation at AF rotors targeting the pivot point was recently shown to suppress AF in a canine model [50] which now supports the growing consensus of AF maintenance by rotors.

EGMs provide a direct relationship between wave front direction and wave amplitude [84]. The wave front of electrical signal changes its direction near the rotor pivot point, thus leading to changes in electrogram morphology and information content.

Electrogram from the pivot zone might consist of:

- early local deflections as the wave front initially passes
- secondary deflections consisting of inverted double split
- potentials as the wave front turns, and
- intermediate electrical activity between initial and inverted potentials.

Electrograms from the periphery of rotating waves should have relatively stable morphology, due to consistency of wave front direction approaching these locations.

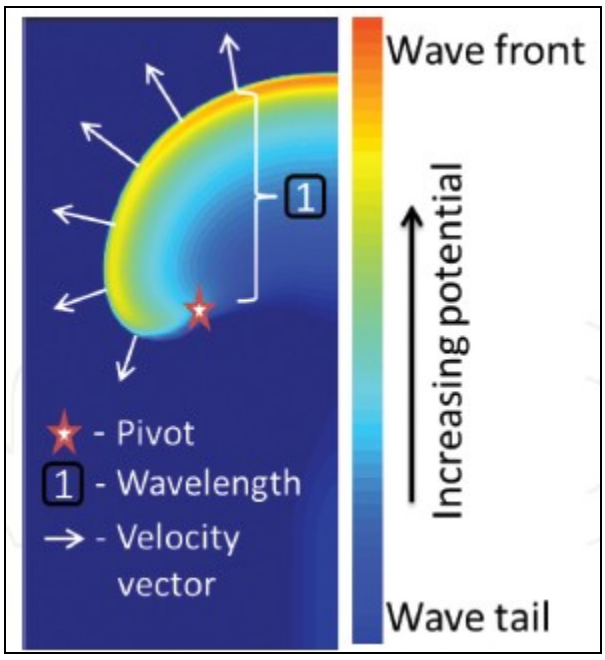

Figure 2-21: Schematic showing propagation of a rotor wave. *The different components of a rotor wave are illustrated in the figure. The arrows points in the direction of the wavefront propagation. (Adapted from [18])*

With the growing consensus with the rotor mechanisms several groups have attempted rotor mapping in human AF with invasive catheter mapping [7, 85-86] discussed in detail in section 2.7. Non-invasive rotor mapping is also gaining steady attention, with the ability of body surface potentials mapping to detect rotors and stable propagation patterns during AF [87]. An inverse-solution ECGI system [88-89] is also reported to have some success in rotor mapping during AF. Nevertheless, novel research is being attempted to better understand rotor mechanisms and strategies to map rotor core which is believed to be suitable ablation targets to terminate AF. Figure 2-22 shows the first study demonstrating the presence of rotors in human AF through phase mapping technique in both right and left atria [90]. This study also demonstrated 86% success rate in terminating AF in persistent AF patients by targeting rotor core through their FIRM trial.

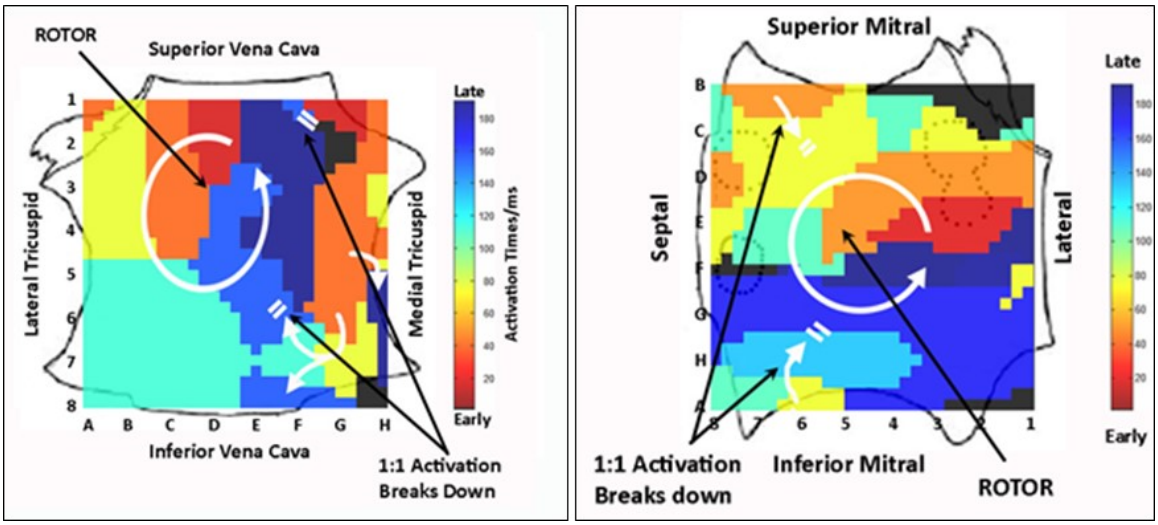

Figure 2-22: Demonstration of rotors driving human atrial fibrillation. *(Left) shows the rotor activity in the right atria and (Right) shows the rotor activity in the left atria (Adapted from [90]).*

2.3.3.4 AF initiation and maintenance through atrial remodeling

The atria may display some electrical and structural remodeling over time which may favor the maintenance of AF. Electrical remodeling refers to the modifications primarily affecting excitability and action potentials characteristics while the changes in atrial volume and tissue structure are referred to as structural remodeling. Contractile remodeling refers to the hemodynamic impairment such as loss of atrial contractile function. Experimental studies have shown that electrical and structural remodeling play a major role in the initiation and maintenance of AF [91]. Each of these remodeling affects the atrial function and structure at different stages of the disease. The electrical remodeling develops within the first days of AF and results from high frequency atrial activations, decreasing rapidly the atrial ERP [91]. It has been observed in clinical practice that the time course for persistent AF development is slower than that of the electrical remodeling wherein structural remodeling takes weeks to months after AF

onset leading to long-standing or permanent AF. Therefore, atrial remodeling seems to have significant impact in AF initiation and maintenance for all types of AF.

2.3.4 Clinical management of AF patients

The clinical management of patients with AF [28] is aimed at the following three approaches:

- Preventing thromboembolism – The patients are evaluated for the risk of stroke to determine the need for anticoagulation. Many studies have shown that in the presence of such risk factors patients with paroxysmal AF appear to have an equivalent stroke risk to those with persistent or permanent AF. Therefore, preventing thromboembolism is an essential clinical management strategy.
- Rate control - AF is characterized by a rapid heart rate that may decrease the cardiac output. During AF, rate control is important to prevent hemodynamic distress in AF patients. The main goal of a rate control therapy is to target a ventricular rate between 60 to 80 bpm at rest and 90 to 115 bpm during exercise. The criteria for rate control vary with patient age. However, an adequate ventricular rate control therapy should target a decrease in symptoms and improve hemodynamics.
- Rhythm control - Rhythm control is aimed at restoring and maintaining the sinus rhythm. The restoration of the heart normal rhythm is called a cardioversion.

These three approaches are not mutually exclusive; they can be pursued in parallel. For each patient the clinician shall establish an overall strategy considering several factors such as the patient's age, the type and duration of AF, the severity of symptoms, the

associated cardiovascular disease or medical conditions, short or long-term treatment goals, and therapeutic options such as pharmacological or non-pharmacological approach [28] which is discussed in the following section.

2.3.4.1 Pharmacological therapies for AF management

Rate control

Since rate control strategies attempt to restore normal ventricular rate, the conduction characteristics and refractoriness of the AV node as well as the sympathetic and parasympathetic tones are the main targets for clinical management. Moreover, the functional refractory period of the AV node is inversely correlated with the ventricular rate [24]. Therefore, drugs prolonging the AV node refractory period are generally effective for rate control. The most commonly prescribed drugs are beta-blockers, non-dihydropyridine calcium channel antagonists, digoxin, digitalis, and amiodarone.

Rhythm control

Pharmacological cardioversion of AF may be initiated by the administration of antiarrhythmic drugs such as flecainide, propafenone, sotalol, amiodarone or ibutilide [24].

Rhythm versus rate control

For patients in whom AF related symptoms are considered tolerable (typically the elderly), a rate control strategy may be appropriate. Studies such as AFFIRM and RACE that compared rate control and rhythm control therapies demonstrated that regardless of the selected strategy, embolic events occur with equal frequency after interruption of

anticoagulation [92-93]. Therefore, clinical management of symptomatic AF may differ from one patient to another according to the guidelines shown in Fig 2-23.

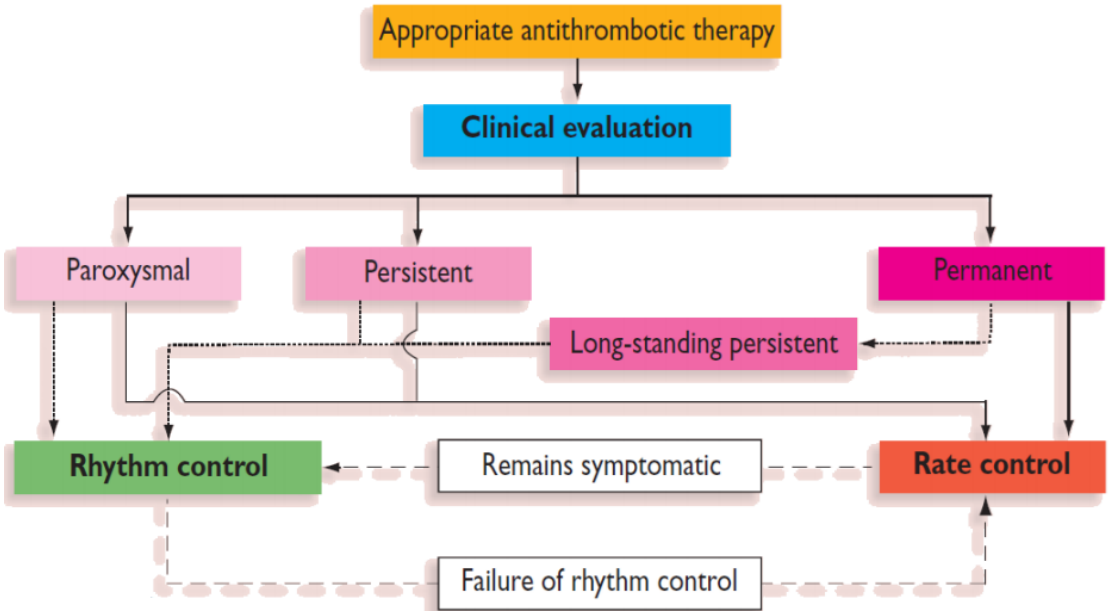

Figure 2-23: Schematic illustrating the choice of rate and rhythm control strategies from ESC 2010 guidelines *(Adapted from [24])*

For symptomatic patients with AF lasting several weeks, the initial therapy should be rate control and anticoagulation. When rate control does not provide sufficient symptom relief, restoration of sinus rhythm may become a long-term goal that may be achieved with non-pharmacological approaches discussed in the following section.

2.3.4.2 Non pharmacological therapies for AF management

Direct-current cardioversion of atrial fibrillation

Direct-current cardioversion (DCC) is a non-pharmacological method for restoring sinus rhythm in AF patients and is generally preferred to a pharmacological approach because of greater efficacy [94]. As cardioversion is associated with an increased risk of thromboembolism, anticoagulation must be initiated several weeks before. DCC consists

in delivering an electrical shock in synchronization with the ventricular activation. It is important to ensure that the electrical shock does not occur during the vulnerable phase of the cardiac cycle such as the T-wave [94]. Most commonly, the current is delivered through special external chest electrodes which are located on either side of the heart or in an antero-posterior configuration. In both configurations, the electrical current delivered between the patches spreads through the heart. Traditionally, the energy output is successively increased in increments of 100 J to a maximum of 400 J [24]. Because the shock is uncomfortable, DCC is performed under general anesthesia. Recurrences after cardioversion can be divided into three phases:

- immediate (seconds to minutes after DCC);
- early (five days after DCC);
- late (more than five days after DCC)

Factors that predispose to AF recurrence are age, AF duration, number of previous DCCs, and a dilated left atrium.

Surgical ablation using Maze procedure

In the 1980s, several studies have identified important factors involved in the termination of AF surgically. The main tenet for the surgical approach is that reentry underlies the development and maintenance of AF and, that atrial incisions at critical locations would produce barriers to the conduction of AF [95] which led to the development of a surgical procedure called maze [96] which went through different iterations of continuous improvement. Results appeared quite effective over fifteen years of follow-up success rates from 75 - 95% have been reported, but decreased in the most

recent studies using long-term ECG recordings [28]. The maze procedure is complex mainly because of the need for cardiopulmonary bypass and requires extensive lesions precluding the atrial function.

Catheter ablation

Radiofrequency catheter ablations techniques were developed for terminating AF in the 90's following the maze procedure by performing linear lesions from the atrial endocardium, i.e., inside the atria [97]. Currently, AF catheter ablation is the cornerstone of non-pharmacological AF therapy. Radiofrequency catheter ablation of AF is discussed in detail in the following section.

2.4 Review of catheter ablation for AF

Catheter ablation treatment for AF has evolved from an experimental procedure to a common procedure and is being widely performed throughout the world to terminate AF and other complex arrhythmias. The following section will elaborate on the technologies and approaches taken for perform catheter based ablation in a clinical setting.

2.4.1 Contemporary catheter ablation technologies and tools

2.4.1.1 Accessing ablation targets inside the heart

From clinical perspective, catheter ablation is considered as a minimally invasive procedure as no major incision is necessary [98]. Figure 2-24 illustrates the steps taken for performing catheter ablation in cardiac catheterization laboratory. Two types of catheters namely mapping and ablation catheter are inserted within the heart using blood vessels, typically the left and/or right femoral veins which are then advanced into the right atrium via the inferior vena cava. Mapping catheter captures the 3D anatomic

information of the atria which is used for real-time visualization for ablation guidance. The ablation catheter carries the energy source to be delivered at the selected target region. Drivers of AF are thought to be mainly localized within the left atrium which is separated from the right atrium by an interatrial septum. In order to access the left atrium, a trans-septal puncture must be performed [98].

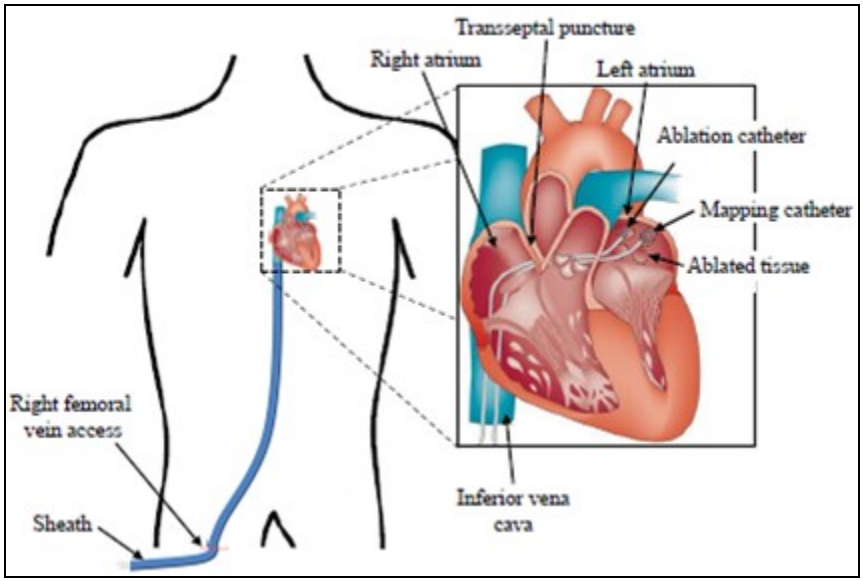

Figure 2-24: Schematic illustration of catheter ablation procedure in cardiac catheterization lab. *Catheters are inserted within the heart using the right femoral vein and enter the right atrium through the inferior vena cava. A trans-septal puncture is performed in order to introduce the catheter within the left atrium (Adapted from [98]).*

2.4.1.2 Ablation using different energy sources

The most dominant energy source used for catheter ablation is by far the radiofrequency energy (RF) which is electrically conducted. Other sources used are microwave energy and cryo-ablation which are gaining popularity [99]. With RF ablation, a unipolar alternating current at a frequency of 500 kHz is delivered from the ablation catheter tip to a dispersive indifferent electrode applied on the patient's skin. RF

current heats up the cardiac tissue to produce variable amount of myocardial edema and necrosis. The assumption of successful AF ablation is the creation of lesions that block the propagation of AF wave fronts [99]. The time and amount of energy delivered to the target region are carefully monitored and controlled to deliver the right amount of energy as real-time lesion monitoring is an ongoing challenge to guide ablation. Various configurations of the mapping and ablation catheters are available in the market.

2.4.1.3 Review of electroanatomical mapping system

Catheter ablation procedure combines mapping and ablation that require accurate navigation within both the atria [100]. Commercially there are several electroanatomical mapping systems available. Few are listed below:

- CARTO System – Biosense Webster, Diamond Bar, CA
- EnSite NavX – St.Jude Medical, Minneapolis, MN
- ECVUE System – CardioInsight, Cleaveland, OH
- RhythmView – Topera Inc, Menlo Park, CA

These electroanatomical systems are aimed both at reconstructing a 3D shell of any cardiac structures, including the atria, and at visualizing on a real-time basis all catheters simultaneously [100]. Figure 2-25 shows the commercially used CARTO and EnSite NavX system. Also, it allows tagging specific sites of interest for future diagnostic maneuvers and ablations. The mapping system may also be classified as invasive and noninvasive as below:

- Invasive Basket Mapping: e.g. Topera Inc.
  - Pros: provides localized contact mapping

- Cons: may not capture all tissue surfaces

❖ Non-invasive Mapping: e.g. CardioInsight Inc.

- Pros: provide panoramic biatrial mapping
- Cons: provides global wave propagation and doesn't capture small PV signals

Figure 2-26 shows the commercially used invasive Topera Inc.'s FIRM mapping catheter and the isochronal map generated from the system and the single use disposable body electrode vest and 3D electroanatomic map obtained from CardioInsight Inc.

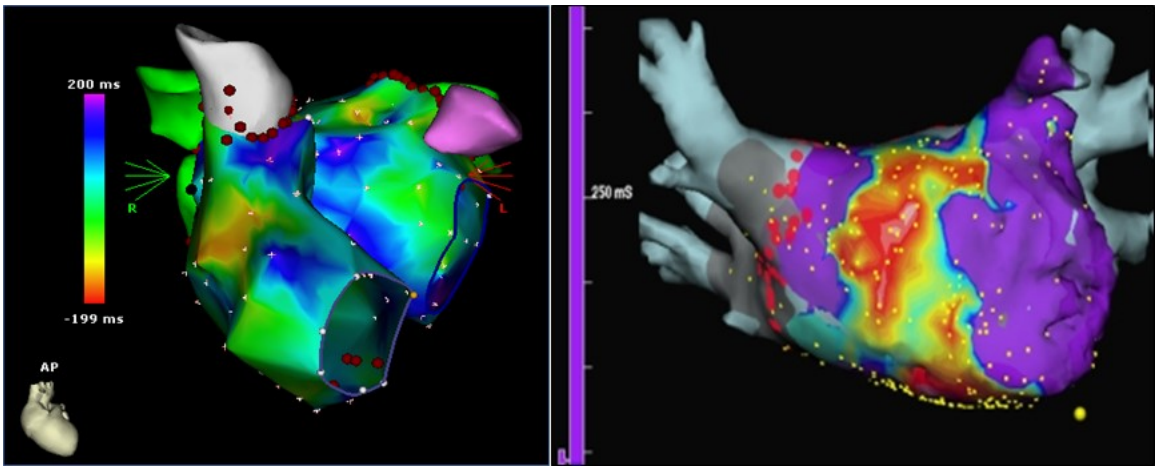

Figure 2-25: Examples of 3D visualizations from electroanatomical mapping system. *Top shows the CARTO system from Biosense Webster Inc.; Bottom shows the EnSite NavX system from St.Jude Inc.*

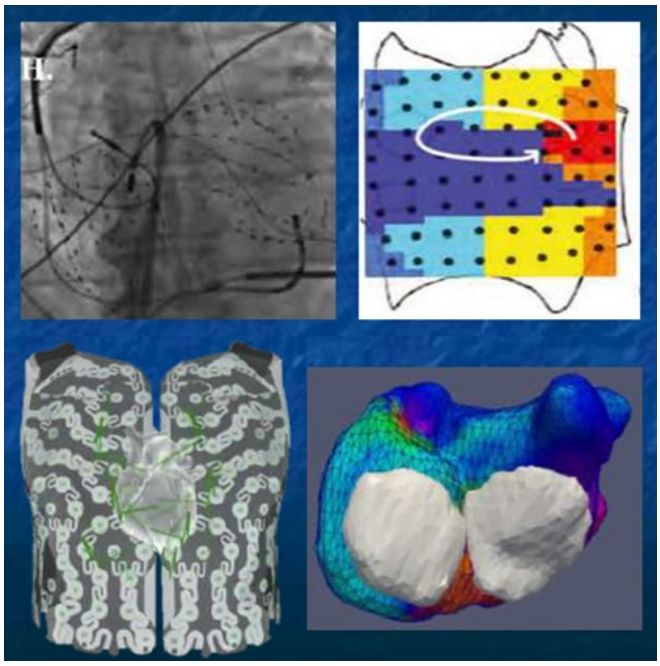

Figure 2-26: Examples of invasive and noninvasive electroanatomical mapping system. *Top shows invasive FIRM contact mapping catheter and isochronal map from Topera Inc.; Bottom shows single use disposable body electrode vest and 3D electroanatomic map obtained from CardioInsight Inc.*

2.4.2 Review of pulmonary veins isolation ablation

Pulmonary veins isolation (PVI) was primarily developed to terminate paroxysmal AF which is commonly initiated by a rapid focal activity coming from the PVs. The procedure involves ablation procedure in which the PVs were electrically isolated [4]. This technique is segmental and involves the sequential identification and ablation of the earliest sites of activation of each PV which is achieved using a circumferential mapping catheter. More recently, PVI involves placing lesions wherein each PV is totally encircled with RF lesions in a figure-of-eight like fashion [101-102]. The main endpoint of PVI procedure is the complete electrical isolation or disconnection of all four PVs. Figure 2-27 shows schematic illustrating PVI ablation.

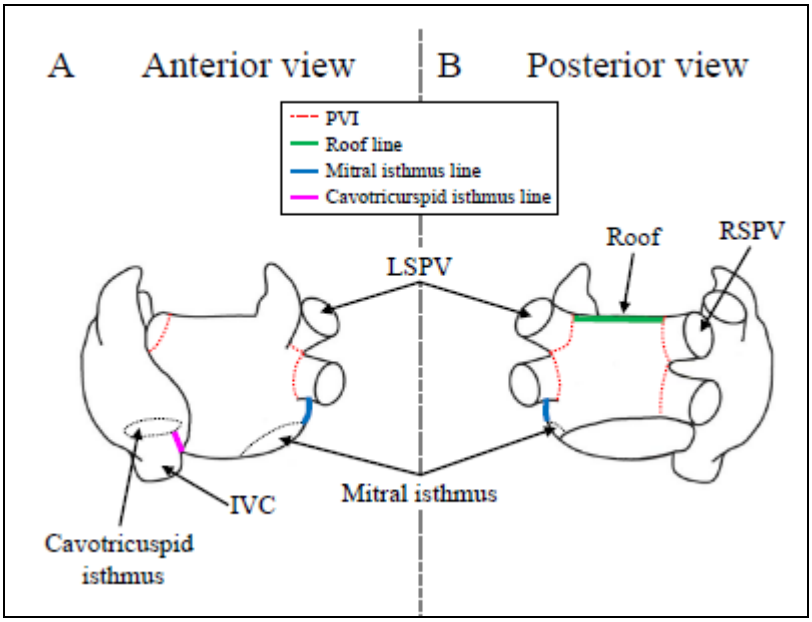

Figure 2-27: Schematic showing PVI and linear atrial ablation. *(Adapted from [98])*

Achieving successful end point for PVI does not ensure permanent electrical isolation of the 4 PVs and 70% success rates has been reported for paroxysmal AF patient [9, 103]. However for non-paroxysmal AF patient's success is less than 30% [10] implying the limitation of PVI indicating that once AF has become sustained, the PVs may play a less critical role in maintaining AF. Active substrates may be present outside the PVI region that initiate and maintain AF in non-paroxysmal AF patients which needs novel strategies to specifically locate and ablate those regions to permanently terminate AF.

2.4.3 Review of linear atrial ablation

The limited success rate of PVI for non-paroxysmal AF patients suggests that a residual substrate is responsible for maintaining AF. Therefore alternative ablation strategies have been attempted in non-paroxysmal AF patients to perform linear lesions covering the LA roof line, LA mitral isthmus line, and/or RA cavotricuspid line as illustrated in Figure 2-27. The endpoint of linear ablation is the effectiveness of

bidirectional conduction block across each line which is confirmed by performing differential on either side of the lines [98]. Many studies have shown the improved success rate of combining linear ablation with PVI [104-106]. However, the recurrence rate is still high which requires investigating of more strategic ablation strategies that embraces the currently accepted hypothesis of AF maintenance shown in Fig 2-20.

2.4.4 Review of complex fractionated atrial electrograms ablation

Recently, Nademanee et al. proposed ablation at sites with high continuous frequency activities described as complex fractionated atrial electrograms (CFAEs) defined as [107]:

1. Atrial EGMs that are fractionated and composed of ≥ two deflections, and/or have a perturbation of the baseline with continuous deflections of prolonged activation complex over a 10 s recording epoch.

2. Atrial EGMs with a very short cycle length (≤120 ms) averaged over a 10 s recording epoch.

CFAEs are believed to be involved in AF maintenance as fractionated and continuous activity may be indicative of the presence of wave collision, and rotors with pivot points where the wavelets turn around [107]. The primary endpoints of CFAEs ablation are either complete elimination of areas with CFAEs, and/or AF termination. CFAE ablation has been shown to restore sinus rhythm in non-paroxysmal AF patients, but the procedure results in extensive atrial lesions that might affect restoration of atrial contractility [108]. More discussion of CFAE is presented in sections 2.7.4.

2.4.5 Review of the CABANA Trial

The **C**atheter **Ab**lation versus **An**tiarrhythmic Drug Therapy for **A**trial Fibrillation (CABANA) trial is being done to compare drug therapy with catheter ablation in patients with atrial fibrillation [109]. This study will help to decide which treatment approach is best and if under certain circumstances, one therapy is preferred over the other treatment. The CABANA study will also compare the cost of care for the two treatment approaches and determine the effect these therapies have on quality of life. CABANA is a global clinical research trial which is currently being conducted in ten countries. In addition to the United States and Canada, international investigators are located throughout Europe, Asia and the Pacific.

The CABANA trial has the overall goal of establishing the appropriate roles for medical and ablative intervention for AF. The CABANA trial is designed to test the hypothesis that the treatment strategy of left atrial catheter ablation for the purpose of eliminating atrial fibrillation (AF) will be superior to current state-of-the-art therapy with either rate control or rhythm control drugs for decreasing the incidence of the composite endpoint of total mortality, disabling stroke, serious bleeding, or cardiac arrest in patients with untreated or incompletely treated AF. The primary and secondary outcomes of this trial are discussed below [109]:

Primary Outcome Measures

LA catheter ablation is superior to rate or rhythm control drug therapy for decreasing the incidence of the composite endpoint of total mortality, disabling stroke, serious

bleeding, or cardiac arrest in patients warranting therapy for AF. [Time Frame: From date of enrollment until date of event]

Secondary Outcome Measures

- LA catheter ablation is superior to rate or rhythm control drug therapy for reducing total mortality [Time Frame: From date of enrollment until date of death]
- Total mortality or cardiovascular hospitalization [Time Frame: From date of enrollment until date of death or CV hospitalization]
- Cardiovascular death [Time Frame: From date of enrollment until date of death]
- Cardiovascular death or disabling stroke [Time Frame: From date of enrollment until date of event]
- Arrhythmic death or cardiac arrest [Time Frame: From date of enrollment until date of event]
- Heart failure death [Time Frame: From date of enrollment until date of event]
- Freedom from recurrent AF [Time Frame: From date of therapy initiation until date of first AF recurrence following a 90 day wait period]
- Cardiovascular hospitalization [Time Frame: From date of enrollment until date of hospitalization]
- Medical costs, resource utilization, and cost effectiveness [Time Frame: From date of enrollment through follow-up (average of 5 years)]
- Quality of Life [Time Frame: At months 3, 6, 12, 18, 24, 30, 36, 42, 48, 54, 60]

- ❖ Composite adverse events [Time Frame: From date of enrollment until date of event]
- ❖ Left atrial size, morphology and function and its relationship to morbidity and mortality [Time Frame: Baseline compared with 3-6 months post therapy initiation]

The outcome of this study will be crucial in determining the right strategy for AF treatment worldwide, and the future scope of catheter ablation depends on positive primary outcomes of this trial.

2.5 Review of optical mapping technique

Optical mapping is an imaging technique which allows for a simultaneous recording of electrical properties from a number of sites on the myocardial surface, unlike a microelectrode recording which measure the action potential from a single site [110-111]. An optical mapping system consist of five main components as below, shown in Figure 2-28.

(i) Heart tissue stained with voltage-sensitive fluorescence dye such as RH-237, Di-4-ANNEPS or Di-8-ANNEPS.

(ii) A light source such as tungsten-halogen lamps or lasers focused on the heart to excite the dye.

(iii) A photo detector that consists of photodiode arrays or CCD cameras to collect the fluoresced light from the heart,

(iv) A system of optics to illuminate the tissue, filter the emitted light and focus the image onto the photo detector, and

(v) Acquisition system to collect, display and store signals from the photo detection system.

As seen from Fig. 2-28 a typical optical mapping system consisting of three major components [112]: (i) the heart preparation; (ii) a system of optics; and (iii) a detector.

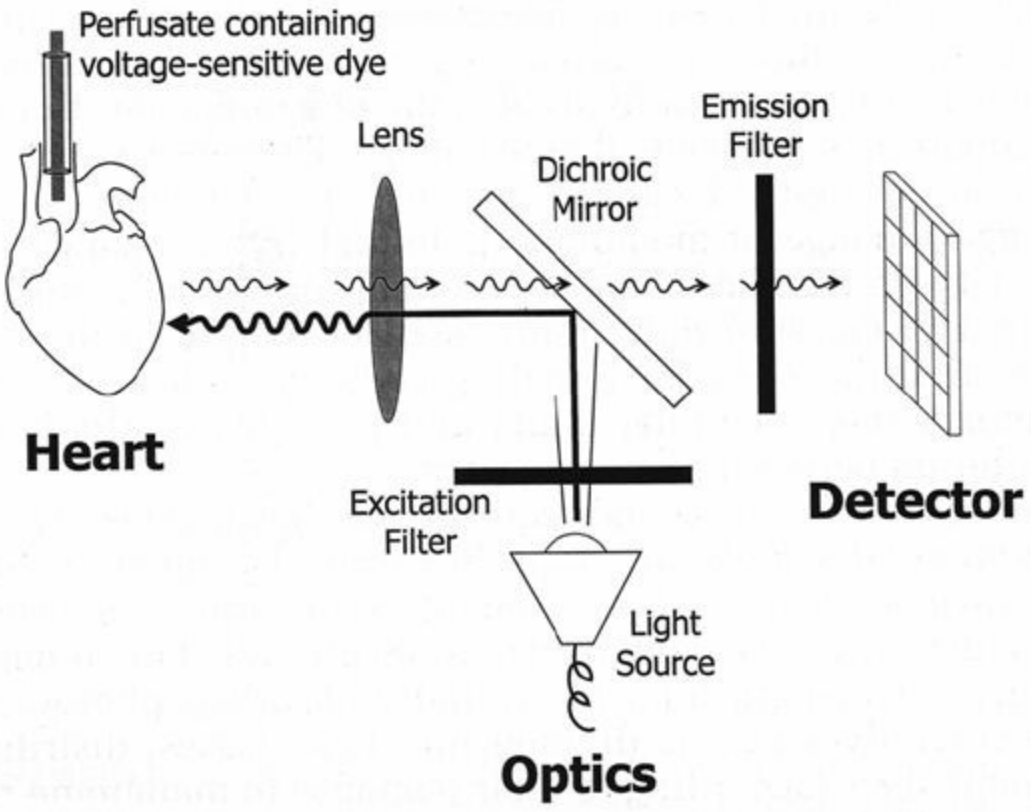

Figure 2-28: Schematic of an optical mapping setup to record membrane voltage from multiple epicardial sites. *(Adapted from [112])*

The data is collected and processed offline to obtain the phase representation (between $-\pi$ and π radians) which can be computed using the Hilbert transform that allows estimating the phase of the action potential over each cycle of the signal for varying cycle lengths, amplitudes and morphologies. In particular, a phase map enables the identification of the wavefront without the detection of activation times, and further

shows its direction of propagation. Points in the phase map toward which all phases converge to, are designated as singularity points (SP) and depict the instantaneous pivoting point of the wave. Figure 2-29 shows the first experimental demonstration of spiral waves in ex vivo rabbit heart with induced ventricular fibrillation (VF) [113].

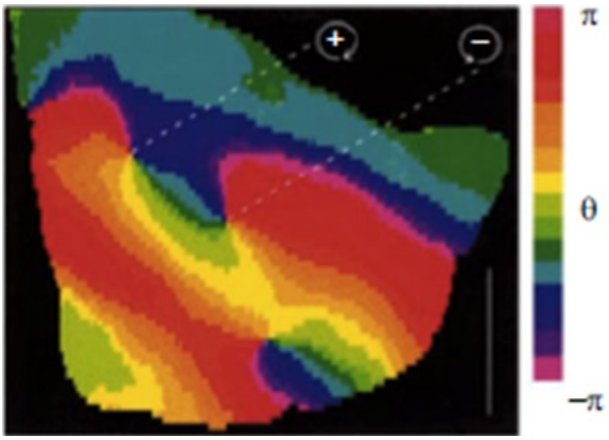

Figure 2-29: Example of optical mapping of cardiac electrical activity in ex vivo rabbit heart. *First experimental demonstration of spiral waves in rabbit VF. Phase is depicted in color with spiral wave chirality indicated by + (clockwise) or – (counter-clockwise). Three phase singularities (PS) are seen. (Adapted from [113])*

Optical mapping data on Langendorff-perfused human heart showing rotors in VF is depicted in Figure 2-30 which is the first study in humans demonstrating the feasibility of visualizing rotors using optical maps *ex vivo* [114].

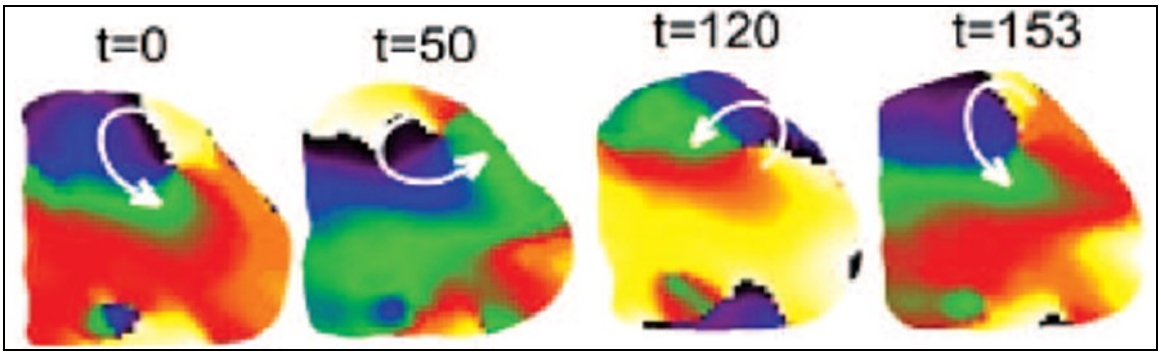

Figure 2-30: Snapshot of phase movie from optical mapping at various time points on Langendorff-perfused human heart showing rotors in VF. *(Adapted from [114])*

Optical mapping data offers a robust means of obtaining complex voltage information, characterizing both depolarization and repolarization, supports the existence of rotors as a critical element in driving atrial fibrillation, idiopathic ventricular tachycardia, and possibly ventricular fibrillation. Applying these data to characterizing rotor locations in patients using intracardiac electrogram data which is generally only depolarization information has proven of limited value thus far. However, validation of novel approaches using optical mapping data with known pivot point locations might be an essential first step prior to attempting characterization of rotors using electrogram data in humans, since there are no other known better methods as yet.

2.6 Review of the Physionet/Physiobank database

PhysioNet offers free access via the World Wide Web (WWW) to large collections of recorded physiologic signals and related open-source software [115]. PhysioNet is a public service of the Research Resource for Complex Physiologic Signals**.** It is a cooperative project initiated by researchers at Boston's Beth Israel Deaconess Medical Center/Harvard Medical School, Boston University, McGill University, and MIT, under the auspices of the National Center for Research Resources of the National Institutes of Health. This resource, intended to stimulate current research and new investigations in the study of complex biomedical and physiologic signals, has three closely interdependent components [115]:

(i) PhysioNet is an on-line forum for dissemination and exchange of recorded biomedical signals and open-source software for analyzing them, by providing facilities for

cooperative analysis of data and evaluation of proposed new algorithms. In addition to providing free electronic access to PhysioBank data and PhysioToolkit software, PhysioNet offers service and training via on-line tutorials to assist users at entry and more advanced levels. PhysioNet is a public service of the Resource, accessible via the World Wide Web.

(ii) PhysioBank is a large and growing archive of well-characterized digital recordings of physiologic signals and related data for use by the biomedical research community. PhysioBank currently includes databases of multi-parameter cardiopulmonary, neural, and other biomedical signals from healthy subjects and patients with a variety of conditions with major public health implications, including sudden cardiac death, congestive heart failure, epilepsy, gait disorders, sleep apnea, and aging. These databases will grow in size and scope, and will eventually include signals from selected *in vitro* and *in vivo* experiments, as developed and contributed by members of the research community. Nearly every published paper on ECG processing presents test results from actual ECG data taken from one of these PhysioBank databases. This allows other researchers to test their new algorithms with identical physiological data reported in scientific publications.

(iii) PhysioToolkit is a large and growing library of software for physiologic signal processing and analysis, detection of physiologically significant events using both classical techniques and novel methods based on statistical physics and nonlinear dynamics, interactive display and characterization of signals, creation of new databases,

simulation of physiologic and other signals, quantitative evaluation and comparison of analysis methods, and analysis of non-equilibrium and nonstationary processes.

PhysioBank now contains over 40 databases that may be freely downloaded. Among the available databases in the PhysioBank, the Multi-Parameter Database has signals that vary, but may include ECG, continuous invasive blood pressure, respiration, oxygen saturation, and EEG. Several ECG datasets from Normal Sinus Rhythm (NSR) and AF were obtained to demonstrate the efficacy of the novel approaches developed in thesis.

2.7 Literature Review of various electrogram analysis methods

The development of catheter based AF ablation motivated several researchers in the development of novel quantitative intraprocedural EGM signal analysis approaches to guide the selection of ablation targets. The following section will discuss several of those approaches that have been attempted thus far in the literature.

2.7.1 Local activation time mapping

Estimation of fibrillatory rate in the time domain, i.e., the AF cycle length (AFCL), is based on the interval between consecutive local activation times (LAT). The precise annotation of LAT from bipolar EGMs in particular during AF is difficult and a number of algorithms have been proposed which attempt to detect LAT. This is achieved by identifying the time when the upstroke of bipolar EGM reaches a 45° angle [116], the time of the maximum bipolar EGM excursion from baseline, the time of the maximum slope in either direction, or the time the sloping segment containing the maximum slope in either direction crossed the baseline as the fastest zero crossing [117]. Several

advanced algorithms to reliably estimate LAT are being developed to obtain 3D LAT maps for intraprocedural guidance during AF ablation.

2.7.2 Dominant frequency mapping

Measuring fibrillatory rates in the frequency domain is a popular alternative to estimating AFCL from LAT [49, 118]. Discrete Fourier transform (DFT) is applied to the time series EGM signal (see equation 2-3) to obtain the frequency components. EGM frequency spectrum during AF is characterized by a more or less well-pronounced peak, the so-called dominant frequency (DF) that mainly reflects timing of the narrow deflections in bipolar EGM and is considered a surrogate for the local activation rate.

$$S_w(k) = \sum_{n=0}^{N} s_w(n) e^{\frac{-2\pi jkn}{N}} \tag{2.3}$$

DF mapping of rotors and active substrates has limited success due to the nonstationary temporal dynamics of EGM signals which has poor correlation with the local cycle length measured in the time domain [119].

2.7.3 Phase mapping

Phase mapping is achieved by obtaining the instantaneous phase of the atrial signals in multichannel EGM recording to map the spatial propagation of local activation waves (LAWs) across the atria. The instantaneous phase Φ(n) of a signal can be obtained from the analytic signal $s^*(n)$ using Hilbert Transform as below:

$$s^*(n) = s_r(n) + js_i(n) \tag{2.4}$$

Where $s_i(n)$ is the imaginary part of the signal obtained from Hilbert Transform of the measured signal $s_r(n)$ The phase Φ(n) is given as:

$$\Phi(n) = \arctan(s_i(n)/s_r(n)) \quad (2.5)$$

To get meaningful interpretation of the phase Φ(n), EGM must have single mode which is not always the case and challenges to obtain the Hilbert Phase from the EGM which is a major setback of this approach. However, several researchers have attempted phase mapping with optical mapping data from animal models and also human AF mapping from EGM. Phase mapping techniques have provided the first depiction of spiral wave rotors as drivers of cardiac fibrillation [113, 120].

2.7.4 CFAE mapping

Fractionated electrograms have been documented to represent the sites of reentrant activities responsible for maintenance of AF. CFAEs are defined as low-voltage fractionated atrial electrograms with a cycle length <120 ms [107]. Rapid electrical impulses emanating from rotors are conducted within the atria, and fragmentation arises from interaction with functional and anatomic boundaries. These sites with CFAE appear spatially stable and ablation at these sites may also result in AF termination [212-122]. As observed by physicians, there are varying types of CFAEs that have different importance to the ablation process [108]. Three types of fractionated atrial electrograms can be described:

C1: fractionated atrial electrogram with periodic activity

C2: mixture of periodic fractionated and periodic non-fractionated atrial electrograms

C3: high frequency atrial electrogram with continuous activity

A 4^{th} type which is a non-fractionated electrogram is also common which is

C0: non-fractionated atrial electrogram with high frequency.

Figure 2-31 shows an example of the implementation of the above process that classifies atrial electrograms [123].

CFAE-mean index calculation

The parameters used for calculation of CFAE-mean, a widely used clinical index of CFAE [124] are based on the following settings: detection method (−dV/dt); reference sensitivity (0.3); minimal width (10 ms); refractory period (30 ms); peak-peak sensitivity (0.1 mv) which are adjustable. The algorithm to calculate CFAE-mean index that will be implemented in this research is based on the one developed by St.Jude Medical as shown in Figure 2-32. CFAE-mean index searches for a falling edge in the EGM fulfilling the sensitivity precept. This point is marked as beginning of a fractionated electrogram complex with the assumed width of 10 ms and a refractory period of 42 ms [123]. The beginning of the following fractionated complex is then searched.

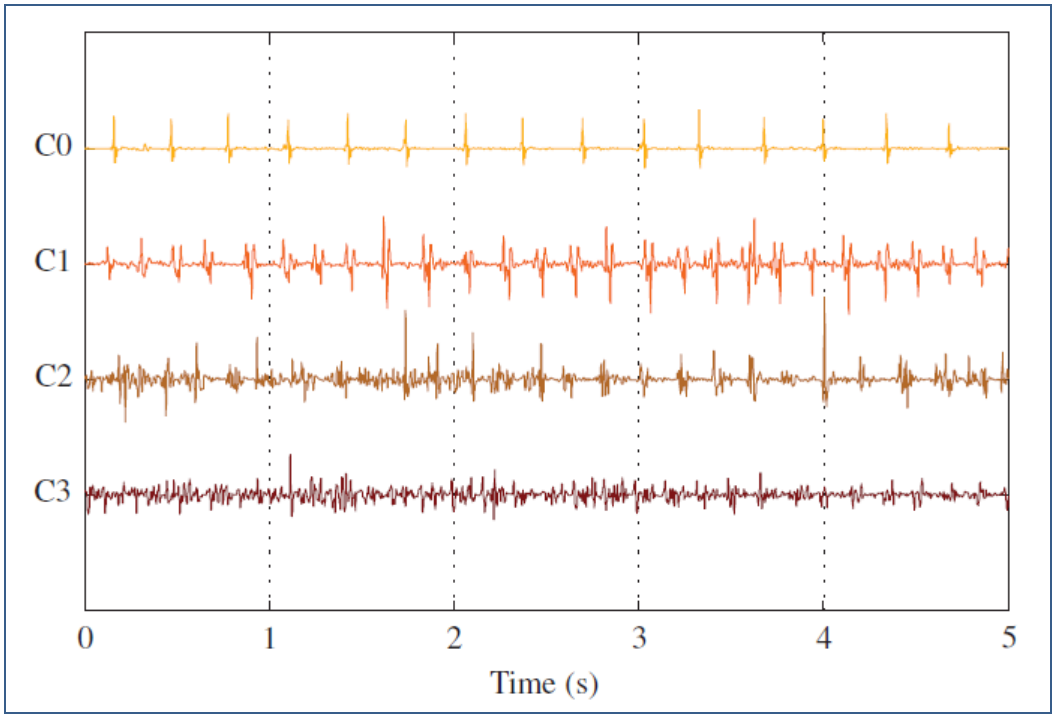

Figure 2-31: Example of CFAE classification scheme. *(Adapted from [123])*

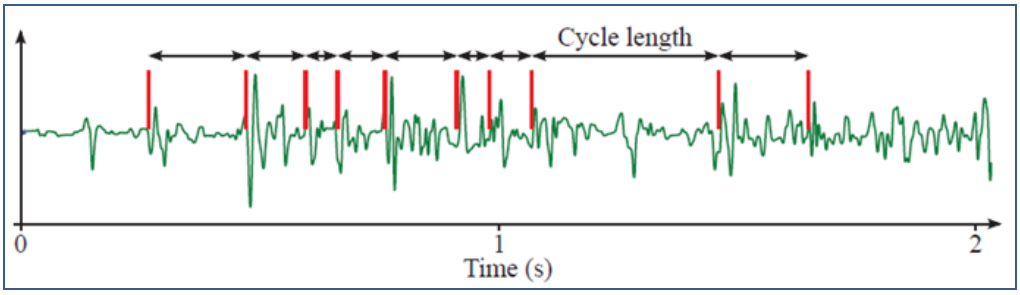

Figure 2-32: CFAE mean calculation algorithm developed by St.Jude Medical Systems. *(Adapted from [123])*

This process is done for the whole electrogram for up to 5 sec. The mean distance between the found marks is defined as CFAE-mean. The CFAE-mean is based on the cycle length between discriminable local activities in the EGM 123]. Several research labs have attempted ablation using CFAE mapping. However, although the spatial relationship between CFAE and DF locations and CFAE properties have been intensively studies, no consensus has been reached on optimal definition of CFAE which challenges universal application across many sites in the world.

2.7.5 Wavelet analysis

To overcome the limitation of DF mapping due to the non-stationarity of EGM data, wavelet analysis [125] has been used to provide time varying frequency information using the equation below:

$$W(\tau, a) = \frac{1}{\sqrt{a}} \int_{-\infty}^{\infty} x(t)\psi\left(\frac{t-\tau}{a}\right) dt \qquad (2.6)$$

Where x(t) is the atrial signal, ψ is the mother wavelet and a is the scaling factor that dilates the wavelet.

2.7.6 Wave morphology similarity

Wave morphology similarity measures the degree of morphological repetitiveness of the LAWs [126]. The similarity index is then defined using the following equation:

$$\rho(\varepsilon) = \frac{2}{N(N-1)} \sum_{i=1}^{N} \sum_{j=i+1}^{N} \Theta(\epsilon - d(\hat{x}_i, \hat{x}_i)) \tag{2.7}$$

$$d(\hat{x}_i, \hat{x}_i) = \cos^{-1}(\hat{x}_i \cdot \hat{x}_j) \tag{2.8}$$

Where, Θ is the Heaviside function and ε is the threshold value, empirically set to ε = π/3 and N is the number of pairs of LAWs (x_i and x_j).

2.7.7 Symbolic dynamics analysis using entropy

Symbolic dynamics is a powerful tool that can quantify system dynamics using short time series. The approach is based on the fact that if the fluctuations of the two time series are governed by different underlying dynamics, then the evolutions of the symbolic sequences are not related. The resulting symbolic sequences histograms give a reconstruction of their respective histories and provide a visual representation of the intrinsic dynamic patterns. The intrinsic dynamics is completely ignored in the time domain and frequency domain analysis, which are the basis for existing signal processing techniques for rotor identification. The process of symbolization can be used to represent any possible variation over time, depending on the number of symbols (such as amplitude bins) and the sequence lengths used. Therefore, symbolic dynamics is a very powerful technique because it does not imply any assumptions about the nature of the signals. Following three entropy approaches have been applied to EGM for identifying active substrates.

- ❖ Shannon Entropy (SE)
- ❖ Renyi Entropy (RE)
- ❖ Approximate Entropy (AE)

Entropy is a statistical measure of information content based on the distribution of amplitude values within the signal histogram [127]. In the context of signal processing entropy is also used as a measure of the degree of organization of a signal. Shannon's entropy has maximum values, if the signal's development over time is not predictable.

2.7.7.1 Shannon entropy

SE measures the distribution of signal values from electrogram within the histogram, and is calculated as the following [84]. Each electrogram from different spatial location is binned using suitable bin size according to its amplitude into a voltage histogram. Then, the relative probability density *p* will be defined as the number of counts in an amplitude bin divided by the sum of bin counts in all bins. The SE will then be defined as:

$$SE = -\sum_{i=0}^{N-1} p_i \log_2 p_i , \tag{2.9}$$

Where, n is the number of amplitude bins, and p is the probability of any sample falling within a particular amplitude bin.

2.7.7.2 Renyi entropy

RE is a generalization of *SE*, whenever necessary. *RE* depends on powers of probability, and is extremely useful in the case when there is a need to distinguish between weaker signals that are being overlapped with stronger signals, which often occur in intracardiac electrograms. The *RE* is calculated as the following:

$$RE = H_a(p_1, p_2, \ldots, p_n) = \frac{1}{1-\alpha} \ln\left(\sum_{i=1}^{N} p_i^{\alpha}\right), \quad (2.10)$$

where $\alpha>0$ and $\alpha\neq1$, p is the probability of any sample falling within a particular amplitude bin. As $\alpha\rightarrow1$, *RE* approaches *SE*. It has been shown that *RE* is more efficient in discriminating between VT/VF patients from normal subjects [128].

2.7.7.3 Approximate entropy

AE is a regularity metric that measures the logarithmic likelihood that runs of patterns similar to each other will remain similar in the next incremental comparison and is defined by the following equation:

$$\mathrm{ApEn}(S_{N,m,r}) = \ln \frac{C_m(r)}{C_{m+1}(r)} \quad (2.11)$$

where m is the pattern length, r is the criterion of similarity, and $C_m(r)$ the prevalence of repetitive patterns of length 'm' in the sequence S_N. Some researchers have reported high AE for highly fractionated EGMs [129-130].

2.7.8 Non-linear dynamics analysis

Phase-space characterization of EGM data has been proposed to capture the nonlinear dynamics of AF [131-132]. Phase space of the input signal is constructed as below:

$$S(n) = [s(n), s(n-L), s(n-2L), \ldots, s(n-(\tau-1)L)]^T \quad (2.12)$$

Where, τ is the embedding delay and L is the embedding dimension. Recurrence plots are then constructed which gives information on EGM fractionation.

2.7.9 Cross-Correlation and nonparametric coherence estimation

Cross-Correlation is computed to measure spatial organization of atrial activation in the time domain between LAWs at different recording sites [133]. Since EGMs are nonstationary signals and exhibit spatio–temporal instability, time-frequency analysis of the coherence function of two EGM has been proposed, using a multitaper method for spectrum estimation [134].

2.7.10 Multivariate autoregressive models

Multivariate autoregressive (AR) process of order 'm' is modeled from the 'n' between EGMs obtained from N different catheter poles as below:

$$s(n) = \sum_{k=1}^{m} A_k s(n-k) + w(n) \tag{2.13}$$

Where, A is the N x N matrix containing AR coefficients and w(n) is a multivariate white noise process. Spatio–temporal propagation of atrial activation from EGMs can be studied using this approach [135].

2.7.11 Preprocessing of intracardiac electrograms

As discussed in section 2.4 intracardiac EGMs can be acquired as "unipolar" and "bipolar" signals and bipolar signals are usually reoffered for offline EGM analysis for the advantaged listed in Table 2-2. However, total absence of baseline wander noise and VFF noise is not guaranteed from bipolar signals as it depends on the electrode spacing and the timing of the ventricular activity when the EGMs are acquired. Therefore any signal processing approach developed should consider preprocessing the digitized bipolar EGMs that is contaminated with three common noises as below:

- Baseline wander noise which is the drift of the isoelectric line
- High frequency noise including the 60 Hz power line interference noise
- Ventricular far field (VFF) noise due to the close distance to the ventricles.

Therefore, preprocessing of intra-atrial electrograms to remove all these noises is an essential first step prior to any other analysis [123].

Baseline wander noise removal

Baseline Wander (BW) noise is the slow movement of the isoelectric line in an ECG which can be caused by patient movement such as chest movement caused by breathing or coughing, poor electrode contact, or interference or drift of the reference potential. The frequency components of baseline wander are below 2 Hz and there are several methods proposed for its removal [123].

Using wavelet transform (WT) a signal is transposed into the time-frequency domain. Compared to the FFT, the WT gives not only information about the frequency content of a signal, but also information at which time segment a frequency occurs. An example approach is to use Discrete Wavelet Transform (DWT) adopted by Schilling [123] using Daubechies wavelet of order 11 and wavelet filter banks to remove baseline wander from the intra-atrial electrograms to achieve results similar to as shown in Fig 2-33. The top panel shows atrial signal with BW noise, the middle panel shows the flat atrial signal after BW removal and the bottom panel shows the removed noise.

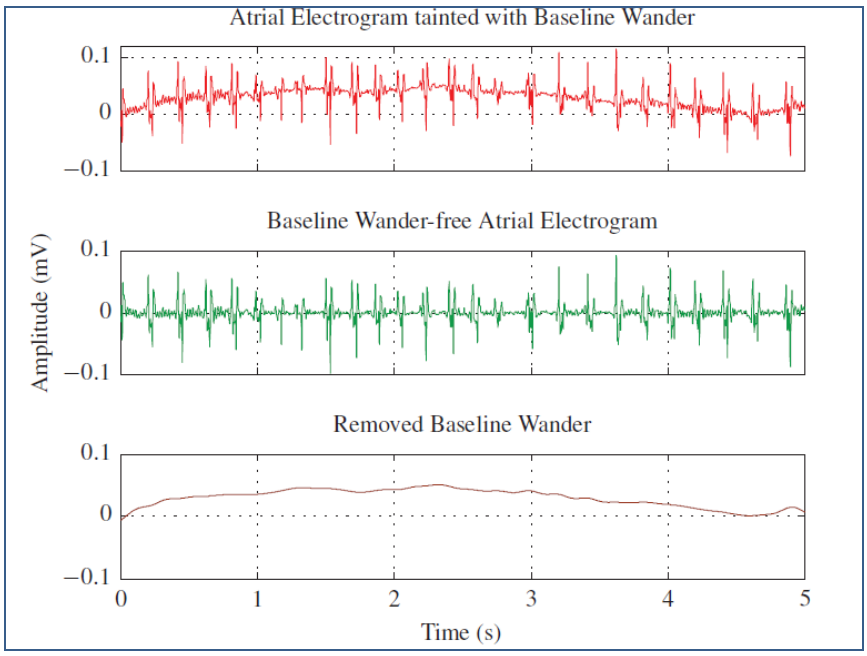

Figure 2-33: Baseline wander noise removal example using DWT *(Adapted from [123])*

High frequency noise removal:

The EGMs gets contaminated with high frequency noise from multitude of sources such as power line interference, other electronic noise sources from the mapping system, electromyogram (EMG) noise, high frequency motion artifact noise, etc. Removal of these high frequency noises is a must for faithful reproduction of the electrical activity of the atria. While, wavelet transform and other methods are quite common to remove the high frequency noise, an IIR Butterworth low pass filter of order between 3-5 with cutoff frequency between 30-400 Hz can be implemented to remove high frequency noise. Care should be taken as not to distort the signal during filtering as it can lose significant signal information.

Ventricular Far Field (VFF) noise removal:

When EGMs are measured in close proximity to the ventricles they can be tainted with ventricular activity which is then superimposed on the atrial activity and is called ventricular far field (VFF). This disturbance of the atrial signals occurs especially in regions of the left atrium like the inferior anterior wall, the inferior posterior wall, or the coronary sinus [123]. The VFF noise pose a problem to the signal analysis of the EGMs as it can modify the complexity estimates. Hence, removal of VFF noise is a mandatory step prior to any further signal processing is they are unipolar recording and strongly recommended for bipolar EGMs.

Several approaches have been proposed for VFF removal. A popular approach is the Principal Component Analysis (PCA) approach [123] which is a classical tool in statistical data analysis to reduce the number of variables or to detect structure in the relationship between variables i.e. classify variables. The PCA transforms a number of correlated variables into a smaller number of uncorrelated variables called principle components preserving all or most of the information. The first principal component covers as much of the variability in the data as possible, and each succeeding component covers as much of the remaining variability as possible. The signal processing steps outlined in the block diagram in Figure 2-34 can be used. Body surface ECG is required to obtain accurate QRS time stamps [136-138] corresponding to the ventricular activity. Lead II ECG will be a convenient choice and the signal processing steps to obtain clean ECG and hence accurate QRS proximity can be obtained. The contaminated EGM will first be segmented based on the QRS timestamps from Lead II ECG to obtain the VFF

from the intra-atrial electrogram in a time window of 180 ms around the estimated R-wave peak. Then the PCA components can be estimated. The criterion for deleting the required number of PCA components to remove VFF can be based on the ventricular to atrial activity signal ratio (VASR) [123]. Inverse PCA operation is then performed to reconstruct VFF free pure intra-atrial electrogram.

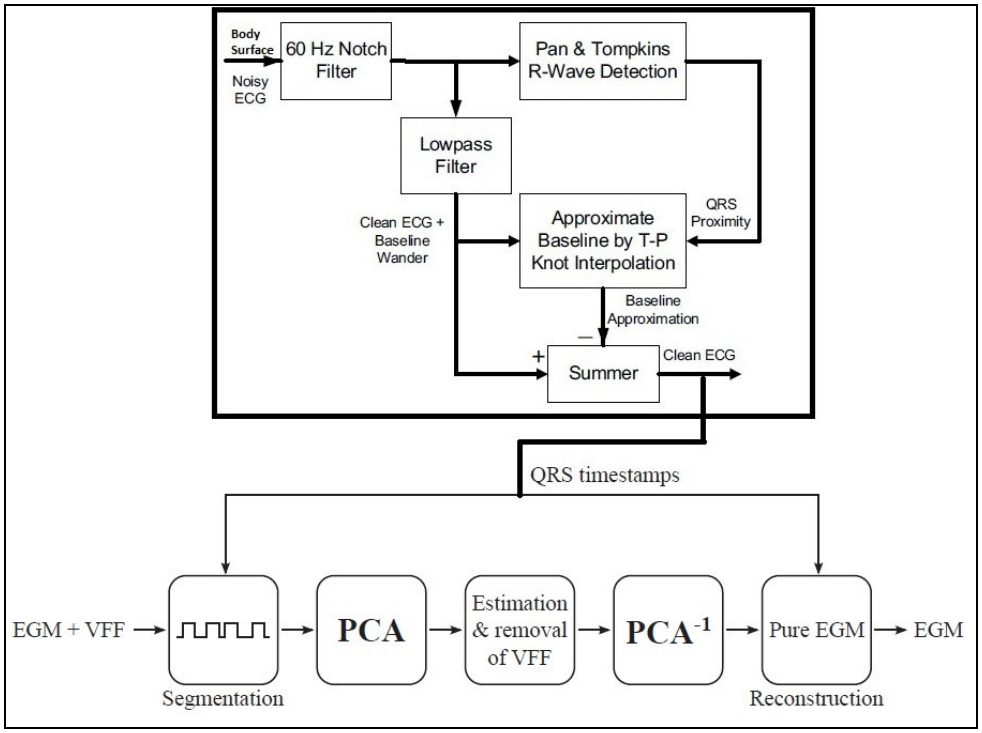

Figure 2-34: Sample schematic of the signal processing steps to remove baseline wander noise, high frequency noise and VFF noise from EGMs.

The preprocessed noise free EGM can now be analyzed further for the estimation of various quantities described on the previous section for complexity analysis for identifying EGM fractionation sites or even the pivot points of the rotor.

2.7.12 Clinical results from popular mapping approaches

While the scientific community is still debating about the mechanistic behavior that causes and maintains AF, significant advancements have been made in quantitative EGM

analysis to guide catheter ablation for AF. Several researchers have attempted clinical trials using DF, CFAE and phase mapping and more recently a novel approach called spatial temporal dispersion. The following section will highlight some of the important studies using these approaches.

2.7.12.1 Clinical ablation results using DF mapping approach

Reduction in the left-to-right DF gradient was demonstrated following ablation of sites with high DF and a reduced risk of atrial arrhythmia recurrence [57]. However, only 11% termination of AF was seen in persistent AF compared with 72% for paroxysmal AF patients. Another study reported a termination of AF for only persistent AF patients out of 30 who were enrolled for DF ablation [139]. The largest study to assess DF ablation to date, the RADAR-AF trial, randomized 232 patients to strategies of high DF site ablation and/or conventional PVI [140]. In persistent AF patients, freedom from atrial arrhythmia was seen in 67% of patients who underwent PVI plus high DF site ablation, similar to the 63% of patients who underwent PVI alone [140]. These results indicate the inefficacy of DF approach to guide catheter based AF ablation for persistent AF patients. Also, it has been shown that the DF for rotor is uniform throughout its spatial locations demonstrating its inability identify the core of the rotor.

2.7.12.2 Clinical ablation results using CFAE mapping approach

Clinical results with CFAE ablation have demonstrated mixed results. Initial studies showed 95% terminating of persistent AF with no recurrence [107], but other groups were not able to reproduce the results [141-144]. In general no advantage was seen with CFAE lesions delivered to paroxysmal AF patients with some degree of improvements in

persistent AF patients in maintaining sinus rhythm according to meta-analysis of CFAE ablation [145]. A more recent STAR-AF 2 trial with randomized 589 persistent AF patients to PVI, PVI plus CFAE ablation, or PVI plus linear ablation in the atrium showed no benefit with CFAE [146]. Moreover, different groups use customized algorithms for calculating CFAE scores for ablation in their patient groups which makes it difficult for reproducibility in other sites. Nevertheless, it appears that CFAE ablation should be attempted with other novel strategies than can provide new directions for clinical guidance which would need validation with more clinical trials.

2.7.12.3 Clinical ablation results using phase mapping approach

Narayan et al used a phase mapping approach known as focal impulse and rotor modulation (FIRM), in their FIRM trial to terminate AF in persistent AF patients [7]. However, one criticism is that the signal processing approaches taken for phase mapping was not disclosed contradicted by non-reproducibility of this approach by other groups, However, the authors demonstrated mapping of rotors in humans using FIRM [43]. The authors also demonstrated 86% termination of AF using FIRM guided ablation in persistent AF patients [147-149]. However, another independent group who used FIRM guided ablation was not able to reproduce these results in a blinded study. More recent study demonstrated discrepancy with low SE and DF in FIRM indicated target sites [150]. These results suggest the need for more rigorous validation of this approach, given the challenge that exists with the Hilbert transform operation to achieve Hilbert phase from EGMs.

2.7.12.4 Clinical ablation results using spatiotemporal dispersion approach

Recently a novel approach called spatiotemporal dispersion approach was used to terminate AF in patient groups. The idea behind this approach is that, electrograms recorded simultaneously by a multipolar catheter displaying both spatial and temporal dispersion areas are indicative of AF drivers, regardless of whether these electrograms are fractionated or not [151]. 105 AF patients were prospectively enrolled in the study and the authors tagged and ablated only regions displaying electrogram dispersion during AF which resulted in 95% success rate in terminating AF. The authors validated the spatiotemporal dispersion of EGMs near the driver source using numerical simulations and optical mapping in ex vivo ovine atrium. The results offer huge promise, which however need further validation from several groups.

2.7.13 Limitations of current mapping approaches

There are several limitations of the above-mentioned techniques, which restricted their successful application in mapping the rotor pivot zones. The high frequency of recurrence of AF in patients specifically with persistent AF after PV isolation and linear ablation show that the current methods of AF analysis to predict critical areas of AF maintenance are not adequate. An individual application of above-mentioned techniques can be compromised by several artifacts. For instance, CFAEs may also arise from passive wave collision or far-field activity [152-153]. A major limitation of this approach is the poor specificity of CFAEs as putative sources for AF perpetuation [154].

While the DF approach has been widely used to estimate atrial activation rate during AF, several factors, which are not related to activation rate, might affect the DF

estimation such as variable or low amplitude electrograms, frequency variability, non-stationary time series signal, presence of double potentials, fractionation, noise, far field ventricular potentials, baseline wander noise, etc. All these factors limit ability of DF analysis to accurately and with high reproducibility predict the ablation sites [22]. Hence quite often, manual verification is required to ensure specific target sites prior to ablation which can become cumbersome and may not aid real time mapping guidance during AF treatment procedure.

Also, a limitation with the use of LAT maps is that the presence of activation times consistent with propagation of an activation front does not necessarily prove such activation actually exists [22]. This challenges the robustness of this mapping method for ablation since non-active substrates should be protected from ablation, otherwise it can subsequently lead to more complex arrhythmias. The major limitation of phase mapping is the characteristic feature of EGMs that does not yield adequate Hilbert phase properly which challenges this approach. Spurious phase information can easily contaminate the phase estimation in this approach which can misguide clinical guidance, and use of other approaches along with phase mapping is preferred. The spatiotemporal dispersion approach is relatively new, although it promises huge success rate reproducibility from other groups will be critical for the future scope of this approach. All other quantitative electrogram analysis methods discussed in section 2.7 have not been thoroughly validated for robustness with short time series analysis for rotor identification or attempted in clinical setting for identifying active substrates that may initiate and maintain AF.

Therefore, there is a clear need for a more robust spatiotemporal mapping technique that can fully capture the intrinsic dynamics of the non-stationary time series intracardiac electrogram signal to accurately identify the rotor pivot zones for faithful ablation of arrhythmogenic substrates that causes and maintains AF.

2.8 Conclusions

This chapter has provided a brief overview of the cardiac anatomy, electrophysiology and atrial fibrillation providing the necessary background information to understand the basic premise of this thesis. Various theories behind the AF initiation and maintenance of AF were discussed and introduced the concept of rotors and its role in the sustained maintenance of AF, whose pivot points are believed to suitable targets for ablation to permanently terminate AF. Brief review of catheter ablation strategies and their limitations in permanently terminating AF was discussed. Review of several quantitative electrogram analysis methods were provided along with their limitations. The high recurrence rates of AF and the inadequacy of the current mapping methods motivated the author to develop novel quantitative EGM analysis approaches in the temporal and frequency domain for accurate identification of rotor pivot points that is potentially translatable in clinical setting discussed in Chapter 3.

CHAPTER 3: NOVEL APPROACHES FOR ELECTROGRAM ANALYSIS

3.1 Introduction

This section of the thesis is devoted to the detailed description of the novel quantitative methods developed for electrogram analysis for rotor pivot point identification. As discussed in Chapter 2 there is a clear need for a robust spatio-temporal mapping system that reliably identifies rotor core zones as potential target for AF ablation and also other cardiac arrhythmias. The challenge that comes with short time series data in clinical setting along with the inherent inadequacy of several mapping approaches limits them for reliable identification of rotors. Hence, this research focused on developing novel approaches that exploits several different temporal and frequency characteristics of the electrogram for accurately identifying rotor pivot points that is also robust for short time series data.

In this thesis four novel time domain based techniques namely multiscale entropy (MSE), recurrence period density entropy (RPDE), kurtosis and intrinsic mode function (IMF) complexity using empirical mode decomposition (EMD) were proposed for quantitative electrogram analysis that captures different temporal characteristics of the electrogram. A novel frequency domain technique namely multiscale frequency (MSF) was developed that captures the intrinsic chaotic frequency components of the electrogram to reliably identify rotor core compared to the periphery during AF. For each of the novel technique the basic methodology including the governing equations, signal processing steps, and the algorithm for complexity analysis are described in detail. The specific characteristic of the electrogram that is exploited for each of the method is

described and the rationale for the method to accurately identify the rotor core complexity compared to the periphery is provided. Single and multi-frequency sinusoidal waveform with short time series is used to demonstrate the efficacy of the complexity analysis for each of the techniques compared with SE for the purposes of this thesis. The following sections will describe each of the approaches and different datasets in detail.

3.2 Novel approaches for electrogram analysis

The first specific aim of this thesis is "*To develop novel quantitative electrogram analysis methods to identify rotor pivot point that is translatable to intra-atrial electrogram analysis for identifying potential targets for AF ablation*". To achieve this goal novel time and frequency domain approaches are proposed and developed in this thesis discussed in the following sections.

3.2.1 Novel time domain approaches

Intracardiac electrogram varies significantly both spatially and temporally where the morphology changes significantly between the normal and diseased state such as AF. Such temporal morphological changes can be quantified using different times series analysis techniques with digital signal processing that is robust when only short time series is available in a clinical setting, where offline analysis are not useful for real-time guidance. Various temporal characteristics such as the repetitiveness and periodicity of the time series in both linear and phase space, characteristics of the probability density functions and complexity of intrinsic mode functions of the electrograms are explored in these novel time domain based approaches for accurate identification of rotor pivot points compared to the periphery in the following sections.

3.2.1.1 Novel multiscale entropy technique

Many biomedical signals are usually captured only for 3-8 s, and therefore are a short non-stationary and/or non-linear time series data, which prevent ordinary biomedical analysis algorithms to completely capture the intrinsic complexity. For instance, Shannon Entropy (SE) is commonly used for biomedical complexity analysis of EEG and ECG [12, 127 & 155]. However, one of the major limitations of the SE approach is related to the specific characteristics of the non-stationary and/or non-linear time series data that works well for long but is not robust for short time series data. Several other symbolic dynamics approaches that use various entropy-based measures, such as Kolmogorov entropy, spectral entropy, wavelet entropy, permutation entropy, approximate entropy, and sample entropy, has been proposed to capture the intrinsic dynamics of non-stationary time series data to quantify their complexity [156-162]. However, it has been shown that these different entropy-based methods are efficient only for long time series, and cannot completely capture the complexities of shorter non-stationary time series data [163].

Recently, multiscale entropy (MSE) approach was proposed to be used with coarse-grained time scaling procedure for more robust determination of the complexity of time series data [164]. Such coarse-graining procedure may result in invalid entropy values estimation for shorter time series; and this limitation was addressed by implementing a moving average time series estimate [165]. However, in [165], the moving average was only performed in the forward direction, which can lead to the significant under-estimation of the complexity information that is present in the time series data. Several variants of MSE have been proposed [166], but all of them provide slight modifications of

original approach [165], and specifically perform one-sided moving average, which yield biased entropy estimate over different time scales. Therefore, using entropy-based approaches for rigorous complexity analysis of a biomedical signal in normal and diseased states has been very limited. In particular, only SE has been widely used for complexity analysis for various biomedical signals such as ECG and EEG [12, 127 & 155]. Several variants of MSE have been applied to test and synthetic biomedical datasets without a rigorous demonstration of their feasibility for a biomedical application [167-169].

In this thesis, I propose a novel MSE approach, which includes significant and robust modification of the previously described MSE approaches that can be used for analysis of non-linear and non-stationary short time series data. Specifically, I propose to compute new time series with a nearest neighbor moving average kernel that uses information from the 'past' and 'future' values to accurately capture the intrinsic dynamics of the short time series by effectively capturing the *'repetitiveness'* and *'periodicity'* of the new time series in the 'temporal-space'. This modification will allow performing a robust analysis of non-linear and non-stationary time series.

MSE approach technical details

The challenge with short time series data analysis is coming from the fact that the complexity of the data may not embed in the raw signal, and therefore most approaches work very well with long time series data. MSE approaches were introduced with time averaged time series over multiple time scales for short time series analysis (165). However, forward averaging introduces a systematic bias in the complexity estimation. To overcome this limitation, we propose to use a nearest neighbor moving average kernel to

better capture the complexity of a non-linear, non-stationary short time series data. We introduce the concept of 'memory' by taking into account the past and future time series value while computing the nearest neighbor moving average for time series data. Therefore, we introduce the time scale factor 'τ', which represents time scaling in both forward and reverse directions with respect to a particular time point. Once this new time series is derived, MSE estimate can be obtained by calculating the entropy of the new time series sample over multiple time scales to fully capture the intrinsic complexity of non-linear and non-stationary time series data.

The novel MSE algorithm consists of several steps and is described below. Let $x = \{x_1, x_2, x_3 \ldots x_N\}$ represent the electrogram time series of length N.

1. Nearest neighbor moving-averaged time series z^τ is computed for the chosen time scale factor 'τ' as illustrated in Figure 3-1 using the following equation:

$$z_j^\tau = \frac{1}{(2\tau+1)} \sum_{i=j}^{2\tau+1} x_i \tag{3.1}$$

where $1 \leq j \leq N-\tau$ and $i = 1,2,3, \ldots N$; Figure 1 shows the schematic to obtain the nearest neighbor moving window averaging approach to obtain the new time series.

2. Template vectors $y_k^m(\delta)$ with dimension m and delay δ are constructed from z^τ (see Eq. 1) at each specific τ as the following:

$$y_k^m(\delta) = \{z_k\, z_{k+\delta} \ldots\ldots z_{k+(m-1)\delta}\}, \tag{3.2}$$

where $1 \leq k \leq N- m\delta$;

3. The Euclidean distance d_{ij}^m for each pair of template vectors $\{y_i^m, y_j^m\}$ is calculated using the infinity norm as below:

$$d_{ij}^{m}(\delta) = || y_i^m(\delta) - y_j^m(\delta) ||_\infty ,$$

(3.3)

where $1 \leq i, j \leq N - m\delta$, and $j > i+\delta$;

4. Matched template vector pairs $\{y_i^m, y_j^m\}$ are computed based on a pre-defined tolerance threshold *r* as

$$d_{ij}^{m}(\delta) \leq r . \quad (3.4)$$

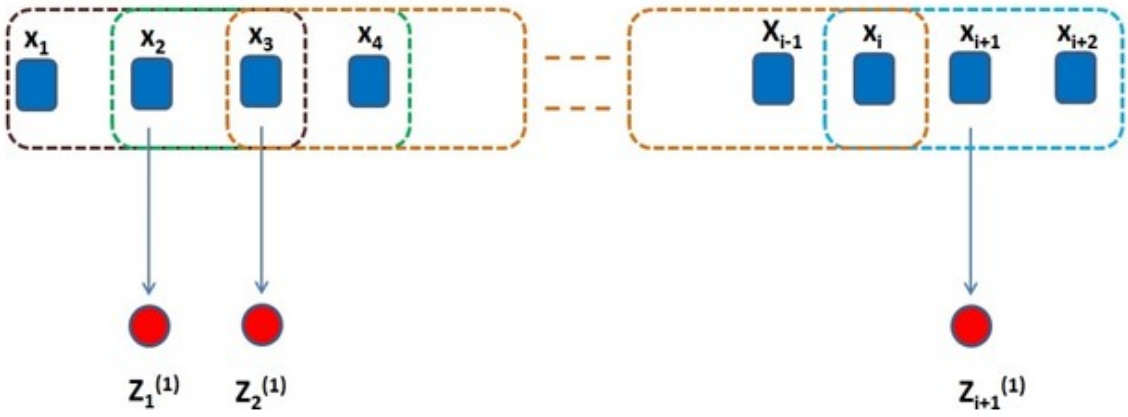

Figure 3-1: Schematic illustration to produce nearest neighbor moving average time series with scale factor τ = 1 for the MSE algorithm. *Blue squares represent raw time series data and red dots represent the nearest neighbor moving-averaged time series from which MSE is obtained. Brown square represent the moving window averaging kernel for the raw second time point (X_2), that averages one neighbor on both sides with τ = 1 to produce the first new time series point $Z_1^{(1)}$. Similarly green square produces $Z_2^{(1)}$ and so on (orange square) with the blue square producing the last time series point $Z_{i+1}^{(1)}$.*

In this work the value for '*r*' is chosen to be 0.2 times the standard deviation of the raw time series *x*. The delay factor δ is chosen to be 1. The total number of matched template vectors is computed and denoted by *n (m, δ, r).*

Steps 2-4 are then repeated for m+1 dimension, and the total number of matched template vectors being computed is denoted by *n (m+1, δ, r)*.

Finally, the MSE is calculated as the following:

$$MSE(x, m, \delta, r) = -ln\frac{n(m+1,\delta,r)}{n(m,\delta,r)}. \quad (3.5)$$

The MSE approach can be applied to various non-stationary and/or nonlinear short time series data including biomedical signals to capture the intrinsic complexity. Computational complexity of the MSE approach is determined by the number of samples in the time series being analyzed and the chosen time scale factor 'τ'. Higher the value of 'τ' implies more computational time and also can result in excessive smoothing of the data and a reasonable choice for 'τ' should be decided for the purposes of the intended complexity analysis which is also capable for near real-time analysis.

In this thesis, it is hypothesized that the core of the rotor will have higher MSE compared to its periphery thereby enabling its accurate identification, which will be validated using optical mapping data with known pivot point locations. Custom MATLAB programs were written, namely "NMSE.m" to compute MSE, which uses "NNMA.m" that computes the nearest neighbor moving average time series and "SampEn.m" to compute sample entropy from the new times series shown in APPENDIX B.

An example of applying MSE technique to simple sinusoidal wave is provided as a demonstration. Single frequency sinusoidal signal at 10 Hz was generated at a sampling rate of 250 Hz for 2 s. Similarly, a multi-frequency sinusoidal signal with frequencies 2, 5, 10, 15 and 20 Hz was generated at a sampling rate of 250 Hz for 2 s. Corresponding amplitude histograms were generated. MSE technique as described above was

implemented using the custom MATLAB program with a scale factor of τ =3. SE values were computed for comparison purposes. MSE was estimated as 0.39 and 0.91 for the single and multifrequency sinusoidal wave compared with SE values of 96.5 and 77.7 demonstrating the efficacy of MSE technique. SE was lower for more complex multifrequency sinusoidal wave than the single frequency wave as expected. MSE measured the complexity correctly with higher values for the multifrequency sinusoidal wave than the single frequency wave. This demonstration offers huge promise for accurate identification of rotor pivot point compared to the periphery due to the chaotic nature at the rotor core.

3.2.1.2 Recurrence period density entropy technique

Recurrence period density entropy (RPDE) is a novel approach developed by Max Little [170-172] for analyzing time series data over different time scales to especially capture the intrinsic complexity of both non-linear and non-stationary short time series data, such as electrocardiograms (ECG). RPDE method is gaining attention in the fields of dynamical systems, stochastic processes, and time series analysis for determining the periodicity or repetitiveness of a signal in the phase space which is a space usually 'a set with an imposed structure', the elements which are the phase points represent the states of the system. The characteristic feature of RPDE is that with phase space reconstruction, it enables studying the complexity of unobserved variables which are very common in any complex system.

RPDE is useful for characterizing the extent to which a time series repeats the same sequence analogous to linear autocorrelation and time delayed mutual information, the

only difference being measuring the repetitiveness in the phase space of the system. Therefore, RPDE is a more reliable measure based upon the dynamics of the underlying system that generated the signal, which offers huge potential for analyzing complex systems including biological systems. Since it operates in phase space, the primary advantage of RPDE is that it does not require the assumptions of linearity, Gaussianity or dynamical determinism.

In RPDE approach the time series data is first embedded in M-dimension in phase space by forming time-delayed time-series data vectors using appropriate time delay 'τ'. Next, a spherical neighborhood of radius 'ε' is formed around each point in the phase space. Every time the time series returns to this sphere after having left it, the time difference 't' between successive returns is recorded in a histogram which is normalized to sum to unity giving an estimate of the recurrence period density function P(t). The normalized entropy of this density gives the RPDE value which can accurately quantify the complexity of the signal under consideration.

The RPDE algorithm proposed in this work is described as below as a list of several steps.

Let $x = \{x_1, x_2, x_3 \ldots x_N\}$ represent the electrogram time series of length N. First, time delayed version of the time series 'x' is created as shown in equation 3.6 below:

$$X = \{x_n, x_{n+\tau}, x_{n+2\tau} \ldots \ldots\ldots x_{n+(M-1)\tau}\} \tag{3.6}$$

where 'τ' is the delay and M is the number of dimensions included within the new time series matrix 'X'.

Next, recurrence time, 't' defined as the number of times the signal returns within a fixed distance of each point within this M-dimensional phase space is counted. This procedure is repeated for all the embedded points in the phase space and is cumulated as a recurrence histogram R(t). This histogram is normalized to sum to one to create a recurrence period density function P(t) shown in equation 3.7 where T_{max} is the largest recurrence period.

$$P(t) = \frac{R(t)}{\sum_i^{Tmax} R(i))} \tag{3.7}$$

The normalized entropy of this function P(t) denoted by H_{norm} is calculated using equation 3.8 as the RPDE value.

$$H_{norm} = -(\ln T_{max})^{-1} \sum_{t=1}^{T_{max}} P(t) \ln P(t) \tag{3.8}$$

Figure 3-2 gives a pictorial illustration of the steps involved to process time series data to obtain RPDE value for complexity analysis. Computational complexity of RPDE depends on the time series length, the embedding dimension 'M' and the time delay factor 'τ' used for the analysis. Therefore, for reasonable computational times that are also feasible for real-time applications, a reasonable choice of 'M' and 'τ' should be decided based on the system being investigated.

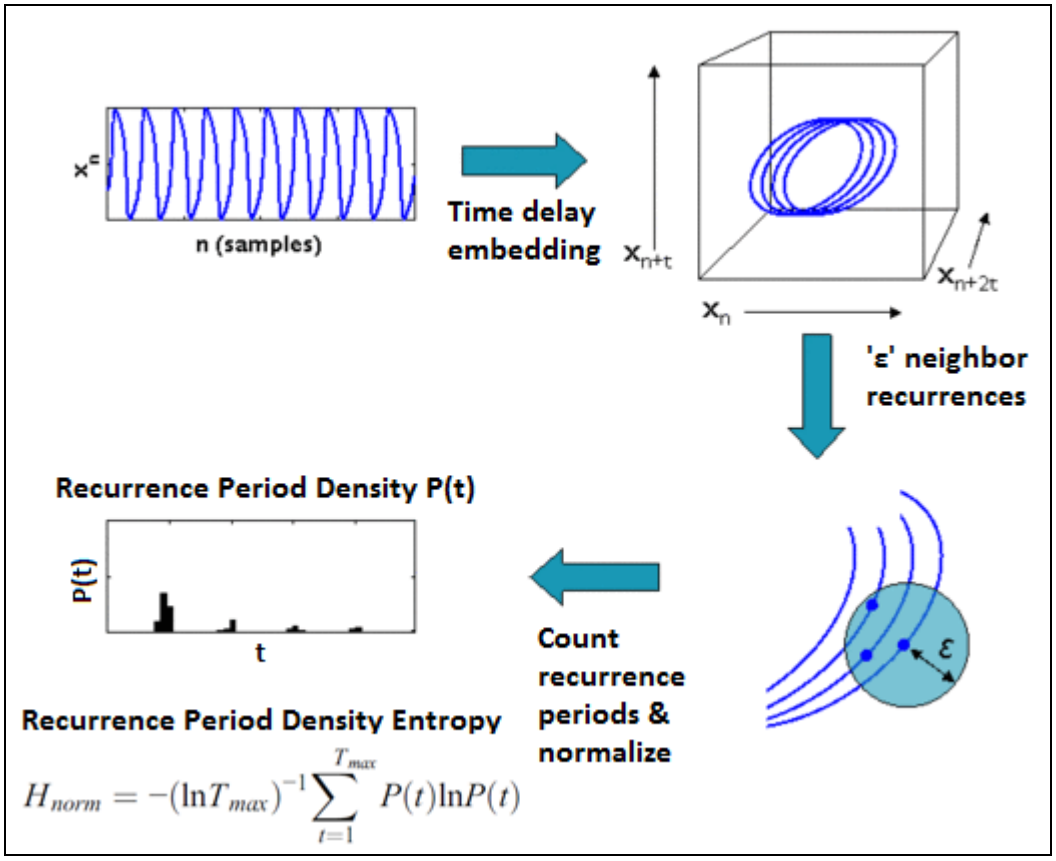

Figure 3-2: Pictorial representation of the RPDE approach. *First time series is embedded with time delay into phase space. Then the recurrence of samples within a spherical neighbored of 'distance epsilon is counted and the recurrence period density is calculated which is used to estimate RPDE. (Adapted from [172])*

RPDE can be used for complexity analysis for any non-linear, non-stationary short and long time series data. Figure 3-3 shows the dynamic range for RPDE across various times series signal. In this thesis, it is hypothesized that the core of the rotor will have higher RPDE value compared to its periphery thereby enabling its accurate identification, which will be validated using optical mapping data with known pivot point locations. RPDE toolbox developed by Max Little in MATLAB was adopted and customized for rotor identification in this thesis. MATLAB program namely "rpde.m" was used to compute RPDE, which uses C program "close_ret.c" and is included in APPENDIX C.

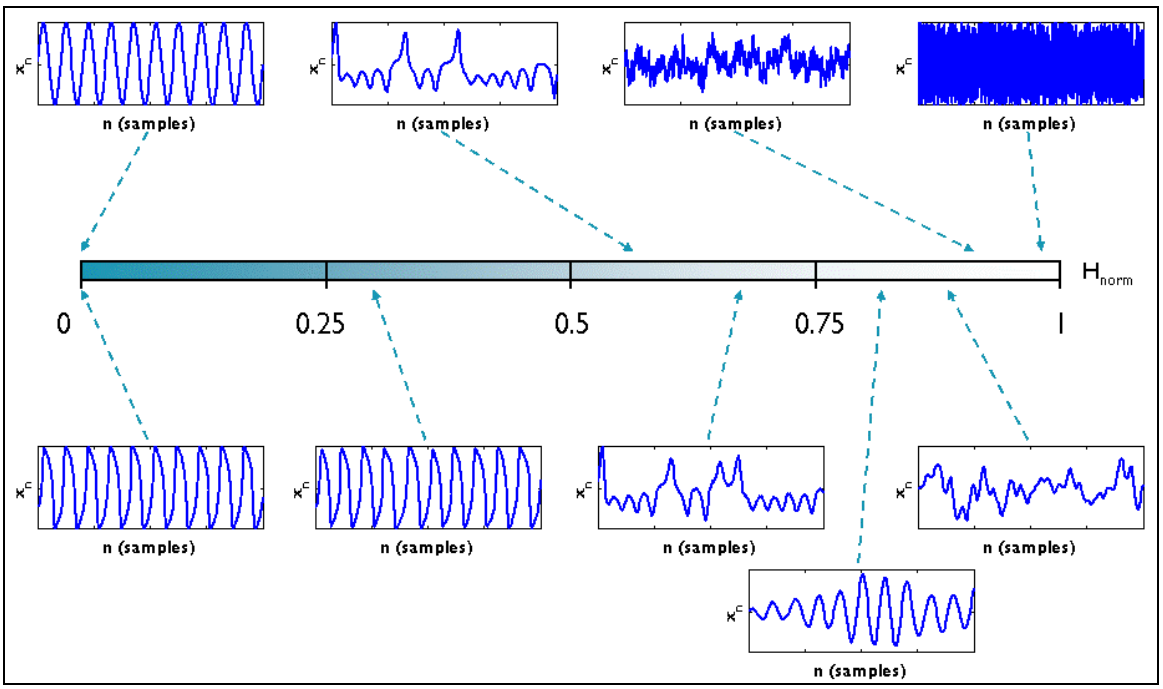

Figure 3-3: Dynamic range of RPDE estimate. *RPDE of periodical waveform is '0' and increases with higher complexity of the time series with a value of '1' for uniform white noise. (Adapted from [172])*

RPDE values were estimated for the sinusoidal waveforms described in section 3.2.1 with M =3 and τ =2 as recommended values (170-172). The single frequency sinusoidal wave had RPDE value of '0' as expected for a purely periodic sinusoidal waveform. RPDE value for the multifrequency sinusoidal wave was 0.52 demonstrating efficacy in complexity measurement compared with SE shown. RPDE measured the complexity correctly with higher values for the multifrequency sinusoidal wave than the single frequency wave. This demonstration offers huge promise for accurate identification of rotor pivot point compared to the periphery due to the chaotic nature at the rotor core.

3.2.1.3 Kurtosis as a statistical technique

In this thesis, the author proposed using higher order statistics by estimating kurtosis of the electrogram data to accurately identify the pivot point of the rotor. Higher order

statistics is useful when dealing with non-Gaussian or possible nonlinear processes which is common in biological signals [173]. The fourth central moment known as “kurtosis” is a measure of the ‘peakedness’ of the probability density function (PDF) of a real-valued random variable [123]. Higher Kurtosis means that more variances are present due to infrequent extreme deviations, as opposed to frequent modestly sized deviations, a characteristic feature that is expected to happen at the rotor pivot zone. Kurtosis has been used in various electrocardiogram (ECG) analysis methods and in particular to describe atrial activity during AF [174].

Kurtosis approach can be applied to any time series data for complexity analysis. In the case of rotor identification, it is expected that the changing wave front direction near the pivot point should cause a broader distribution of amplitudes in the time series data which could cause peakedness as measured by kurtosis which is expected to have a higher value. The periphery region is more uniform and may not display characteristic peakedness unlike the pivot point and should therefore have lower kurtosis. Hence, Kurtosis mapping technique can enable accurate identification of rotor pivot point thereby providing the feasibility to generate patient specific kurtosis maps to guide AF ablation.

The 4th central moment (Kurtosis) can be computed as following [123]:

$$\mathrm{Kurt}(X) = \mathrm{E}\left\{\left[\frac{X - \mathrm{E}\{X\}}{\sigma}\right]^4\right\} = \frac{\mu_X^4}{\sigma_X^4} \tag{3.9}$$

where X is a stochastic univariate variable that describes a random process. The expectation (E) value or mean of a stochastic variable X is defined as the following:

$$\mathrm{E}\{X\} = \int_{-\infty}^{\infty} x \cdot f(x)\, dx = \mu_X \tag{3.10}$$

where x is the time series data and f is the PDF. The standard deviation σ_X is given by the following equation:

$$\sigma_X = \sqrt{\mathrm{Var}(X)} \tag{3.11}$$

where variance Var(X) is called the second central moment, which is a measure of the spread of data and which is described as the following :

$$\mathrm{Var}(X) = \mathrm{E}\{[X - \mathrm{E}\{X\}]^2\} = \sigma_X^2 \tag{3.12}$$

Depending on the Kurtosis value the signal can be classified as sub-Gaussian (Kurtosis < 3), super-Gaussian (Kurtosis > 3) and Gaussian (Kurtosis = 3) [25]. MATLAB program "kurtosis.m" was used to compute kurtosis to validate this technique to accurately identify the rotor pivot points and also process the intracardiac electrograms to obtain patient specific 3D kurtosis map.

Kurtosis values were estimated for the sinusoidal waveforms described in section 3.2.1 using the MATLAB program 'kurtosis.m'. The single frequency sinusoidal wave had a kurtosis value of '1.50' for a purely periodic sinusoidal waveform. Kurtosis value for the multifrequency sinusoidal wave was '3.34' demonstrating efficacy in complexity measurement compared with SE. Kurtosis measured the complexity correctly with higher values for the multifrequency sinusoidal wave than the single frequency wave. This demonstration offers huge promise for accurate identification of rotor pivot point compared to the periphery due to the chaotic nature at the rotor core.

3.2.1.4 Intrinsic mode function complexity index using empirical mode decomposition

Empirical mode decomposition (EMD) method was originally developed by Huang et al. (175) which is a data driven signal processing algorithm that has been established to obtain local features and time-frequency distribution of a complex nonlinear and non-stationary time series data. EMD decomposes signals into basis functions called characteristic intrinsic mode functions (IMFs) and the signal energy associated with those IMFs on various time scales are directly extracted. The EMD approach is based on the concept of instantaneous frequency which becomes valid only in the event the signal is made symmetric with respect to the local zero-mean line. Upper and lower envelopes of the input signal which cover all local maxima and local minima are first constructed. Next, the signal mean is iteratively removed in order to force local symmetry about the zero mean line and this process is referred to as 'sifting'. The sifting process results in the generation of IMFs which are adaptively derived from the signal within the local time scale of the signal and therefore, IMFs have instantaneous frequency associated with them at every point. Hence, higher the complexity of the signal more IMFs to define the signal compared to a relatively less complex signal which needs fewer IMF's. The EMD method is based on the following assumptions [176]:

(1) The number of extrema and the number of zero-crossings must either equal or differ at most by one in the entire time series data.

(2) The mean value of the envelope defined by the local maxima and the envelope defined by the local minima is zero at any point which requires that the signal has at

least two extrema-one maximum and one minimum.

(3) The characteristic time scale is defined by the time lapse between the extrema.

(4) If the time series doesn't not have extrema but contains only inflection points, then it can be differentiated once or more times to reveal the extrema and the final result be obtained by integration of the components.

There are several steps involved with EMD approach to obtain the IMFs. Let the given signal be x(t) which is digitized into a time series signal $x(n) = \{x_1, x_2, x_3 \ldots x_N\}$ of length N. Now the EMD effective algorithm has the following steps:

1) Identify all extrema of x(n).

2) Interpolate between the maxima and connect them by a cubic spline curve to obtain the upper envelope $e_{max}(t)$. Similarly interpolate between the minima using cubic spline curve to obtain the lower envelope $e_{min}(t)$.

3) Compute the mean m(n) of the envelopes.

$m(n) = (e_{max}(n) + e_{min}(n)) /2$

4) Now the first component is extracted by subtracting the mean from the signal:

$d_1(n) = x(n) – m_1(n);$

5) Now $d_1(n)$ is considered as input data and steps 1-4 are repeated until the detail signal $d_k(n)$ can be considered an IMF based on a predefined stopping criteria: $c_k(n) = d_k(n);$

6) Now, iterate steps 1-5 on the residual $r_n(n) = x(n) – c_n(n)$ in order to obtain all the IMFs of the signal. Figure 3-4 shows a pictorial representation of the EMD approach.

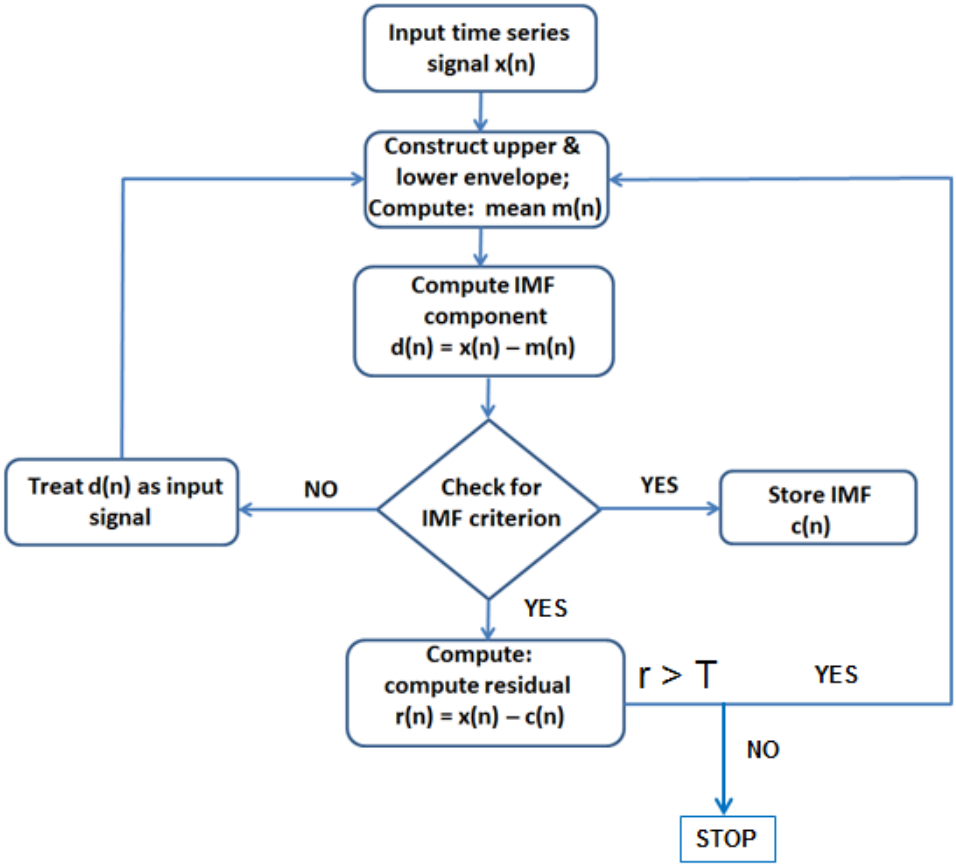

Figure 3-4: Pictorial representation of the EMD approach.

EMD has been used by several researchers to analyze the complexities of electrocardiograms such as extracting chaotic parameters [177]. Once the non-stationary signal is decomposed using EMD to obtain the IMF's the complexity of the IMF is quantified using Lyapunov exponent, entropy, or correlation dimension [178]. Lyapunov exponent or Lyapunov characteristic exponent of a dynamical system is a quantity that characterizes the rate of separation of infinitesimally close trajectories in phase space of n-dimensions that can be used to quantify the complexity of the signal being investigated. Entropy measures the uncertainty in the information and correlation dimension is a type of fractal dimension which is a measure of the dimensionality of the space occupied by a set of random points. ECG's with diseased state have higher complexity therefore more

IMF's are required to describe the signal compared to a normal ECG which has been used to discriminate normal and abnormal ECG's. Intra-atrial electrograms with rotors are highly chaotic and specifically, the rotor pivot region is highly chaotic compared to the periphery. Therefore, it can be expected that mapping using EMD method can capture the complexity of the rotor core area with better contrast using one or all of the chosen complexity parameter such as Lyapunov exponent, entropy, or correlation dimension.

The IMFs represent the natural oscillatory mode embedded in the signal and work as the basis functions, which are determined by the signal itself, rather than pre-determined kernels or basis functions such as in wavelet transform. A major limitation of the EMD approach is the issue of mode mixing, which is defined as either a single IMF consisting of components of widely disparate scales, or a component of a similar scale residing in different IMFs [179-180]. More advanced approaches are being investigated to address these issues such as the ensemble EMD (EEMD) and several other variants which have shown better results (180-181). However, for the purposes of this work, since only complexity measure is desired for the top three IMF's the author chose to use the basic EMD approach to measure the complexity of rotor core compared with periphery in this thesis.

The EMD approach can be applied to electrograms with known pivot point locations such as optical data from imaging the electrical activity of an isolated rabbit heart to validate the efficacy of this approach as well as intra-atrial electrograms obtained from AF patients to measure its complexity to identify rotor core region. At the rotor core, chaotic distribution of the amplitude implies that more IMF's are required to decompose the signal

near the rotor core area compared to the periphery where the amplitude is expected to have uniform distribution. In this thesis, the author chose to use a variant of previously described multiscale entropy called modified multiscale entropy (MMSE) [165] to measure the complexity of the IMF's denoted as the complexity index of the IMF (i-IMF). Therefore, higher i-IMF values are expected at the rotor core region and relatively lower i-IMF values in the periphery, thus enabling accurate identification of the rotor core region. The overall methodology to measure signal complexity using EMD approach proposed in this thesis described as below:

Let $x = \{x_1, x_2, x_3 \ldots x_N\}$ represent the electrogram time series of length N. First, EMD is applied to the time series data and the IMF's are computed. Next, for each IMF moving-averaged time series z^{τ} is computed for the chosen time scale factor 'τ' as illustrated in Figure 3-5 using the following equation:

$$z_j^{\tau} = \frac{1}{(\tau)} \sum_{i=j}^{\tau+j-1} x_i \tag{3.13}$$

where, $1 \leq j \leq N-\tau$ and $i = 1,2,3, \ldots N$;

MSE value for the 2nd, 3rd and 4th IMF is computed using the MMSE approach described in [165] using equations 3.2-3.5 with a scale factor $\tau = 2$. Now, i-IMF is computed as the average MSE of 2nd, 3rd and 4th IMF. The procedure is repeated for each of the electrogram to obtain 2D and 3D i-IMF maps to visually locate the rotor core area which is expected to have high i-IMF compared to the periphery. MATLAB program "emd.m" (APPENDIX D) was used from the EMD toolbox from MATLAB central, Mathworks to decompose the electrograms and measure the complexity to accurately

identify the rotor pivot points and also process the intracardiac electrograms to obtain patient specific 3D i-IMF map.

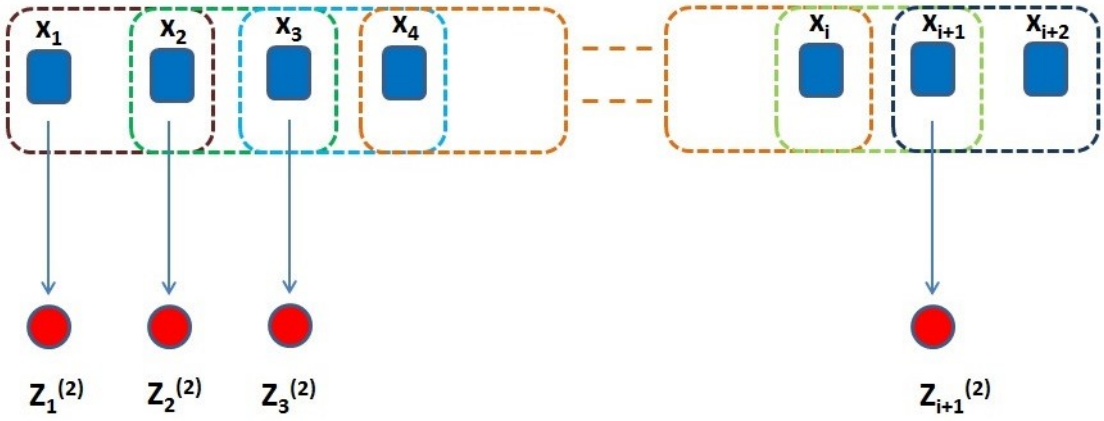

Figure 3-5: Schematic illustration to produce forward moving average time series with scale factor τ = 2 for the MMSE algorithm. *Blue squares represent raw time series data and red dots represent the nearest neighbor moving-averaged time series from which MSE is obtained. Brown square represent the moving window averaging kernel for the raw second time point (X_2), that averages with one forward neighbor with τ = 2 to produce the first new time series point $Z_1^{(2)}$. Similarly green square produces $Z_2^{(2)}$ and so on (orange square) with the dark blue square producing the last time series point $Z_{i+1}^{(2)}$.*

Computational complexity of the EMD approach is determined by the number of samples in the time series being analyzed and the chosen time scale factor 'τ'. The computational time for the EMD approach will be higher compared to other methods developed due to the computation time needed to decompose each electrogram into IMF's which is further processed with MMSE algorithm to obtain complexity values. EMD was performed for the sinusoidal waveforms described in section 3.2.1 using the MATLAB program 'emd.m' to estimate the complexity of IMF's. Figure 3-6 & 3-7 shows the EMD of the single frequency and multi frequency sine wave with 5 and 7 IMFs respectively demonstrating that more complex signal has more IMFs to describe the signal as expected.

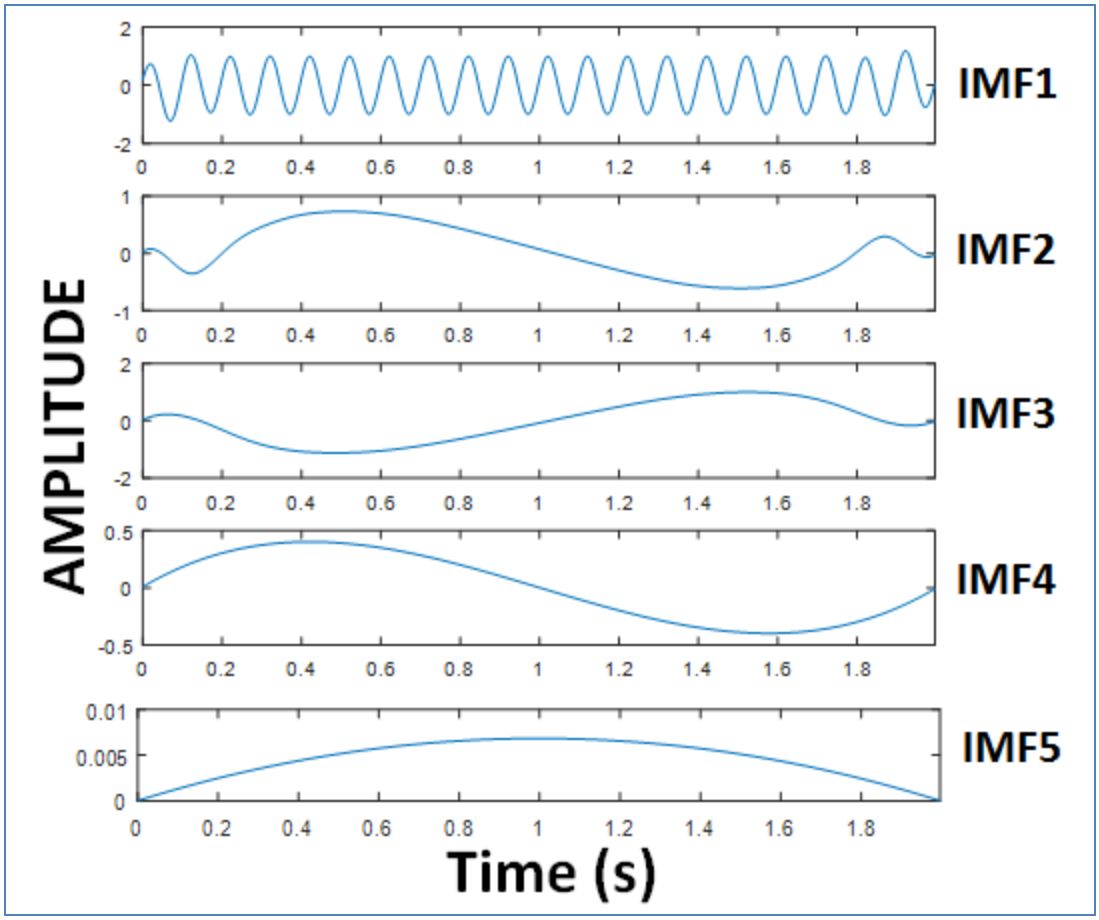

Figure 3-6: Intrinsic mode functions for the single frequency sinusoidal wave. *The sinusoidal waveform was decomposed into 5 IMF's.*

It is conventional to estimate the complexity of the top 3 IMF's and in this demonstration the IMF complexity is estimated as the average of the MMSE value of the first three IMF's. The single frequency sinusoidal wave had an IMF complexity value of '0.18' for a purely periodic sinusoidal waveform and '0.45' for the multifrequency sinusoidal wave demonstrating efficacy in complexity measurement compared with SE. IMF measured the complexity correctly with higher values for the multifrequency sinusoidal wave than the single frequency wave. This demonstration offers huge promise for accurate

identification of rotor pivot point compared to the periphery due to the chaotic nature at the rotor core.

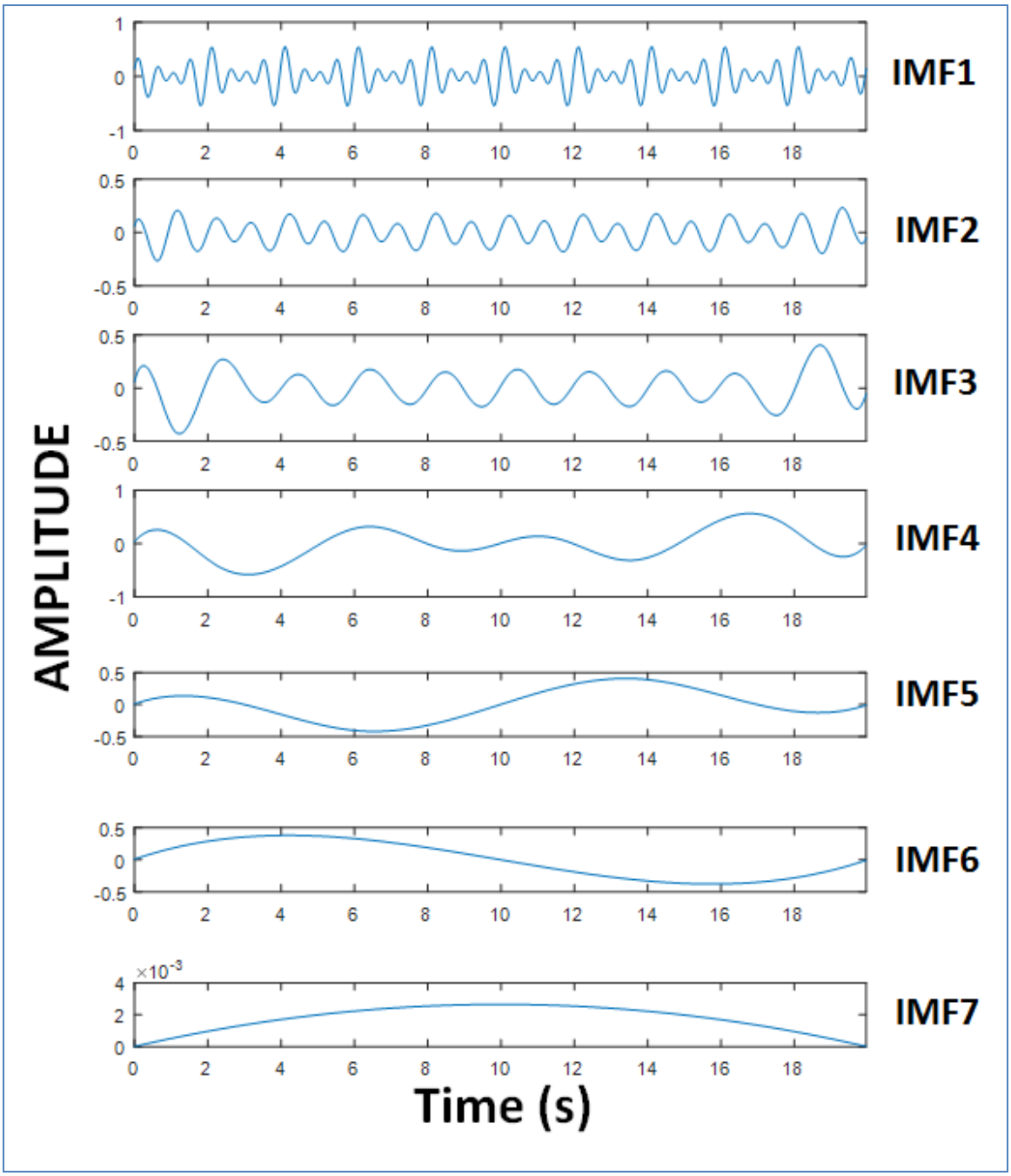

Figure 3-7: Intrinsic mode functions for the multifrequency sinusoidal wave. *The sinusoidal waveform was decomposed into 7 IMF's.*

Figure 3-8 shows the single frequency (A) and multifrequency (B) sinusoidal wave, corresponding amplitude histograms (C & D) and their MSE, RPDE, Kurtosis, IMF and SE values.

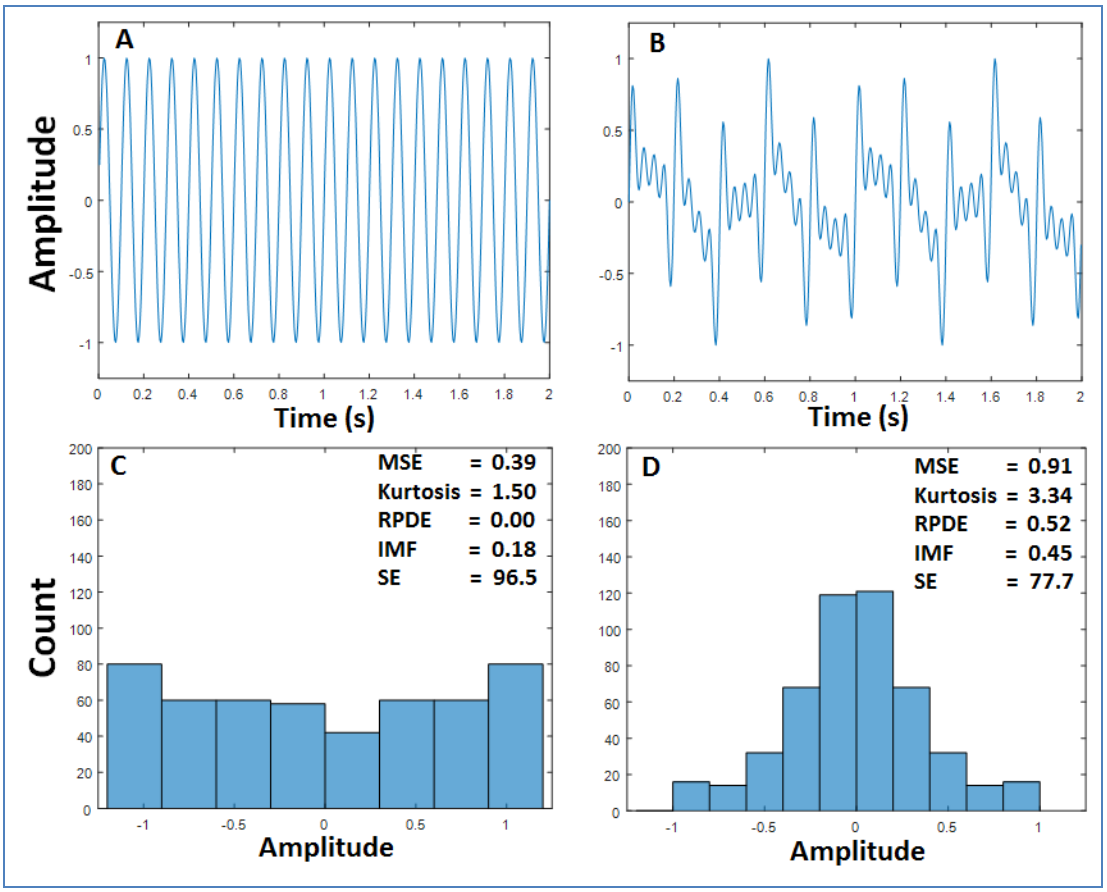

Figure 3-8: Demonstration of novel time domain approaches using single and multi-frequency sinusoidal wave. *(A) shows 10 Hz sinusoidal wave, (B) shows Multifrequency sinusoidal wave, (C) and (D) shows amplitude histograms of (A) and (B with MSE, Kurtosis, RPDE and IMF complexity values respectively.*

As the Figure 3-8 shows all four novel time domain based approaches proposed in this thesis such as MSE, RPDE, Kurtosis and IMF measured the complexity of the signal better than SE for the multifrequency complex signal compared with the single frequency sinusoidal signal. These preliminary results demonstrate the feasibility to use these

approaches to accurately identify rotor core region compared to the periphery based on the different temporal characteristics of the time series signal. The sinusoidal waveforms generated for this demonstration is short time series signal with only 500 sample points that is typical in a clinical setting to obtain intracardiac electrogram for processing to identify the active sites that causes and maintains AF.

3.2.2 Novel frequency domain approach

Previous section discussed several novel time domain methods that captured variety of temporal characteristics of a time series data to quantify the signal complexity that can be potentially used for rotor pivot point identification. While temporal characteristics of a time series data are very useful, frequency characteristics of the time series signal carries signature information of the signal which can be exploited in frequency domain approaches to quantify the complexity of the signal. Biomedical signals such as ECG especially present different temporal and frequency characteristics between normal and diseased states which can be used for prognosis and diagnosis of various heart diseases. As discussed in Chapter 2, DF analysis is the common frequency domain approach that has been explored by several researchers especially to identify active arrhythmogenic sites in AF to guide AF ablation. The primary limitation of DF approach is that, uniform DF is seen throughout the rotor region providing no information on the rotor core zone and therefore challenges clinical guidance for AF ablation.

To address this major limitation, this section of the thesis is devoted to discuss the development of a novel MSF approach that will capture the intrinsic complexity of a non-stationary and nonlinear short or long time series data in the frequency domain. The

following section will introduce the concept of instantaneous frequency and discuss the several approaches that have been used literature. This thesis, particularly exploits the instantaneous frequency formulation used in Knutsson et al. to estimate wide range frequency estimation which is adapted for analyzing signals from physiological processes such as ECG and intracardiac electrograms in addressing the challenge of accurately identifying rotor pivot point with better contrast compared to the periphery.

3.2.2.1 Novel multiscale frequency MSF technique

Frequency content of stationary and non-stationary signals

The term frequency is a well-defined mathematical entity which simply refers to the number of cycles or completed alternations per unit time of a wave or oscillation with units of Hertz (Hz) which refers to cycles/second or can be expressed in radians. Stationary signal is one if its frequency or spectral contents are not changing with respect to time. Any stationary signal can be represented as a weighted sum of sine and cosine functions having particular amplitudes, phases and frequencies. Non-stationary signals are those whose spectral characteristics change with time and therefore a simplistic representation as a weighted sum of sine and cosine functions having particular amplitudes, phases and frequencies is impossible [182].

Concept of Instantaneous Frequency

Many real life signals are non-stationary (such as biological signals) which challenges conventional frequency domain approaches using Fourier transform and warranted developing novel methods to analyze non stationary signals in a frequency-like manner. This led to the introduction of a novel concept called ‘instantaneous frequency’

which is commonly defined as the rate of change in phase of the analytical signal [182]. The analytic signal is a complex signal uniquely defined by a real signal that can be obtained using Hilbert transform. Instantaneous frequency is global entities in that local alterations of the signal will affect the instantaneous frequency everywhere due to the infinite kernel associated with the Hilbert transform [182].

Methods to obtain instantaneous frequency

Earlier attempts to tackle the local alterations issue are to estimate local frequency estimates, and Gabor proposed a combined time and frequency representation by modifying Fourier transform with a Gaussian window in order to better describe local signal properties [182]. This approach commonly referred to as Gabor transform uses modulated Gaussian functions or basis functions called Gabor filters that are maximally compact in time and frequency. A major limitation of Gabor transform is that Gabor functions are non-orthogonal and although they are well localized, have infinite support which forces truncation in all practical implementations of these filters [182]. A solution to this issue was to use a general window function instead of the Gaussian window that gave rise to windowed Fourier transform which has different complex modulated windows as 'basis' functions. Short Time Fourier Transform (STFT) provides the time-frequency representation called the 'spectrogram' which has been widely used for many applications in analyzing non-stationary time series signal [182].

Recent advances in this field include the S-transform which is an invertible time-frequency analysis technique that combines elements of wavelet transforms and short-time Fourier transforms (183). Wavelet transform has gained much popularity by

decomposing non-stationary signals into wavelets by translation and dilatations of a "mother wavelet" for time-frequency analysis to infer instantaneous frequency. Recently, a new time-frequency analysis approach was introduced using local attributes by localizing frequency content in time using an iterative inversion framework [184]. In this method time-varying Fourier coefficients are calculated by solving a least-squares problem that uses regularized nonstationary regression and the time-frequency map is obtained as the norm of time-varying coefficients. This approach is also being widely used in a variety of applications in analyzing complex non-stationary time series data.

The objective of this section of the thesis is to propose and develop a novel frequency domain technique that can accurately capture the rotor pivot point complexity thereby enabling its accurate identification compared to the periphery. The author specifically reviewed the instantaneous frequency concept developed by Knutsson et al. using narrowband analysis using band-pass quadrature filters such as log-normal or Gabor filters over a number of scales [182]. The estimates are weighted and summed to produce a wide range frequency estimate. Band-pass quadrature filters are robust to estimating local multi-scale information, such as the energy, phase, radial frequency and orientation/angular frequency. The Hilbert transform operation transforms a real-valued signal to analytic signal with no negative frequencies, and its utility with the quadrature filter can yield multiscale frequency **(**MSF) information by weighting the various frequency components. This approach is robust enough to capture the time varying chaotic frequency components of electrograms during AF with a potential to discriminate rotor pivot point from periphery based on its frequency content by estimate MSF. The

following section will discuss the design of log-normal filters and the steps involved in wide range frequency estimation to quantify MSF by adapting the technique developed by Knutsson et al [182].

Log-normal/Gabor filter design:

The lognormal filter Q(u) is a spherically separable quadrature filter with a radial frequency function $R_i(\rho)$ which is Gaussian on a logarithmic scale.

$$Q(u) = R_i(\rho)\, D_k(\hat{u}) \tag{3.14}$$

$$Ri(\rho) = e^{-C_B \ln^2(\rho/\rho_i)} \tag{3.15}$$

$$C_B = \frac{4}{B^2 \ln(2)} \tag{3.16}$$

$$B = \frac{\ln(\rho_u/\rho_l)}{\ln(2)} \tag{3.17}$$

$\rho = \|\boldsymbol{u}\|$ is the norm of the frequency vector;

ρ_u and ρ_l are the 'ρ' values for which $R_i(\rho) = 0.5$.

ρ_i is the center frequency; $D_k(\hat{u})$ is the directional function of the quadrature filters;

B is the 6 dB relative bandwidth of the quadrature filters in octaves.

Wide range frequency estimation:

Now a local frequency estimate can be obtained by combining the outputs from two or more sets of filters which differ only in center frequency 'ρ_i'. A wide range local frequency estimate can easily be obtained by weighted summation over a number of different filter pairs. In this work a wide range frequency estimate which we refer to as 'multiscale frequency (MSF)' is obtained as the ratio between sums of lognormal filter outputs. In this work eight Log-Gabor filters were designed and used with a relative filter bandwidth B of $2\sqrt{2}$, and one octave apart. The center frequencies for the log-Gabor

filters were chosen to span a physiological range for human heart rate. A wide range of local MSF estimate can be obtained by weighted summation over the eight different filter pairs using the following equation [182]:

$$MSF = \rho_o \left[\sum_{i=1}^{N-1} q_i\right]^{-1} \sum_{i=1}^{N-1} 2^{i+0.5}\, q_{i+1} \tag{3.18}$$

MSF can be used for complexity analysis for any non-linear, non-stationary short and long time series data. In this thesis, it is hypothesized that the core of the rotor will have higher MSF value compared to its periphery thereby enabling its accurate identification, which will be validated using optical mapping data with known pivot point locations. Custom MATLAB program '*FrequencyEstimation_1D.m'* was written implementing the filter design discussed above for MSF estimation and is included in APPENDIX E.

MSF demonstration with a simulated non-stationary sinusoidal waveform:

Demonstration of MSF estimation using simulated sinusoidal signal with time evolving frequency (0.1, 0.2 and 0.8 radians) is provided to provide insight into this approach. Custom MATLAB software was used to simulate the non-stationary signal shown in Figure 3-9 (375 seconds in time) with sampling frequency of 200 Hz and MSF estimation was performed without any preprocessing steps. Figure 3-10 shows the single sided power specturm of y(t) correctly identifying the dominant frequencies at 0.1, 0.2 and 0.8 radians identified by the peaks. Figure 3-11 shows the frequency response of the eight Log-Gabor filters in radians with center frequencies at π/128, π/64, π/32, π/16, π/8, π/4, π/2 and π radians. Figure 3-12 shows the time-frequency plot showing wide range frequency estimation for the simulated non-stationary sinusoidal waveform. Correct

frequencies of 0.1, 0.2 and 0.8 radians were observed for their corresponding time frames in reference to Figure 3-9. Gibb's ringing is noted in the 0.8 radians frequency time frame that can be attributed to the sharp transitions from the band pass filter response.

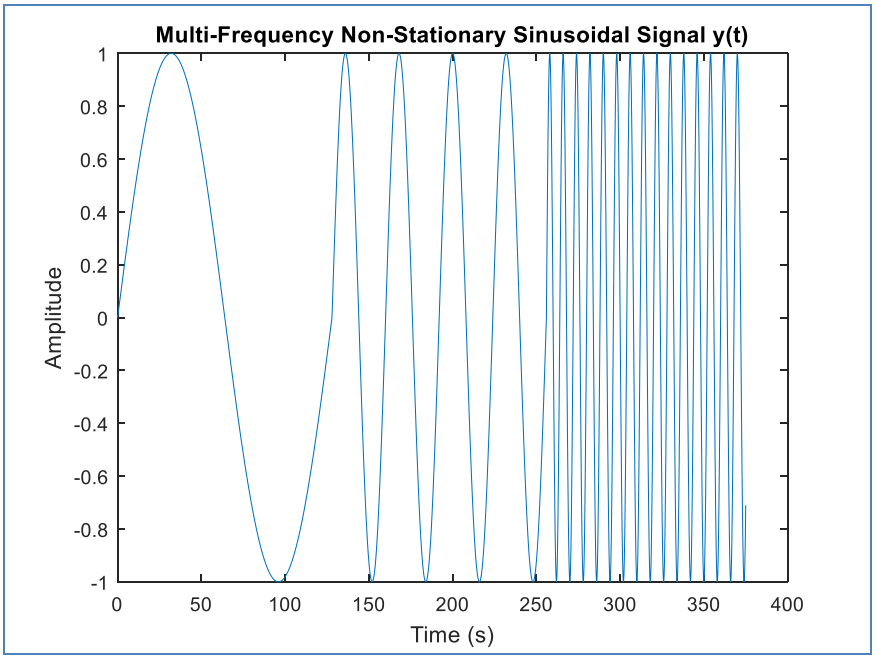

Figure 3-9: Simulated non-stationary multifrequency sinusoidal waveform with frequencies @ 0.1, 0.2 and 0.8 radians

The MSF estimate for the non-stationary sinusoidal signal is the average of the wide range estimation which is 0.37 radians. If some *a priori* knowledge of the energies associated with various frequencies in the signal is known then a reasonable weighting factor could be used to obtain a more reasonable MSF estimate. Nevertheless, the results demonstrate the robustness of the MSF technique in capturing the instantaneous frequency of a non-stationary signal which provides immense potential to accurately identify the rotor core.

DF and MSF analysis was performed on the simulated single and multifrequency sinusoidal signal described in the previous section. The quadrature filters center

frequency ranged from 0.625 Hz to 80 Hz with -6dB roll off per octave as shown in Figure 3-13. Figure 3-14 (A) and (B) shows the single and multifrequency sinusoidal signal. Figure 3-14 (C) and (D) shows their corresponding normalized power spectrum. The power spectrum of the single frequency signal correctly shows a peak at the 10 Hz and the MSF estimate was 27.82 Hz. Similarly, the power spectrum of the multifrequency signal correctly shows peaks at 2, 5, 10, 15 and 20 Hz with an MSF estimate of 30.43 Hz which is higher than that of the single frequency MSF estimate.

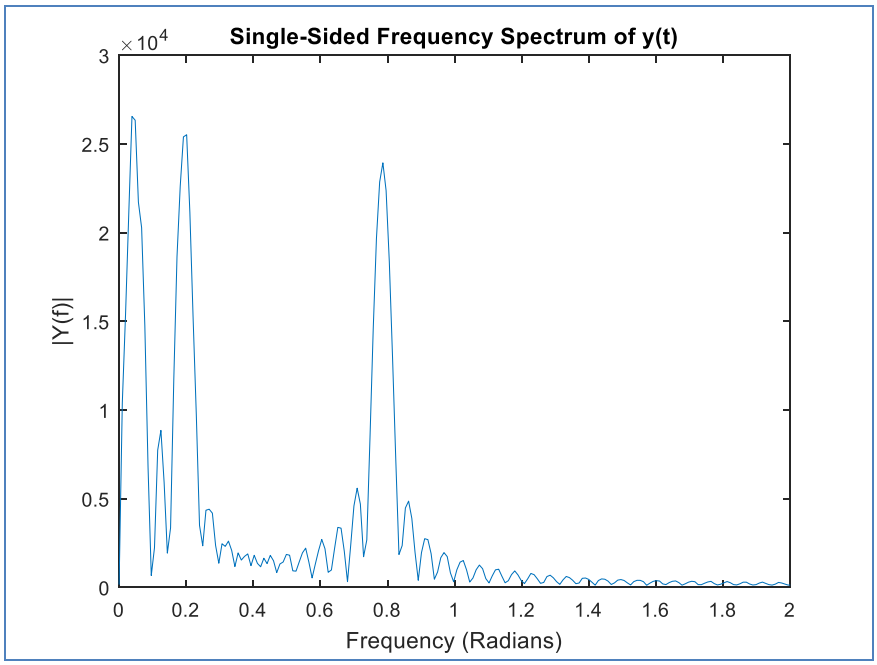

Figure 3-10: Single sided power spectrum of the non-stationary multifrequency sinusoidal waveform. *Peak frequencies are noted at 0.1, 0.2 and 0.8 radians.*

The results of the two analyses: (i) non-stationary multifrequency sinusoidal signal and (ii) stationary single and multifrequency sinusoidal signal demonstrate the functionality of the MSF technique by capturing the entire frequency content of the signal in providing wide range frequency estimation.

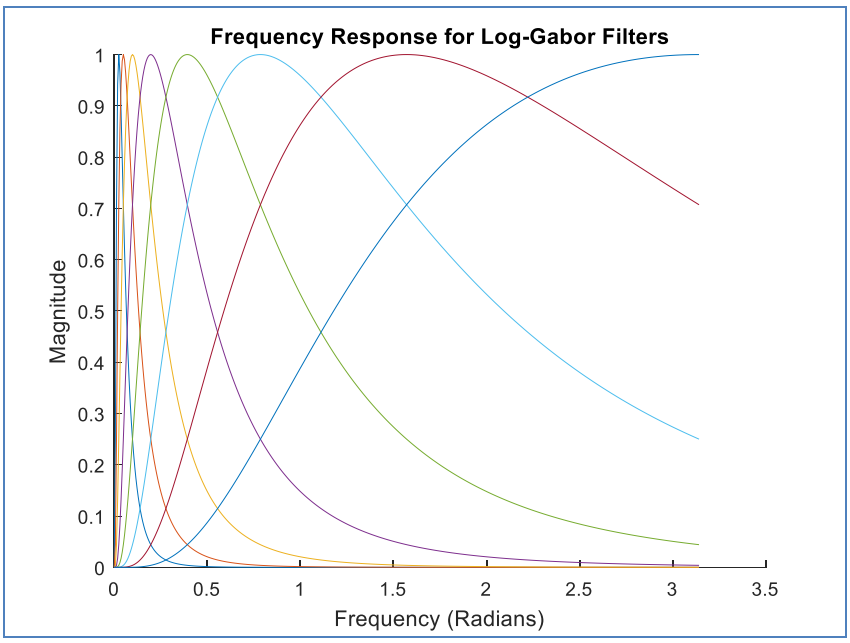

Figure 3-11: Frequency response of the Log-Gabor filters in radians. *Eight filters were designed with center frequencies at π/128, π/64, π/32, π/16, π/8, π/4, π/2 and π radians.*

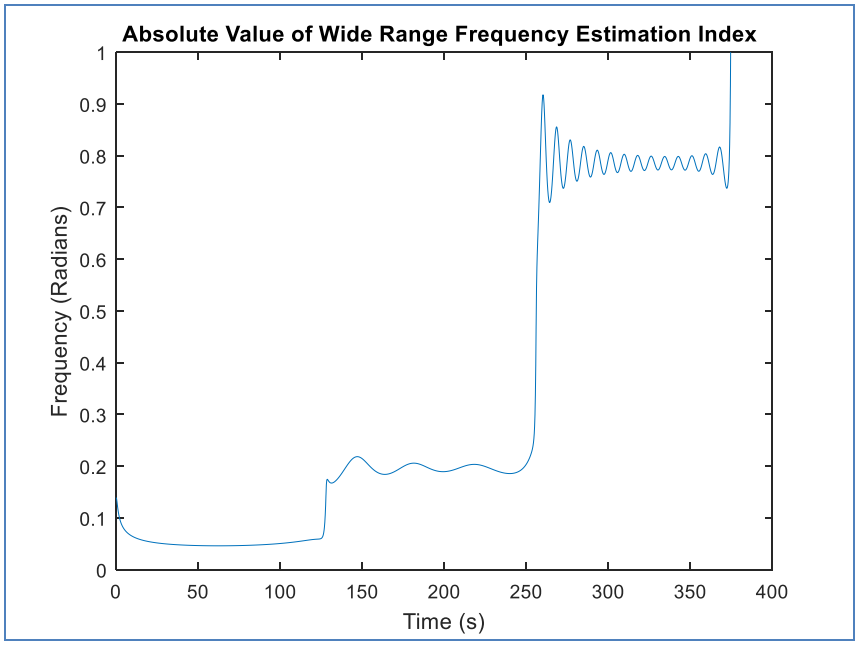

Figure 3-12: Time-Frequency plot showing wide range frequency estimation for the simulated non-stationary sinusoidal waveform. *Correct frequencies of 0.1, 0.2 and 0.8 radians were observed for their corresponding time frames in reference to Figure 3-x. Gibb's ringing is noted in the 0.8 radians frequency time frame.*

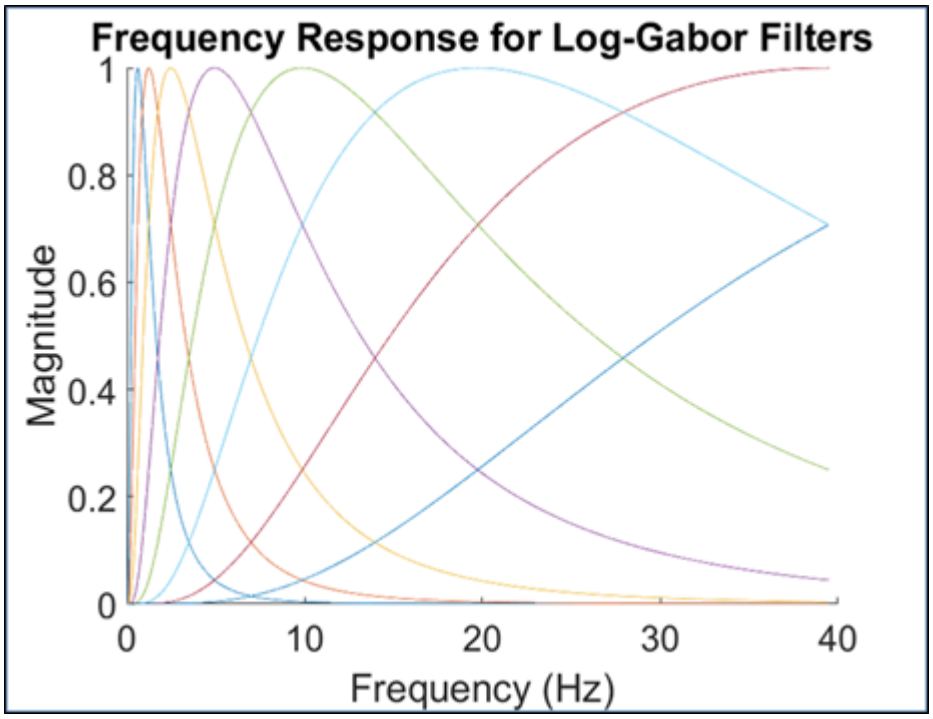

Figure 3-13: Frequency response of the Log-Gabor filters in Hertz. *Eight filters were designed with center frequencies at 0.625, 1.25, 2.5, 5, 10, 20, 40 and 80 Hz.*

It should be noted that, for the stationary 10 Hz signal, the MSF estimate was 27.82 Hz which results from the outputs of the eight filters which has -6 dB roll off that contributes to the filter outputs which falls in the bandwidth of the respective filters. MSF of multifrequency sinusoidal wave was only 30.43 Hz which is slightly higher than the single frequency MSF estimate. It is important to note that this MSF estimate is the average value of the instantaneous wide range frequency estimate and the frequency response of the 8 quadrature filters shown in Figure 3-13 explains the contribution of each of the filter outputs based on the input signal frequency content. Nevertheless, this discrimination seems to be sufficient to perform complexity analysis on real life signals such as ECG and intracardiac electrograms for the purposes of this thesis to accurately identify rotor core with known pivot point locations.

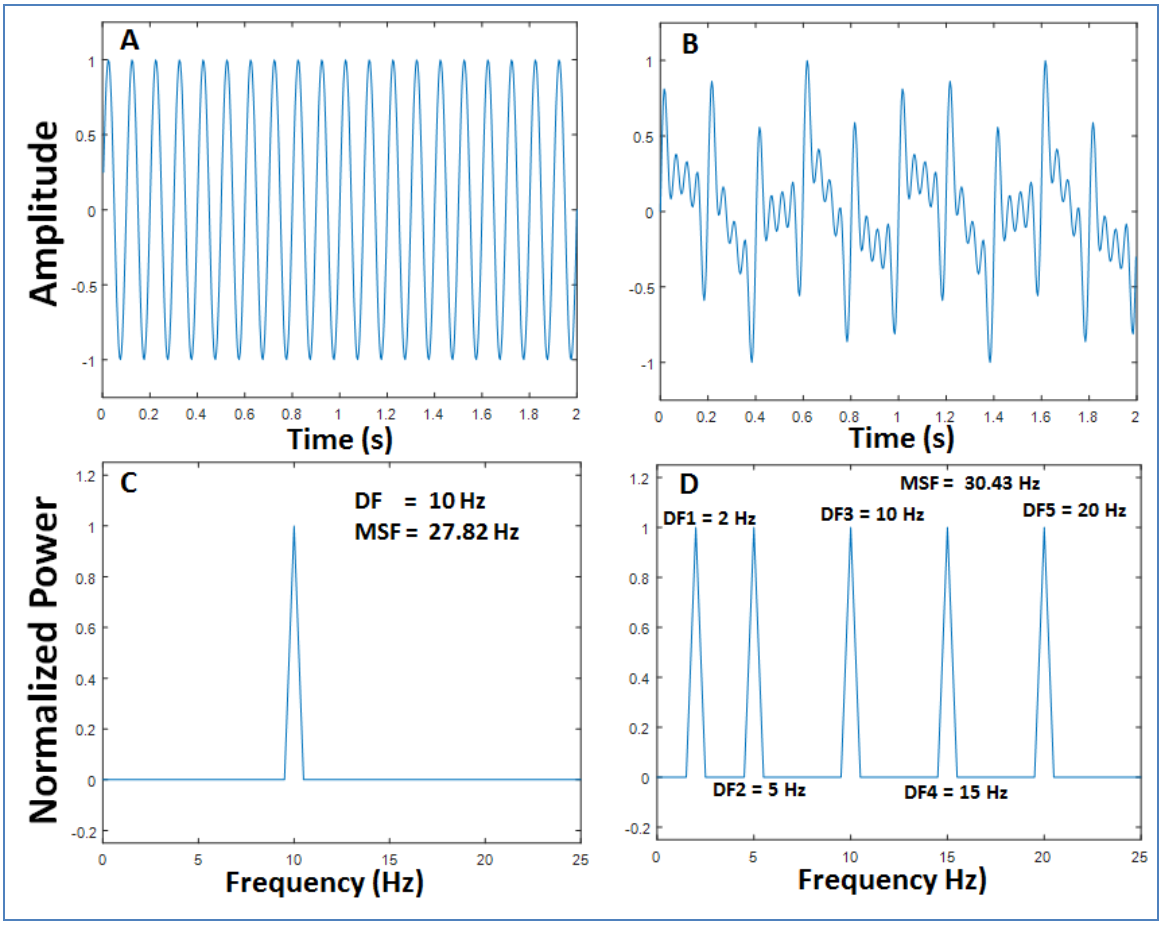

Figure 3-14: Demonstration of MSF approach using single and multi-frequency stationary sinusoidal wave. *(A) shows 10 Hz sinusoidal wave, (B) shows Multifrequency sinusoidal wave, (C) and (D) shows normalized power spectrum of (A) and (B with DF and MSF estimates respectively.*

Since non-stationary signals have changing spectral contents based on the dynamical system that causes it, there can be some limitations with the fixed quadrature filter designs used in this thesis for MSF estimation. However, realistic center frequencies can be chosen to best represent the physiological range for robust MSF estimation.

3.3 Discussion

Five novel quantitative electrogram analysis approaches were proposed and described in this thesis. MSE, RPDE, kurtosis, and EMD approaches explored the time series data

in time domain to capture the intrinsic complexity of the data. MSF approach takes into account the contributions from various frequency components that describe the time series data for complexity analysis. As, evident each of these approaches explore different aspects of the time series i.e. MSE captures periodicity or repetitiveness in linear space, while RPDE captures periodicity or repetitiveness in phase space, kurtosis captures the 'peaknedness' of the probability distribution function in linear space, EMD approach computes the complexity of the IMF time series in temporal domain by preserving frequency contents and MSF computes the instantaneous frequency using filter bank design.

The robustness of each of the approach was demonstrated with a short time series single and multi-frequency stationary sinusoidal waveform by comparing it with SE approach considered as gold standard for the purposes of this work. The results indicate that MSE, RPDE, kurtosis and EMD quantified the complexity of the multi-frequency sinusoidal waveform better than SE. For rotor analysis, it is known that at the rotor core the time series is highly chaotic similar to the multifrequency sinusoidal waveform compared to the periphery which is similar to the single frequency sinusoidal waveform which is more uniform compared to the multi-frequency wave. All the time domain based approaches correctly quantified the multifrequency sinusoidal waveform with higher complexity compared to the single frequency waveform which indicates that these approaches will robustly discriminate rotor core and periphery by their complexity estimates better than SE approach. Similarly, MSF approaches used the various frequency components of the multifrequency wave which yielded a higher MSF

compared to the single frequency wave enabling it robust discrimination. Rotor core is highly chaotic that will have broader range of frequency components including the dominant frequency compared to the periphery. MSF estimate at the rotor core thus will have higher value i.e. complexity compared to the periphery that will enable its robust discrimination to accurately identify the rotor pivot point. These preliminary results suggest that the novel approaches developed in this section will support the goals of this thesis for accurate identification of rotor pivot point. Also, the approaches demonstrated efficacy with short time series with only 500 sample points. For a sampling rate of 250 Hz it represents 2 s data, which is mimics clinical setting for acquiring intracardiac electrograms from AF patients, demonstrating the suitability of these approaches for clinical electrogram data analysis for rotor identification. Demonstration of robustness of each of these approaches using noise analysis, discrimination of normal sinus rhythm and AF on single lead ECG and validation with optical mapping and numerical rotor data are presented in chapters 4, 5 and 6 respectively.

3.4 Conclusion

This chapter has introduced and discussed the novel quantitative electrogram analysis approaches for rotor pivot point identification. The rationale of each of the approach for accurate quantification of the complexity of the time series was provided which can enable accurate rotor pivot point identification compared to periphery with better contrast, supported by the preliminary validation using simulated sinusoidal waveforms. Custom MATLAB programs were written to implement each of these novel approaches based on the algorithm outlined in each section.

CHAPTER 4: DEMONSTRATION OF ROBUSTNESS OF NOVEL APPROACHES USING NOISE ANALYSIS

4.1 Introduction

This section of the thesis is devoted to the discussion of the rigorous testing of the novel approaches described in Chapter 3 for performances in presence of various noises such as white, pink and brown noise. Additionally, robustness with various time series lengths is tested to demonstrate the efficacy of these novel approaches for short time series analysis by comparing with SE as "gold standard' in measuring the complexity of biomedical signals for the purposes of this thesis. The robustness of these approaches is further validated with simulated test sinusoidal waveforms with stationary single and multifrequency signals mimicking rotor periphery and core regions in its raw form and with noise contamination for various time series lengths to estimate complexity by comparing it with SE approach. Finally, simulated ECG dataset is used for testing robustness of these approaches for estimating complexity in its raw form and with noise for various time series lengths in comparison with SE approach. The following section will describe each of the steps involved for noise analysis and present the results for each approach for the variety of simulate data sets.

4.2 Noise analysis using simulated white, pink and brown noise

The second specific aim of this thesis is "*To demonstrate the robustness of the novel electrogram analysis approaches with noise and validate their efficacy using short time series data using simulated sinusoidal wave and flat baseline ECG".* The presence of noise sources is very common in many time series data including biomedical signals.

Therefore, the influence of noise on the complexity analysis of the novel methods developed in this thesis has to be evaluated to demonstrate the robustness and efficacy of the techniques. This section of the thesis is devoted to discussing performance evaluation of the novel MSE, RPDE, kurtosis, IMF and MSF approaches and compare it with performance of SE (as gold standard) with respect to the most common sources of noise [185-186] such as (i) zero mean white noise with wide range flat spectrum as shown in Figure 4-1, (ii) pink noise which has the inverse frequency response (1/f) as shown in Figure 4-2 and (iii) brown noise which has the inverse frequency squared response ($1/f^2$) as shown in Figure 4-3.

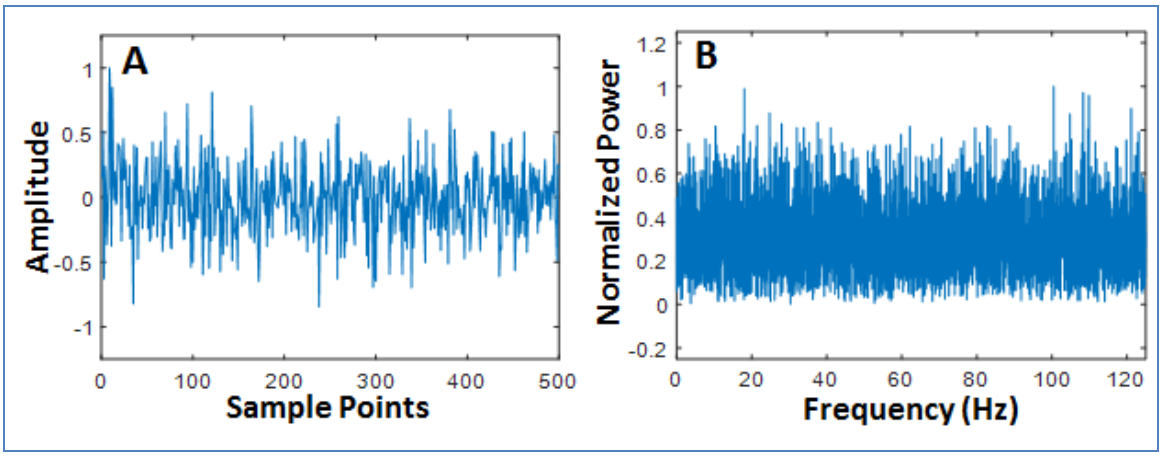

Figure 4-1: Raw white noise and its normalized power spectrum. *(A) shows the random nature of the white noise and (B) shows the flat spectrum over wide range of frequencies.*

As seen from Fig. 4-1 white noise has flat frequency spectrum which will distort any time series data that challenges the novel approaches in estimating the complexity of signals contaminated with white noise. Pink noise shows inverse frequency response as seen in Fig. 4-2 that will variably distort the frequency content of the time series data offering challenge for its removal. Similarly, brown noise shows inverse frequency squared response as seen in Figure 4-3 that will variably distort the frequency content of

the time series data offering challenge for its removal. Therefore, most often complexity estimates with these noises are performed without attempting to remove them which may distort the original signal. Therefore, robustness of the novel approaches in estimating complexity with short time series is extremely important in the presence of these noises when its removal is challenging. Complexity analysis with noise testing using test sinusoidal and ECG data with various time series lengths can demonstrate robustness by comparing with SE to achieve the objective of this section of the thesis.

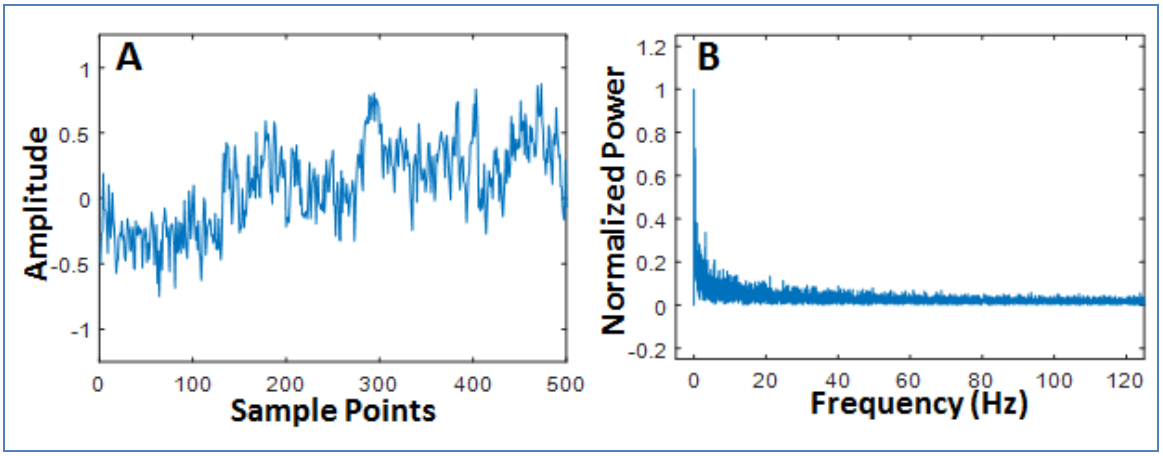

Figure 4-2: Raw pink noise and its normalized power spectrum. *(A) shows the temporal behavior of pink noise and (B) shows the spectrum with (1/f) response.*

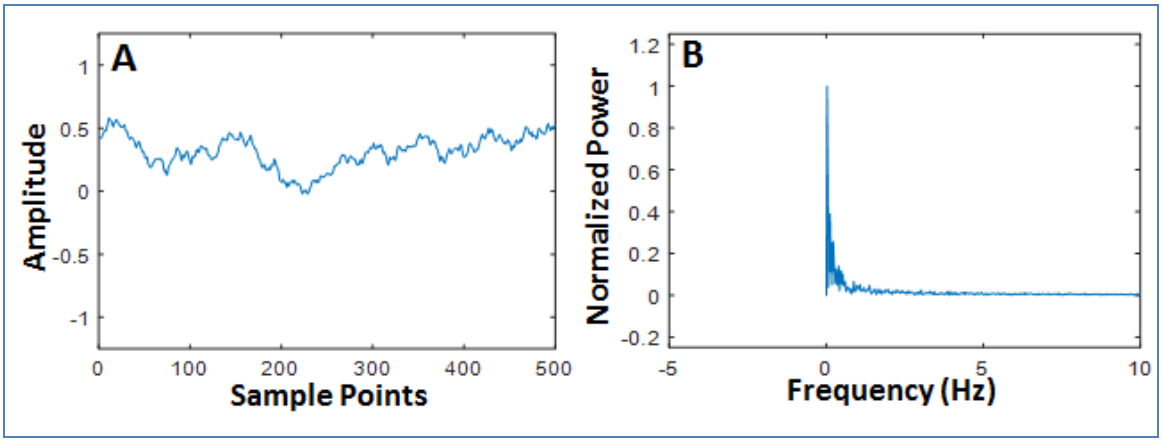

Figure 4-3: Raw brown noise and its normalized power spectrum. *(A) shows the temporal behavior of brown noise and (B) shows the spectrum with* $(1/f^2)$ *response.*

4.2.1 Noise simulation

White noise, pink noise and brown noise were simulated in MATLAB, with 10000 sample points. Ten short time series (TS) versions of these data were created with 250, 500, 750, 1000, 2000, 4000, 5000, 6000, 8000 and 10000 samples. TS is represented from a scale of 1 to 10 for these various length time series for plotting purposes. MSE, RPDE, Kurtosis, IMF and MSF values were calculated as described in the previous sections for each noise.

For MSE approach different time scale factors 'τ' from 1 to 20 over varying time series lengths were explored. Normalized MSE (for τ = 1, 2, 3, 5) and SE were calculated by dividing the MSE (and SE) values by maximum value of MSE (and SE) across varying time series. Similarly, normalized values for RPDE, kurtosis, IMF and MSF were obtained and compared with SE for performance evaluation.

4.2.2 Noise analysis on single and multi-frequency stationary sinusoidal waves

Sinusoidal wave represents the simplest form of a time series signal which can be used to test the robustness of a novel approaches developed in the presence of various noises. Biomedical signals can be represented as a complex superposition of these sinusoidal signals with multiple frequencies, which will correspond to different morphological as well as frequency domains that are present in the diseased state compared to the normal state.

In section 3.2, stationary sinusoidal wave with single frequency of 10 Hz and multi-frequency sinusoidal wave with superposition of 2, 5, 10, 15 and 20 Hz frequencies was simulated with 500 samples for demonstrating the performances of each of the novel

approaches such as MSE, RPDE, kurtosis, IMF and MSF (Figure 3-8). To observe the effect of the time series lengths on the performance of each of these approaches these sinusoidal waveforms were created with ten time series (TS) versions as described in the previous section 3.4.1 in MATLAB and analyzed in its raw form. Next, white, pink and brown noise was added to the single and multi-frequency sinusoidal wave and the analysis was performed as before to compare the performance of each of the approaches with SE to demonstrate their robustness.

4.2.3 Flat baseline noise-free ECG analysis

ECG is the most commonly used time series signal for diagnostic of various diseases of the heart. Conventionally, 12-lead ECG is used in a clinical setting for a comprehensive diagnosis. Recently, the use of single lead ECG analysis has been proposed for ambulatory and remote settings for a quick diagnosis which prompts for early and timely care. ECG is commonly affected by electromagnetic interference noise, powerline noise, baseline wander noise, electromyogram noise and various other low and high frequency noises for which there are robust methods are available for denoising [136-138]. However, ECG is also affected by white, pink and brown which embed within the ECG offering denoising challenges and in particular affects complexity analysis of ECG during normal and diseased states [185-186]. Therefore, it is important to analyze the influence of these noises in ECG to demonstrate efficacy of the novel approaches proposed in this thesis. A noise-free flat baseline ECG was obtained using a simulator device with 10000 sample points [187]. Figure 4-4 A shows the ECG wave and its

normalized power spectrum is shown in Fig. 4-4 B and its complexity was analyzed in its raw form using the novel approaches.

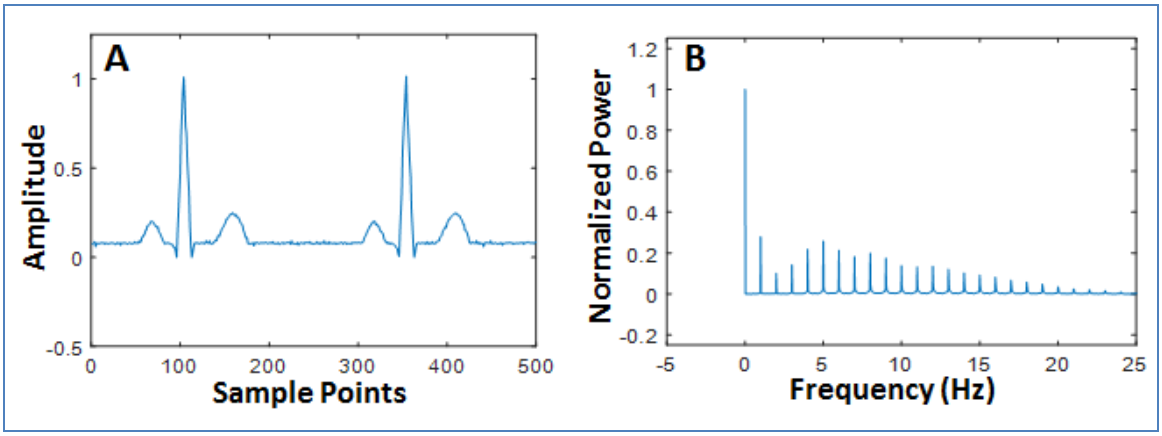

Figure 4-4: Noise free flat baseline ECG waveform and its normalized power spectrum. *(A) shows 2 ECG traces with flat baseline and (B) shows the spectrum with several artificial frequencies used to simulate the flat baseline noise free ECG.*

Next, ten short time series versions of these data were created as before and white, pink and brown noise was added to the ECG data. The analysis was performed as described in the previous section to compare the performance of each of the approaches with SE to demonstrate their robustness.

4.3 Robustness of MSE approach

This section will justify the robustness of MSE approach based on the results of complexity analysis with raw noise, and noise contaminated with sinusoidal and flat baseline ECG waveforms for various TS lengths by comparing it with SE approach.

4.3.1 Complexity analysis of raw noise with MSE

Figure 4-5 shows the robustness of MSE compared with SE approach with respect to different types of noise: white (panel A), pink (panel B) and brown (panel C). The middle row of Fig. 4-5 A-C shows the MSE values as a function of τ for varying TS lengths.

MSE and SE results for $\tau > 5$ are quantitatively similar to that of $\tau = 5$ and therefore it is not shown. As expected, for white noise, MSE monotonically decreases as τ increases and changing TS length does not affect the data. For pink noise, MSE increases with the increase of TS length, and for long TS (1000 samples) MSE does not depend on τ. For brown noise, MSE decreases with increase in TS length and does not depend on τ for long TS. These results demonstrate the robustness of MSE since the expected behavior is observed for each noise. The bottom row of Fig. 4-5 A-C shows the normalized values of MSE (for different τ) and SE as a function of TS length. As seen from these data, the values of SE decreases as TS is getting shorter for all types of noises, while MSE values do not depend on the TS length. These results demonstrate that the performance of MSE is better than SE, especially for short time series.

MSE of white noise is expected to show a monotonically decreasing response with higher scale factors [164-166] which was seen in Fig. 4-5 A middle panel with increasing scale factor due to the nearest neighbor averaging that leads to lower MSE for white noise is shown. For pink noise which has a 1/f response higher MSE than white noise is expected but with a constant value across multiple time scales [164]. As expected MSE levels out at higher time series lengths after 1000 sample points across the different time scales seen in Fig. 4-5 B middle-panel. This means that for a sampling rate of 250 Hz, MSE can capture the complexity with just 4 s of data. Similarly, for brown noise MSE is expected to be constant and as seen from Fig 4-5 C middle-panel after 750 sample length MSE is more or less the same across multiple time scales.

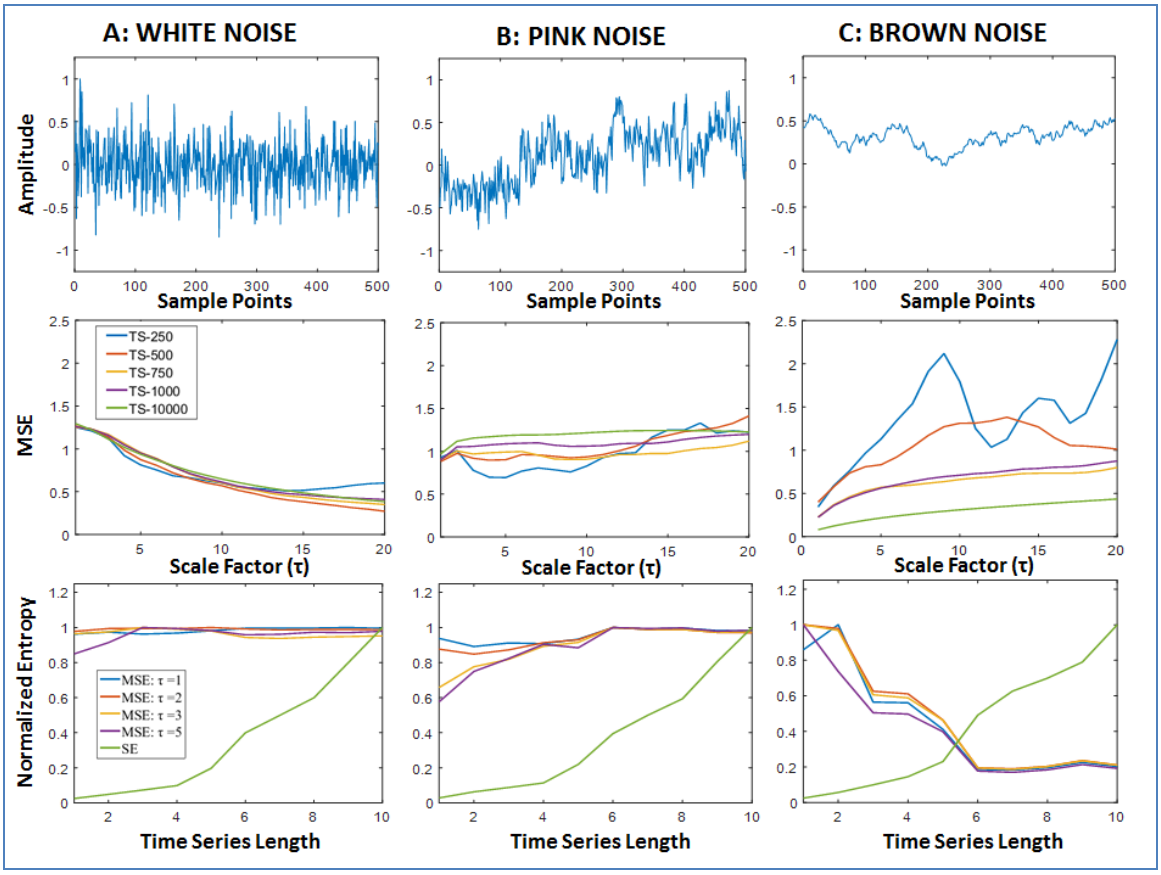

Figure 4-5: Raw noise analysis with MSE. *(A) Top- Panel shows white noise with 500 sample points; Middle-Panel shows the multiscale entropy for various time series (TS) lengths; Bottom-Panel shows normalized MSE (for scale factors τ = 1,2,3 & 5) and SE; (B) Top- Panel shows pink noise with 500 sample points; Middle-Panel shows the multiscale entropy for various time series (TS) lengths; Bottom-Panel shows normalized MSE (for scale factors τ = 1,2,3 & 5) and SE; (C) Top- Panel shows brown noise with 500 sample points; Middle-Panel shows the multiscale entropy for various time series (TS) lengths; Bottom-Panel shows normalized MSE (for scale factors τ = 1,2,3 & 5) and SE.*

Figures 4-5 A-C bottom panel demonstrates the fact that SE estimates lower values for short time series and gradually increases with increasing time series length for all three types of noise. MSE has higher values even for the shortest time series, thereby capturing the complexity better than SE. Overall, the results indicate that if at least 1000

sample points are available MSE can capture the complexity robustly compared to SE. For most physiological monitoring 250 Hz sampling frequency is common, which indicates that 4 s short time series data should be sufficient for robust analysis using MSE.

4.3.2 Complexity analysis of single frequency sinusoidal wave with MSE

Figure 4-6 demonstrates the robustness of MSE compared with SE approaches for single frequency sinusoidal wave in the absence and presence of different noises. Fig. 4-6 A shows the single frequency sinusoidal wave at 10 Hz for 500 samples points (left panel), the MSE values as a function of τ for varying TS (middle panel) and the normalized values of MSE (for different τ) and SE as a function of TS length (right panel) in the absence of noise. These data demonstrate that the efficacy of MSE approach in capturing the complexity of the sine wave is much better than SE, which only work well for larger TS lengths.

The robustness of the MSE and SE approaches in identifying the complexity of a single frequency sinusoidal wave in the presence of noise is shown in Fig. 4-6 for the white (panel B), pink (panel C) and brown (panel D) noises. The top row of Fig. 4-6 B-D shows the amplitude of sinusoidal wave with noise, while the bottom row shows the normalized values of MSE (for different τ) and SE as a function of TS length. The results suggest that MSE captures the complexity of sinusoidal waves better than SE in the presence of these noises.

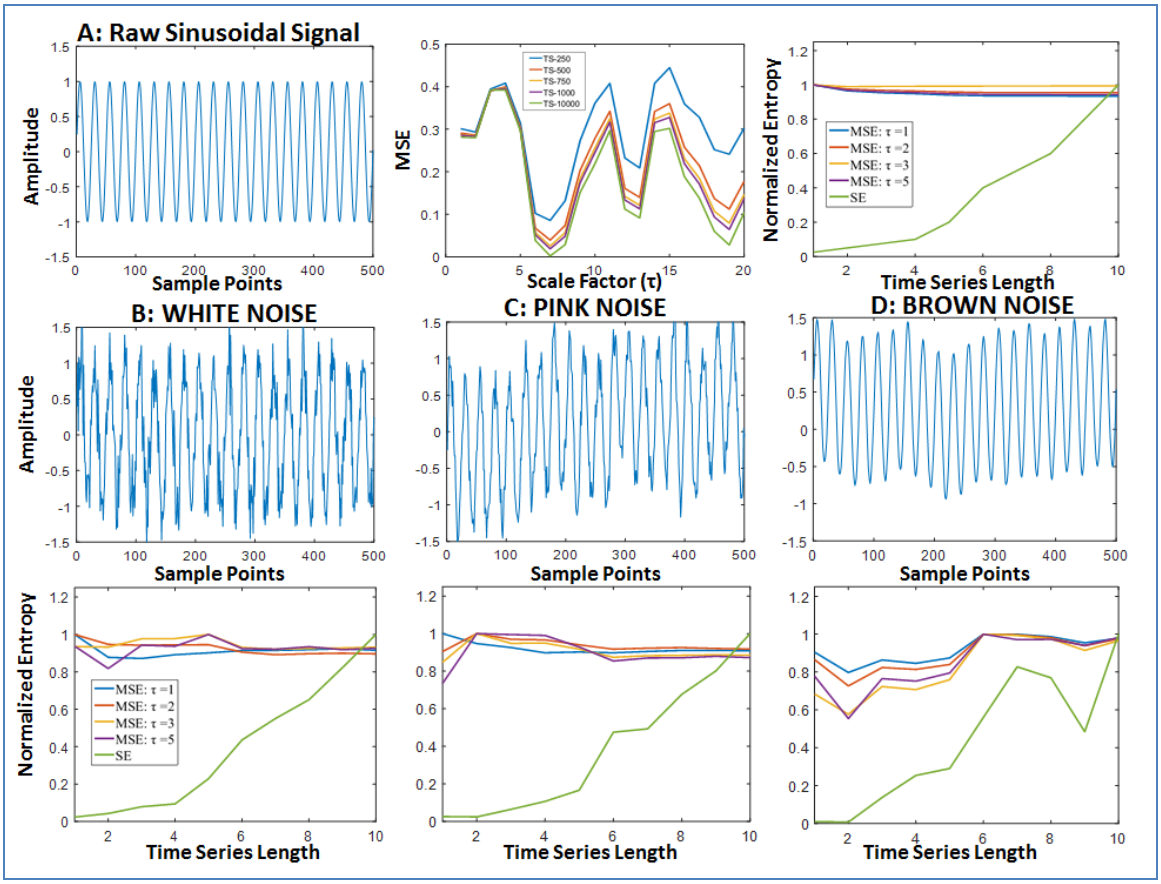

Figure 4-6: Single frequency sinusoidal wave analysis with MSE. *(A) left-panel shows single frequency (10 Hz) sine wave with 500 sample points; middle-panel shows the multiscale entropy for various length time series across several scaling factors; right-panel shows normalized MSE (for scale factors τ = 1,2,3 & 5) and SE ; (B) top row shows sine wave with white noise , pink noise (C) and brown noise (D); (B) bottom row shows normalized MSE (for scale factors τ = 1,2,3 & 5) and SE for sine wave with white noise, pink noise (C) and brown noise (D) respectively.*

4.3.3 Complexity analysis of multi frequency sinusoidal wave with MSE

Figure 4-7 shows the results for the multi-frequency sinusoidal wave. Similar to the response seen in Figure 4-5 for raw noise, panels B-D of Fig. 4-7 demonstrate that SE is very small for short TS and gradually increases with increasing TS length, while MSE has high values even for the shortest TS, thereby capturing the complexity better than SE.

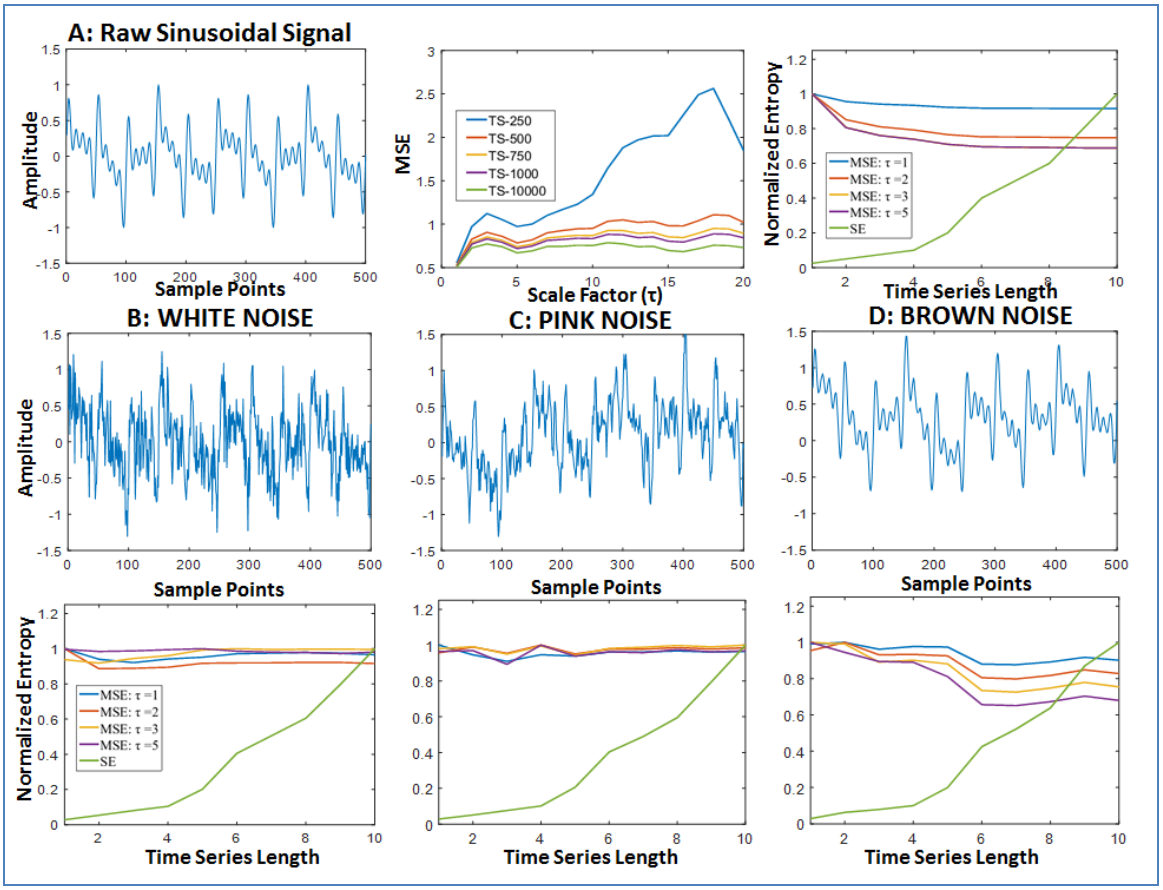

Figure 4-7: Multi frequency sinusoidal wave analysis with MSE; *(A) left-panel shows multi-frequency sine wave with 500 sample points; middle-panel shows the multiscale entropy for various length time series across several scaling factors; right-panel shows normalized MSE (for scale factors τ = 1,2,3 & 5) and SE ; (B) top row shows sine wave with white noise , pink noise (C) and brown noise (D); (B) bottom row shows normalized MSE (for scale factors τ = 1,2,3 & 5) and SE for sine wave with white noise, pink noise (C) and brown noise (D) respectively.*

The results demonstrate the efficacy of the novel MSE approach in quantifying the complexity of complex time series data in the presence of noise better than the commonly used SE approach.

4.3.4 Complexity analysis of flat baseline ECG wave with MSE

Figure 4-8 shows the results for flat baseline noise free ECG waveform.

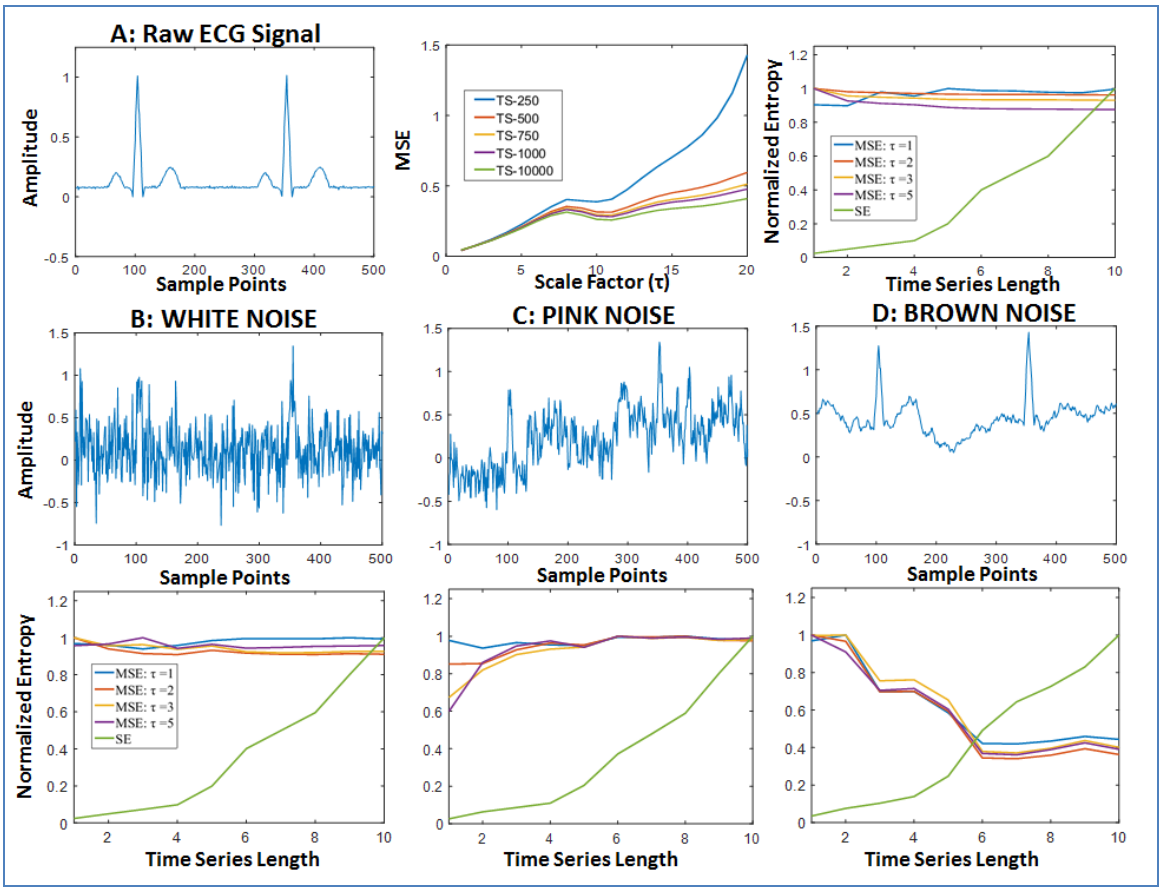

Figure 4-8: Flat baseline ECG wave analysis with MSE. *(A) left-panel shows flat baseline ECG wave with 500 sample points; middle-panel shows the multiscale entropy for various length time series across several scaling factors; right-panel shows normalized MSE (for scale factors τ = 1,2,3 & 5) and SE ; (B) top row shows ECG wave with white noise , pink noise (C) and brown noise (D); (B) bottom row shows normalized MSE (for scale factors τ = 1,2,3 & 5) and SE for sine wave with white noise, pink noise (C) and brown noise (D) respectively.*

Similar to the response seen in Figure 4-5 for raw noise, panels B-D of Fig. 4-8 demonstrate that SE is very small for short TS and gradually increases with increasing TS length, while MSE has high values even for the shortest TS, thereby capturing the

complexity better than SE. The results demonstrate the efficacy of the novel MSE approach in quantifying the complexity of complex time series data such as ECG in the presence of noise better than the commonly used SE approach.

4.4 Robustness of RPDE approach

This section will justify the robustness of RPDE approach based on the results of complexity analysis with raw noise, and noise contaminated with sinusoidal and flat baseline ECG waveforms for various TS lengths by comparing it with SE approach.

4.4.1 Complexity analysis of raw noise with RPDE

Figure 4-9 shows raw noise analysis with RPDE approach compared with SE.

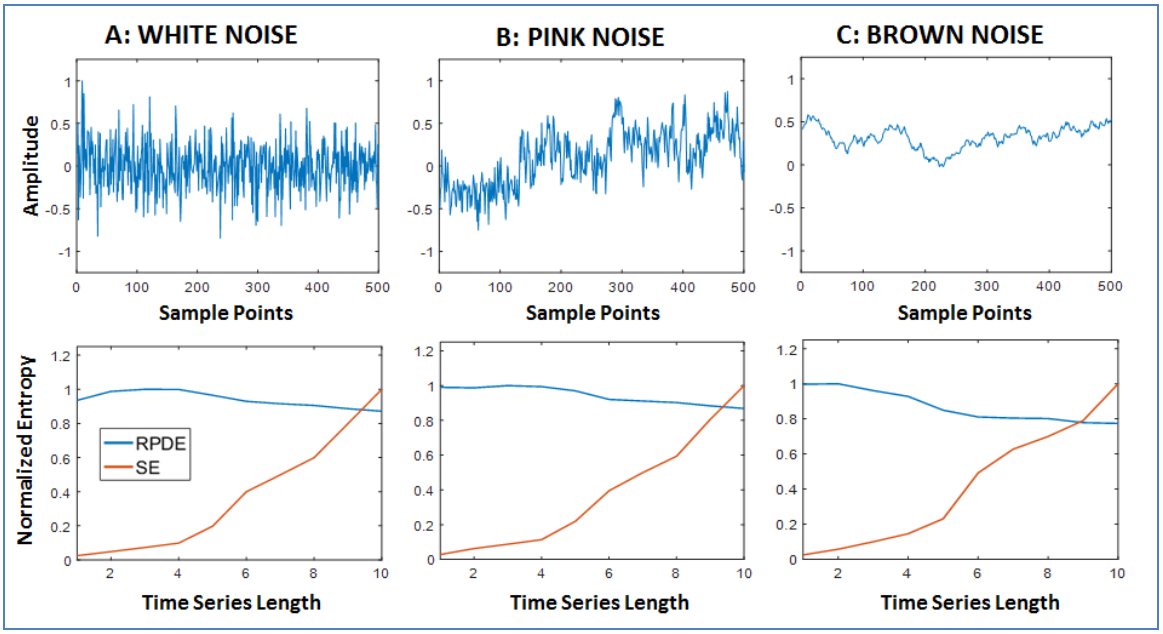

Figure 4-9: Raw noise analysis with RPDE. *(A) Top- Panel shows white noise with 500 sample points; Bottom-Panel shows its normalized RPDE and SE; (B) Top- Panel shows pink noise with 500 sample points; Bottom-Panel shows its normalized RPDE and SE; (C) Top- Panel shows brown noise with 500 sample points; Bottom-Panel shows its normalized RPDE and SE.*

As seen from Figure 4-9 RPDE measures complexity of white, pink and brown noise better than SE for various TS lengths, and therefore demonstrates its robustness.

4.4.2 Complexity analysis of single frequency sinusoidal wave with RPDE

Figure 4-10 shows the results of single frequency sinusoidal waveform analysis with RPDE approach.

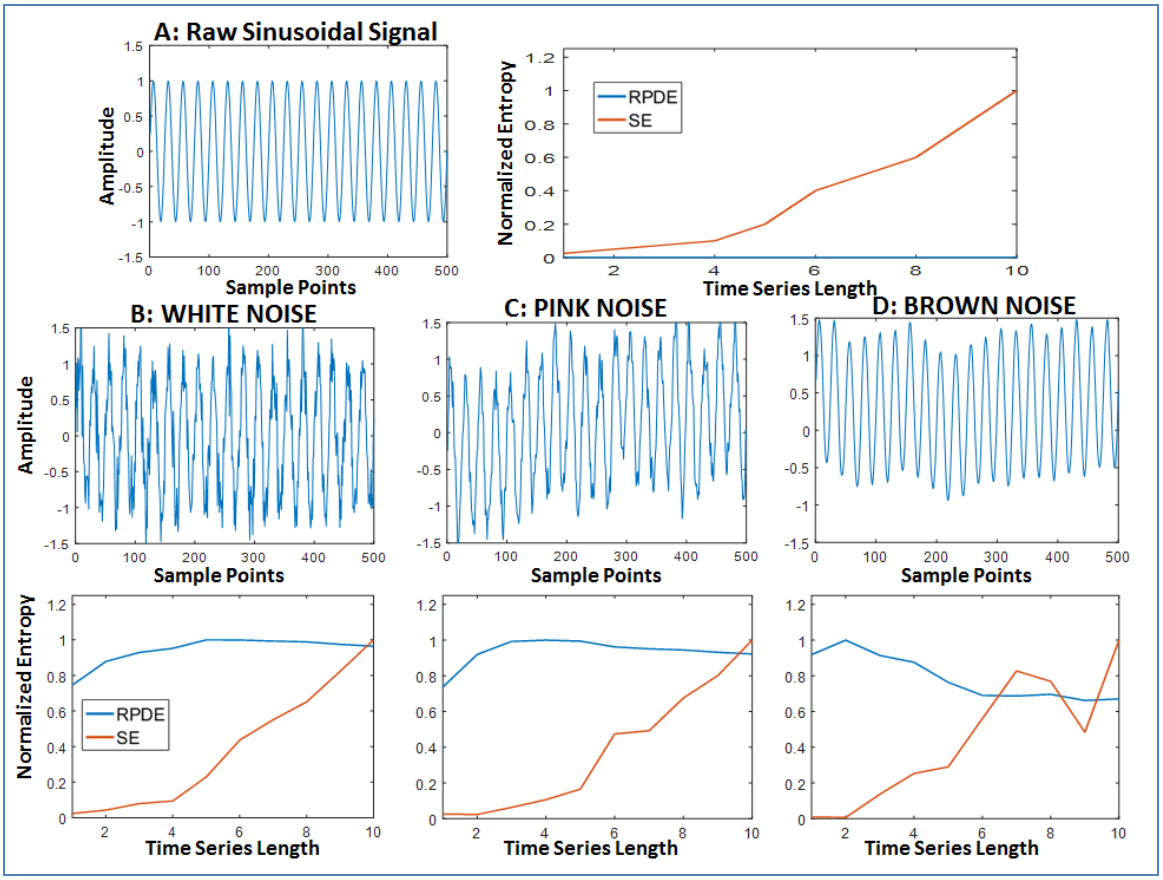

Figure 4-10: Single frequency sinusoidal wave analysis with RPDE. *(A) left-panel shows single frequency (10 Hz) sine wave with 500 sample points; right-panel shows its normalized RPDE and SE; (B) top row shows sine wave with white noise, pink noise (C) and brown noise (D); (B) bottom row shows normalized RPDE and SE for sine wave with white noise, pink noise (C) and brown noise (D) respectively.*

As discussed in Chapter 3, RPDE of purely periodic wave is zero which was observed in the right panel of Figure 4-10 A irrespective of the TS length compared to improved

complexity measurement of SE with increasing TS lengths. Hence, RPDE can be used to make inference on unknown signals based on its RPDE value for its periodicity. However once noise is added to the purely periodic sinusoidal waveform, RPDE is no longer zero, and it measures complexity better than SE for all three noises for various TS lengths as seen in the bottom panel of Figure 4-10. These results demonstrate the efficacy of RPDE for short time series analysis with similar performance to MSE.

4.4.3 Complexity analysis of multi frequency sinusoidal wave with RPDE approach

Figure 4-11 shows the results of multifrequency sinusoidal waveform analysis with RPDE approach. Unlike the results for the single frequency purely periodic sinusoidal waveform, RPDE measured higher complexity for the multi frequency sinusoidal waveform with better performance compared to SE for various TS lengths. Similar results are observed with added white, pink and brown noise for various TS lengths compared with SE shown in the bottom panel of Figure 4-11. These results demonstrate the efficacy of RPDE for short time series analysis with similar performance to MSE.

4.4.4 Complexity analysis of flat baseline ECG wave with RPDE

Figure 4-12 shows the results of noise free flat baseline ECG waveform analysis with RPDE approach. Similar to the result for multi frequency sinusoidal signal, RPDE measured higher complexity for the ECG trace with better performance compared to SE for various TS lengths. Similar results are observed for the ECG waveform added with white, pink and brown noise for various TS lengths compared with SE as seen in the bottom panel of Figure 4-12. These results demonstrate the efficacy of RPDE for short time series ECG analysis with similar performance to MSE.

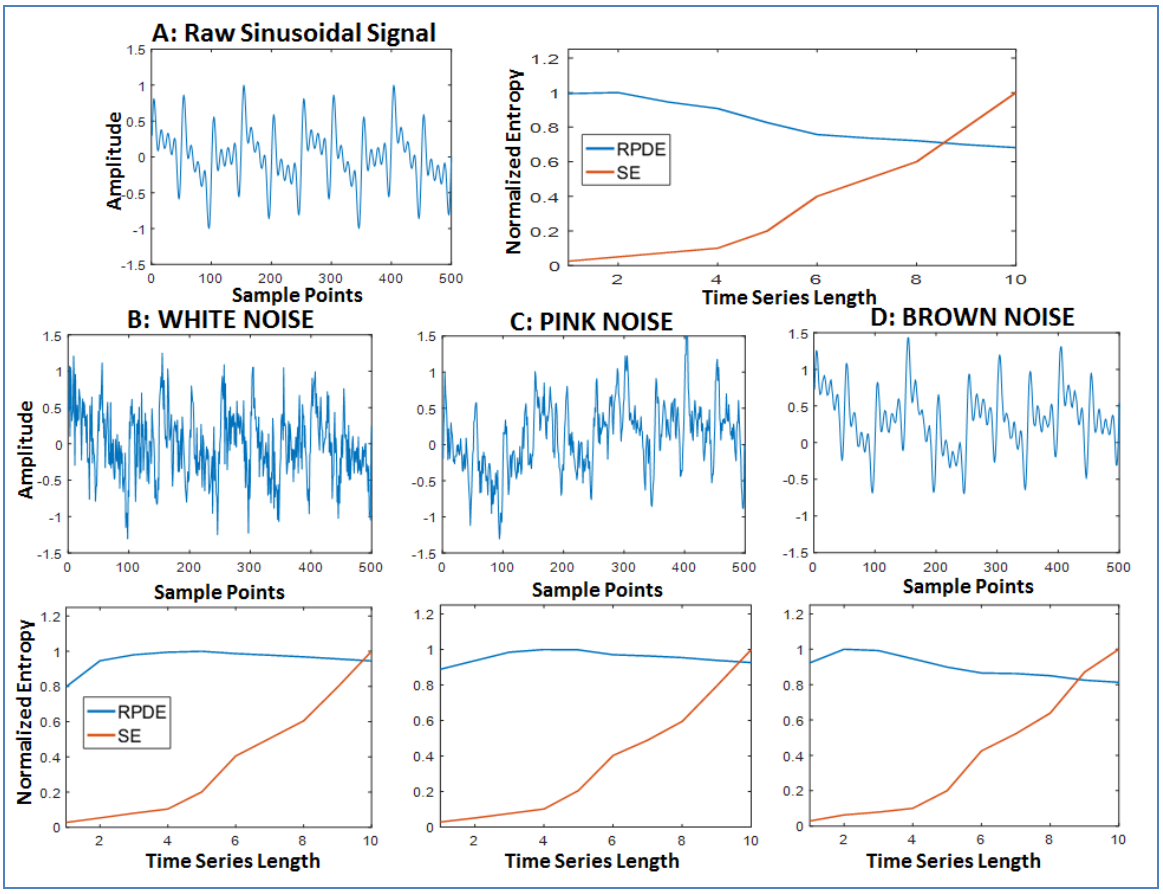

Figure 4-11: Multi frequency sinusoidal wave analysis with RPDE. *(A) left-panel shows multi frequency sine wave with 500 sample points; right-panel shows its normalized RPDE and SE; (B) top row shows sine wave with white noise, pink noise (C) and brown noise (D); (B) bottom row shows normalized RPDE and SE for sine wave with white noise, pink noise (C) and brown noise (D) respectively.*

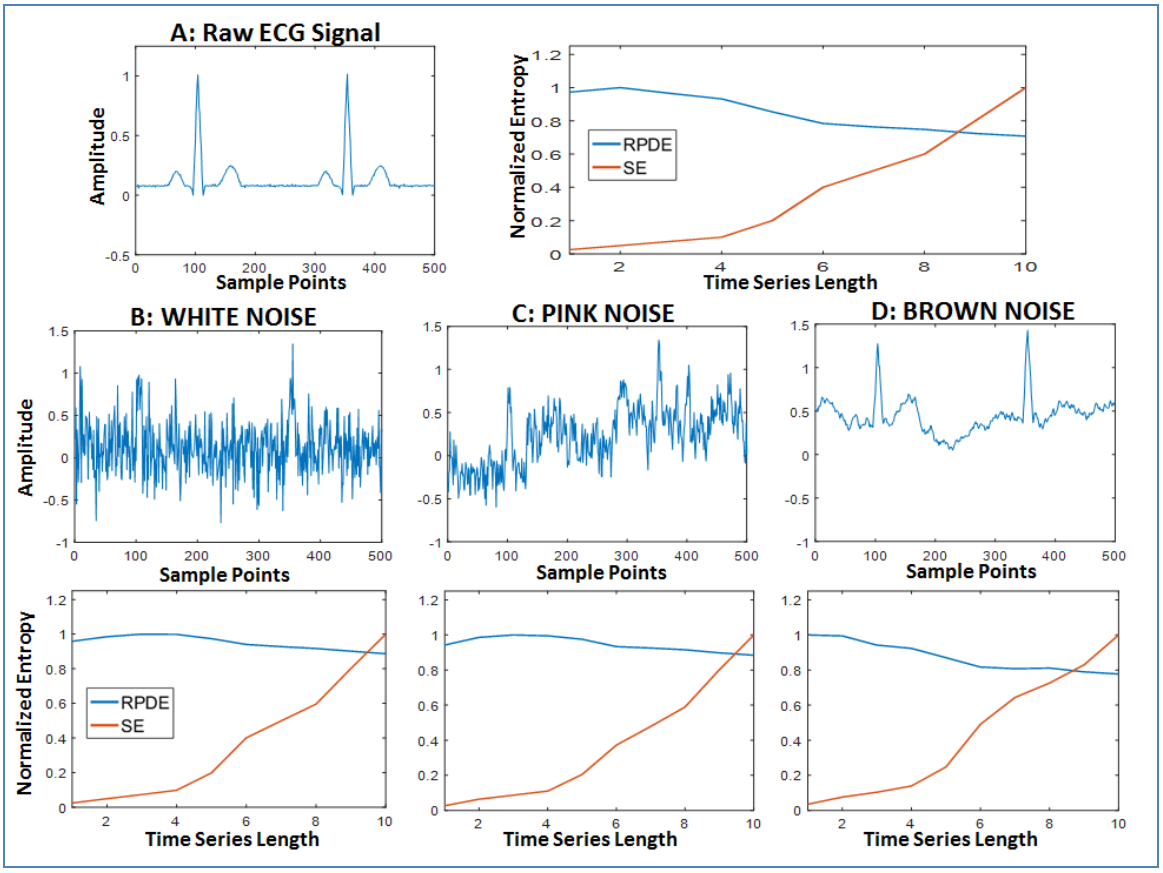

Figure 4-12: Flat baseline ECG wave analysis with RPDE. *(A) left-panel shows flat baseline ECG wave with 500 sample points; right-panel shows its normalized RPDE and SE; (B) top row shows ECG wave with white noise, pink noise (C) and brown noise (D); (B) bottom row shows normalized RPDE and SE for sine wave with white noise, pink noise (C) and brown noise (D) respectively.*

4.5 Robustness of kurtosis approach

This section will justify the robustness of kurtosis approach based on the results of complexity analysis with raw noise, and noise contaminated with sinusoidal and flat baseline ECG waveforms for various TS lengths by comparing it with SE approach.

4.5.1 Complexity analysis of raw noise with kurtosis

Figure 4-13 shows raw noise analysis with kurtosis approach compared with SE. As seen from Figure 4-13, kurtosis measures complexity of white and pink noise better than

SE for various TS lengths. For brown noise, the performances of kurtosis and SE are comparable after TS lengths of 4000 sample points. Overall, kurtosis performs better than SE with short time series data and therefore demonstrates its robustness.

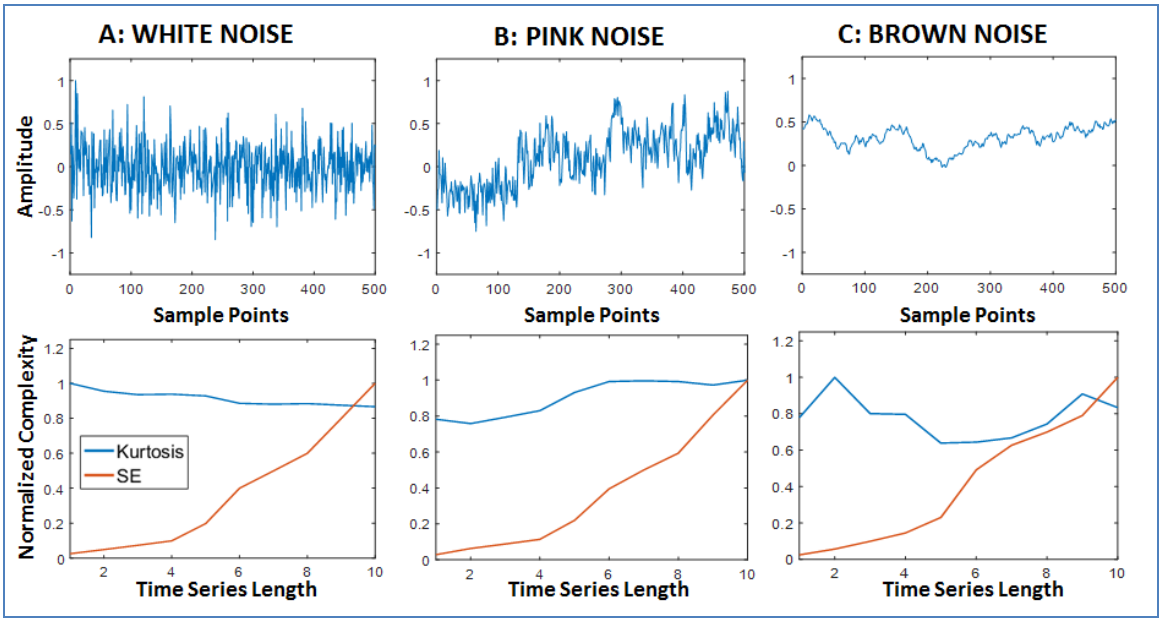

Figure 4-13: Raw noise analysis with kurtosis. *(A) Top- Panel shows white noise with 500 sample points; Bottom-Panel shows its normalized complexity with Kurtosis and SE; (B) Top- Panel shows pink noise with 500 sample points; Bottom-Panel shows its normalized complexity with Kurtosis and SE; (C) Top- Panel shows brown noise with 500 sample points; Bottom-Panel shows its normalized complexity with Kurtosis and SE.*

4.5.2 Complexity analysis of single frequency sinusoidal wave with kurtosis

Figure 4-14 shows the results of single frequency sinusoidal waveform analysis with kurtosis approach. As observed in the Fig. 4-14 A, kurtosis of purely periodic wave is same irrespective of the TS length compared to improved complexity measurement of SE with increasing TS lengths. With the addition of noise to the sinusoidal waveform kurtosis shows more or less flat response across various TS lengths as seen in the bottom

panel of Figure 4-14 better than SE. These results demonstrate the efficacy of kurtosis for short time series analysis with similar performance compared to MSE and RPDE.

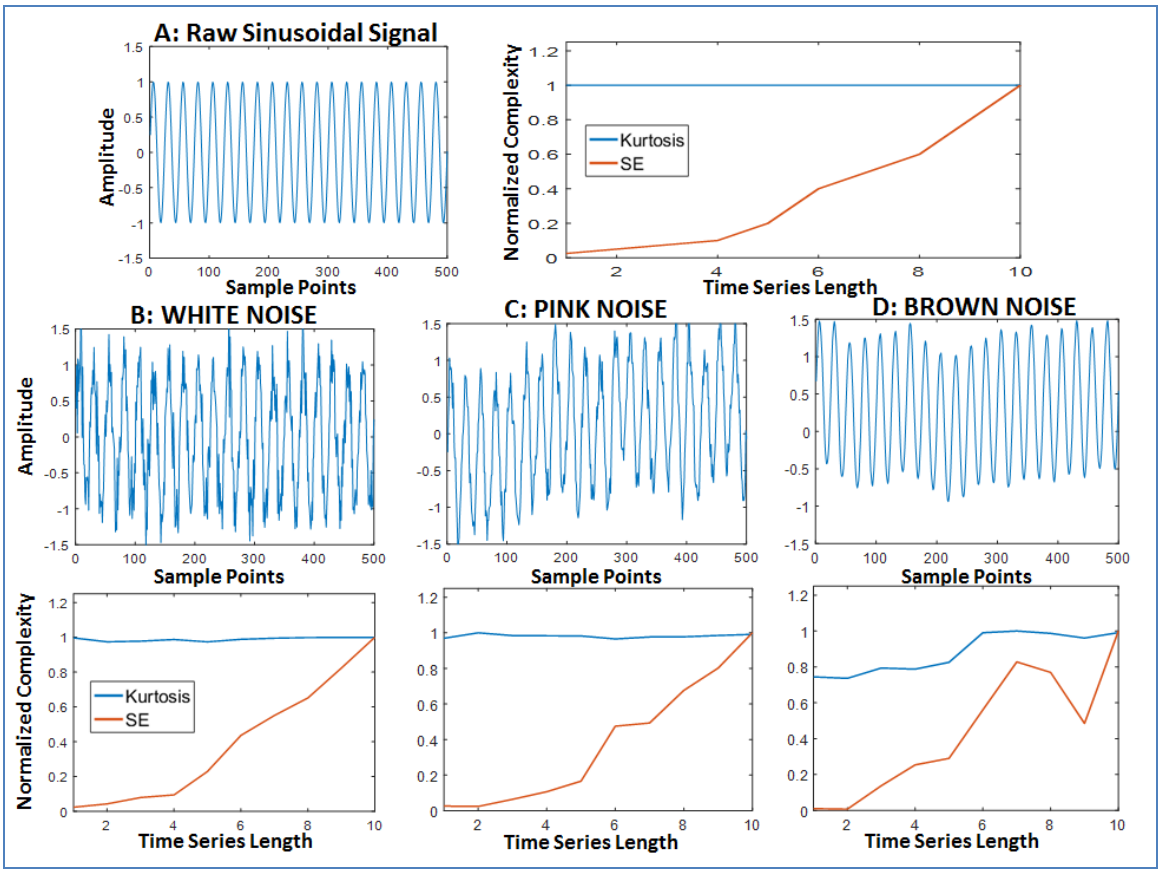

Figure 4-14: Single frequency sinusoidal wave analysis with kurtosis. *(A) left-panel shows single frequency (10 Hz) sine wave with 500 sample points; right-panel shows its normalized complexity with Kurtosis and SE; (B) top row shows sine wave with white noise, pink noise (C) and brown noise (D); (B) bottom row shows normalized complexity with Kurtosis and SE for sine wave with white noise, pink noise (C) and brown noise (D) respectively.*

4.5.3 Complexity analysis of multifrequency sinusoidal wave with kurtosis

Figure 4-15 shows the results of multifrequency sinusoidal waveform analysis with kurtosis approach. Kurtosis measured higher complexity with a flat response for the multi frequency sinusoidal waveform with better performance compared to SE for various TS

lengths. Similar results are observed with added white, pink and brown noise for various TS lengths compared with SE shown in the bottom panel of Figure 4-15. These results demonstrate the efficacy of kurtosis for measuring complexity with short time series comparable to MSE and RPDE and better than SE approach.

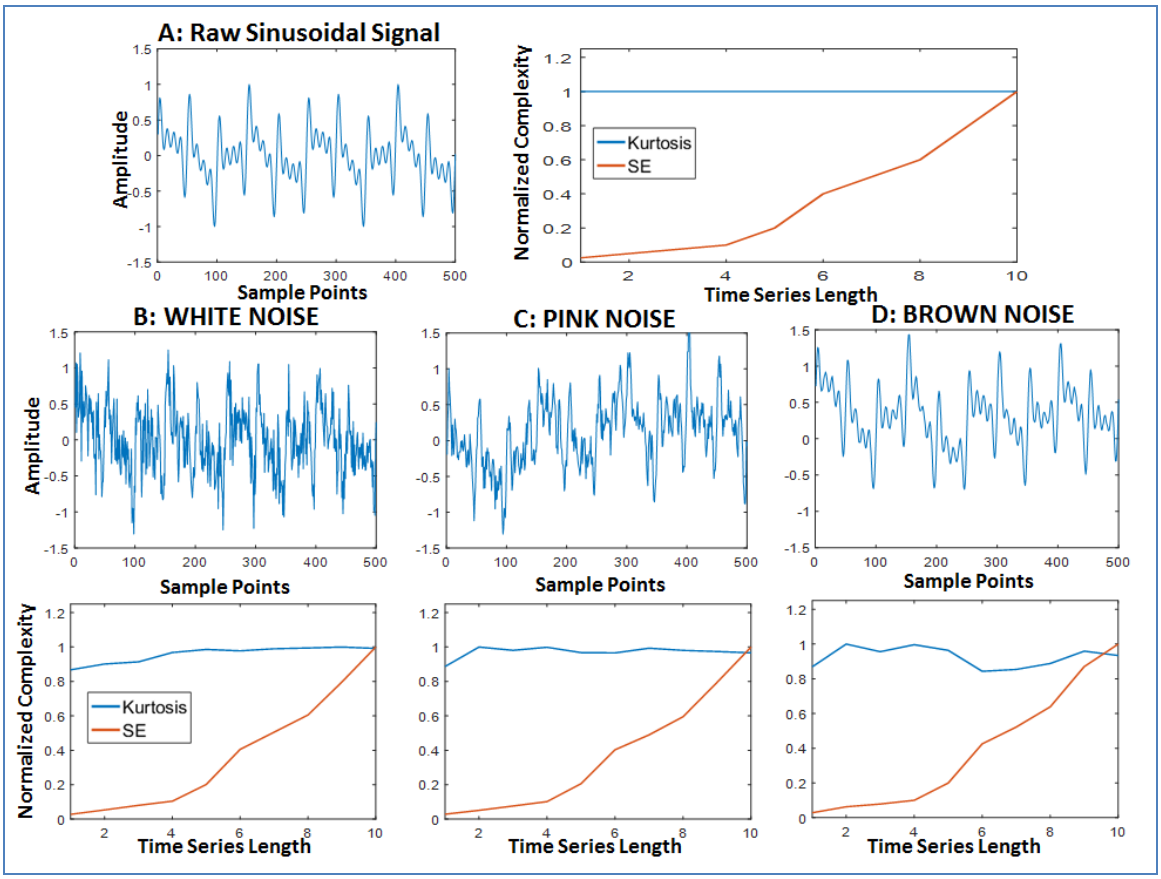

Figure 4-15: Multi frequency sinusoidal wave analysis with kurtosis. *(A) left-panel shows single frequency (10 Hz) sine wave with 500 sample points; right-panel shows its normalized complexity with Kurtosis and SE; (B) top row shows sine wave with white noise, pink noise (C) and brown noise (D); (B) bottom row shows normalized complexity with Kurtosis and SE for sine wave with white noise, pink noise (C) and brown noise (D) respectively.*

4.5.4 Complexity analysis of flat baseline ECG wave with kurtosis

Figure 4-16 shows the results of noise free flat baseline ECG waveform analysis with kurtosis approach.

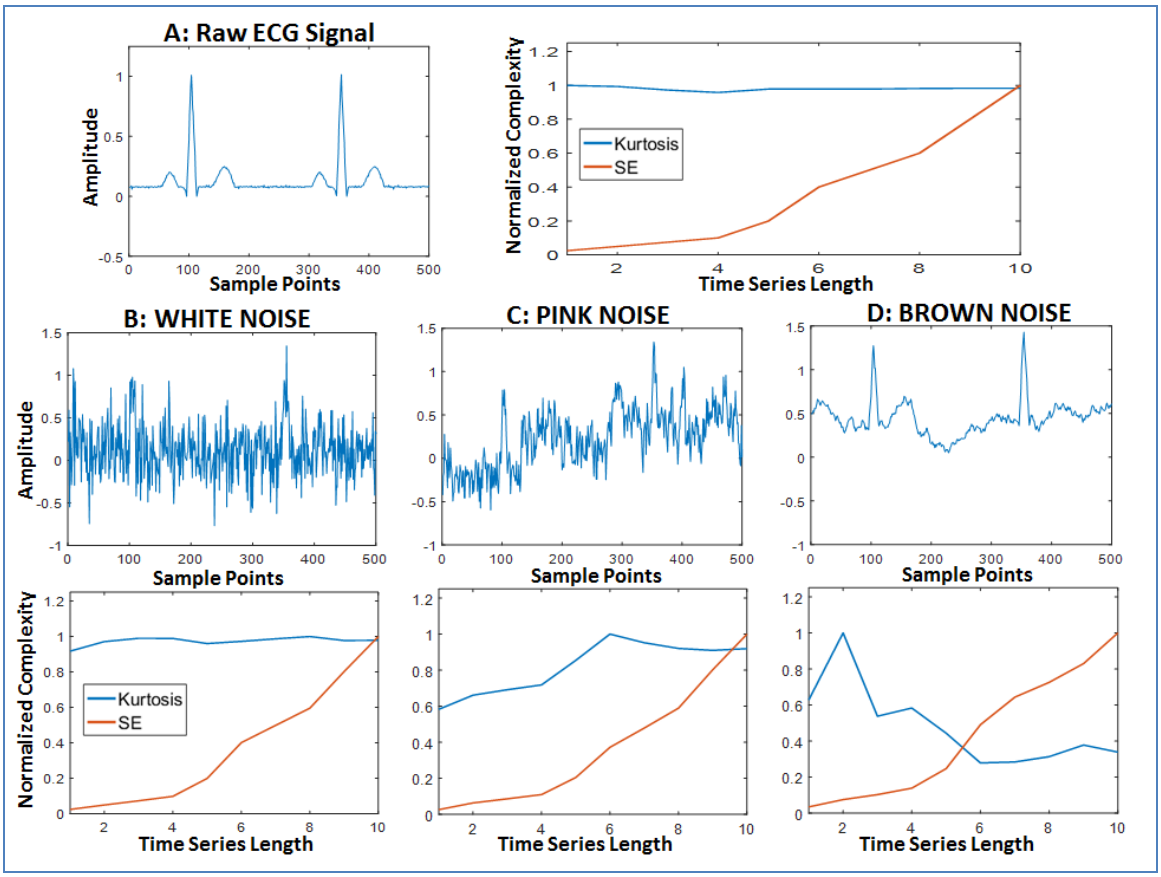

Figure 4-16: Flat baseline ECG wave analysis with kurtosis. *(A) left-panel shows flat baseline ECG wave with 500 sample points; right-panel shows its normalized complexity with Kurtosis and SE; (B) top row shows ECG wave with white noise, pink noise (C) and brown noise (D); (B) bottom row shows normalized complexity with Kurtosis and SE for sine wave with white noise, pink noise (C) and brown noise (D) respectively.*

Similar to the result for multi frequency sinusoidal signal, kurtosis measured higher complexity for the ECG trace with better performance compared to SE for various TS lengths. Similar results are observed for the ECG waveform added with white and pink noise for various TS lengths compared with SE as seen in the bottom panel of Figure 4-

16. However, brown noise distorts the flat baseline of the ECG trace affecting its kurtosis measurements in particular after 4000 sample points.

4.6 Robustness of EMD approach

This section will justify the robustness of EMD approach based on the results of complexity analysis with raw noise, and noise contaminated with sinusoidal and flat baseline ECG waveforms for various TS lengths by comparing it with SE approach.

4.6.1 Complexity analysis of raw noise with EMD

Figure 4-17 shows raw noise analysis with RPDE approach compared with SE. As seen from Figure 4-17 EMD measures IMF complexity of white, pink and brown noise better than SE for various TS lengths compared to SE demonstrating its robustness.

4.6.2 Complexity analysis of single frequency sinusoidal wave with EMD

Figure 4-18 shows the results of single frequency sinusoidal waveform analysis with EMD approach. As seen from Fig 4-18, IMF complexity of purely periodic wave decreases with increasing TS lengths where SE shows the opposite trend which is an interesting finding. Specifically after TS length of 1000 sample points SE performs better with this dataset. However once noise is added to the purely periodic sinusoidal waveform, IMF complexity performs superior to SE for various TS lengths as seen in the bottom panel of Figure 4-18. These results demonstrate the efficacy of EMD approach with added noise comparable to MSE, RPDE and kurtosis approaches.

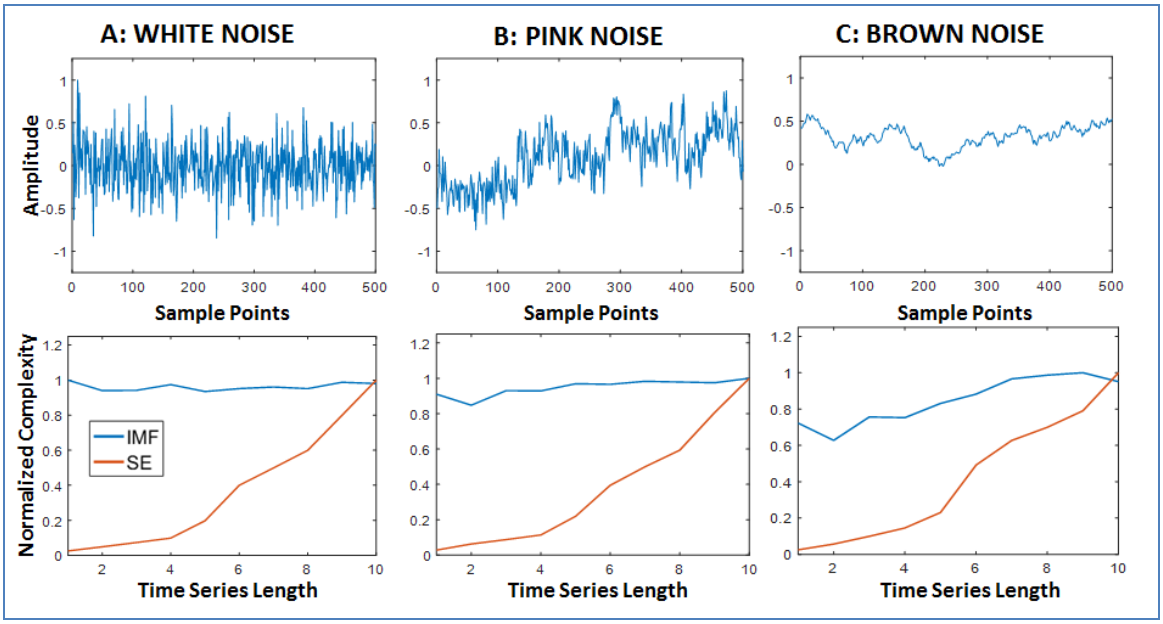

Figure 4-17: Raw noise analysis with EMD. *(A) Top- Panel shows white noise with 500 sample points; Bottom-Panel shows its normalized complexity with EMD and SE; (B) Top- Panel shows pink noise with 500 sample points; Bottom-Panel shows its normalized complexity with EMD and SE; (C) Top- Panel shows brown noise with 500 sample points; Bottom-Panel shows its normalized complexity with EMD and SE.*

4.6.3 Complexity analysis of multi frequency sinusoidal wave with EMD

Figure 4-19 shows the results of multifrequency sinusoidal waveform analysis with EMD approach. As seen from Fig 4-19, IMF complexity of the complex multifrequency sinusoidal wave decreases with increasing TS lengths where SE shows the opposite trend similar to the single frequency results, but the rate of decrease is much less relatively. IMF complexity performs better up to 6000 sample points after which SE is better. However once noise is added to the multifrequency sinusoidal waveform, IMF complexity performs superior to SE for various TS lengths as seen in the bottom panel of Figure 4-19. These results demonstrate the efficacy of EMD approach with added noise comparable to MSE, RPDE and kurtosis approaches.

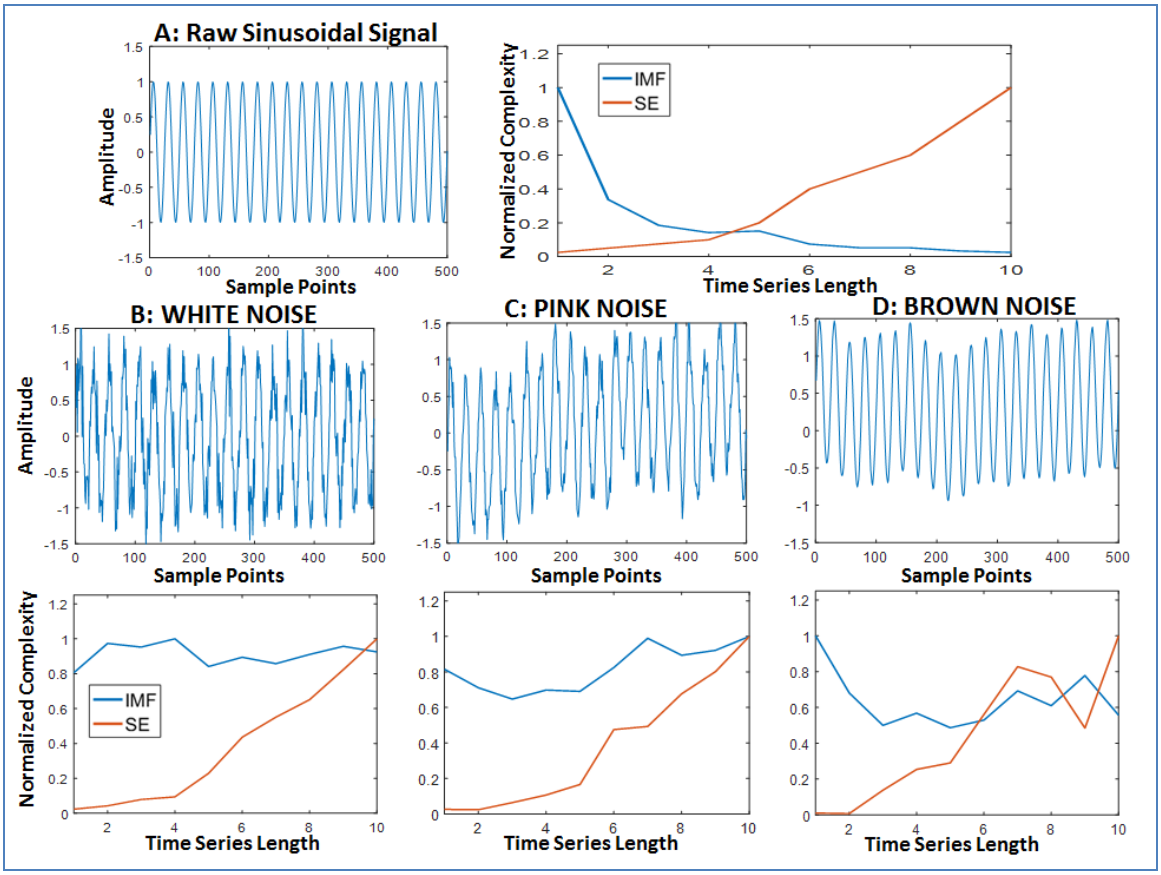

Figure 4-18: Single frequency sinusoidal wave analysis with EMD. *(A) left-panel shows single frequency (10 Hz) sine wave with 500 sample points; right-panel shows its normalized complexity with EMD and SE; (B) top row shows sine wave with white noise, pink noise (C) and brown noise (D); (B) bottom row shows normalized complexity with EMD and SE for sine wave with white noise, pink noise (C) and brown noise (D) respectively.*

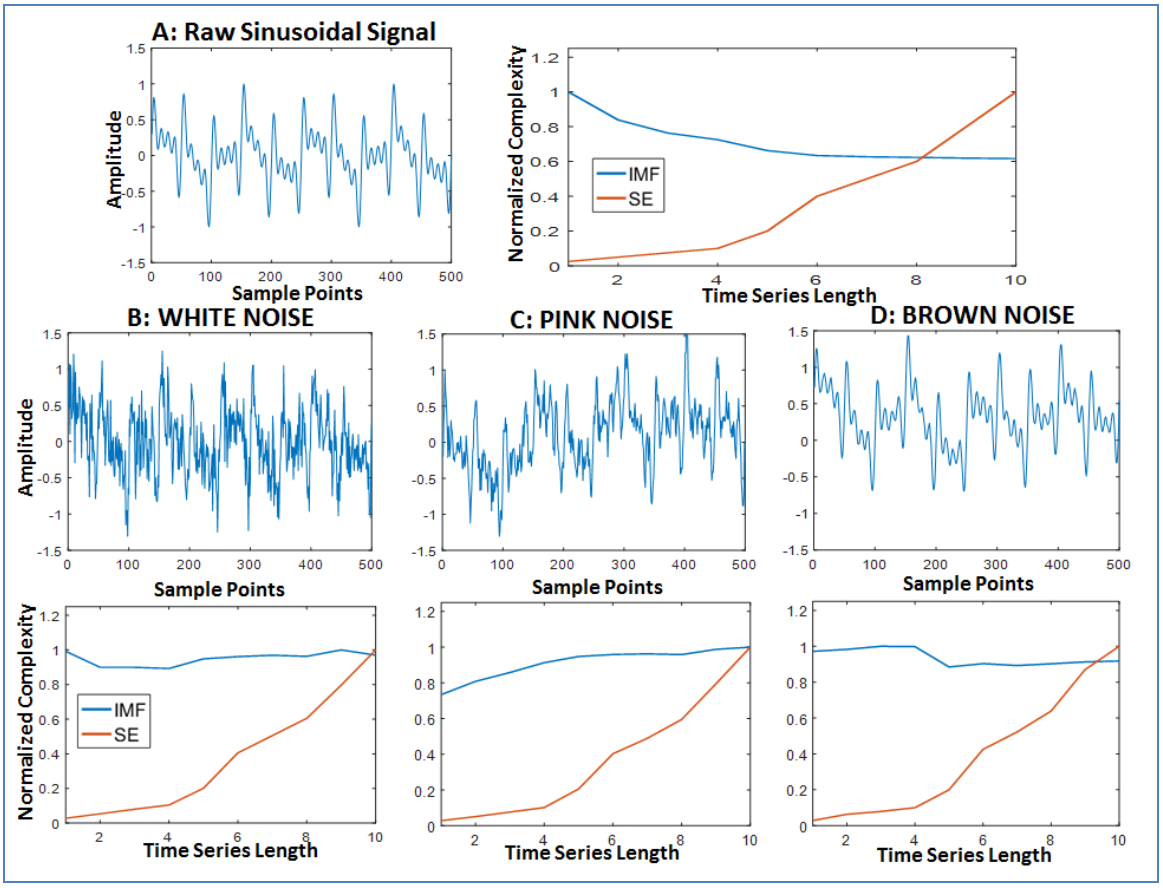

Figure 4-19: Multi frequency sinusoidal wave analysis with EMD. *(A) left-panel shows single frequency (10 Hz) sine wave with 500 sample points; right-panel shows its normalized complexity with EMD and SE; (B) top row shows sine wave with white noise, pink noise (C) and brown noise (D); (B) bottom row shows normalized complexity with EMD and SE for sine wave with white noise, pink noise (C) and brown noise (D) respectively.*

4.6.4 Complexity analysis of flat baseline ECG wave with EMD

Figure 4-20 shows the results of noise free flat baseline ECG waveform analysis with EMD approach. Similar to the result for multi frequency sinusoidal signal, EMD measured higher complexity for the ECG trace with better performance compared to SE up to 4000 sample points after which SE performed better. IMF complexity performed

better for the ECG waveform added with white, pink and brown noise for various TS lengths compared with SE as seen in the bottom panel of Figure 4-20.

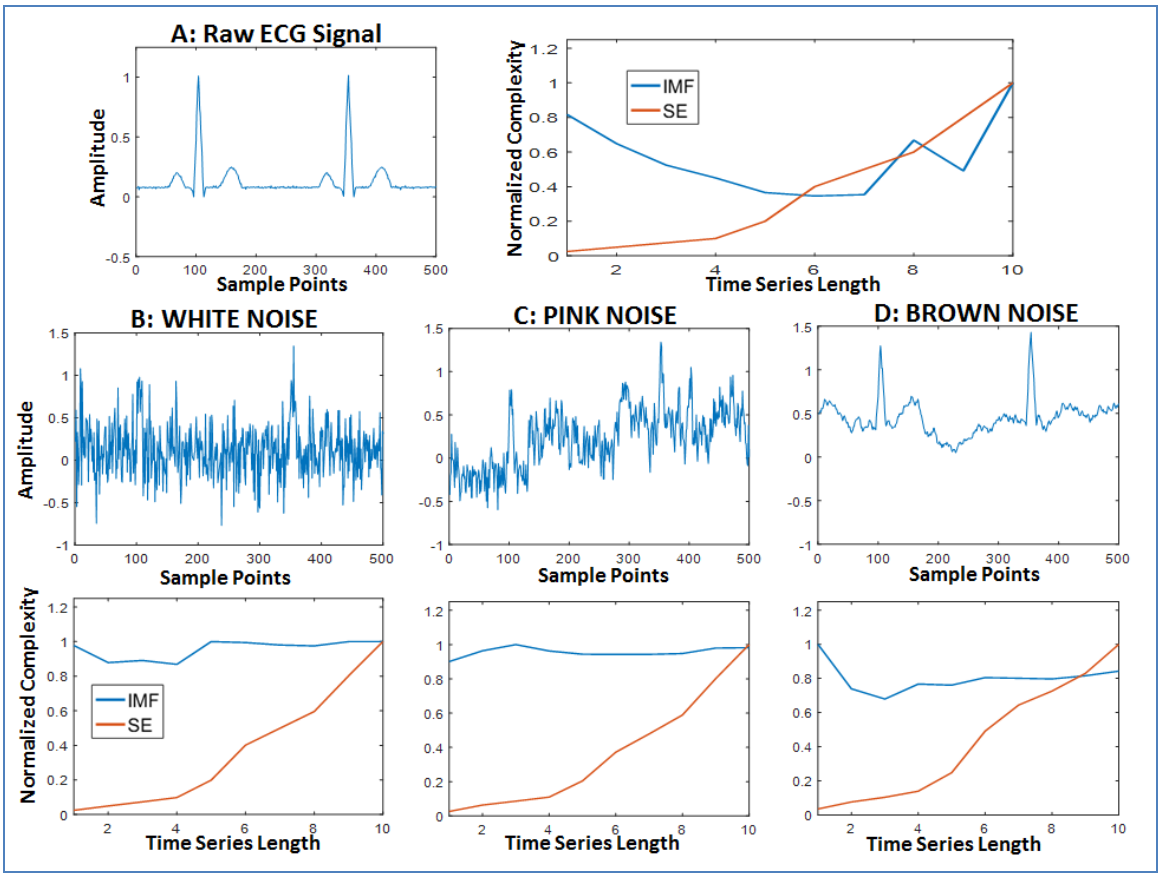

Figure 4-20: Flat baseline ECG wave analysis with EMD. *(A) left-panel shows flat baseline ECG wave with 500 sample points; right-panel shows its normalized complexity with EMD and SE; (B) top row shows ECG wave with white noise, pink noise (C) and brown noise (D); (B) bottom row shows normalized complexity with EMD and SE for sine wave with white noise, pink noise (C) and brown noise (D) respectively.*

4.7 Robustness of MSF approach

This section will justify the robustness of MSF approach based on the results of complexity analysis with raw noise, and noise contaminated with sinusoidal and flat baseline ECG waveforms for various TS lengths by comparing it with SE approach.

4.7.1 Complexity analysis of raw noise with MSF

Figure 4-21 shows raw noise analysis with MSF approach compared with SE. Figs. 4- 1-3 show the power spectrum of these noises illustrating their frequency characteristics which are captured by MSF technique in measuring their complexity. As seen from Figure 4-21 MSF measures complexity of white, pink and brown noise better than SE for various TS lengths compared to SE demonstrating its robustness.

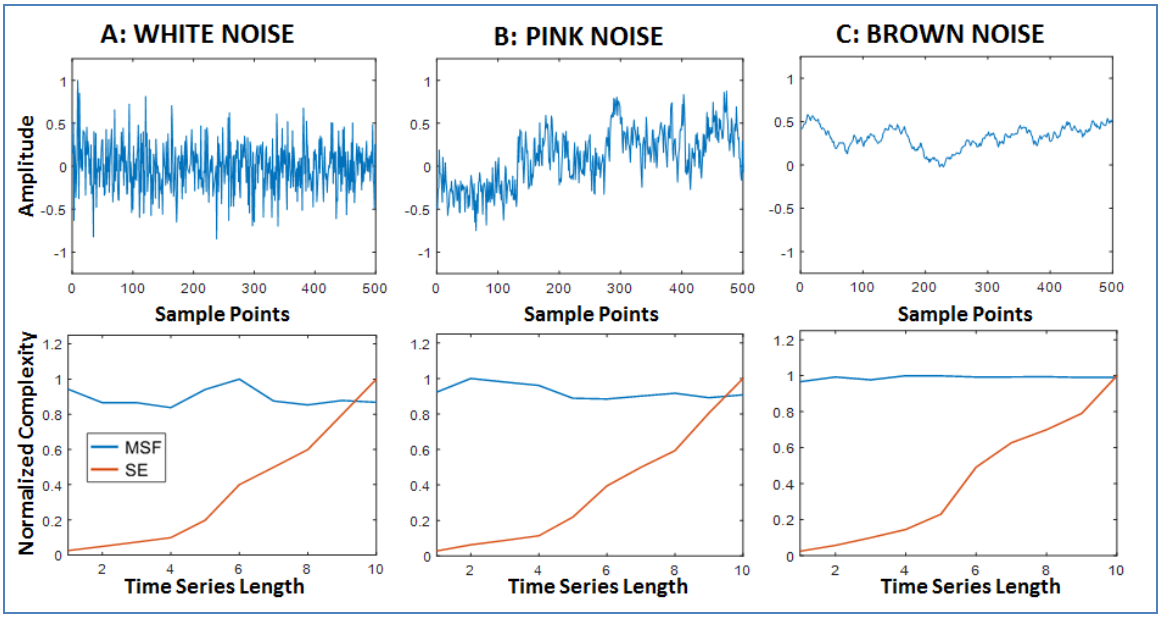

Figure 4-21: Raw noise analysis with Multiscale Frequency (MSF). *(A) Top- Panel shows white noise with 500 sample points; Bottom-Panel shows its normalized complexity with MSF and SE; (B) Top- Panel shows pink noise with 500 sample points; Bottom-Panel shows its normalized complexity with MSF and SE; (C) Top- Panel shows brown noise with 500 sample points; Bottom-Panel shows its normalized complexity with MSF and SE.*

4.7.2 Complexity analysis of single frequency sinusoidal wave with MSF

Figure 4-22 shows the results of single frequency sinusoidal waveform analysis with MSF approach.

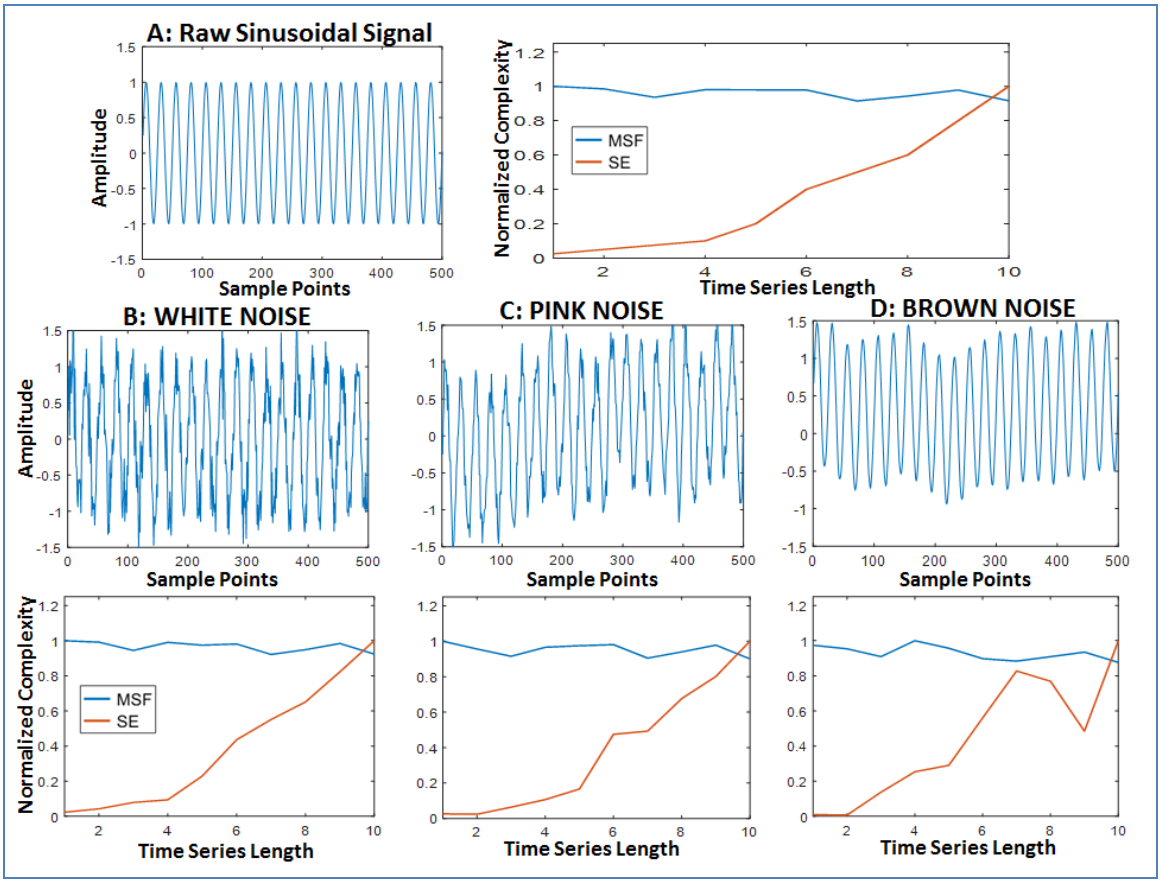

Figure 4-22: Single frequency sinusoidal wave analysis with MSF. *(A) left-panel shows single frequency (10 Hz) sine wave with 500 sample points; right-panel shows its normalized complexity with MSF and SE; (B) top row shows sine wave with white noise, pink noise (C) and brown noise (D); (B) bottom row shows normalized complexity with MSF and SE for sine wave with white noise, pink noise (C) and brown noise (D) respectively.*

MSF measured the complexity better than SE irrespective of the TS length. Since this the test signal was a stationary single frequency (@ 10 Hz) sinusoidal waveform its frequency contents are not changing that resulted in a constant MSF irrespective of TS lengths, while SE performed better with increasing TS lengths. Similar results are observed with added noise and MSF measures complexity better than SE for all three

noises for various TS lengths as seen in the bottom panel of Figure 4-22. These results demonstrate the efficacy of MSF for short time series analysis in the frequency domain.

4.7.3 Complexity analysis of multi frequency sinusoidal wave with MSF

Figure 4-23 shows the results of multifrequency sinusoidal waveform analysis with MSF approach. MSF measured the complexity better than SE irrespective of the TS length. Since this the test signal was a stationary multifrequency (with 2, 5, 10, 15, & 20 Hz) sinusoidal waveform its frequency contents are not changing that resulted in a constant MSF irrespective of TS lengths, while SE performed better with increasing TS lengths. Similar results are observed with added noise and MSF measures complexity better than SE for all three noises for various TS lengths as seen in the bottom panel of Figure 4-23. These results demonstrate the efficacy of MSF for short time series analysis of complex multifrequency signals in the frequency domain.

4.7.4 Complexity analysis of flat baseline ECG wave with MSF

Figure 4-24 shows the results of flat baseline ECG waveform analysis with MSF approach. Figure 4-4 shows the power spectrum of the ECG waveform which shows the artificial frequencies with several peaks used to generate the simulated ECG waveform. MSF estimate of this ECG waveform resulted in better performance till sample lengths of 2000 and comparable performance with SE at higher sample lengths as seen in Fig 4-24. Similar results are observed with added noise and MSF measures complexity better than SE for white and pink noise up to 200 sample points and comparable to SE at higher TS lengths. Interestingly, MSF showed increasing performance with brown noise with varying TS lengths but at a higher performance level

compared to SE as seen in the bottom panel of Figure 4-24. These results demonstrate the efficacy of MSF for short time series analysis of ECG waveforms in the frequency domain.

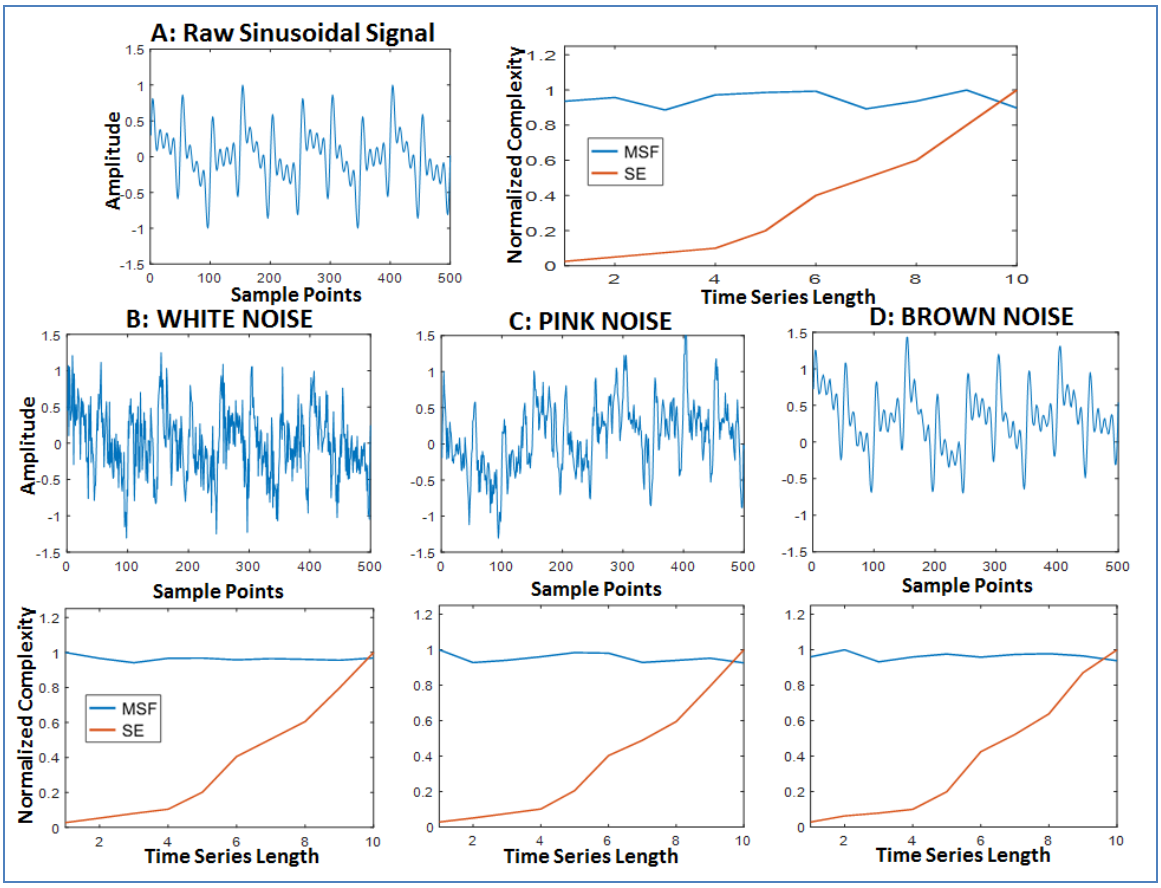

Figure 4-23: Multi frequency sinusoidal wave analysis with MSF. *(A) left-panel shows multifrequency sine wave with 500 sample points; right-panel shows its normalized complexity with MSF and SE; (B) top row shows sine wave with white noise, pink noise (C) and brown noise (D); (B) bottom row shows normalized complexity with MSF and SE for sine wave with white noise, pink noise (C) and brown noise (D) respectively.*

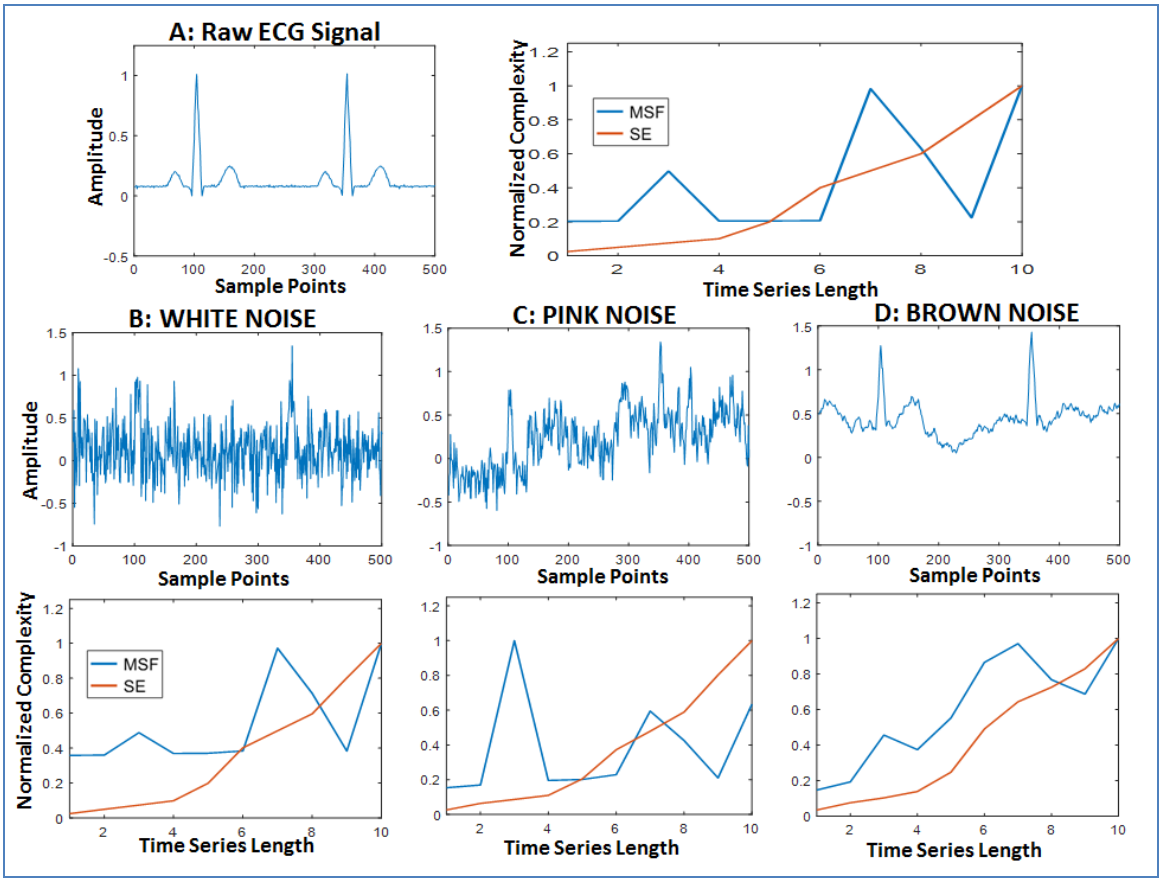

Figure 4-24: Flat baseline ECG wave analysis with MSF. *(A) left-panel shows flat baseline ECG wave with 500 sample points; right-panel shows its normalized complexity with MSF and SE; (B) top row shows sine wave with white noise, pink noise (C) and brown noise (D); (B) bottom row shows normalized complexity with MSF and SE for the ECG wave with white noise, pink noise (C) and brown noise (D) respectively.*

4.8 Discussion

Robustness test using raw noise analysis

In this thesis, five novel approaches were developed for electrogram analysis which is both non-linear and non-stationary and often presented as short time series data that is also often contaminated with white, pink and brown noise. Therefore, demonstrating robustness of these approaches in the presence of these noises were performed and all

five approaches demonstrates robustness in estimating complexity even with short time series compared to gold standard SE approach.

Robustness test using sinusoidal wave analysis

Sinusoidal wave analysis is the most elegant approach to demonstrate the efficacy of the newly developed quantitative approaches over conventionally used SE approach for short time series analysis of biomedical signals. Major findings of this thesis with sinusoidal wave analysis is that for single frequency and multi-frequency sinusoidal waves with added noise, SE underestimated the complexity at short time series for all three noise cases and performed better at longer time series lengths. All five approaches MSE was robust even at shorter time series with 1000 sample points in the presence of the three types of noise. The results suggest the value of these approaches in analyzing complex short time series physiological signals that can be contaminated with these noises, and that it can used be for prognosis and diagnosis of various disease states such as rotor identification explored in this thesis.

Robustness test using noise-free ECG analysis

ECG analysis is very commonly used for a wide variety of cardiac conditions to yield information regarding the state of the heart. With the growing importance of remote and mobile single lead ECG technologies, the importance of making accurate cardiac diagnoses using short time series data that is often contaminated with a variety of noises is clear. The major finding of this thesis is that all five novel approaches robustly estimated the complexity of short time series ECG even in the presence of noise compared with SE. Since, most remote and ambulatory real-time ECG monitoring

present at most 3-5 seconds of ECG data for quick analysis, conventional complexity analysis methods such as SE are limited while MSE, RPDE, kurtosis, EMD and MSF approaches has demonstrated robustness suitable for such applications.

The objectives of this section of the thesis were achieved by the results of rigorous noise testing with each of the novel approaches which demonstrate robustness in estimating complexity in the presence of noise over varying TS lengths, in comparison with SE approach. These results offer huge promise for robust discrimination of rotor pivot point with much better contrast compared to periphery than SE approach making them suitable for rotor identification analysis. The next chapter will evaluate the efficacy of some of these approaches (MSE and MSF) in discriminating normal sinus rhythm and AF on a single lead ECG without any preprocessing which can further demonstrate its robustness as an essential next step prior to its application with optical mapping and intracardiac electrogram data analysis.

4.9 Conclusion

This chapter has demonstrated the robustness of MSE, RPDE, kurtosis, EMD and MSF approaches compared with SE approach with rigorous noise testing. The author achieved the objectives of this section of thesis by performing complexity analysis using simulated sinusoidal and ECG waveform contaminated with white, pink and brown noise of various time series lengths which performed better than ‘gold standard’ SE approach. The results suggest the potential of these approaches for accurate rotor pivot point identification. Custom MATLAB programs were written for noise analysis for testing each of these novel approaches based on the algorithm described in Chapter 3.

CHAPTER 5: DISCRIMINATING NORMAL SINUS RHYTHM AND ATRIAL FIBRILLATION ON SINGLE LEAD ECG

5.1 Introduction

This chapter focuses on the ability of the novel approaches developed in Chapter 3 to robustly discriminate normal sinus rhythm (NSR) and AF on a single lead ECG. As described in the previous section, single lead ECG analysis is common for the prognosis and diagnosis of variety of heart diseases in a remote and ambulatory setting. There is even a growing demand with mobile and e-health setup where patients prefer wearing remote ECG monitors to constantly track the status of their heart for any abnormal activity. This chapter will elaborate on the clinical need for single lead ECG diagnosis of various arrhythmias such as AF. The novel techniques can be tested and validated for ECG analysis for their robustness in discriminating normal and diseased ECG tracings such as AF. Kurtosis, RPDE and EMD based approaches have been explored by many investigators for ECG and other biological signal analysis [170-174, 178-179] and therefore will not be performed in this thesis. Therefore, novel MSE and MSF techniques will be tested and validated to discriminate NSR and AF on a single lead ECG.

To realize the objectives of this section of the thesis, publically available ECG datasets for NSR and AF are preferred so that other groups may use this technique for comparison purposes with the same datasets. As described in Chapter 2 Physionet/PhysioBank database offers excellent resources for testing novel approaches such as developed in this thesis. MSE and MSF estimates will be computed for the NSR and AF data sets for discrimination on a single lead ECG.

5.2 Why discrimination of NSR and AF on single lead ECG?

The third specific aim of this thesis is "*To demonstrate the efficacy of MSE and MSF technique to robustly discriminate normal sinus rhythm and AF on a single lead ECG".* In a clinical setting, 12-lead electrocardiogram (ECG) is used to monitor normal sinus rhythm (NSR) and also detect AF and other cardiac arrhythmias. In general, detecting persistent AF on an ECG is easy due to its nature mostly with the absence of prominent P-waves on a consistent fashion [188]. However, challenges exist in detecting paroxysmal AF (which is episodic) as it requires continuous ECG monitoring over long period of time and therefore it is both difficult and expensive to collect such large volumes of 12-lead ECG for paroxysmal AF detection [188]. Several researchers have attempted to develop new methods to discriminate NSR and AF which are based on P-wave analysis and or detection of absence of P-waves, R-R interval analysis, linear methods, filtering, spectral analysis, statistical approaches such as entropy etc. which faces limitation of successfully detecting AF of all types with high sensitivity and specificity using short time ECG data [189-192].

The limitations of several ECG analysis approaches available to date can be attributed to several reasons such as: ECG distortion by several pre-processing steps [136-138] such as baseline wander removal, high frequency, electromyogram (EMG) and other noise removal using filters and other nonlinear approaches; availability of short time-series ECG data in a clinical setting that challenges several approaches that require long time series ECG data for reliable discrimination between NSR, AF and other cardiac arrhythmias; and many of them lack real-time capability that makes it difficult to trust the

data for diagnosis and subsequent treatment. Therefore at no doubt, both the clinical and scientific communities recognize these limitations and difficulties and the necessity to develop novel methods that can enable accurate monitoring and detection of AF [193]. With the growing trend for remote monitoring of ECG, there are research interests in using single lead ECG for detecting such AF and other cardiac arrhythmias. Given the limitations for 12-lead ECG detection, the challenges are even higher for single lead ECG for real-time and remote ECG monitoring. In addition, robust detection and classification algorithms are essential for accurately discriminating NSR, AF and ventricular arrhythmias such as ventricular tachycardia and ventricular fibrillation (VF) so that appropriate energy could be delivered while using implantable cardioverter defibrillators (ICD) to provide lifesaving timely action.

Therefore, there is a clear clinical need for robust discrimination algorithms for NSR and AF on a single lead ECG that can be of high prognostic and diagnostic significance in detecting AF and other arrhythmias in a timely fashion for live saving therapies and clinical management of these patients. The novel quantitative electrogram analysis techniques developed in this thesis can be excellent candidates for such discrimination between NSR and AF. In this chapter, MSE (time domain) and MSF (frequency domain) approaches are tested for this discrimination analysis using NSR and AF data sets from single lead ECG.

The objectives of this section of the thesis will be accomplished by quantitative comparison of MSE and MSF estimates for NSR and AF using statistical significance to demonstrate robust discrimination using these techniques.

5.3 ECG analysis from Physionet/PhysioBank Database for NSR and AF discrimination

To accomplish this task in this thesis, publically available ECG traces of NSR (n=10) and AF (n=10) were taken randomly from the MIT-BIH Physionet and Physiobank AF and NSR database [194] for the discrimination analysis. Each trace was 10 seconds long and was sampled at 250 Hz. Figure 5-1 A shows a sample NSR ECG trace for the 1000 sample points and Fig. 5-1 B shows its normalized power spectrum. Figure 5-2 A shows a sample AF ECG trace for the 1000 sample points and Fig. 5-20 B shows its normalized power spectrum.

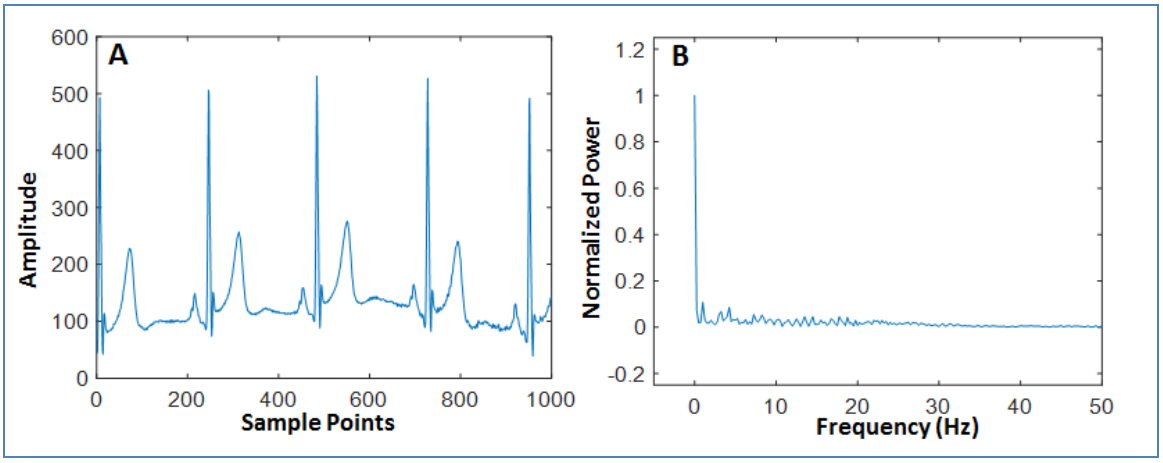

Figure 5-1: ECG waveform with Normal Sinus Rhythm and its normalized power spectrum. *(A) shows ECG wave with NSR and (B) shows the spectrum with natural frequencies. Frequency peak around 1 Hz is seen for a 60 bpm heart rate.*

The signals were not pre-processed for noise-removal etc. and MSE/MSF estimation was performed on the raw extracted dataset as to discriminate NSR and AF using custom MATLAB software. Statistical significance test was performed using Mann-Whitney test using OriginPro software (OriginLab Corporation, Northampton, Massachusetts) and $p < 0.05$ is considered statistically significant for the purposes of this thesis.

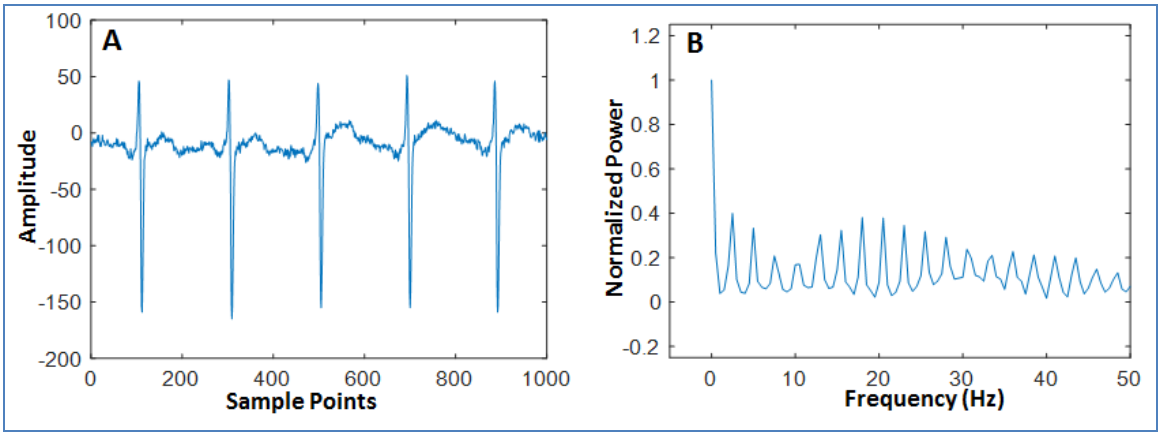

Figure 5-2: ECG waveform with Atrial Fibrillation and its normalized power spectrum. *(A) shows ECG wave with AF and (B) shows the spectrum demonstrating the fibrillatory nature with several high frequency peaks distinguishing the spectrum from NSR.*

As seen from Figure 5-1 B the NSR ECG has naturally occurring frequencies for NSR with a peak at 1 Hz corresponding to 60 beats per minute (bpm) heart rate and other associated frequencies that make up the P-QRS-T complex of the ECG. As seen from Figure 5-2 A it is rather visually difficult to infer AF from the trace, as it has fibrillatory P-wave which challenges visual inspection. However, Figure 5-2 B shows that AF ECG has chaotic frequencies different than the NSR spectrum. These data sets are analyzed with MSE and MSF approaches to investigate whether they can successfully discriminate NSR and AF on a single lead ECG in this thesis.

5.4 NSR and AF discrimination with MSE approach

Fig. 5-3 shows the raw ECG with NSR (panel A) and AF (panel B). Note that visual inspection of these traces cannot be used to correctly discriminate between NSR and AF. Fig. 5-3 C shows the boxplot of MSE values for 10 AF and NSR data sets demonstrating

statistically significant differences ($p<0.01$) and therefore accurate discrimination between NSR and AF.

As observed in Fig.5-3 A-B visually it is difficult to interpret the difference between NSR and AF on the ECG as the chaotic nature of AF manifests itself into small morphological disturbances which need robust algorithms to effectively capture the complexity. MSE robustly discriminates NSR and AF, which offers huge promise for various applications which use single lead ECG for remote monitoring.

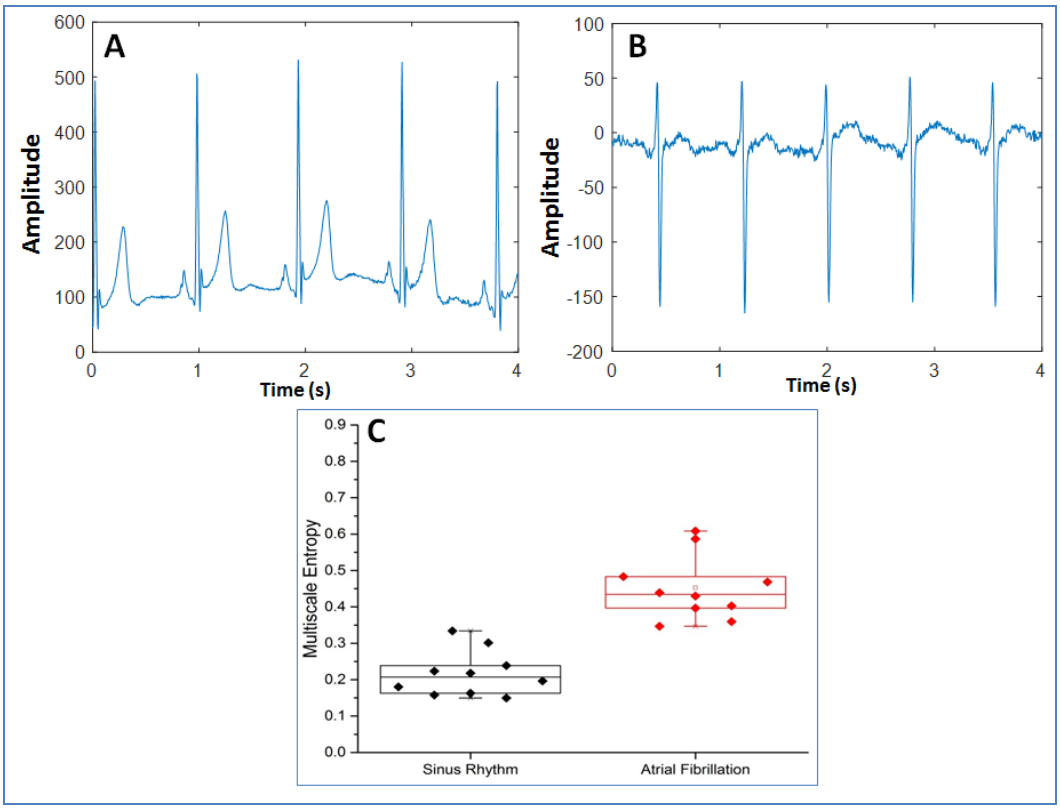

Figure 5-3: Discrimination of NSR and AF using MSE. *(A) Representative example of an ECG trace with normal sinus rhythm; (B) Representative example of an ECG trace with atrial fibrillation; (C) Box plot showing multiscale entropy values for sinus rhythm and atrial fibrillation ECG datasets. The NSR and AF were significantly different ($p < 0.01$) on MSE.*

5.5 NSR and AF discrimination with MSF approach

Fig. 5-4 shows the raw ECG with NSR (panel A) and AF (panel B) and Fig. 5-4 C shows the boxplot of MSE values for 10 AF and NSR data sets. Figs. 5-1 and 5-2 shows the power spectrum of the NSR and AF ECG waveform demonstrating their differences in their frequency characteristics.

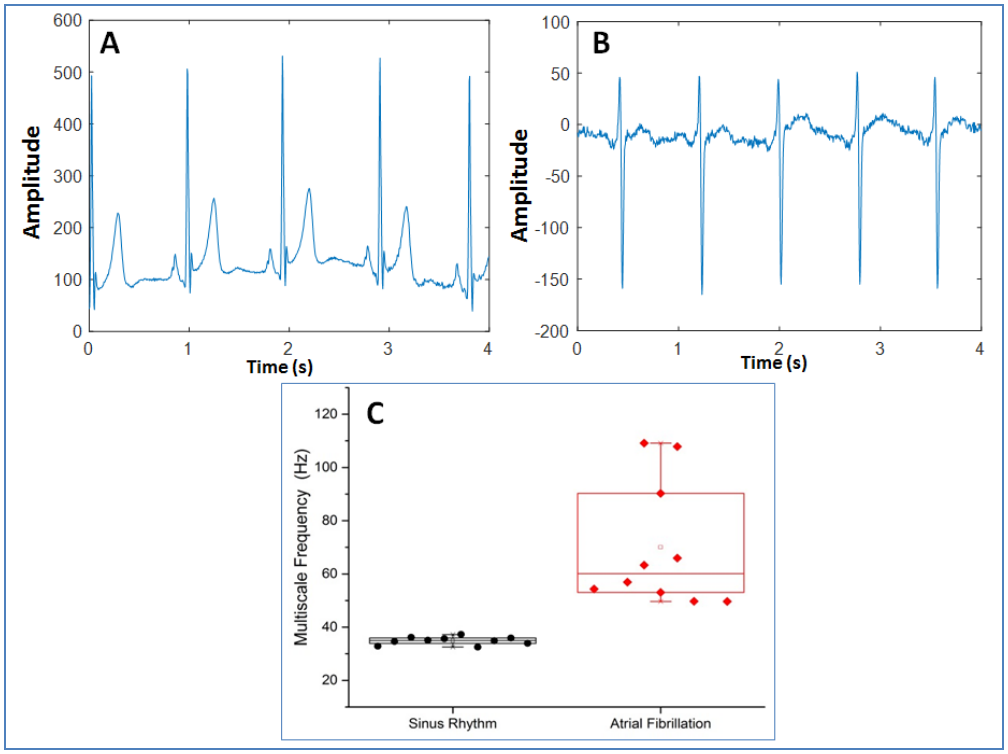

Figure 5-4: Discrimination of NSR and AF using MSF. *(A) Representative example of an ECG trace with normal sinus rhythm; (B) Representative example of an ECG trace with atrial fibrillation; (C) Box plot showing MSF values for NSR and AF ECG datasets. The NSR and AF were significantly different ($p < 0.01$) on MSF.*

MSF for ECG with NSR shown in Fig 5-4 A is 37.24 Hz and 53.06 Hz for AF shown in Fig 5-4 B. The mean MSF for NSR was 34.68+/-1.48 Hz, and the mean MSF for AF was 70.02+/-23.49 Hz. As seen from Fig. 5-4 C MSF demonstrated statistically significant differences ($p<0.01$) between NSR and AF and therefore accurate

discrimination between them using a single lead ECG waveform. As observed in Fig.5-4 A-B visually it is difficult to interpret the difference between NSR and AF on the ECG as the chaotic nature of AF manifests itself into small morphological disturbances which need robust algorithms to effectively capture the complexity. However, as seen from their power spectrum in Figures 5-1 and 5-2, AF presents several significant frequency components that are not prominent in NSR. MSF approach uses this frequency information to calculate MSF index based on the output of the 8 filter banks that results in higher MSF for AF and relatively lower MSF for NSR. This resulted in robust discrimination between NSR and AF which offers huge promise for various applications which use single lead ECG for remote monitoring.

5.6 Discussion

This section of the thesis evaluated the feasibility of the novel MSE and MSF approaches to capture the intrinsic complexity of ECG to discriminate AF from NSR on a single lead ECG. Since the efficacy of RPDE, kurtosis and EMD for ECG analysis has already been demonstrated by several groups in the literature they were not explored in this thesis. The observed robustness of MSE and MSF approach with respect to SE approach demonstrated in Chapters 3 and 4 showed additional values for discrimination of NSR and AF on a single lead ECG. The major finding of this thesis was that MSE and MSF robustly discriminated NSR and AF on a single lead ECG without any preprocessing steps. MSE approach captures the repetitive nature of chaotic time series in linear space to quantify the differences between the AF and NSR time series that resulted in statistically significant discrimination. With MSF approach, the chaotic nature of AF

yields more frequency components compared to NSR, which are processed through the various weighted Log-Gabor filters, resulting in a higher MSF value for AF. It appears that a threshold MSF value of 40 can be effectively used to discriminate AF from NSR, which however needs to be further validated with more datasets.

The objectives of this section of the thesis was accomplished, from the results which demonstrates the efficacy of both MSE and MSF technique by accurate detection of AF using a short ECG time series data of only 10 s, without preprocessing, which often distorts the data, and without R-wave detection, which needs highly reliable methods. These techniques therefore addresses several limitations of other existing techniques mainly by reducing the ECG recording time needed for analysis for AF detection and can be successfully integrated into any existing ECG monitoring devices for real-time monitoring and detection. MSE and MSF technique provided a highly robust and reliable discrimination of NSR and AF with high clinical utility for real-time ECG monitoring for NSR and other arrhythmias. Incorporation of this technique in ICD may lead to adequate differential therapy in patients suffering from spontaneous episodes of AF and also other complex arrhythmias such as ventricular fibrillation (VF). Optimal MSF thresholds for AF/VF detection can be obtained by analyzing several such datasets. Future studies are required to validate the result from MSE and MSF further using NSR and AF datasets with various noises.

5.7 Conclusion

This chapter had demonstrated the efficacy of MSE and MSF approach in robustly discriminating NSR and AF on a single lead ECG without any preprocessing.

CHAPTER 6: VALIDATION OF NOVEL APPROACHES USING OPTICAL MAPPING AND NUMERICAL ROTOR DATA

6.1 Introduction

This chapter presents the results of testing and validation of the novel time and frequency domain approaches for rotor pivot point identification developed in this thesis. Several data sets were used for validation including optical mapping data from isolated rabbit hearts with known pivot points for single and double rotors, numerically simulated and optical mapping meandering rotors from isolated rabbit hearts for which the results from the approaches are compared with visual inspection of the voltage and phase movies for pivot point locations. A brief description of the optical mapping procedure and numerical simulation for obtaining rotor data is discussed followed by the description of the dataset and the processing steps to obtain 2D maps for each of the novel approaches which were implemented using custom MATLAB programs discussed in Chapter 3. Specific pixel locations corresponding to the rotor core and periphery are labelled for reference for each data set and their amplitude histogram and spectrum are provided.

This chapter is organized as follows. Results of SE, RE and DF approaches are presented first for each dataset that can be compared with the results from new approaches developed in this thesis. For each of the novel approach such as MSE, RPDE, Kurtosis, IMF and MSF the results of single, double and meandering rotors are presented and discussed separately in each subsection. References are made to the amplitude histogram and power spectrum provided for the specified pixel locations for optical mapping data for discussion of the performance of each approaches.

6.2 Rotor data collection and analysis

The fourth specific aim of this thesis is "*To validate the efficacy of the novel electrogram analysis approaches using numerically simulated and optical mapping rotor data with known pivot point locations".* As described in Chapter 2, optical mapping data of rotors with known pivot point locations from ex vivo animal experiments and numerical simulation data offers excellent resource for testing and validating novel approaches, which is used to realize the objectives of this section of the thesis. The following sections will describe the optical mapping and numerical rotor data and their analysis using the novel approaches.

6.2.1 Optical mapping data from isolated rabbit heart

Optical mapping experiments were performed as described previously [195-196] to obtain variety of rotor data such as (i) single rotor; (ii) figure-of-eight double rotor and (iii) meandering rotor for this thesis. Briefly, isolated rabbit hearts were put in the Langendorff-perfusion system, and voltage-sensitive dye di-4-ANEPPS (5 μg/mL) was added to the perfusate. After staining, two 532 nm green lasers were used to illuminate both LV and RV of the heart. Fluorescence intensity was captured with two 12-bit CCD cameras, which were connected via a frame grabber to a computer. The cameras run synchronously at 600 frames per second with 64x64 pixel resolution. VT was induced via burst pacing, and phase movies of the rotors where obtained from optical mapping recordings as described previously [189-190] for the single rotor data. For figure-of-eight double and meandering rotors VF was induced via burst pacing and the phase movies were obtained for processing. Singularity analysis was performed on these data to obtain

the precise location of the rotor pivot points for the single and double rotor. For the meandering rotor however, visual inspection of the phase movies can provide information on the trajectories of the many meandering rotors present in the data set. The phase movies were processed using custom MATLAB software with the novel approaches as described in the previous sections to generate the 2D map and compared. Also, SE, RE and DF analysis are also performed for each of these datasets to obtain their 2D maps for comparison with the results from the novel approaches developed in this thesis.

A snapshot of a phase movie of the single rotor with pixel locations '1' at rotor core and '2' at the periphery in isolated rabbit heart is shown in the left panel of Figure 6-1. In this movie, different colors represent different phases of action potential, and the pivot point of the rotor can be easily identified as the point where different phases converge. Right panel of Fig. 6-1 shows corresponding voltage traces from the core (pixel '1') and periphery of the rotor (pixel '2'). At the core of the rotor, broader distribution of voltage amplitude occurs due to the chaotic nature at the rotor pivot point and therefore higher complexity as measured by the novel MSE, kurtosis, IMF, RPDE and MSF values are expected. At the periphery of the rotor, a more uniform electrical activity is observed and hence lower values are expected from these novel approaches, thus enabling accurate and reliable identification. Figure 6-2 & 6-3 shows the voltage distribution, amplitude histogram and normalized power spectrum at pixel locations '1' and '2' respectively for the single rotor.

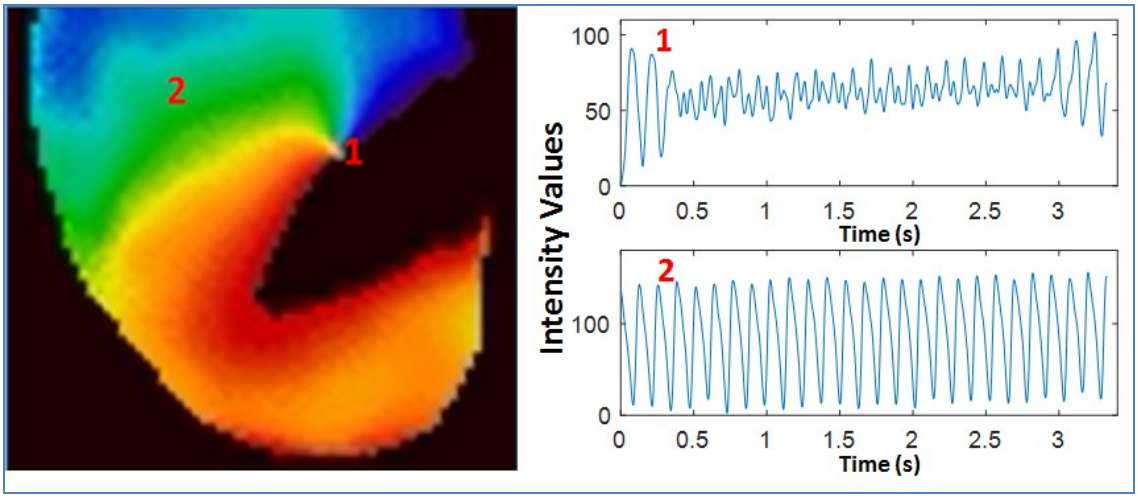

Figure 6-1: Optical mapping data of single rotor. *Top panel shows a representative example of a single rotor. Pixel locations '1' represent rotor core region and '2' represent rotor periphery; bottom panel shows corresponding voltage traces at those pixel locations.*

Amplitude histogram and normalized power spectrum for each pixel locations considered for reference in each of the dataset are provided to provide insights into the nature of the time series in the time and frequency domain. Changes in the temporal and frequency characteristics at the rotor core and periphery can be inferred which will be utilized by the novel approaches in this thesis for their discrimination for accurate and reliable identification of rotor pivot point. Figure 6-4 shows a snapshot of a figure-of-eight double rotor movie with pixel locations '1' and '2' at rotor core and '3' at the periphery and is processed as before to obtain the 2D maps. Figures 6-5, 6-6 & 6-7 shows the voltage distribution, amplitude histogram and normalized power spectrum at pixel locations '1' , '2' and '3' respectively for the double rotor.

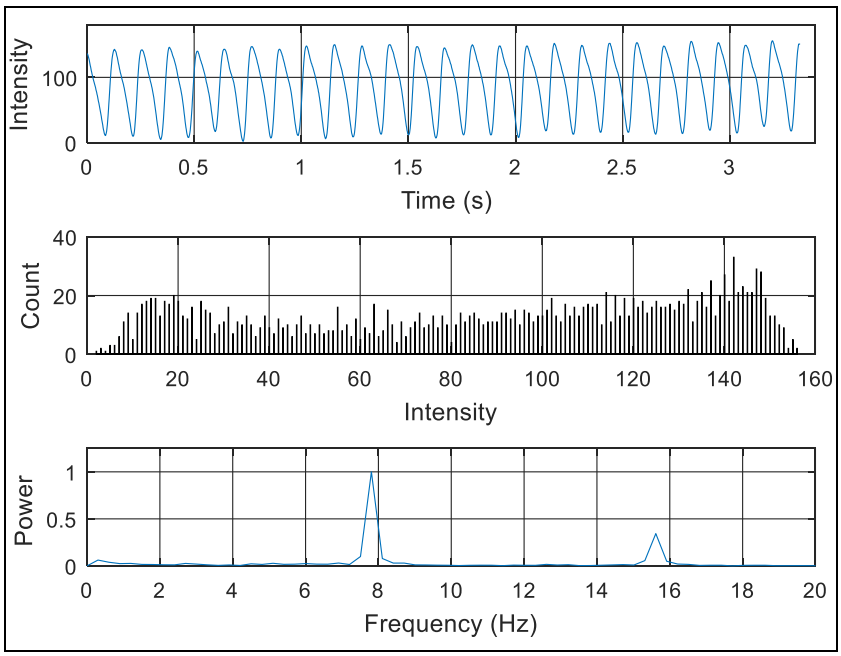

Figure 6-2: Single rotor pixel analysis at rotor periphery at pixel location '2'. *(Top) - Voltage distribution. (Middle) - Amplitude histogram; (Bottom) - Normalized power spectrum*

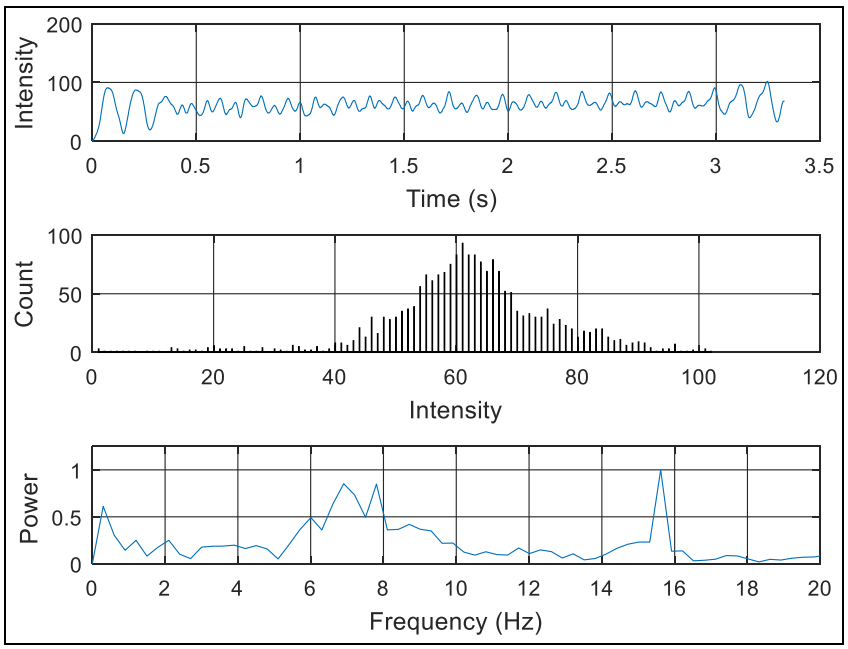

Figure 6-3: Single rotor pixel analysis at rotor core at pixel location '1'. *(Top) - Voltage distribution. (Middle) - Amplitude histogram; (Bottom) - Normalized power spectrum*

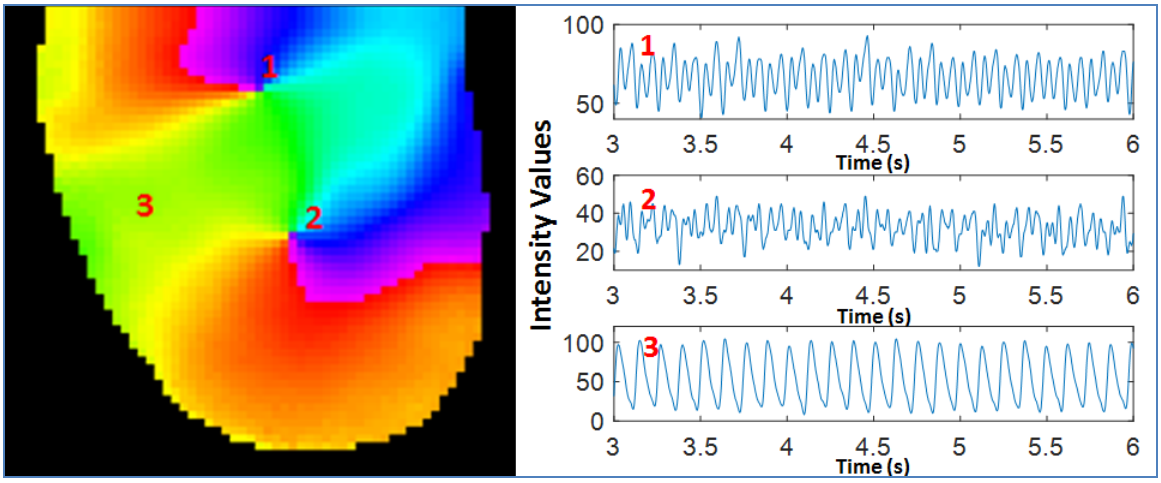

Figure 6-4: Optical mapping data of figure-of-eight double rotor. *Top panel shows a representative example of a double rotor. Pixel locations '1' & '2' represent rotor core region and '3' represent rotor periphery; bottom panel shows corresponding voltage traces at those pixel locations.*

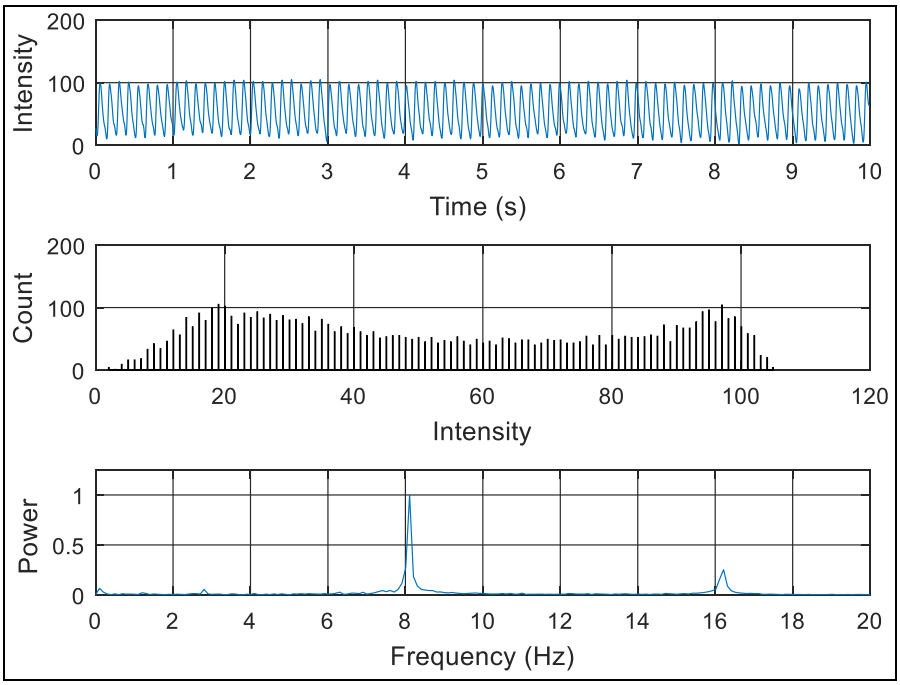

Figure 6-5: Double rotor pixel analysis at rotor periphery at pixel location '3'. *(Top) - Voltage distribution. (Middle) - Amplitude histogram; (Bottom) - Normalized power spectrum*

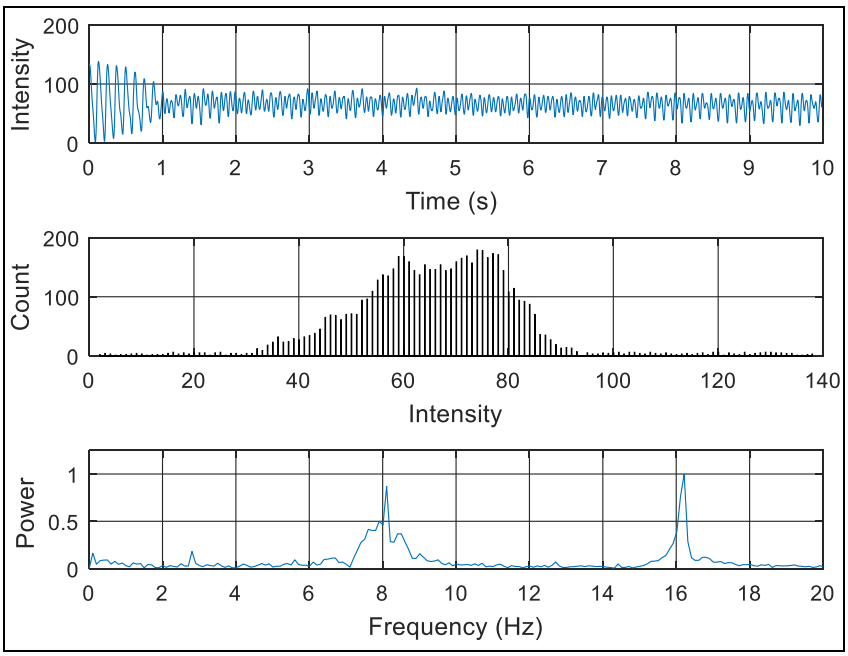

Figure 6-6: Double rotor pixel analysis at rotor core at pixel location '1'. *(Top) - Voltage distribution. (Middle) - Amplitude histogram; (Bottom) - Normalized power spectrum*

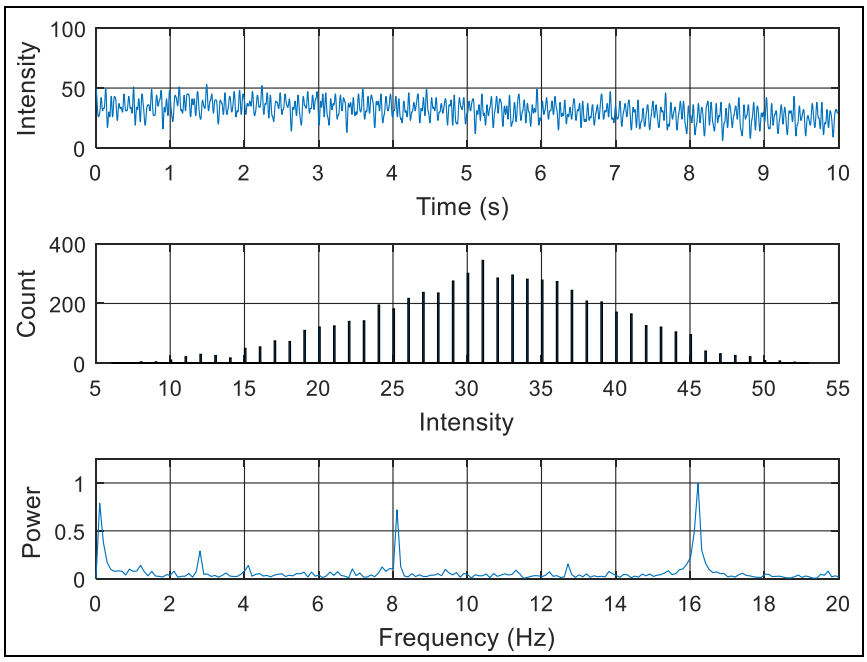

Figure 6-7: Double rotor pixel analysis at rotor core at pixel location '2'. *(Top) - Voltage distribution. (Middle) - Amplitude histogram; (Bottom) - Normalized power spectrum*

As seen from Figure 6-4 there are two rotors and the pivot points are identified at pixel locations ‘1’ and ‘2’. Visual inspection of the phase movie revealed that rotor core corresponding to pixel location ‘1’ is meandering to some extent while the other rotor is relatively stable. Figure 6-8 shows the snapshot of a phase movie of meandering rotors in isolated rabbit heart at 80x80 pixel resolution obtained at 1000 frames per second. Pixel locations ‘1’ represent the periphery of the rotor, ‘2’, ‘3’and ‘4’ are at the rotor core during the time frame of this snapshot movie and their amplitude histogram and normalized power spectrum are shown in Figures 6-9, 6-10, 6-11 & 6-12 respectively.

Visual inspection of the phase movie revealed several meandering rotors in this data set which appears then meanders and vanishes throughout the time frame of the dataset. The voltage distributions at the pixel locations corresponding to the rotor core, shows episodic chaotic distributions representing the meandering rotor traversing spatially while the distributions looks uniform at the rotor periphery throughout the time frame. The data is processed using the novel approaches as described before to obtain the 2D maps. It was observed that the optical data was free of 60 Hz and other high frequency noise and no preprocessing steps were necessary prior to processing with these novel approaches.

6.2.2 Meandering rotor from numerical simulation

The electrical activity in a 30x30mm human atrial tissue was simulated using an extended bi-domain model that incorporates both fibroblasts and myocytes in a bi-layer scheme similarly to our previous work [191-192]. The incorporation of diffuse fibrosis will allow easy control over the extent of rotor meandering. The purpose of this section of the thesis is to test the feasibility of the novel approaches to track the pivot point of the

meandering rotor under controlled conditions that can provide new insights into rotor mapping research.

Two sets of simulated data was obtained with 100x100 pixel resolution at 1000 frames per second and was processed similar to the optical mapping data described in the previous section. Figure 6-13 shows snapshot of the voltage distributions of a numerically simulated meandering rotor. Pixel location '1' correspond to the rotor periphery and pixel locations '2' & '3' at the rotor core during the time frame of this snapshot movie with their corresponding histogram and spectrum in Figures 6-14, 6-15 & 6-16 respectively. Visual inspection of the phase movie revealed the trajectory of rotor pivot point which meanders throughout the atrial space. This numerical rotor data is designated as "Meandering rotor dataset1" for the purposes of this thesis. Similarly, Figure 6-17 shows snapshot of voltage distribution movie of another numerically simulated meandering rotor designated as "Meandering rotor dataset2".

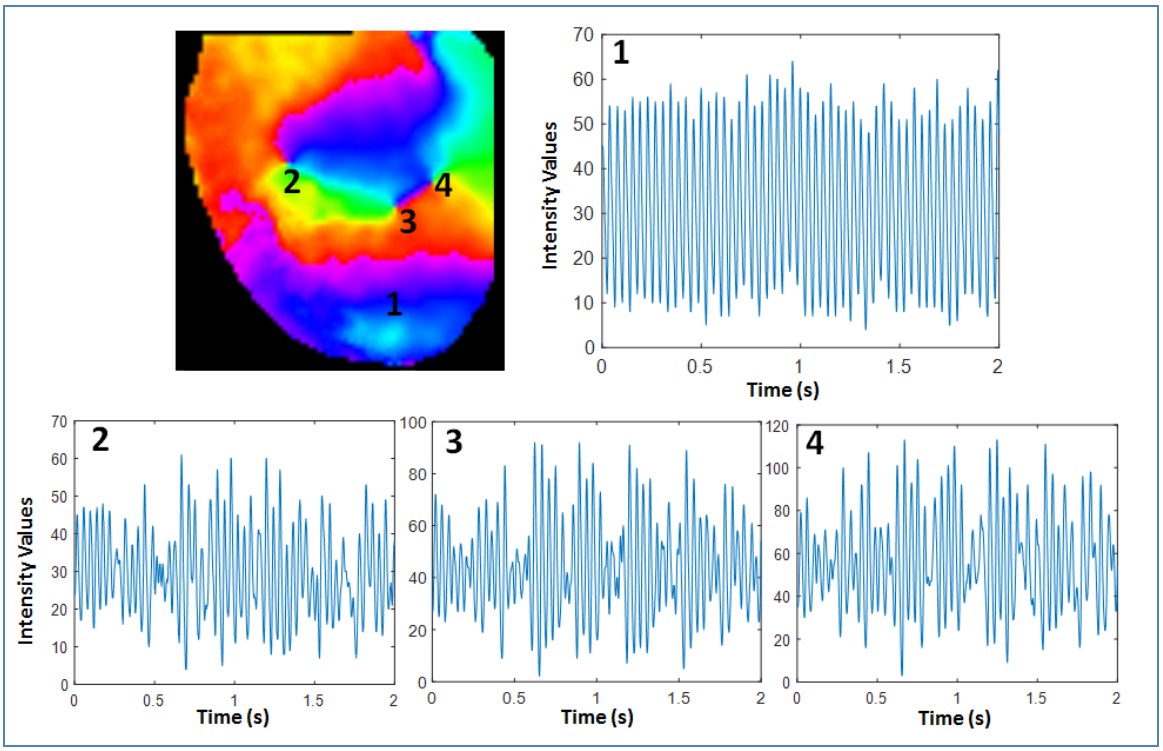

Figure 6-8: Optical mapping data of a meandering rotor. *Top left panel shows a representative example of meandering rotors with pixel locations '1' at periphery and '2', '3' and '4' at the rotor core at the time of the snapshot of the phase movie. Top right panel shows the intensity values at pixel location '1' and bottom panel shows the voltage distribution at pixel locations '2', '3' & '4'.*

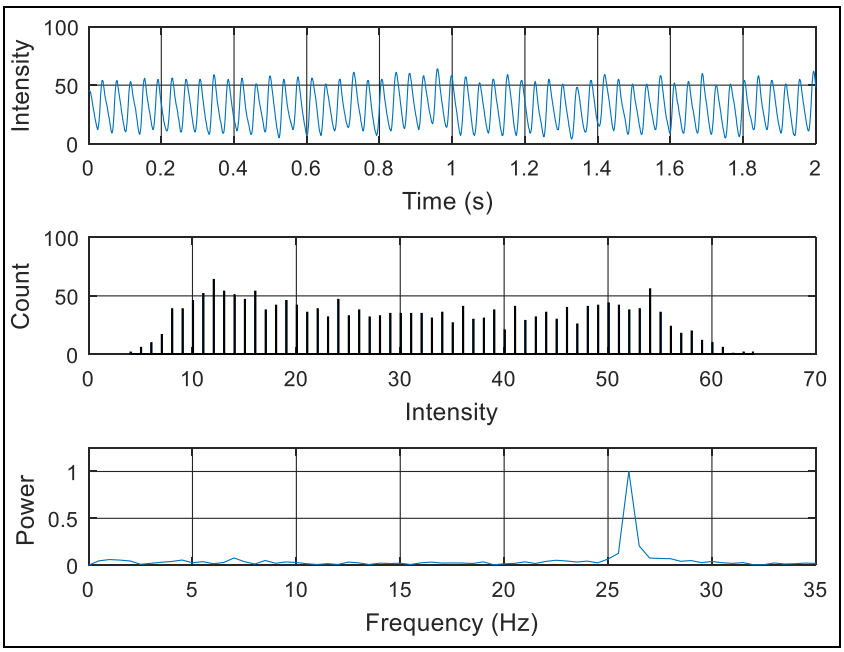

Figure 6-9: Meandering rotor pixel analysis at rotor periphery at pixel location '1' from optical mapping. *(Top) - Voltage distribution. (Middle) - Amplitude histogram; (Bottom) - Normalized power spectrum*

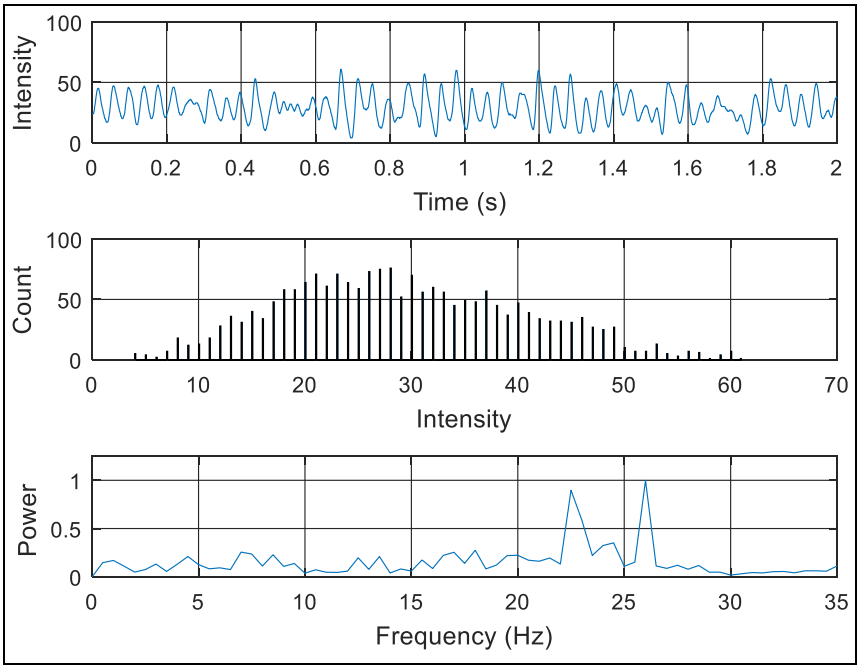

Figure 6-10: Meandering rotor pixel analysis at rotor core at pixel location '2' from optical mapping. *(Top) - Voltage distribution. (Middle) - Amplitude histogram; (Bottom) - Normalized power spectrum*

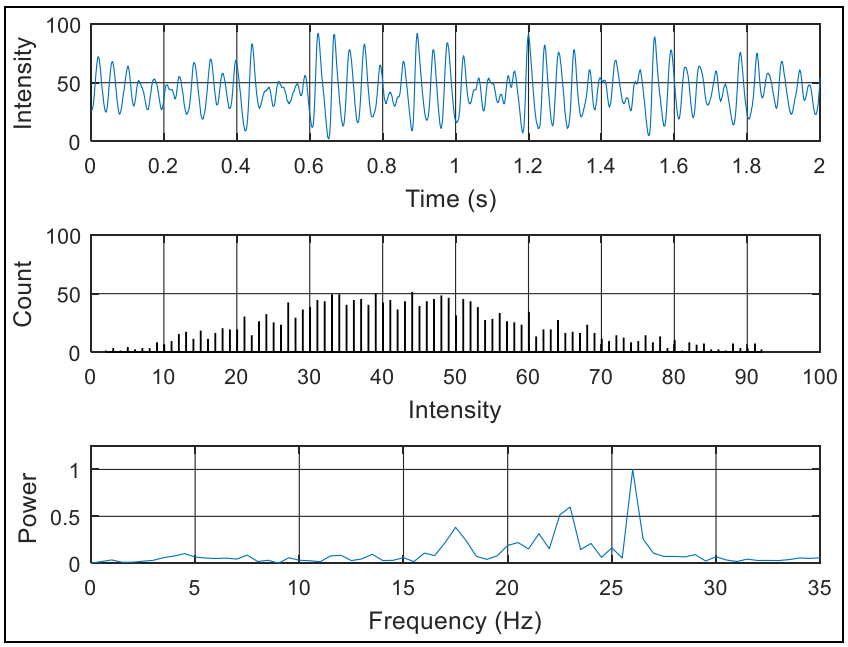

Figure 6-11: Meandering rotor pixel analysis at rotor core at pixel location '3' from optical mapping. *(Top) - Voltage distribution. (Middle) - Amplitude histogram; (Bottom) - Normalized power spectrum*

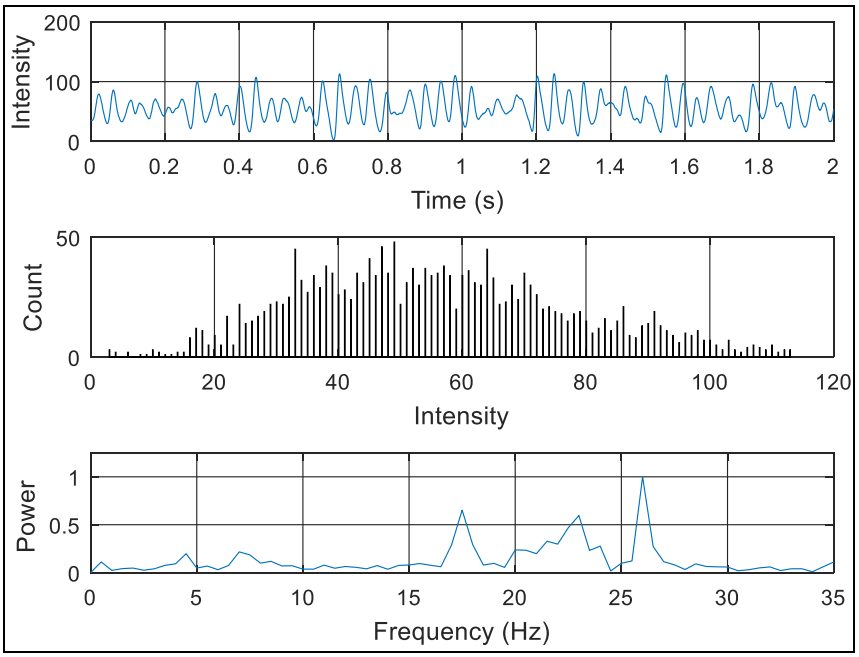

Figure 6-12: Meandering rotor pixel analysis at rotor core at pixel location '4' from optical mapping. *(Top) - Voltage distribution. (Middle) - Amplitude histogram; (Bottom) - Normalized power spectrum*

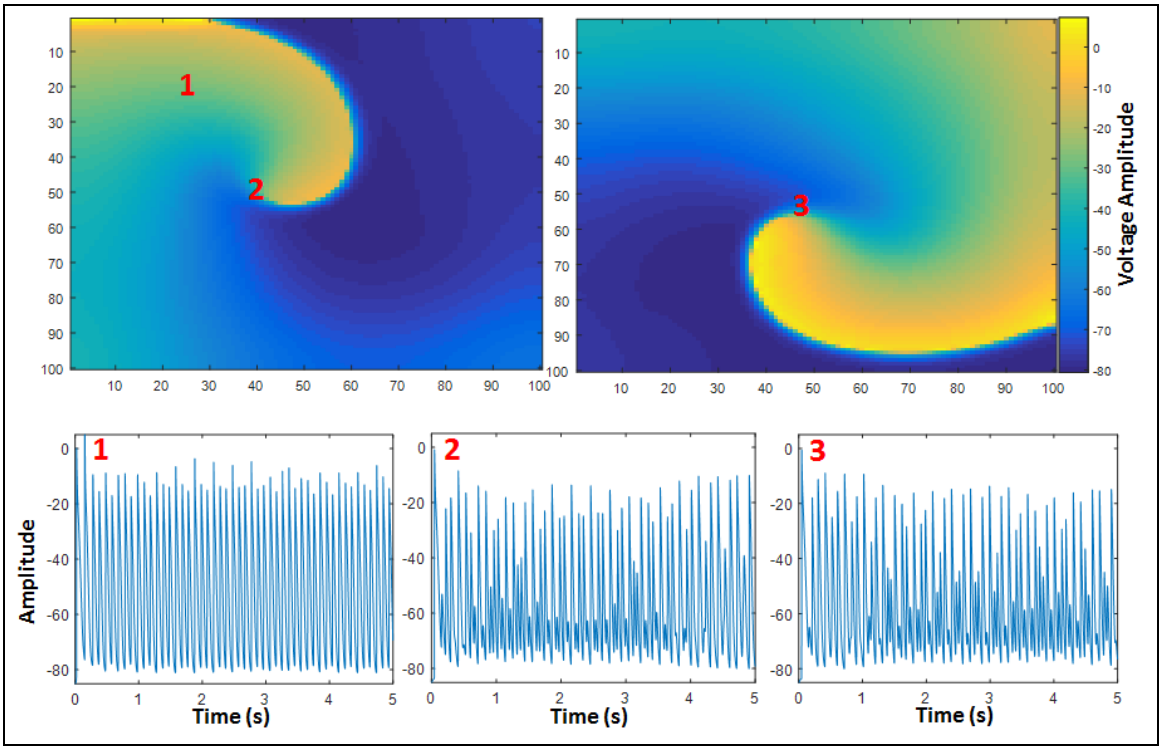

Figure 6-13: Meandering rotor dataset1 from numerical simulation. *Top left panel shows a meandering rotor with pixel locations '1' at periphery and '2'' at the rotor core at the time of the snapshot of the simulation voltage movie. Top right panel shows a snapshot with the rotor core at a different location at pixel '3'. Bottom panel shows the voltage distribution at pixel locations '1', '2' & '3'.*

As seen from Figure 6-13 there is a single meandering rotor numerically simulated which meanders spatially. Uniform voltage distribution at pixel location '1' is observed throughout the time frame which implies the complexity measured by the novel approaches should be lower at this location. Voltage distribution at pixel locations '2' and '3' has instances of chaotic behavior implying the meandering of the pivot point and several crossings at this same location. This suggests that the complexity measured at this location should be higher than at pixel local '1'.

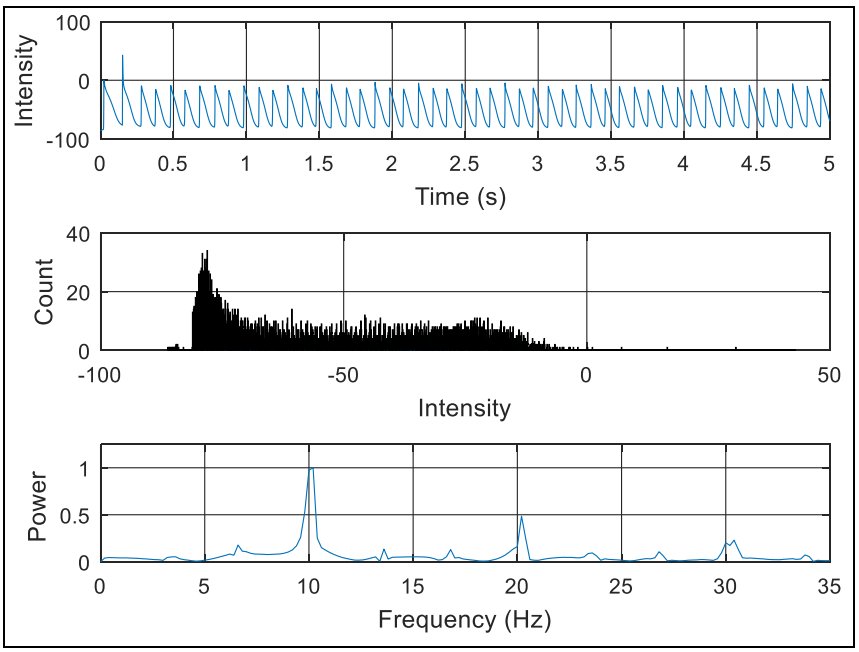

Figure 6-14: Meandering rotor pixel analysis at rotor core at pixel location '1' from numerical simulation dataset1. *(Top) - Voltage distribution. (Middle) - Amplitude histogram; (Bottom) - Normalized power spectrum*

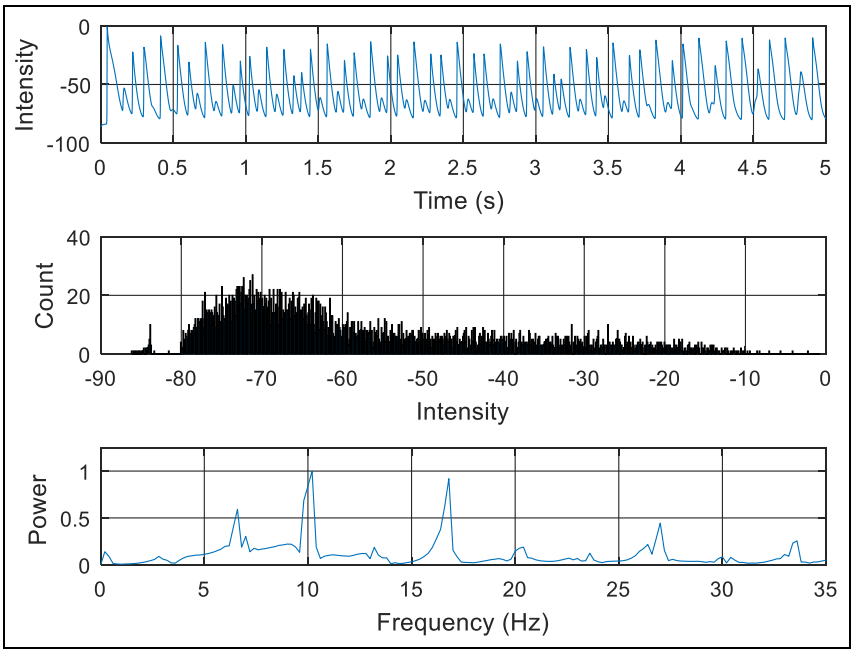

Figure 6-15: Meandering rotor pixel analysis at rotor core at pixel location '2' from numerical simulation dataset1. *(Top) - Voltage distribution. (Middle) - Amplitude histogram; (Bottom) - Normalized power spectrum*

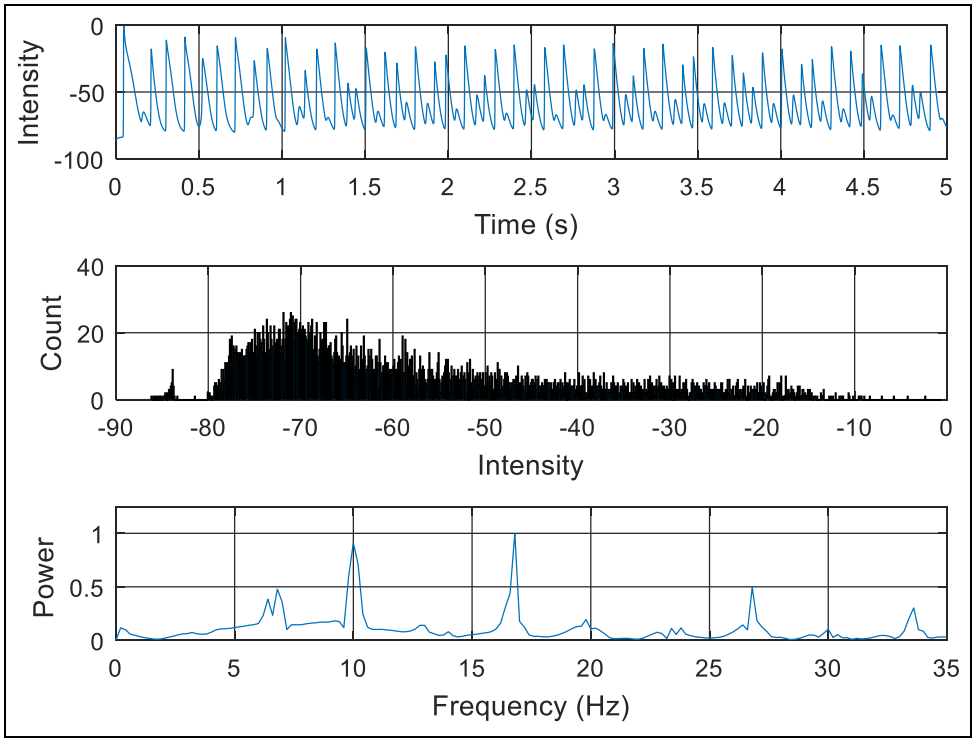

Figure 6-16: Meandering rotor pixel analysis at rotor core at pixel location '3' from numerical simulation dataset1. *(Top) - Voltage distribution. (Middle) - Amplitude histogram; (Bottom) - Normalized power spectrum*

Optically mapped and numerically simulated rotor data with known pivot point locations offers an excellent platform to test and demonstrate the efficacy and robustness of the novel approaches developed in this thesis. 2D SE, RE and DF maps were computed for each of these five datasets to compare the performances of the novel methods. As evident, the time series lengths of these data varied from 3-8 s similar to the time frame in a clinical setting to obtain intracardiac electrograms which also provides the right platform for validating these novel techniques with short time series data. As seen from Figure 6-17 there is a single meandering rotor numerically simulated which meanders spatially. Figures 6-18, 6-19 and 6-20 shows the amplitude histogram and normalized power spectrum at pixel locations '1', '2' and '3' respectively. Uniform

voltage distribution at pixel location ‘1’ is observed throughout the time frame which implies the complexity measured by the novel approaches should be lower at this location. Voltage distribution at pixel locations ‘2’ and ‘3’ has instances of chaotic behavior implying the meandering of the pivot point and several crossings at this same location. This suggests that the complexity measured at this location should be higher than at pixel local ‘1’.

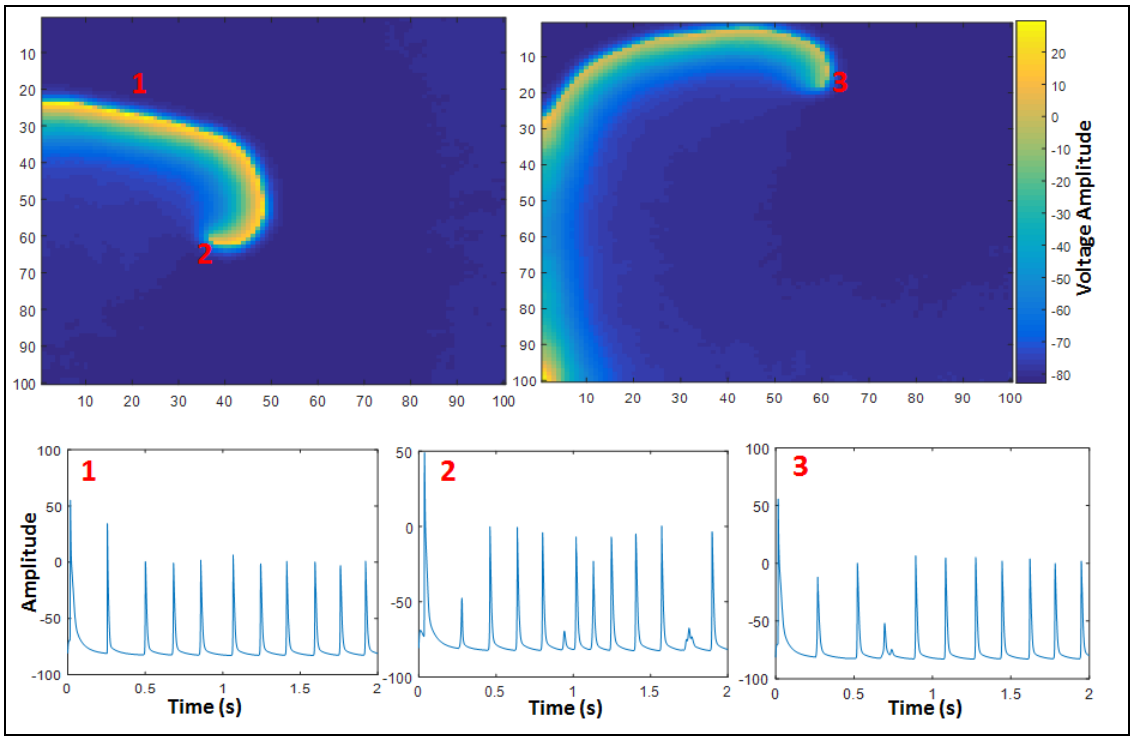

Figure 6-17: Meandering rotor dataset2 from numerical simulation. *Top left panel shows a meandering rotor with pixel locations ‘1’ at periphery and ‘2’’ at the rotor core at the time of the snapshot of the simulation voltage movie. Top right panel shows a snapshot with the rotor core at a different location at pixel ‘3’. Bottom panel shows the voltage distribution at pixel locations ‘1’, ‘2’ & ‘3’.*

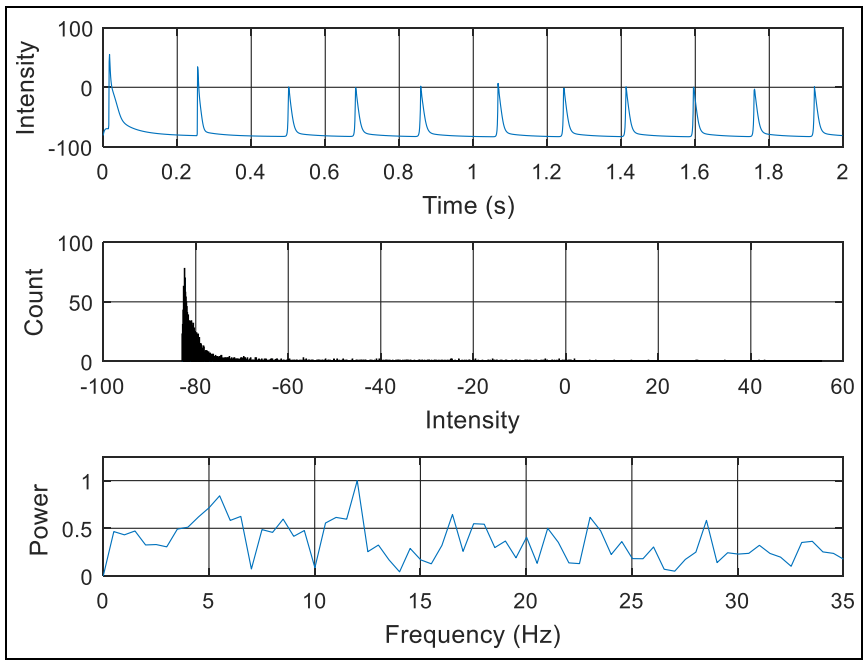

Figure 6-18: Meandering rotor pixel analysis at rotor core at pixel location '1' from numerical simulation dataset2. *(Top) - Voltage distribution. (Middle) - Amplitude histogram; (Bottom) - Normalized power spectrum*

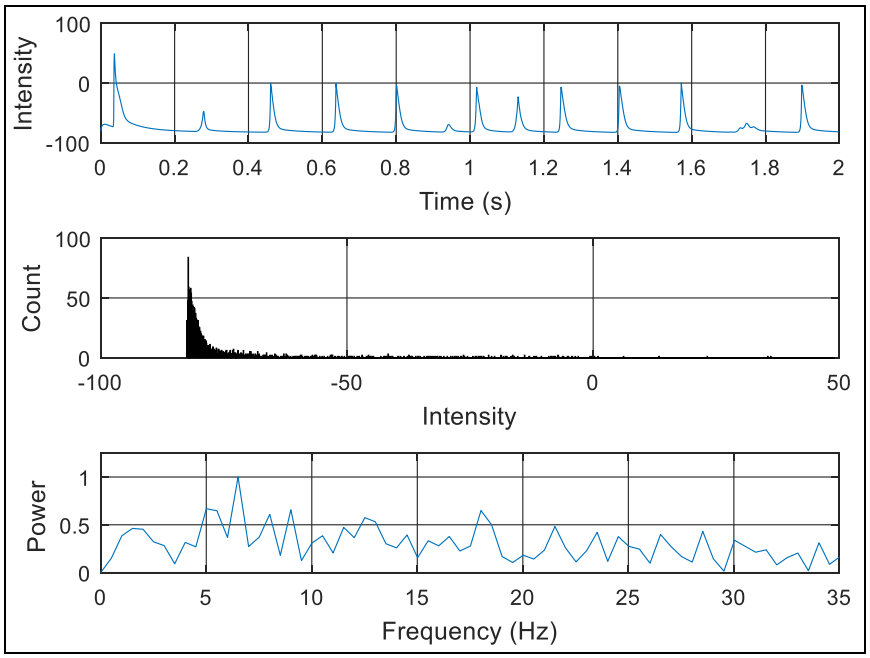

Figure 6-19: Meandering rotor pixel analysis at rotor core at pixel location '2' from numerical simulation dataset2. *(Top) - Voltage distribution. (Middle) - Amplitude histogram; (Bottom) - Normalized power spectrum*

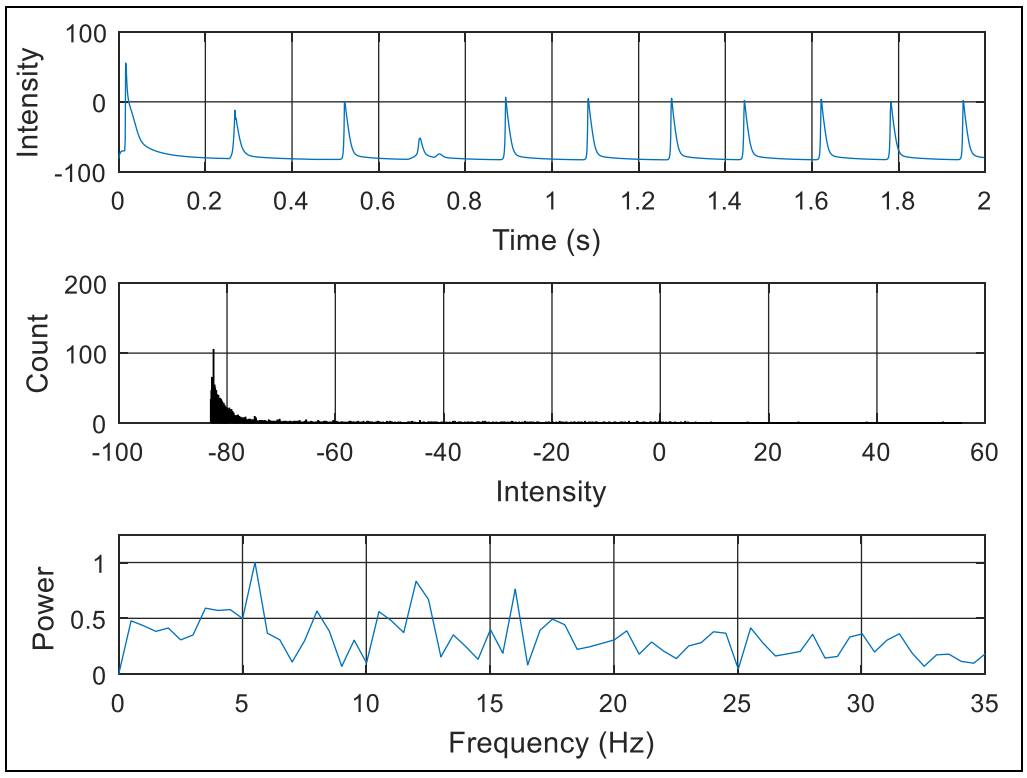

Figure 6-20: Meandering rotor pixel analysis at rotor core at pixel location '3' from numerical simulation dataset2. *(Top) - Voltage distribution. (Middle) - Amplitude histogram; (Bottom) - Normalized power spectrum*

Consolidated MATLAB program to implement the novel approaches for analyzing optical mapping data was achieved using *'Novel_Approaches_Optical_Data_Analysis.m'* included in APPENDIX F.

6.3 Testing of SE approach with rotor data

6.3.1 Performance of SE on single rotor identification

Figure 6-21 shows the snap shot of the phase movie for single rotor with the rotor core at pixel location '1' and '2' at the periphery. As seen in the middle panels of Figures 6-2 and 6-3 narrow distribution of intensity values occurs due to the chaotic nature at the rotor pivot point at the core of the rotor, with a more uniform electrical activity at the periphery resulting in broader distribution of intensity values. Low SE value is observed

at the core compared to the periphery, which was expected based on the results observed with the test samples using single and multifrequency sinusoidal wave in Chapter 3 for short time series analysis. Although rotor core identification was feasible, the contrast between the rotor core and periphery is relatively less, which makes it challenging for accurate and reliable identification. The result can be further challenged in the presence of noise such as in the clinical setting while acquiring intracardiac electrograms.

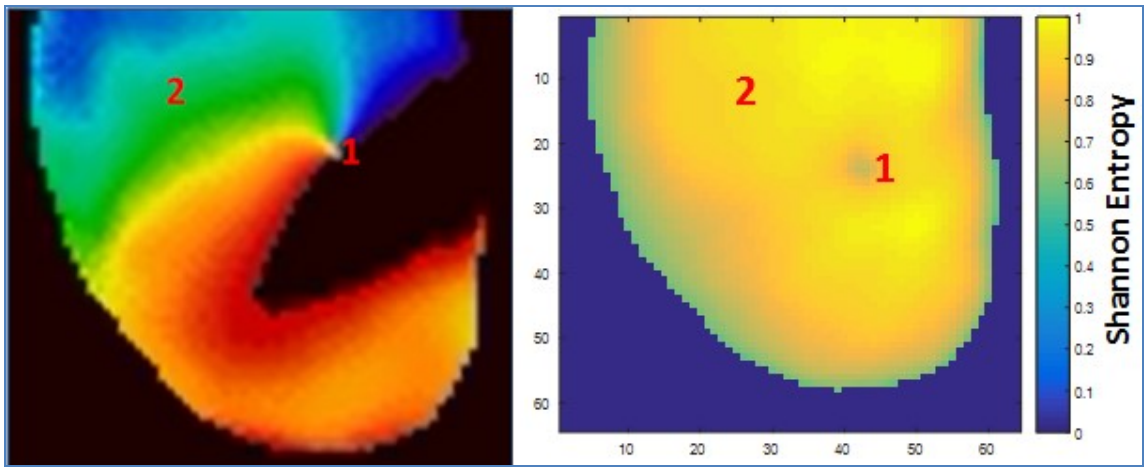

Figure 6-21: Results of SE approach with single rotor from optical mapping. *(Left) Snapshot of a phase movie showing single rotor with reference pixel locations'1' at rotor core and '2' at rotor periphery; (Right) Normalized 2D SE map showing low SE values at rotor core compared to periphery.*

6.3.2 Performance of SE on double rotor identification

Figure 6-22 shows the snap shot of the phase movie for double rotor with the rotor core at pixel locations '1' and '2' , and '3' at the periphery. As seen in the middle panels of Figures 6-5, 6-6 and 6-7, narrow distribution of intensity values occurs due to the chaotic nature at the rotor pivot point with a more uniform electrical activity at the periphery resulting in broader distribution of intensity values. Similar to the results from

single rotor, lower SE values at the rotor core and higher at the periphery are observed challenging reliable identification of rotor core using SE approach.

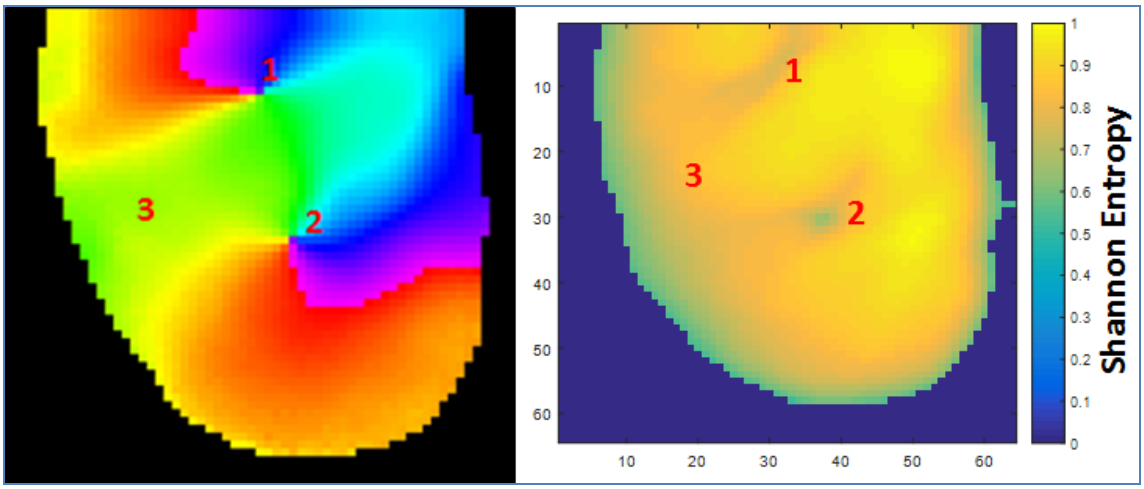

Figure 6-22: Results of SE approach with double rotor from optical mapping. *(Left) Snapshot of a phase movie showing double rotor with reference pixel locations'1',& '2' at rotor core and '3' at rotor periphery; (Right) Normalized 2D SE map showing low SE values at rotor core compared to periphery.*

6.3.3 Performance of SE approach on meandering rotor identification

Two sets of numerically simulated meandering rotors with different spatial profiles were tested for tracking the rotor pivot point by visual inspection. Results and analysis at reference pixel locations discussed in Chapter 3 during specified time frames showing meandering rotor pivot point and periphery are presented.

6.3.3.1 Performance of SE on meandering rotor from numerical simulation dataset1

Figure 6-23 top panel shows the snap shot of the voltage distribution movie of the meandering rotor with rotor periphery at pixel location '1' and rotor core at '2' and '3' , at the time of the snapshot. Middle panels of Figures 6-14, 6-15 and 6-16 demonstrate the differences in their temporal profiles and lower SE is observed at the rotor core region compared to the periphery in the bottom panel of Figure 6-23.

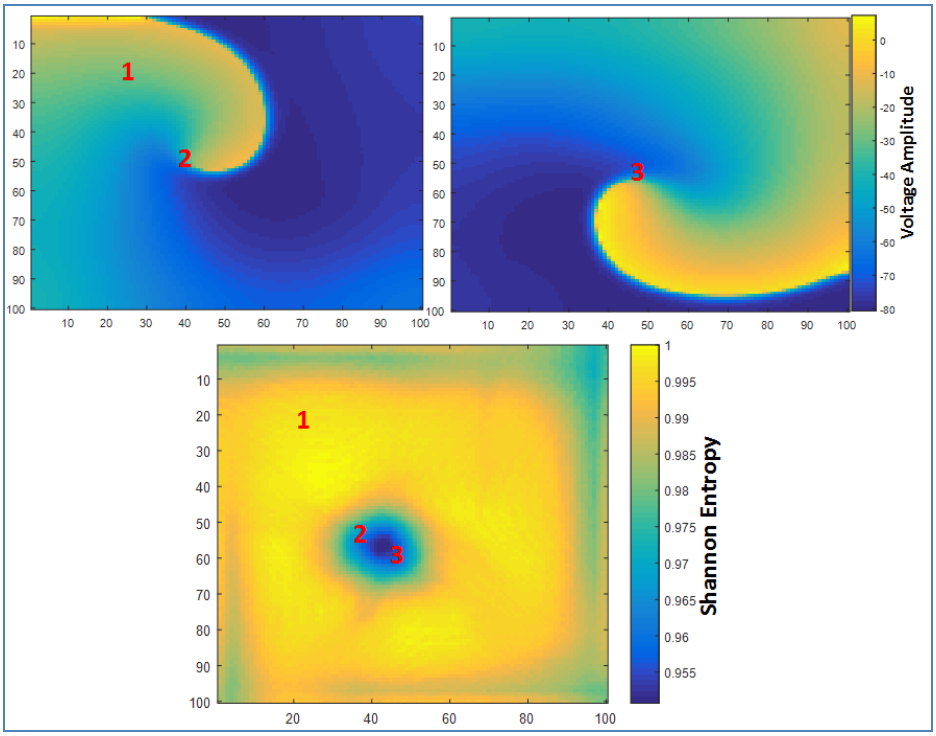

Figure 6-23: Results of SE approach with numerically simulated meandering rotor dataset1. *(Top-Left) Snapshot of voltage distributions showing single rotor with reference pixel locations'1' at rotor periphery and '2' at rotor core. (Top-Right) shows rotor core at pixel location '3'at the time of snapshot.; (Bottom) shows normalized 2D SE map showing low SE values at rotor core compared to periphery.*

Visual inspection of the phase movie revealed frequent traversing of the rotor core near the pixel locations '2' and '3' resulting in more chaotic distributions throughout the time frame causing lower SE compared to the periphery.

6.3.3.2 Performance of SE on meandering rotor from numerical simulation dataset2

Figure 6-24 top panel shows the snap shot of the voltage distribution movie of the meandering rotor with rotor periphery at pixel location '1' and rotor core at '2' and '3' , at the time of the snapshot. Middle panels of Figures 6-18, 6-19 and 6-20 demonstrate the differences in their temporal profiles. Visual inspection of the phase movie revealed dynamically changing trajectory of the rotor core throughout the spatial area. Figure 6-24

bottom panel shows the 2D SE map showing higher SE region at the center. However, inferences on the exact trajectory of the pivot point cannot be made with these results, given the limitation of SE with short time series analysis.

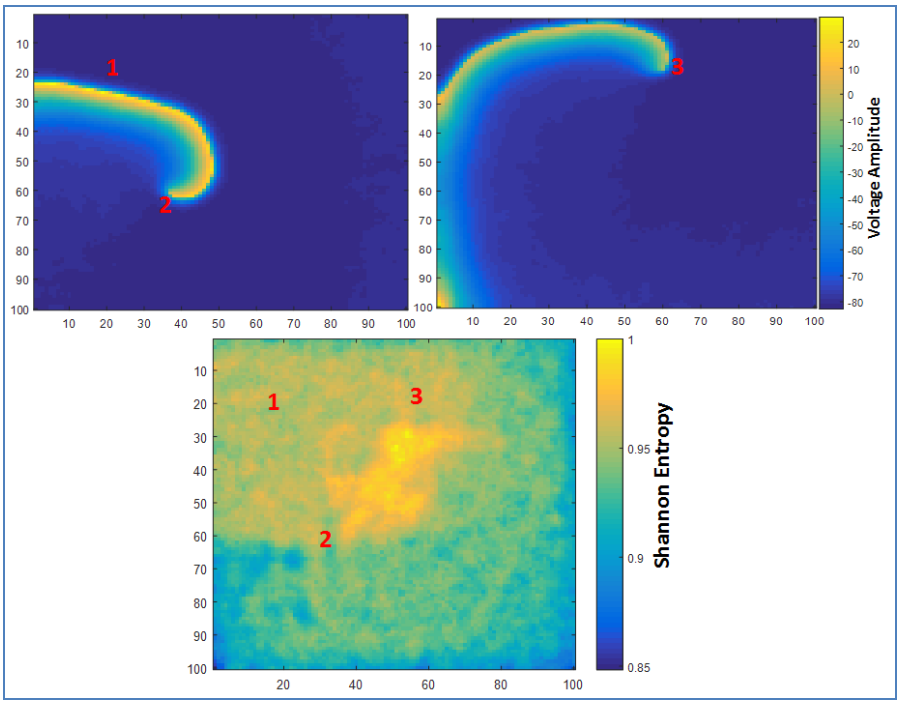

Figure 6-24: Results of SE approach with numerically simulated meandering rotor dataset2. *(Top-Left) 2D Voltage distributions showing single rotor with reference pixel locations'1' at rotor periphery and '2' at rotor core at the time of snapshot; (Top-Right) shows rotor core at pixel location '3'at the time of snapshot.; (Bottom) shows normalized 2D SE map.*

6.3.3.3 Performance of SE on meandering rotor from optical mapping

Figure 6-25 left panel shows the snap shot of the phase movie of the meandering rotor with rotor periphery at pixel location '1' and rotor core at '2', '3' and '4' at the time of the snapshot. Visual inspection of the phase movie revealed several meandering rotors traversing specifically in the central area at the rotor cores near the pixel locations '2' , '3' and '4'. Top and middle panels of Figures 6-9, 6-12, 6-11 and 6-12 demonstrate the

differences in their temporal profiles. Figure 6-25 right panel shows the 2D SE map showing higher SE region throughout the ventricular region with some lower SE regions in the bottom left region. Given the complexity of several meandering rotors and the limitations of SE, no specific inferences can be made on rotor core trajectories.

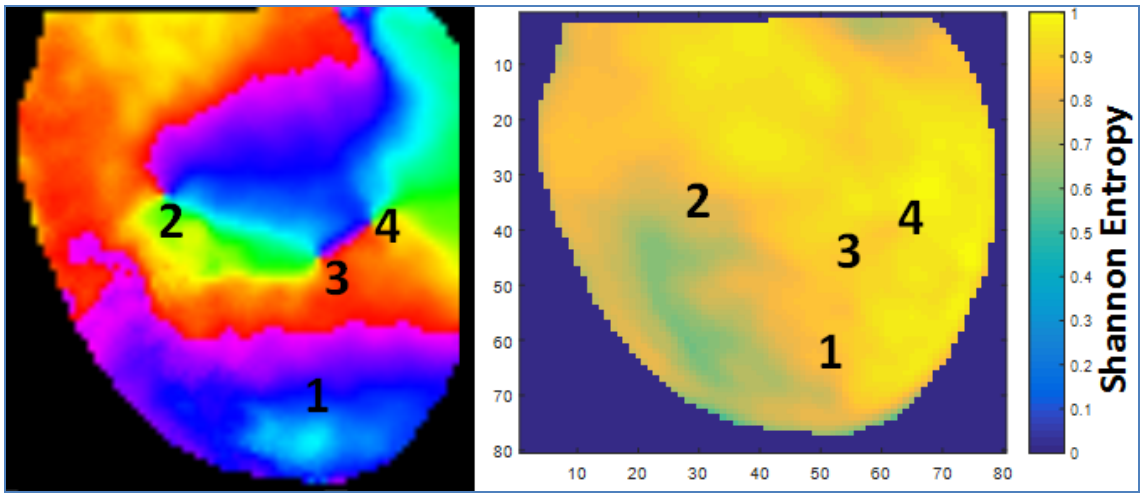

Figure 6-25: Results of SE approach with meandering rotor from optical mapping. *(Left) Snapshot of a phase movie showing several meandering rotors with reference pixel locations '1' at the rotor periphery, '2', '3' and '4' at rotor cores; (Right) Normalized 2D SE map.*

6.4 Testing of RE approach with rotor data

6.4.1 Performance of RE on single rotor identification

Figure 6-26 shows the snapshot of the single rotor and normalized 2D RE map. The results are similar to SE with lower RE values at the rotor core compared to the periphery. Results indicate that RE is also limited for short time series analysis in capturing the complexity of time series similar to SE for accurate rotor identification.

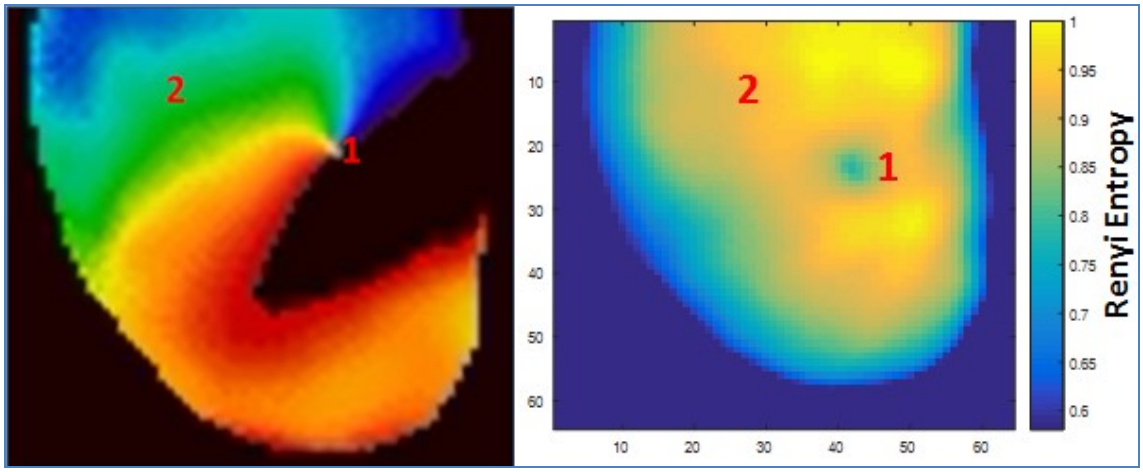

Figure 6-26: Results of RE approach with single rotor from optical mapping. *(Left) Snapshot of a phase movie showing single rotor with reference pixel locations'1' at rotor core and '2' at rotor periphery; (Right) Normalized 2D RE map showing low RE values at rotor core compared to periphery.*

6.4.2 Performance of RE on double rotor identification

Figure 6-27 shows the snapshot of the double rotor and normalized 2D RE map.

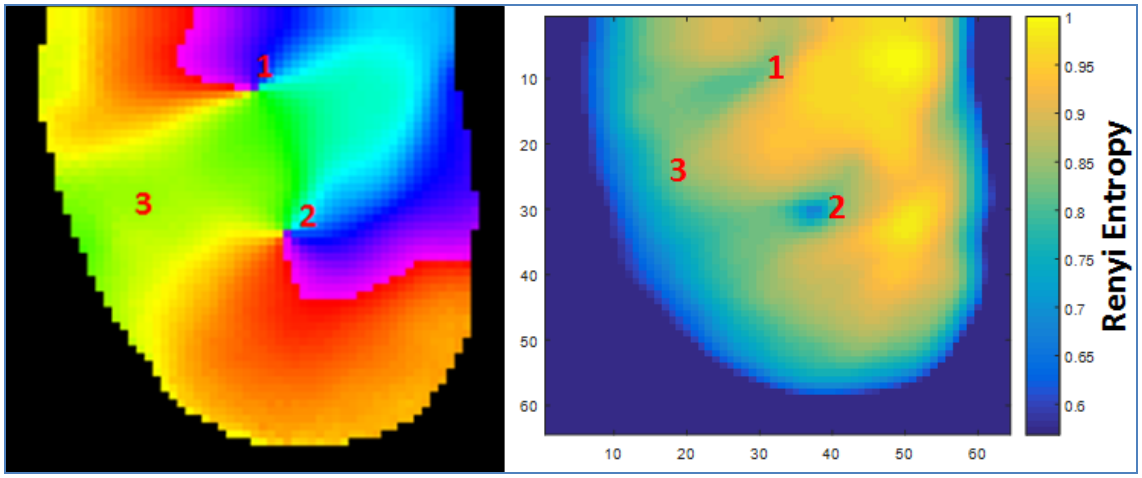

Figure 6-27: Results of RE approach with double rotor from optical mapping. *(Left) Snapshot of a phase movie showing double rotor with reference pixel locations'1',& '2' at rotor core and '3' at rotor periphery; (Right) Normalized 2D RE map showing low RE values at rotor core compared to periphery.*

The results are similar to SE with lower RE values at both the rotor core regions compared to the periphery which challenges accurate identification of rotor core with better contrast. Clinical use of RE therefore can be challenged with short time series analysis with RE.

6.4.3 Performance of RE approach on meandering rotor identification

6.4.3.1 Performance of RE on meandering rotor from numerical simulation dataset1

Figure 6-28 shows the snap shot of the voltage distribution movie of the numerically simulated meandering rotor from dataset1 and the corresponding normalized 2 D RE map. Lower RE values are seen in the central area similar to that observed in the 2D SE map where the rotor core traverses that location frequently as evident from the time domain plot and amplitude histogram of the time series in Figures 6-14 to 6-16. Similar to the optical mapping data, numerically simulated rotor data is also limited by short time series analysis in complexity quantification as evident from the results.

6.4.3.2 Performance of RE on meandering rotor from numerical simulation dataset2

Figure 6-29 shows the snap shot of the voltage distribution movie of the numerically simulated meandering rotor from dataset2 and the corresponding normalized 2 D RE map with higher regions of RE dispersed throughout the upper half of the map. Similar to the result obtained with SE, no conclusive results can be inferred on the trajectory of the rotor pivot as it traverses all spatial locations throughout the time frame that challenges RE approach.

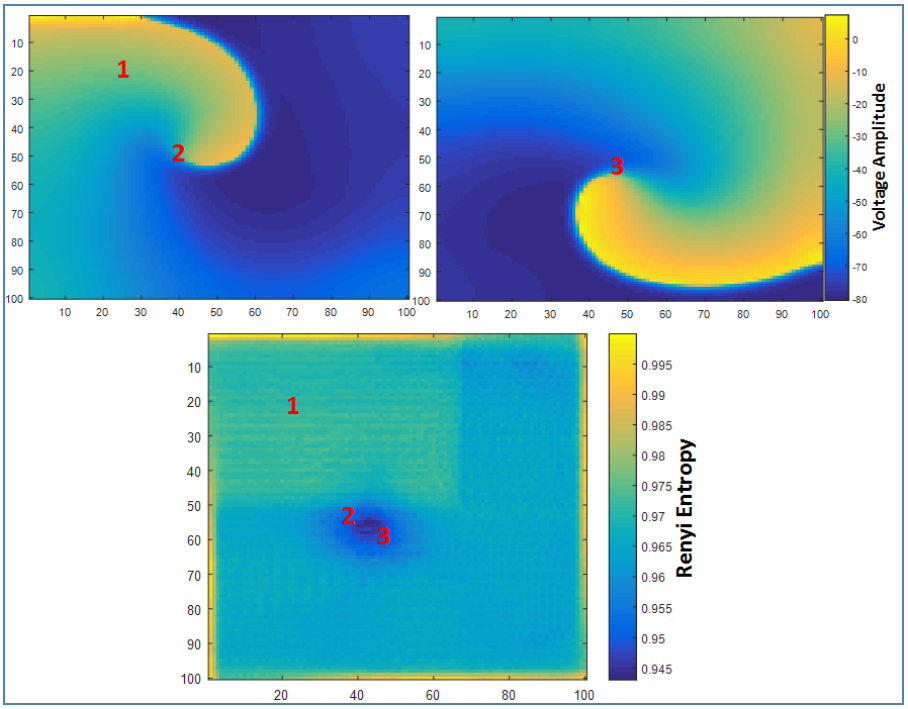

Figure 6-28: Results of RE approach with numerically simulated meandering rotor dataset1. *(Top-Left) Snapshot of voltage distributions showing single rotor with reference pixel locations'1' at rotor periphery and '2' at rotor core. (Top-Right) shows rotor core at pixel location '3'at the time of snapshot; (Bottom) shows normalized 2D RE map showing low RE values at rotor core compared to periphery.*

6.4.3.3 Performance of RE on meandering rotor from optical mapping

Figure 6-30 shows the snap shot of the phase movie of the meandering rotor and normalized 2D RE map showing higher RE region towards the right side of the ventricular region with lower RE regions to the left. The presence of several meandering rotors that varies spatially and temporally significantly challenges RE approach with the short time series available for complexity analysis similar to SE.

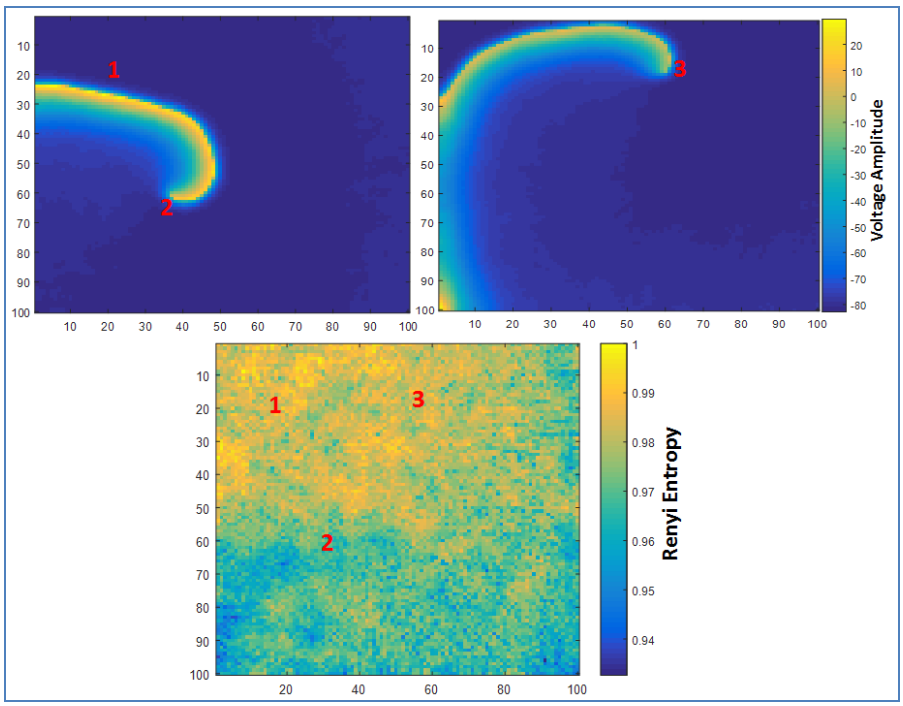

Figure 6-29: Results of RE approach with numerically simulated meandering rotor dataset2. *(Top-Left) 2D Voltage distributions showing single rotor with reference pixel locations'1' at rotor periphery and '2' at rotor core at the time of snapshot; (Top-Right) shows rotor core at pixel location '3'; (Bottom) shows normalized 2D RE map.*

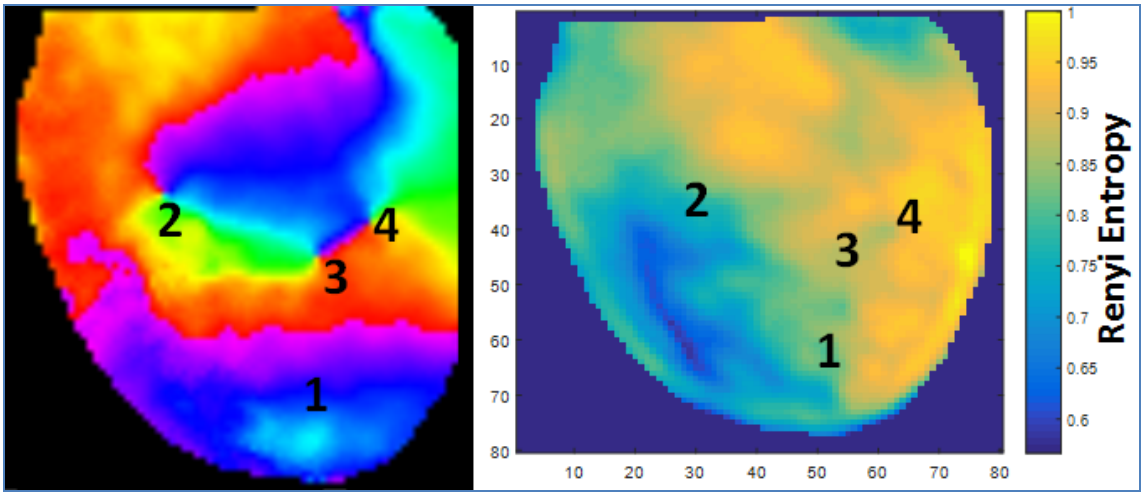

Figure 6-30: Results of RE approach with meandering rotor from optical mapping. *(Left) Snapshot of a phase movie showing several meandering rotors with reference pixel locations'1' at the rotor periphery, '2', '3' and '4' at rotor cores; (Right) Normalized 2D RE map.*

6.5 Testing of DF approach with rotor data

6.5.1 Performance of DF on single rotor identification

Figure 6-31 shows the snapshot of the single rotor and normalized 2D DF map. Figs. 6-2 & 6-3 bottom panel's shows the power spectrum with DF peak at 7.8 Hz at the rotor periphery as well as at the rotor core area.

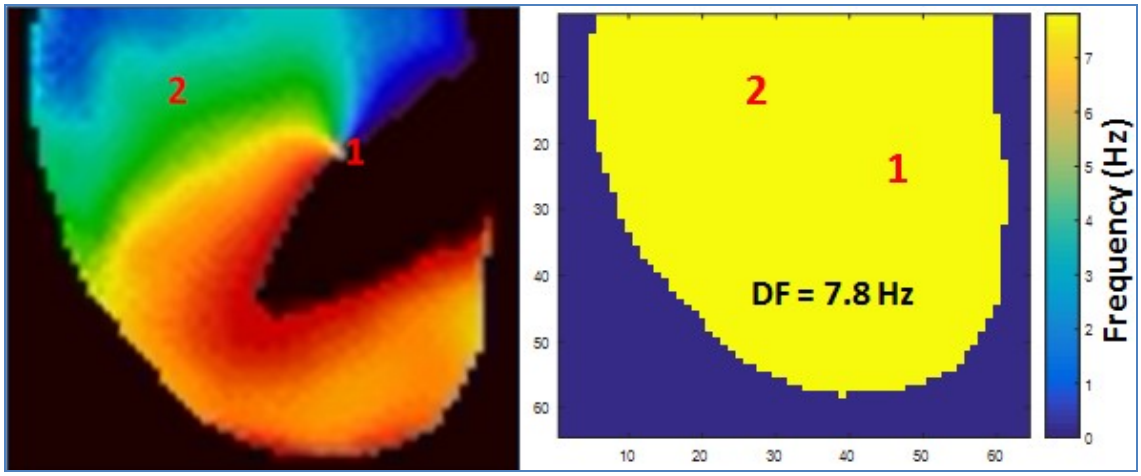

Figure 6-31: Results of DF approach with single rotor from optical mapping. *(Left) Snapshot of a phase movie showing single rotor with reference pixel locations'1' at rotor core and '2' at rotor periphery; (Right) 2D DF map showing uniform DF at 7.8 Hz.*

Uniform DF at 7.8 Hz is seen in Figure 6-31 throughout the rotor region thereby demonstrating the inability of DF approach to locate the rotor pivot point which is consistent with the literature. However, DF maps can localize AF active zones compared to normal regions.

6.5.2 Performance of DF on double rotor identification

Figure 6-32 shows the snapshot of the double rotor and normalized 2D DF map. Figures 6-5, 6-6 & 6-7 bottom panel's shows the power spectrum with DF peak at 8.1 Hz at the rotor periphery as well as at both the rotor core areas. Uniform DF at 8.1 Hz is seen

throughout the double rotor region thereby demonstrating the inability of DF approach to locate the rotor pivot point similar to single rotor results.

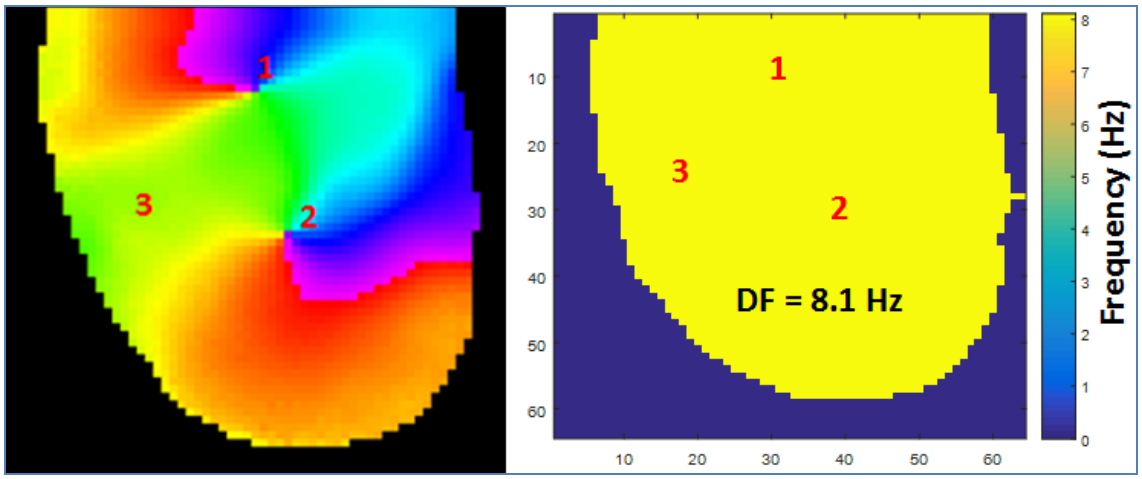

Figure 6-32: Results of DF approach with double rotor from optical mapping. *(Left) Snapshot of a phase movie showing double rotor with reference pixel locations '1',& '2' at rotor core and '3' at rotor periphery; (Right) 2D DF map showing uniform DF at 8.1 Hz.*

6.5.3 Performance of DF approach on meandering rotor identification

6.5.3.1 Performance of DF on meandering rotor from numerical simulation dataset1

Figure 6-33 shows the snap shot of the voltage distribution movie of the numerically simulated meandering rotor from dataset1 and the corresponding normalized 2 D DF map. Figures 6-14, 6-15 & 6-16 bottom panel's shows the power spectrum at the reference pixel locations identifying peaks at 10.1 Hz near the periphery and 16.8 Hz around the rotor core. 2D DF map shows high DF region in the lower central area (see the yellow color region) at 16.8 Hz at the locations where SE and RE showed lower values indicating the possible presence of rotor core in this region.

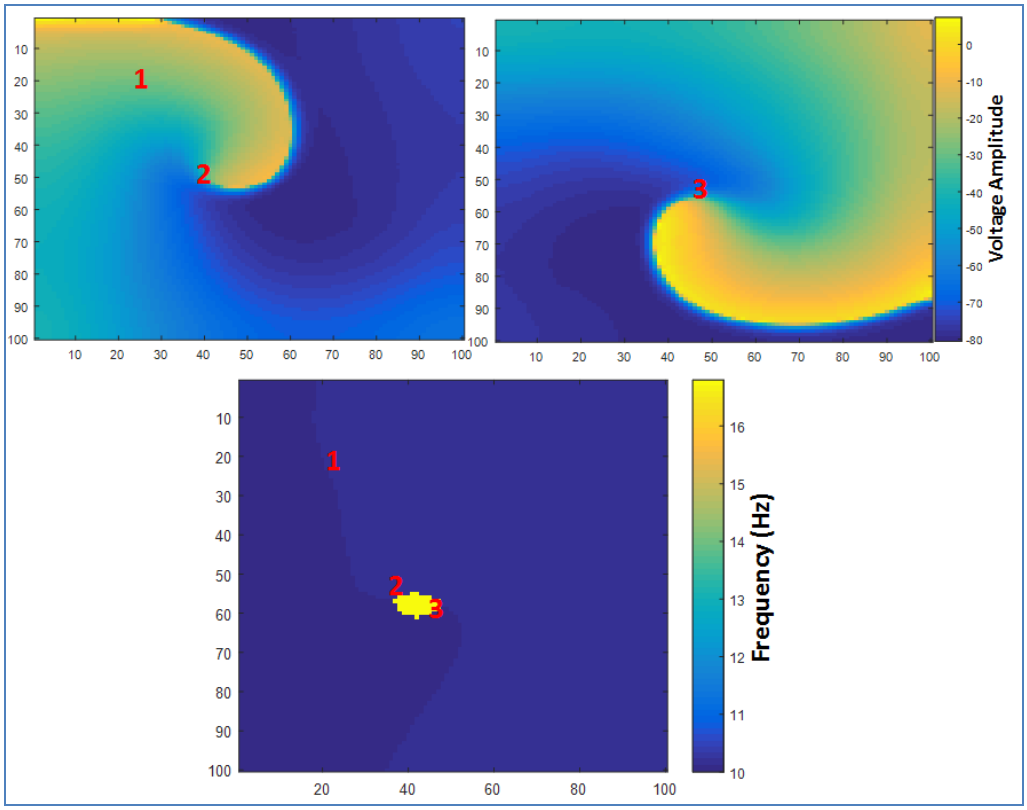

Figure 6-33: Results of DF approach with numerically simulated meandering rotor dataset1. *(Top-Left) Snapshot of voltage distributions showing single rotor with reference pixel locations'1' at rotor periphery and '2' at rotor core. (Top-Right) shows rotor core at pixel location '3'at the time of snapshot; (Bottom) shows 2D DF map with higher DF near pixel locations '2' and '3' compared to other spatial locations.*

6.5.3.2 Performance of DF on meandering rotor from numerical simulation dataset2

Figure 6-34 shows the snap shot of the voltage distribution movie of the numerically simulated meandering rotor from dataset2 and the corresponding normalized 2D DF map with higher regions of DF indicated by the yellow region at 16.8 Hz with other DF regions dispersed throughout the 2D map. Figures 6-18, 6-19 & 6-20 bottom panel's shows the power spectrum at the reference pixel locations identifying peaks at 10.1 Hz near the periphery and 16.8 Hz around the rotor core. Similar to the result obtained with

SE and RE, no conclusive results can be inferred on the trajectory of the rotor pivot for this dataset using DF analysis.

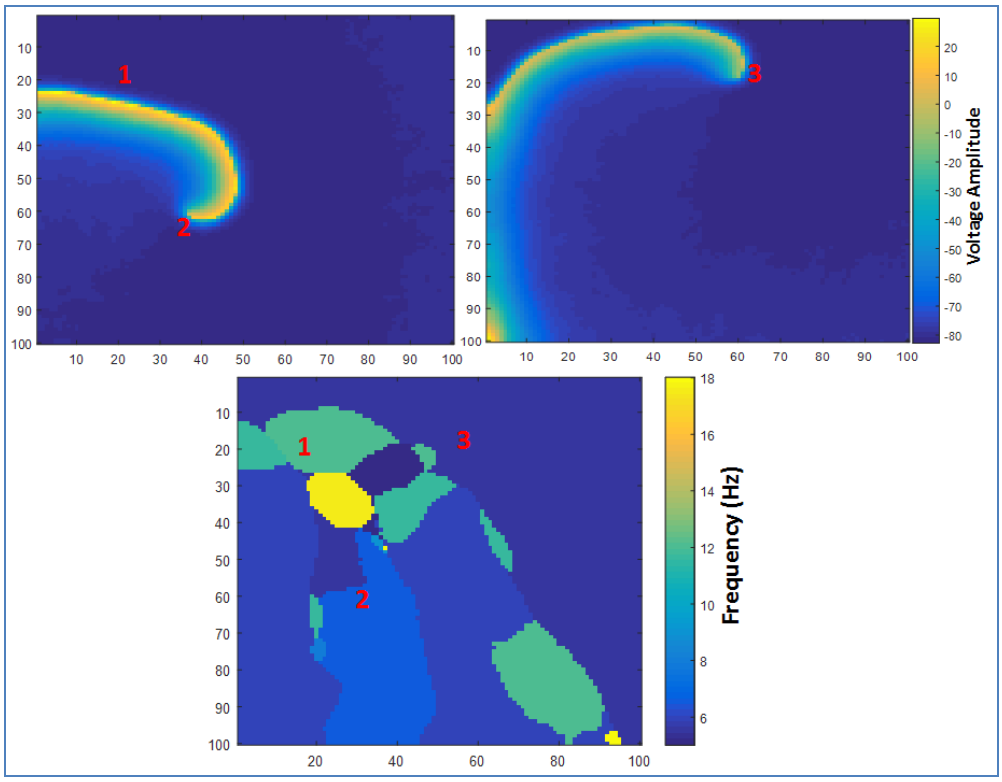

Figure 6-34: Results of DF approach with numerically simulated meandering rotor dataset2. *(Top-Left) 2D Voltage distributions showing single rotor with reference pixel locations'1' at rotor periphery and '2' at rotor core at the time of snapshot; (Top-Right) shows rotor core at pixel location '3'at the time of snapshot; (Bottom) shows 2D DF map with varying DF values across different spatial locations.*

6.5.3.3 Performance of DF on meandering rotor from optical mapping

Figure 6-35 shows the snap shot of the phase movie of the meandering rotor and normalized 2D DF map showing mostly uniform DF at 25 Hz. Figs.6-9 to 6-12 bottom panel's shows the power spectrum at the reference pixel locations identifying peaks at 25 Hz near the periphery and the rotor core regions. Mostly uniform DF map for this dataset renders this approach inadequate to track the trajectories of the rotor pivot points.

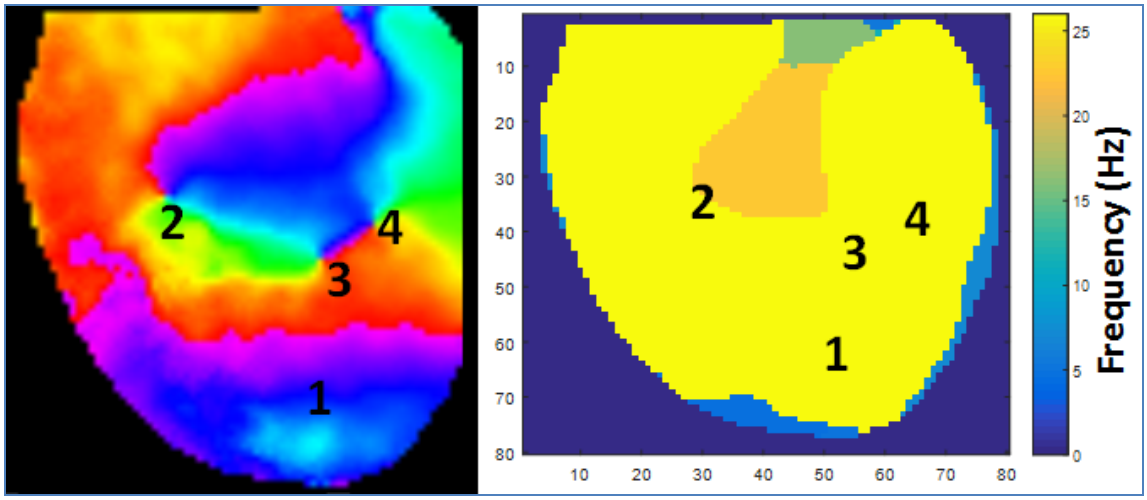

Figure 6-35: Results of DF approach with meandering rotor from optical mapping. *(Left) Snapshot of a phase movie showing several meandering rotors with reference pixel locations '1' at the rotor periphery, '2', '3' and '4' at rotor cores; (Right) shows 2D DF map with varying DF values across different spatial locations.*

6.6 Testing and validation of MSE approach with rotor data

6.6.1 Performance of MSE on single rotor identification

Fig. 6-36 shows the snapshot of the single rotor (top-left) and 2D MSE maps for scale factors τ = 1, 2 and 3 are shown in top-right, bottom-left and bottom-right panels. Note the MSE approach can accurately identify the location of the pivot point of the rotor for each τ. As seen from 2D MSE maps, the pivot point has higher MSE values than the periphery thereby enabling its precise location and the higher the value of 'τ' results in better contrast between the rotor core and periphery compared with 2D SE map for the single rotor in Figure 6-21.

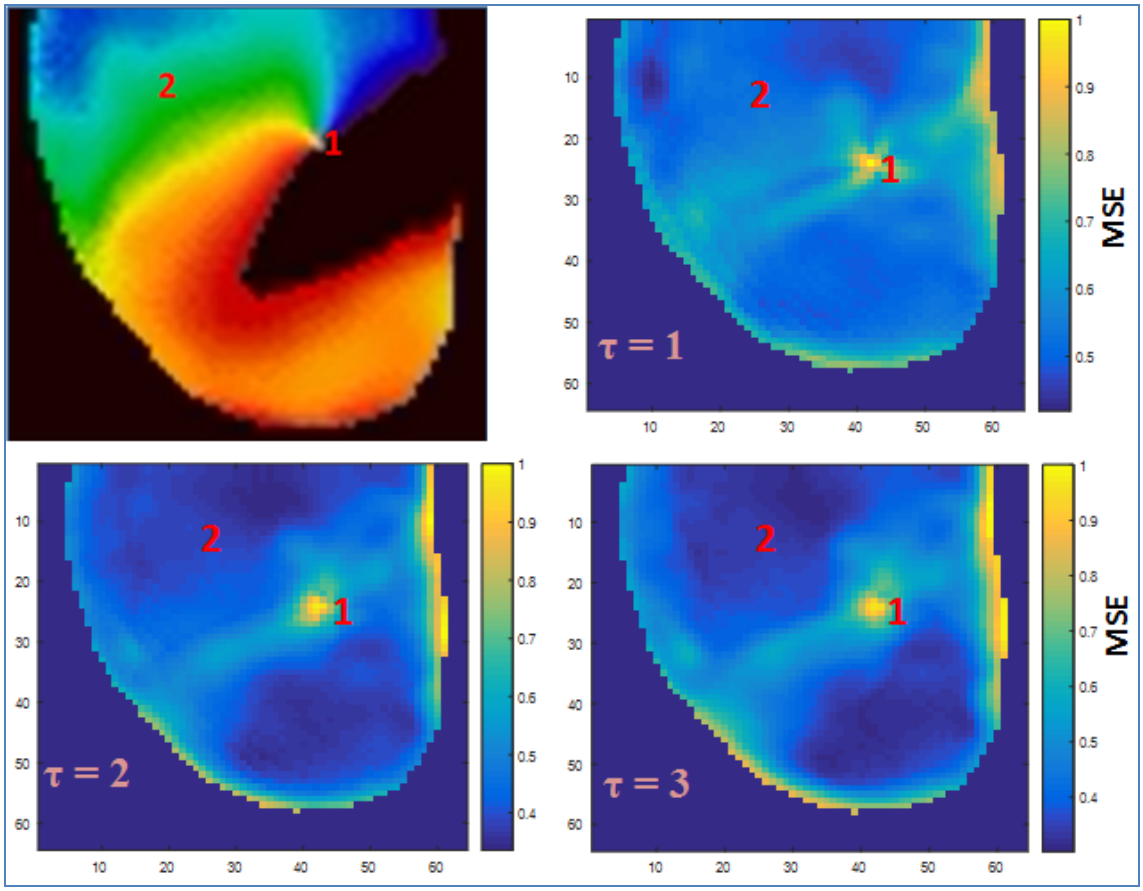

Figure 6-36: Results of MSE approach with single rotor from optical mapping. *Top row (Left) shows snapshot of a phase movie showing single rotor with reference pixel locations '1' at rotor core and '2' at rotor periphery; (Right) shows normalized 2D MSE map with τ = 1; Bottom row (Right) shows 2D MSE with τ = 2 and (Left) shows 2D MSE with τ = 3, all showing correct identification of rotor core.*

6.6.2 Performance of MSE on double rotor identification

Figure 6-37 shows a snapshot of the phase movie for the double rotor and 2D MSE maps in similar configuration as Figure 6-36.

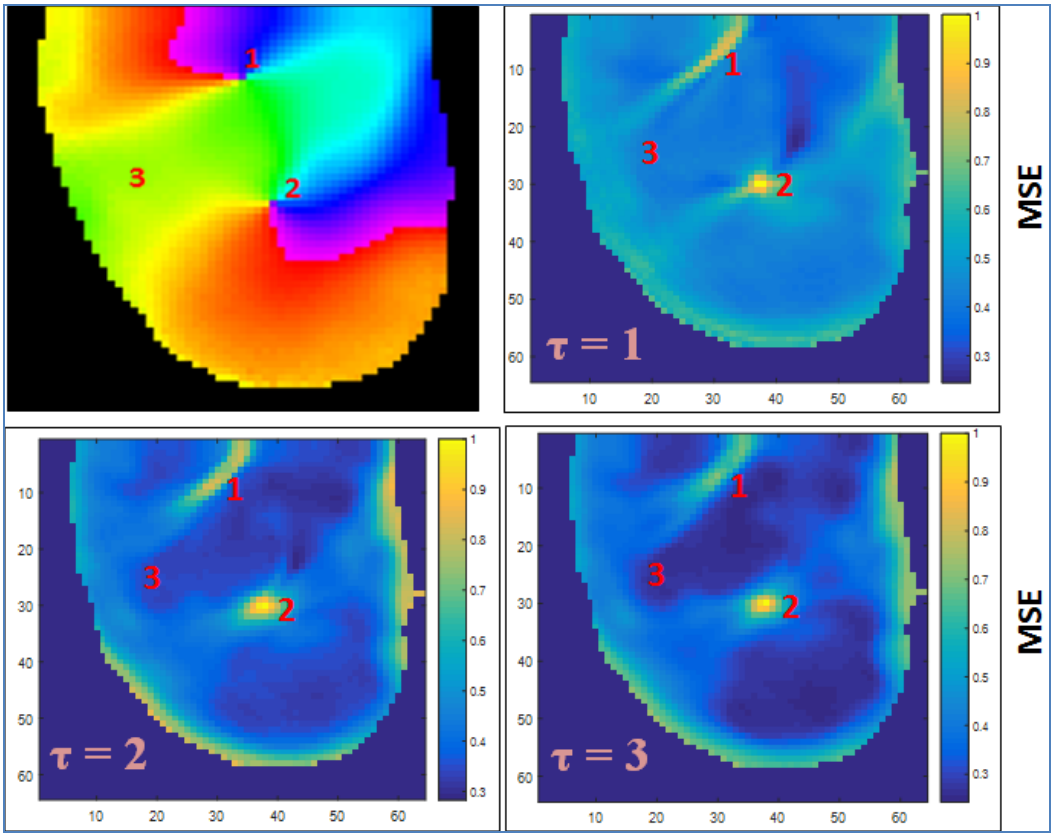

Figure 6-37: Results of MSE approach with double rotor from optical mapping. *Top row (Left) shows snapshot of a phase movie showing double rotor with reference pixel locations'1' & '2' at rotor core and '3' at rotor periphery; (Right) shows normalized 2D MSE map with τ = 1; Bottom row (Right) shows 2D MSE with τ = 2 and (Left) shows 2D MSE with τ = 3, all showing correct identification of rotor core.*

Similar to Fig. 6-36, it can be seen that the MSE approach can correctly identify the location of the pivot point of the rotor for each τ, and that the performance of the MSE approach is much better than SE observed in Fig. 6-22 for the double rotor.

6.6.3 Performance of MSE approach on meandering rotor identification

6.6.3.1 Performance of MSE on meandering rotor from numerical simulation dataset1

Figure 6-38 shows the snap shot of the voltage distribution movie of the numerically simulated meandering rotor from dataset1 and normalized 2D MSE map with τ =3.

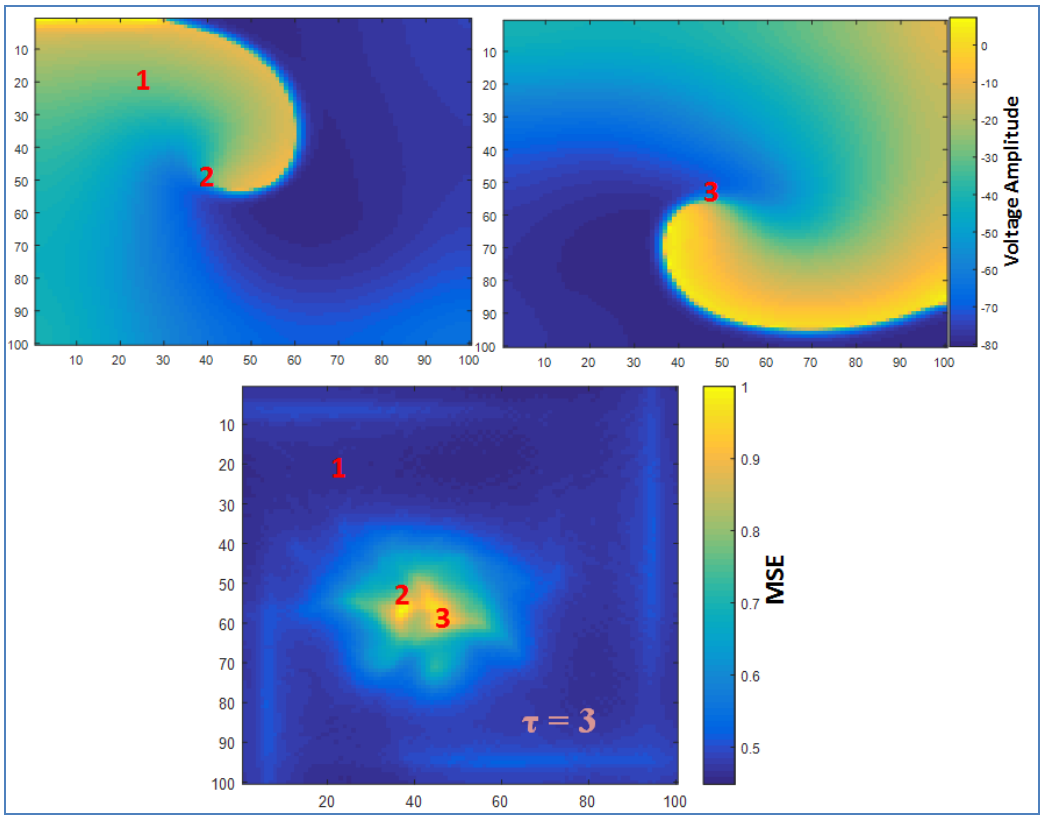

Figure 6-38: Results of MSE approach with numerically simulated meandering rotor dataset1. *(Top-Left) Snapshot of voltage distributions showing single rotor with reference pixel locations'1' at rotor periphery and '2' at rotor core. (Top-Right) shows rotor core at pixel location '3'at the time of snapshot; (Bottom) shows normalized 2D MSE map (τ = 3) showing correct identification of rotor core.*

Higher MSE values are seen in the central area identified by low SE and RE values is observed in the 2D MSE map where the rotor core traverses that location frequently implying correct and accurate tracking of the rotor core for this dataset at the reference pixel locations '2' and '3' compared to periphery at '1'. This implies superior performance of MSE compared to SE, RE and DF approaches.

6.6.3.2 Performance of MSE on meandering rotor from numerical simulation dataset2

Figure 6-39 shows the snap shot of the voltage distribution movie of the numerically simulated meandering rotor from dataset2 and normalized 2D MSE map with τ =3.

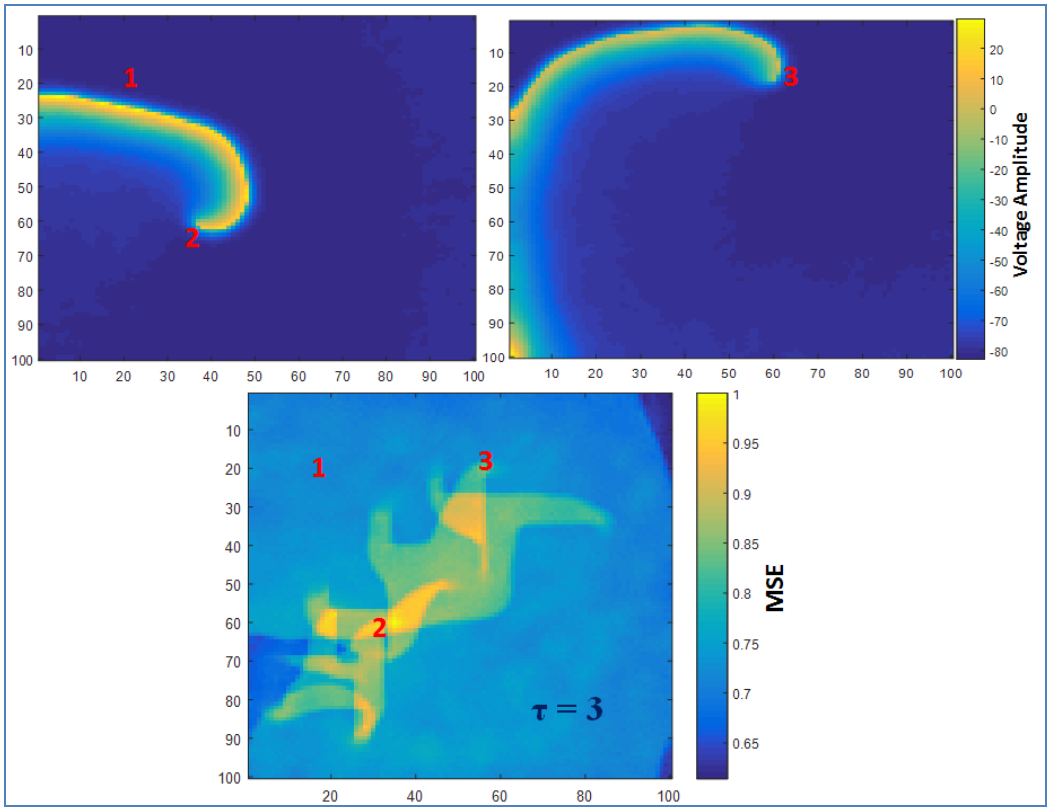

Figure 6-39: Results of MSE approach with numerically simulated meandering rotor dataset2. *(Top-Left) 2D Voltage distributions showing single rotor with reference pixel locations'1' at rotor periphery and '2' at rotor core at the time of snapshot; (Top-Right) shows rotor core at pixel location '3'at the time of snapshot.; (Bottom) shows normalized 2D MSE map (τ = 3).*

Higher MSE values are seen along a specific trajectory spatially in the 2D MSE map encompassing pixel locations '2' and '3' at rotor core which correlates with the trajectory of the rotor pivot point by visual inspection with lower MSE value at pixel location '1' at

periphery. This result is significant given the complexity of the rotor trajectory which SE, RE and DF was not able to track demonstrating the robustness of the MSE approach.

6.6.3.3 Performance of MSE on meandering rotor from optical mapping

Figure 6-40 shows the snap shot of the phase movie of the meandering rotor and normalized 2D MSE map with τ =3.

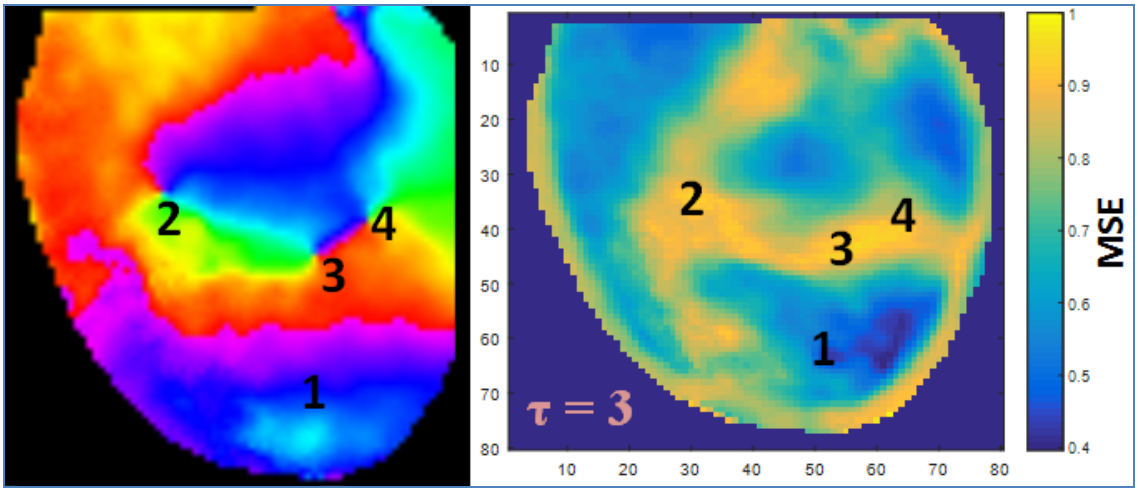

Figure 6-40: Results of MSE approach with meandering rotor from optical mapping. *(Left) Snapshot of a phase movie showing several meandering rotors with reference pixel locations '1' at the rotor periphery, '2', '3' and '4' at rotor cores; (Right) shows normalized 2D MSE map (τ = 3).*

2D MSE map shows higher MSE along a specific trajectory along the center and middle region which correlates with the trajectories observed from several meandering rotors. Specifically higher MSE are observed at pixel locations '2', '3' and '4' corresponding to the rotor core area with lower MSE at the periphery at pixel location '1'. MSE demonstrated robustness even with the presence of several meandering rotors that varies spatially and temporally which significantly challenges SE, RE and DF approach with the short time series data.

6.7 Testing and validation of RPDE approach with rotor data

6.7.1 Performance of RPDE on single rotor identification

Fig. 6-41 shows the snapshot of the single rotor and normalized 2D RPDE map. As seen from the Figure, RPDE accurately identified the rotor core area with better contrast than the periphery with higher RPDE at the core better in performance compared to SE, RE and DF. However, MSE showed better contrast than RPDE. This result validates the presence of rotor core location through phase space recurrence analysis with RPDE.

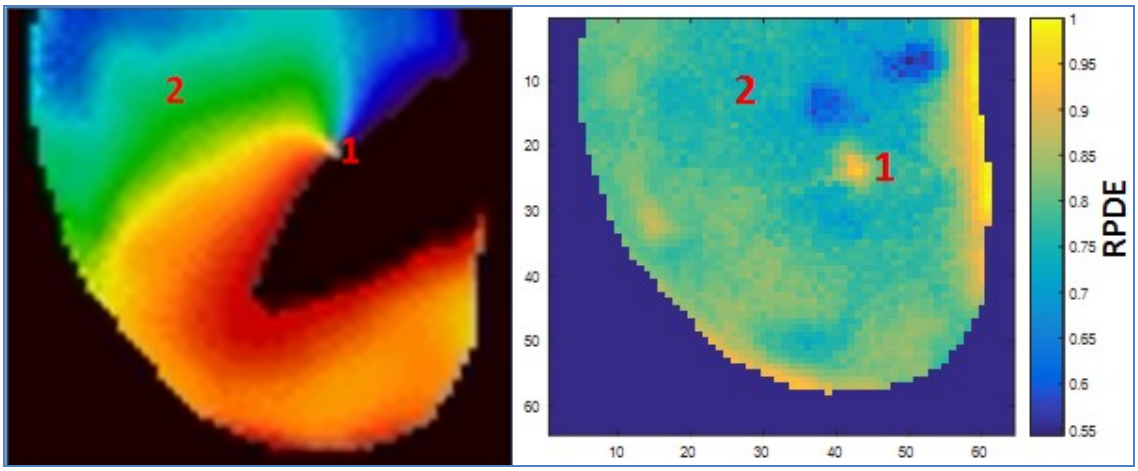

Figure 6-41: Results of RPDE approach with single rotor from optical mapping. *(Left) Snapshot of a phase movie showing single rotor with reference pixel locations'1' at rotor core and '2' at rotor periphery; (Right) Normalized 2D RPDE map showing correct identification of the rotor core.*

6.7.2 Performance of RPDE on double rotor identification

Fig. 6-42 shows the snapshot of the double rotor and normalized 2D RPDE map. As seen from the Figure, RPDE accurately identified both the rotor core regions with better contrast than the periphery compared to SE, RE and DF; MSE had better contrast.

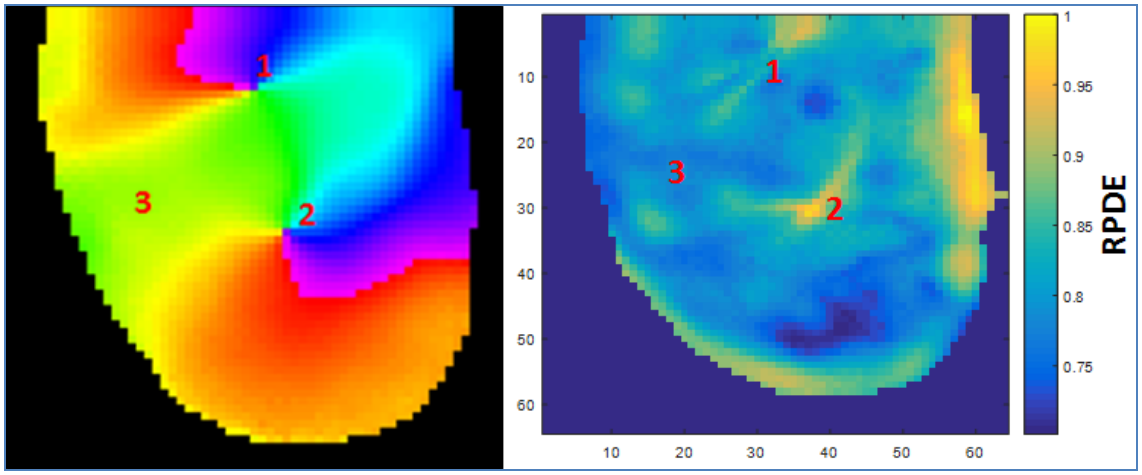

Figure 6-42: Results of RPDE approach with double rotor from optical mapping. *(Left) Snapshot of a phase movie showing double rotor with reference pixel locations'1',& '2' at rotor core and '3' at rotor periphery; (Right) Normalized 2D RPDE map showing correct identification of the rotor core.*

6.7.3 Performance of RPDE approach on meandering rotor identification

6.7.3.1 Performance of RPDE on meandering rotor from numerical simulation dataset1

Figure 6-43 shows the snap shot of the voltage distribution movie of the numerically simulated meandering rotor from dataset1 and normalized 2D RPDE map. Higher RPDE values are seen in the central area similar to the 2D MSE map implying correct and accurate tracking of the rotor core for this dataset at the reference pixel locations '2' and '3' compared to periphery at '1'. This implies superior performance of RPDE compared to SE, RE and DF approaches and comparable performance with MSE.

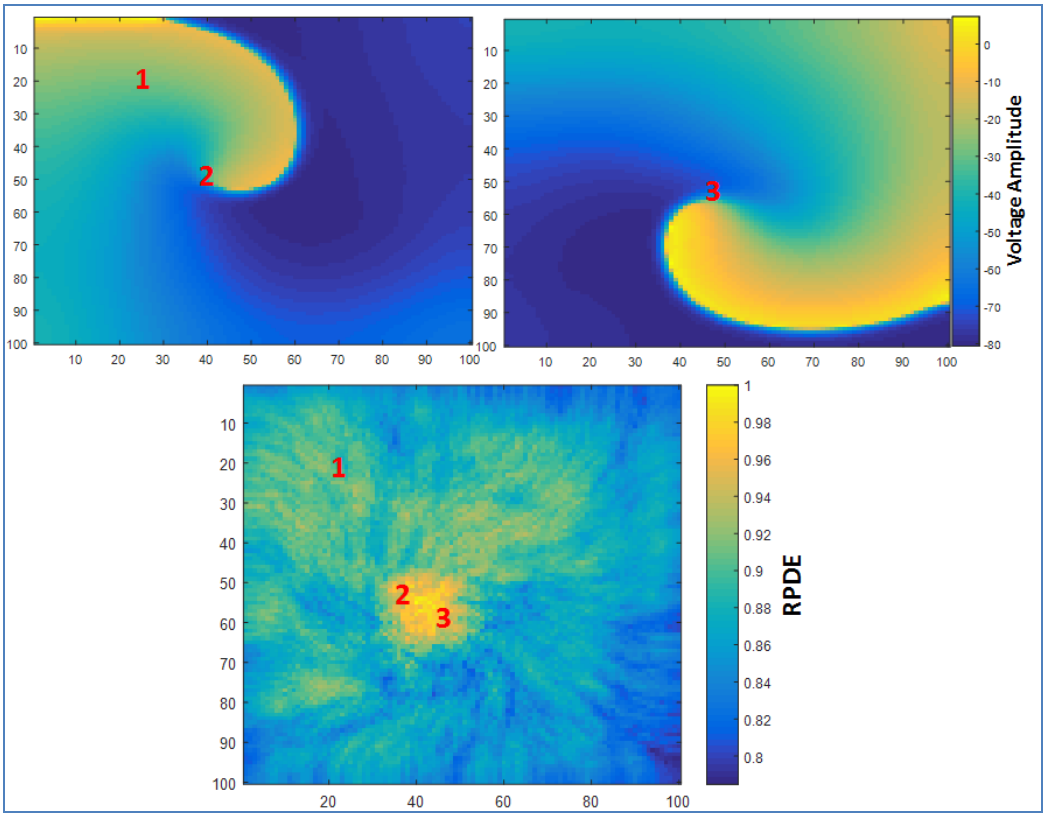

Figure 6-43: Results of RPDE approach with numerically simulated meandering rotor dataset1. *(Top-Left) Snapshot of voltage distributions showing single rotor with reference pixel locations'1' at rotor periphery and '2' at rotor core. (Top-Right) shows rotor core at pixel location '3'at the time of snapshot; (Bottom) shows normalized 2D RPDE map showing correct identification of the rotor core.*

6.7.3.2 Performance of RPDE on meandering rotor from numerical simulation dataset2

Figure 6-44 shows the snap shot of the voltage distribution movie of the numerically simulated meandering rotor from dataset1 and normalized 2D RPDE map. The 2D RPDE map shows high RPDE values at the lower left corner implying high recurrence of the rotor pivot point in this area. Visual inspection of the voltage movie reveals frequent traversing of the rotor core at the lower left corner resulting in high RPDE value with

phase space recurrence analysis encompassing pixel locations '2' and '3' at rotor core with lower RPDE value at pixel location '1' at periphery. The results still demonstrate better performance than SE, RE and DF but inferior to MSE.

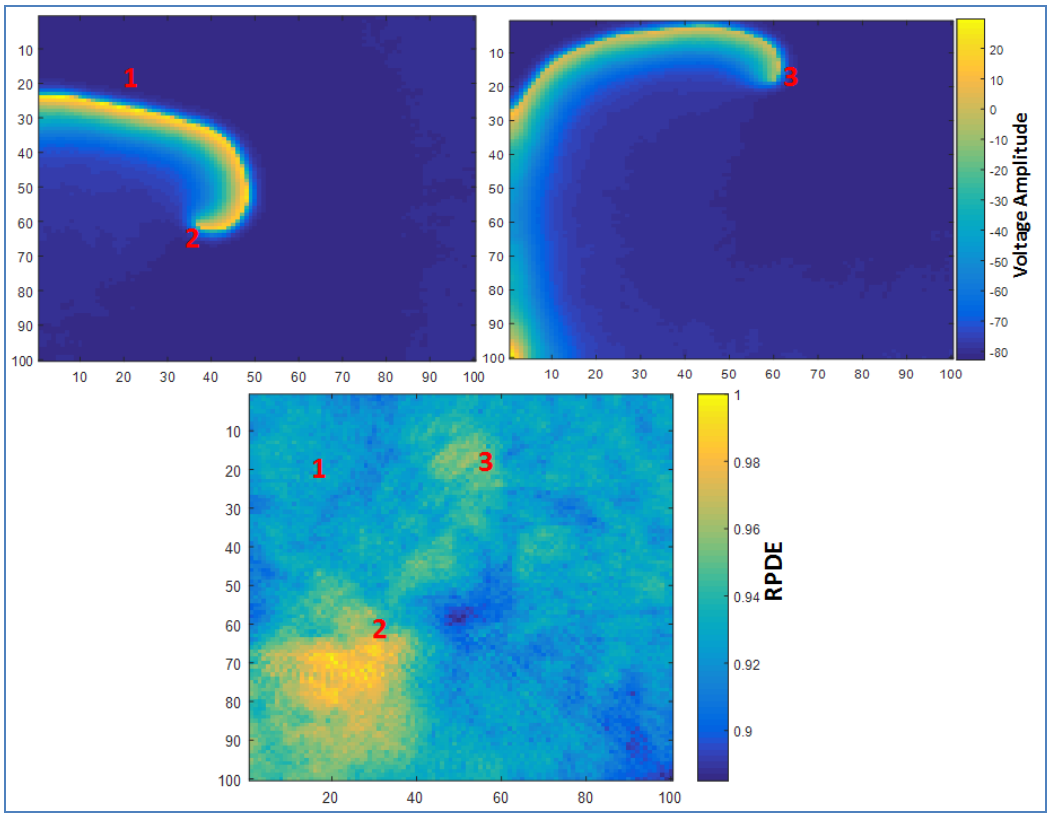

Figure 6-44: Results of RPDE approach with numerically simulated meandering rotor dataset2. *(Top-Left) 2D Voltage distributions showing single rotor with reference pixel locations'1' at rotor periphery and '2' at rotor core at the time of snapshot; (Top-Right) shows rotor core at pixel location '3; (Bottom) shows normalized 2D RPDE map.*

6.7.3.3 Performance of RPDE on meandering rotor from optical mapping

Figure 6-45 shows the snap shot of the phase movie of the meandering rotor and normalized 2D RPDE map.

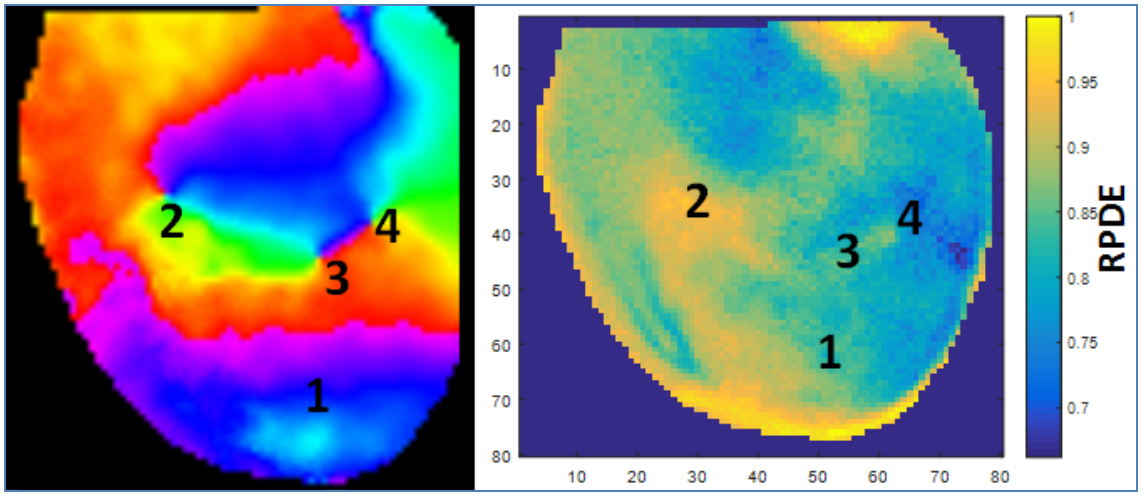

Figure 6-45: Results of RPDE approach with meandering rotor from optical mapping. *(Left) Snapshot of a phase movie showing several meandering rotors with reference pixel locations '1' at the rotor periphery, '2', '3' and '4' at rotor cores; (Right) shows normalized 2D RPDE map.*

2D RPDE map shows higher RPDE regions along a specific trajectory similar to the 2D MSE map shown in Figure 6-40 which correlates with the trajectories observed from several meandering rotors. Specifically higher RPDE are observed at pixel locations '2', '3' and '4' corresponding to the rotor core area with lower RPDE at the periphery at pixel location '1'. The results demonstrate superior performance of RPDE compared to SE, RE and DF and comparable performance to MSE.

6.8 Testing and validation of kurtosis approach with rotor data

6.8.1 Performance of kurtosis on single rotor identification

Fig. 6-46 shows the snapshot of the single rotor and normalized 2D kurtosis map. As seen from the Figure, kurtosis accurately identified the rotor core area with better contrast than the periphery with higher kurtosis at the core better in performance compared to SE, RE and DF. The results demonstrate the efficacy of kurtosis approach to robustly identify the core of the rotor and are comparable with MSE and RPDE for rotor identification.

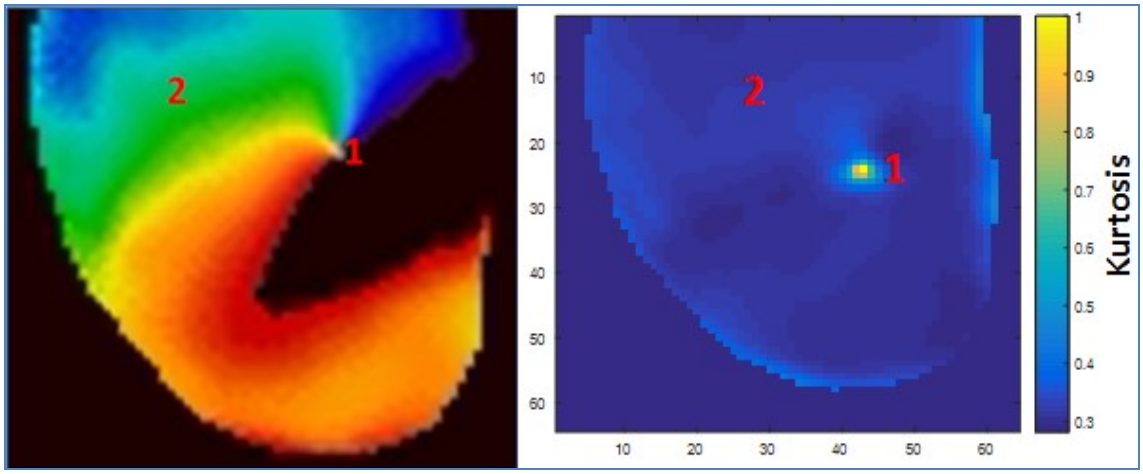

Figure 6-46: Results of kurtosis approach with single rotor from optical mapping. *(Left) Snapshot of a phase movie showing single rotor with reference pixel locations'1' at rotor core and '2' at rotor periphery; (Right) Normalized 2D kurtosis map showing correct identification of the rotor core.*

6.8.2 Performance of kurtosis on double rotor identification

Fig. 6-47 shows the snapshot of the double rotor and normalized 2D RPDE map. As seen from the Figure, kurtosis accurately identified both the rotor core regions with better contrast than the periphery compared to SE, RE and DF. Kurtosis shows better contrast for the rotor at pixel '1' compared to RPDE (Fig 6-42), where RPDE shows better contrast for the rotor core at pixel '2'. MSE (Fig 6-37) shows relatively better contrast in identifying both the rotor cores with better contrast than the periphery region.

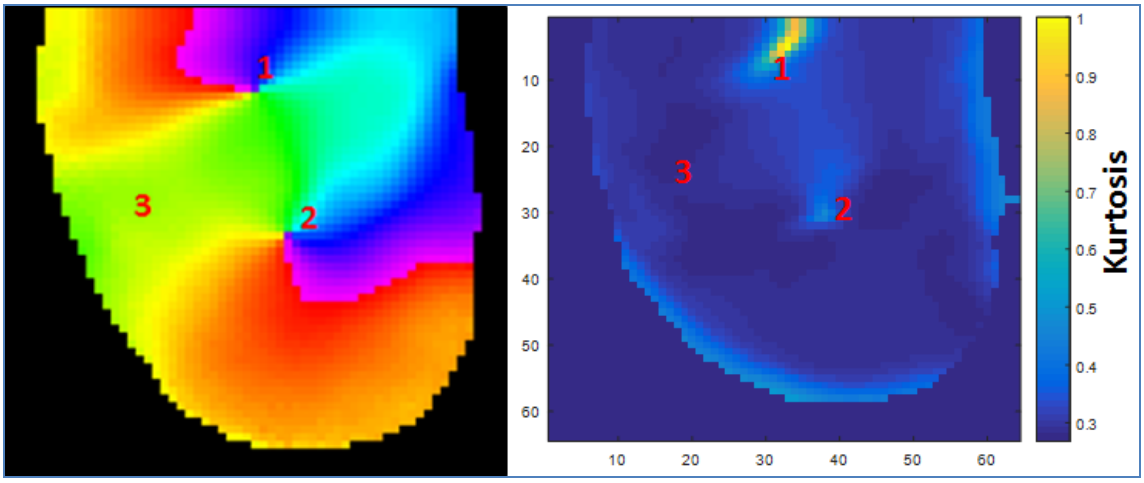

Figure 6-47: Results of kurtosis approach with double rotor from optical mapping. *(Left) Snapshot of a phase movie showing double rotor with reference pixel locations'1',& '2' at rotor core and '3' at rotor periphery; (Right) Normalized 2D kurtosis map showing correct identification of the rotor core.*

6.8.3 Performance of kurtosis approach on meandering rotor identification

6.8.3.1 Performance of kurtosis on meandering rotor from numerical simulation dataset1

Figure 6-48 shows the snap shot of the voltage distribution movie of the numerically simulated meandering rotor from dataset1 and normalized 2D kurtosis map. Higher kurtosis values are seen in the central area similar to the 2D MSE (Fig 6-38) and RPDE map (Fig 6-43) implying correct and accurate tracking of the rotor core for this dataset at the reference pixel locations '2' and '3' compared to periphery at '1'. This implies superior performance of kurtosis compared to SE, RE and DF approaches and comparable performance with RPDE and MSE.

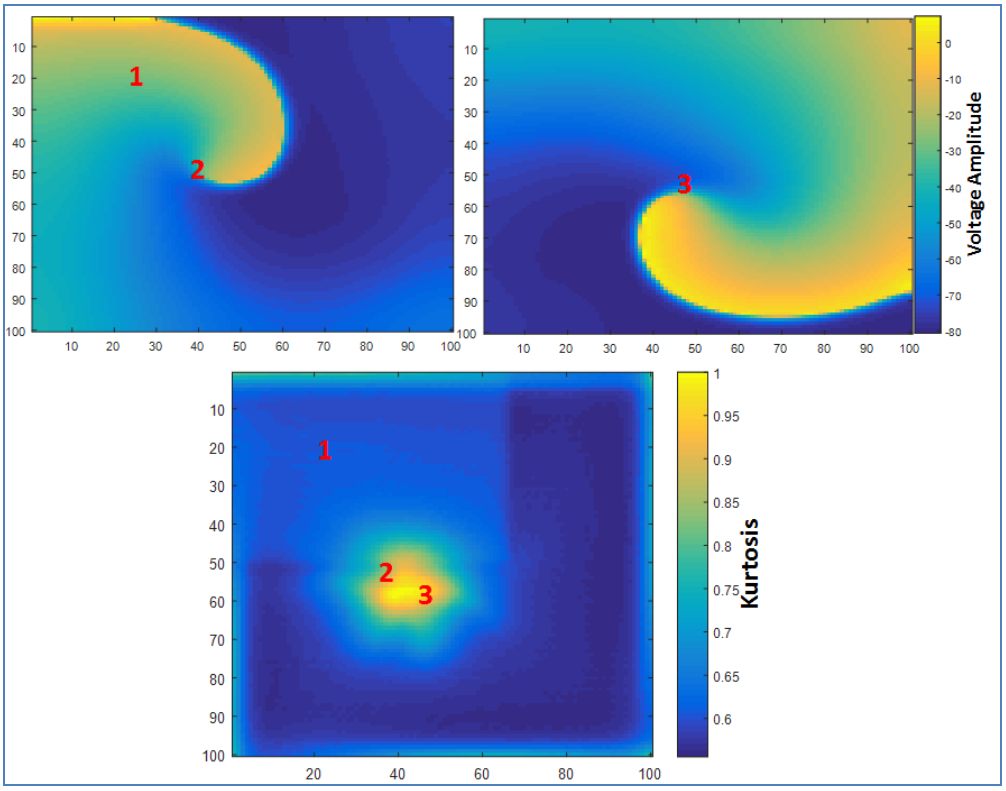

Figure 6-48: Results of kurtosis approach with numerically simulated meandering rotor dataset1. *(Top-Left) Snapshot of voltage distributions showing single rotor with reference pixel locations'1' at rotor periphery and '2' at rotor core. (Top-Right) shows rotor core at pixel location '3'at the time of snapshot; (Bottom) shows normalized 2D kurtosis map showing correct identification of the rotor core.*

6.8.3.2 Performance of kurtosis on meandering rotor from numerical simulation dataset2

Figure 6-49 shows the snap shot of the voltage distribution movie of the numerically simulated meandering rotor from dataset2 and normalized 2D kurtosis map.

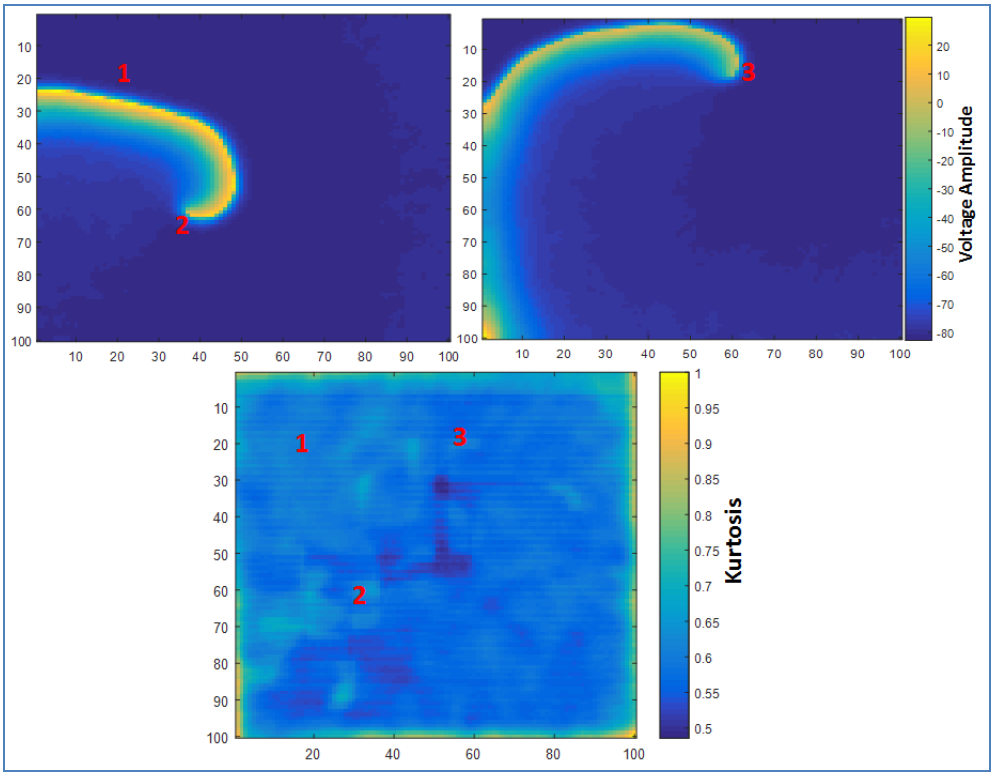

Figure 6-49: Results of kurtosis approach with numerically simulated meandering rotor dataset2. *(Top-Left) 2D Voltage distributions showing single rotor with reference pixel locations'1' at rotor periphery and '2' at rotor core at the time of snapshot; (Top-Right) shows rotor core at pixel location '3'at the time of snapshot.; (Bottom) shows normalized 2D kurtosis map.*

The 2D kurtosis map shows high kurtosis values at similar locations shown in the 2D RPDE map (Fig 6-44) encompassing pixel locations '2' and '3' at rotor core with lower kurtosis value at pixel location '1' at periphery. The results still demonstrate better performance than SE, RE and DF but inferior to MSE (Fig. 6-39) and comparable with RPDE approach.

6.8.3.3 Performance of kurtosis on meandering rotor from optical mapping

Figure 6-50 shows the snap shot of the phase movie of the meandering rotor and normalized 2D kurtosis map.

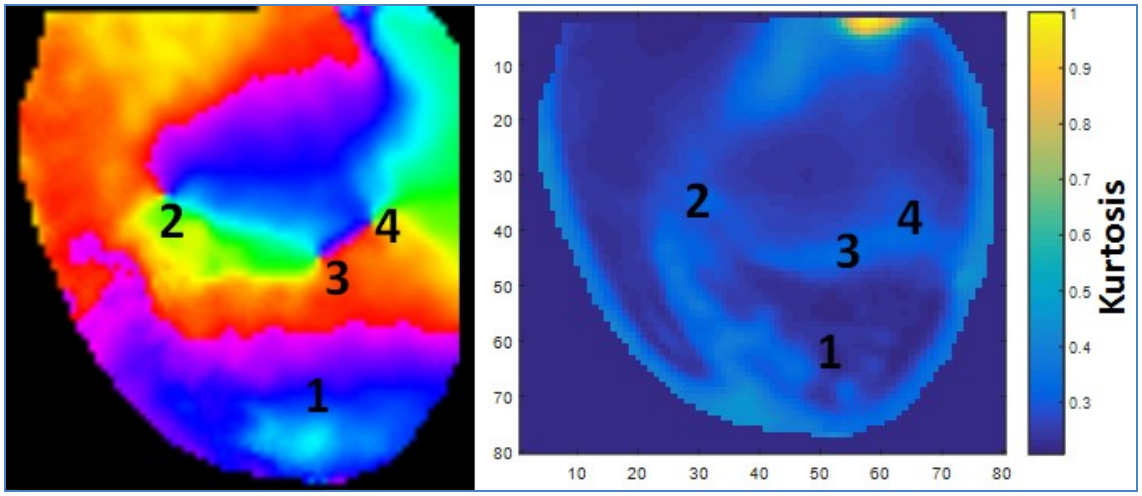

Figure 6-50: Results of kurtosis approach with meandering rotor from optical mapping. *(Left) Snapshot of a phase movie showing several meandering rotors with reference pixel locations'1' at the rotor periphery, '2', '3' and '4' at rotor cores; (Right) Normalized 2D kurtosis map*

2D kurtosis map shows higher kurtosis regions along a specific trajectory similar to the 2D MSE map (Fig. 6-40) and 2D RPDE (Fig. 6-45) map which correlates with the trajectories observed from several meandering rotors. Specifically higher kurtosis are observed at pixel locations '2', '3' and '4' corresponding to the rotor core area with lower RPDE at the periphery at pixel location '1'. The results demonstrate superior performance of kurtosis approach compared to SE, RE and DF and comparable performances to MSE and RPDE.

6.9 Testing and validation of EMD approach with rotor data

6.9.1 Performance of EMD on single rotor identification

Fig. 6-51 shows the snapshot of the single rotor and normalized 2D IMF complexity map. As seen from the Figure, IMF complexity accurately identified the rotor core area with better contrast than the periphery with higher IMF complexity at the core better in performance compared to SE, RE and DF. By comparing the 2D maps with MSE (Fig. 6-

36), RPDE (Fig. 6-41), and Kurtosis (Fig. 6-46), it can be seen that these approaches identified a narrow region of the rotor core with higher corresponding values in agreement with the phase singularity measurements for the exact location of the pivot point. Interestingly, IMF complexity measures broader region at the rotor core, implying its ability to measure the intrinsic changes with the electrical signal around the neighborhood the rotor core which are also chaotic, which other methods cannot capture. This is a major finding in the sense that, the lesions required for ablation to terminate AF or other arrhythmias should cover neighboring chaotic sites which may also cause and maintain arrhythmia.

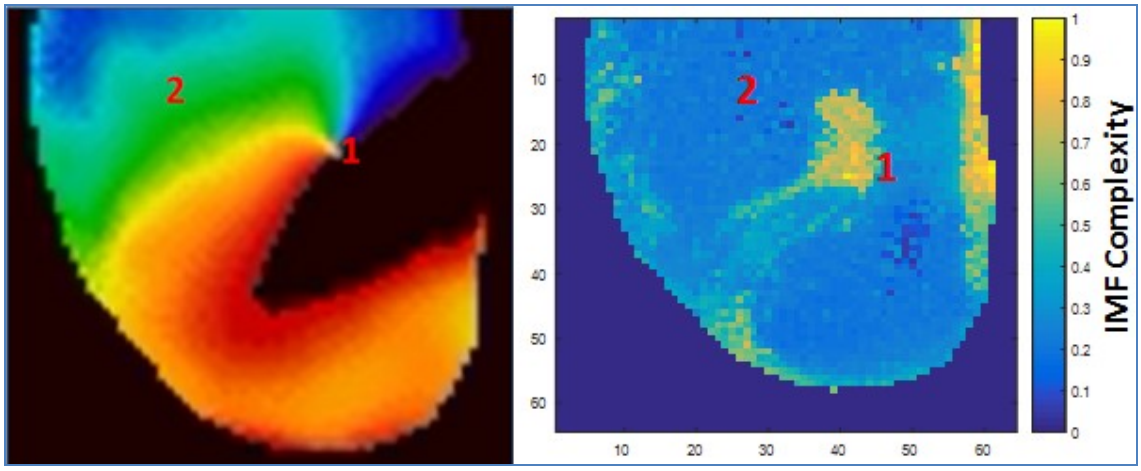

Figure 6-51: Results of EMD approach with single rotor from optical mapping. *(Left) Snapshot of a phase movie showing single rotor with reference pixel locations'1' at rotor core and '2' at rotor periphery; (Right) Normalized 2D IMF map showing correct identification of the rotor core.*

Figure 6-52 and 6-53 shows the decomposition of the optical electrogram at pixel locations '2' at the rotor periphery and '1' at the rotor core respectively. As seen from Fig. 6-52, 7 IMF's were required to completely describe and reconstruct the waveform at the periphery.

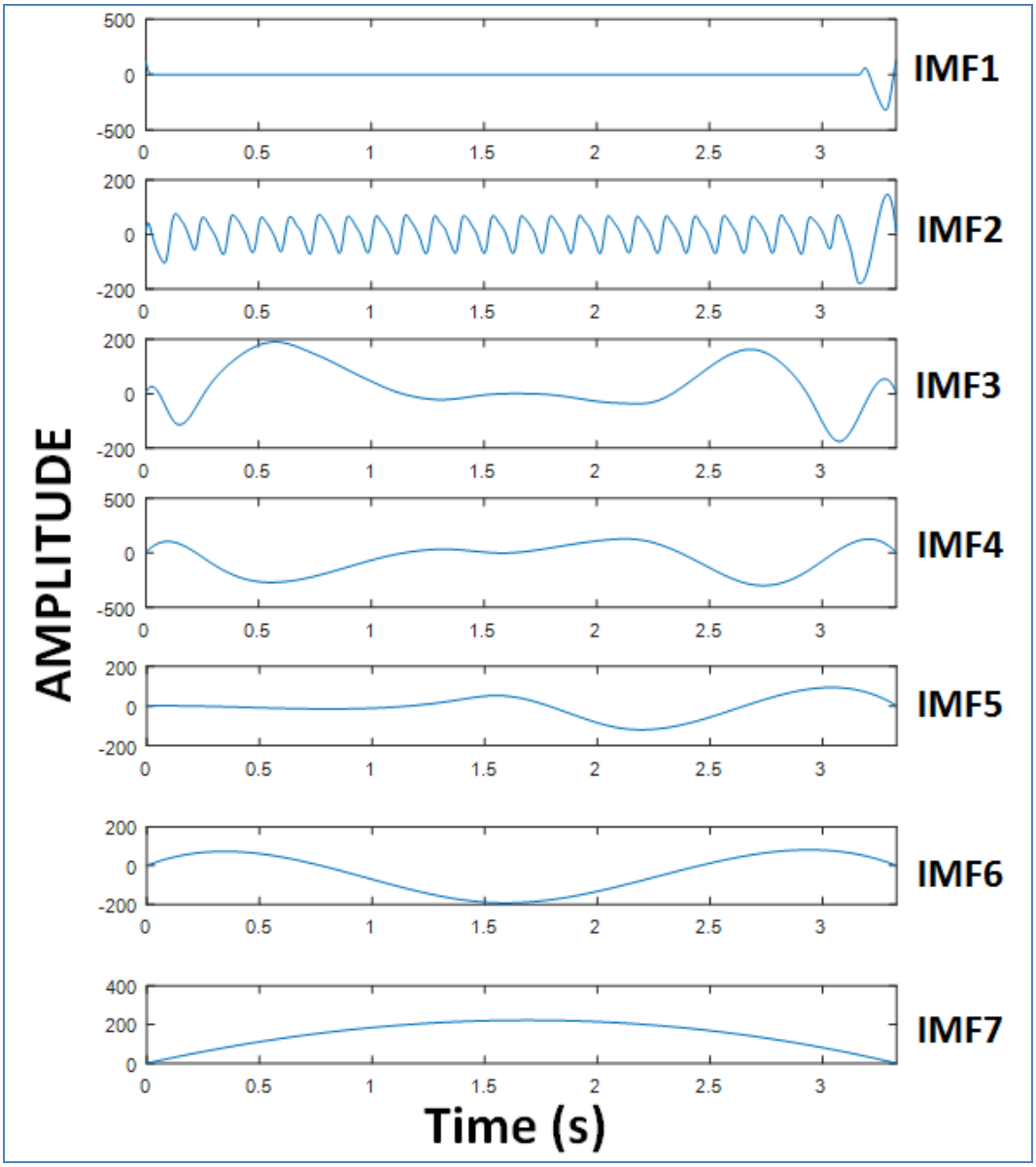

Figure 6-52: Intrinsic mode functions for the single rotor at periphery from optical mapping. *At pixel location '2' the optical electrogram was decomposed into 7 IMF's*

Fig. 6-53 shows that 8 IMF's were required to completely describe and reconstruct the waveform at the rotor core. The first IMF at these pixels are not useful as the EMD is just starting to decompose the signal with extrema calculations which becomes better from

IMF # 2 for both cases and therefore IMF's 2,3 and 4 were considered for calculating IMF complexity used in this thesis.

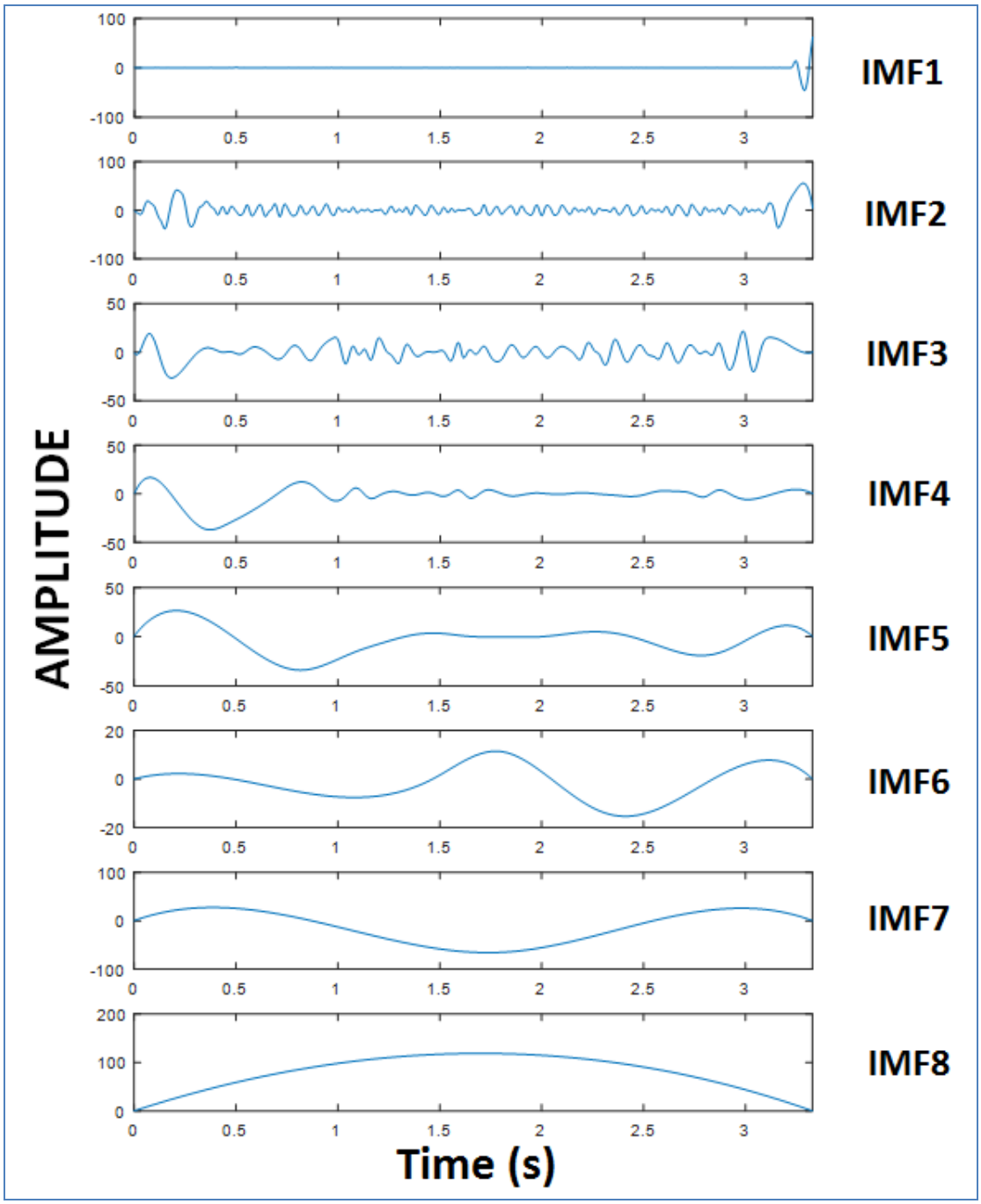

Figure 6-53: Intrinsic mode functions for the single rotor at the core from optical mapping. *At pixel location '1' the optical electrogram was decomposed into 8 IMF's*

Clearly IMF's 2, 3 and 4 are much more complex at the rotor core compared to the periphery thereby enabling its accurate identification. This result demonstrates the efficacy of the EMD approach for accurate identification of the rotor core with much more reliable location of the intrinsic complexities of the neighboring active sites

6.9.2 Performance of EMD on double rotor identification

Fig. 6-54 shows the snapshot of the double rotor and normalized 2D IMF complexity map.

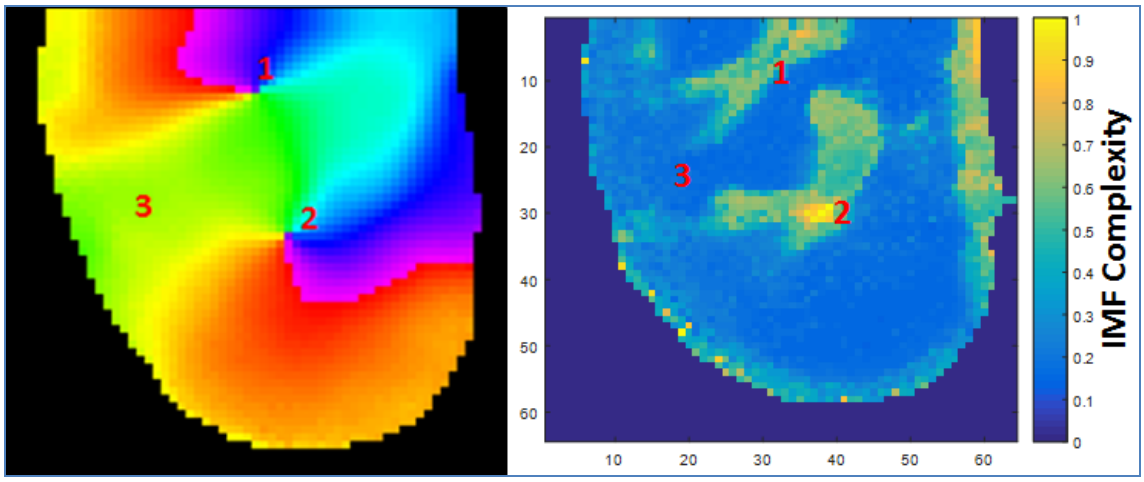

Figure 6-54: Results of EMD approach with double rotor from optical mapping. *(Left) Snapshot of a phase movie showing double rotor with reference pixel locations'1',& '2' at rotor core and '3' at rotor periphery; (Right) Normalized 2D IMF map showing correct identification of the rotor core.*

As seen from Fig. 6-54, IMF complexity accurately identified the rotor core area with better contrast than the periphery with higher IMF complexity at the core better in performance compared to SE, RE and DF. Similar to the single rotor identification results, by comparing the 2D maps for double rotor with MSE (Fig. 6-37), RPDE (Fig. 6-42), and Kurtosis (Fig. 6-47), it can be seen that these approaches identified a narrow region of the rotor core with higher corresponding values while IMF complexity

measures broader region at the rotor core encompassing rotor core pixel locations at '1' and '2' with lower IMF complexity at pixel location '3'. These results demonstrate the robustness of EMD approach to reliably and accurately capture broader regions of the active rotor core sites that may cause and maintain arrhythmia.

6.9.3 Performance of EMD approach on meandering rotor identification

6.9.3.1 Performance of EMD on meandering rotor from numerical simulation dataset1

Figure 6-55 shows the snap shot of the voltage distribution movie of the numerically simulated meandering rotor from dataset1 and normalized 2D IMF complexity map.

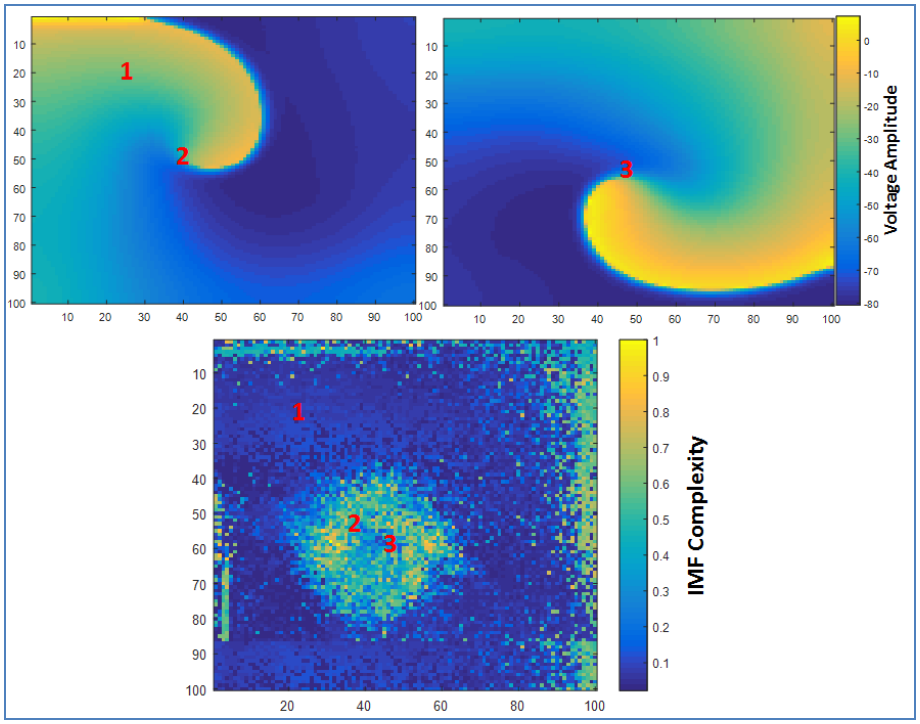

Figure 6-55: Results of EMD approach with numerically simulated meandering rotor dataset1. *(Top-Left) Snapshot of voltage distributions showing single rotor with reference pixel locations'1' at rotor periphery and '2' at rotor core. (Top-Right) shows rotor core at pixel location '3'at the time of snapshot; (Bottom) shows normalized 2D IMF map showing correct identification of the rotor core.*

Higher IMF complexity values are seen in the central area similar to the 2D MSE (Fig 6-38), RPDE (Fig 6-43) and kurtosis (Fig 6-48) maps implying correct and accurate tracking of the rotor core for this dataset at the reference pixel locations '2' and '3' compared to periphery at '1'. This implies superior performance of EMD compared to SE, RE and DF approaches and comparable performance with MSE, RPDE and kurtosis.

6.9.3.2 Meandering rotor from numerical simulation dataset2

Figure 6-56 shows the snap shot of the voltage distribution movie of the numerically simulated meandering rotor from dataset2 and normalized 2D IMF complexity map.

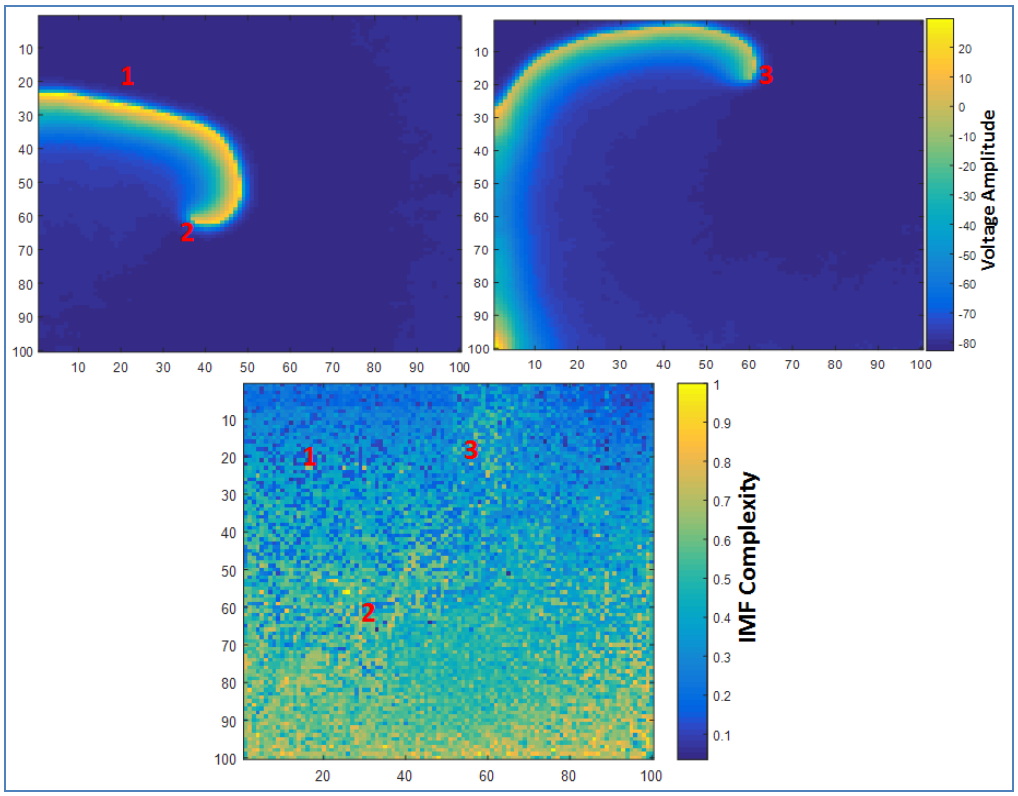

Figure 6-56: Results of EMD approach with numerically simulated meandering rotor dataset2. *(Top-Left) 2D Voltage distributions showing single rotor with reference pixel locations'1' at rotor periphery and '2' at rotor core at the time of snapshot; (Top-Right) shows rotor core at pixel location '3'at the time of snapshot.; (Bottom) shows normalized 2D IMF map.*

The 2D IMF complexity map shows high complexity values at the lower left corner encompassing pixel locations '2' and '3' at rotor core with lower IMF complexity value at pixel location '1' at periphery. Although, a clear trajectory is not observed with this map, the results still demonstrate better performance than SE, RE and DF, and comparable performance to MSE, RPDE and kurtosis based on the rotor trajectory from visual inspection.

6.9.3.3 Performance of EMD on meandering rotor from optical mapping

Figure 6-57 shows the snap shot of the phase movie of the meandering rotor and normalized 2D IMF complexity map.

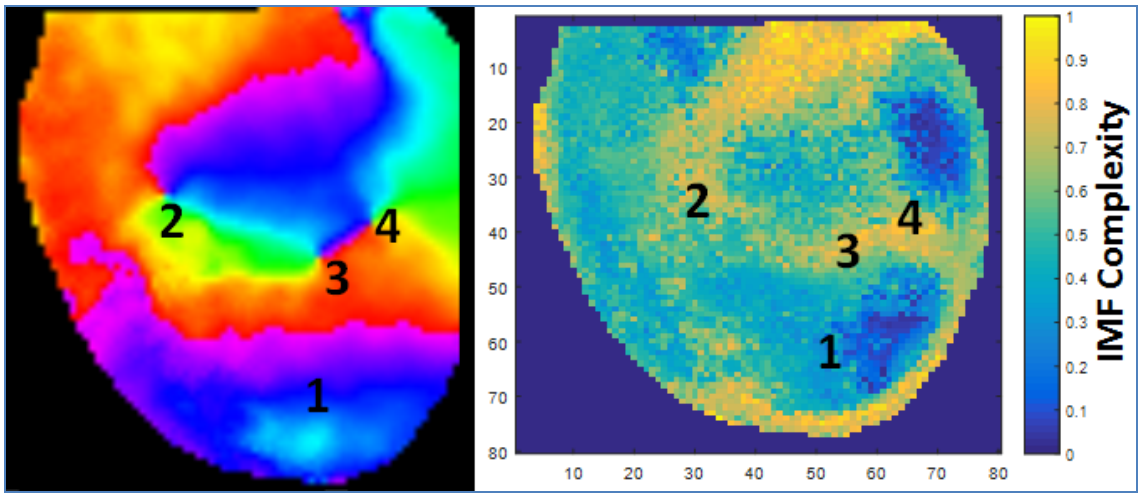

Figure 6-57: Results of EMD approach with meandering rotor from optical mapping. *(Left) Snapshot of a phase movie showing several meandering rotors with reference pixel locations '1' at the rotor periphery, '2', '3' and '4' at rotor cores; (Right) Normalized 2D IMF map.*

As seen from Fig 6-57 2D IMF complexity map shows higher complexity regions along a specific trajectory similar to the 2D MSE (Fig 6-40), RPDE (Fig 6-45) and kurtosis (Fig 6-50) maps which correlates with the trajectories observed from several meandering rotors. Specifically higher IMF complexity are observed at pixel locations

‘2’, ‘3’ and ‘4’ corresponding to the rotor core area with lower IMF complexity at the periphery at pixel location ‘1’. The results demonstrate superior performance of IMF complexity compared to SE, RE and DF and comparable performance to MSE, RPDE and kurtosis.

6.10 Testing and validation of MSF approach with rotor data

6.10.1 Performance of MSF on single rotor identification

Fig. 6-58 shows the snapshot of the single rotor and 2D MSF map. As seen from Fig 6-58 MSF accurately identified the rotor core area with better contrast than the periphery with higher MSF at the core better in performance compared to SE, RE and DF. As seen from the power spectrum of the optical electrograms at pixel locations ‘1’ at the rotor core in Fig 6-3 broader frequency spectrum is seen at the rotor with several frequency components that represents the chaotic nature at the rotor core. However, only a single frequency peak at 7.8 Hz is seen at the rotor periphery in pixel location ‘2’ in Figure 6-2. This difference in the frequency content is best used by the 8 filter banks to compute MSF that robustly discriminates rotor core from the periphery with MSF of 9.4 Hz at the periphery and 16.3 Hz at the rotor core. The results demonstrate the robustness of the MSF approach in the frequency domain to accurately identify rotor pivot point better than SE, RE and DF approaches and comparable with MSE, RPDE, kurtosis and IMF approaches.

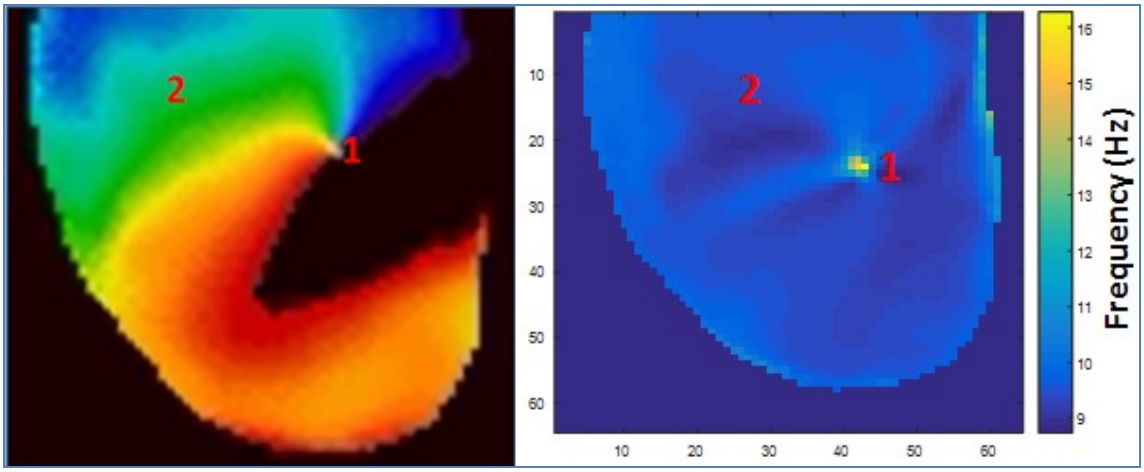

Figure 6-58: Results of MSF approach with single rotor from optical mapping. *(Left) Snapshot of a phase movie showing single rotor with reference pixel locations'1' at rotor core and '2' at rotor periphery; (Right) Normalized 2D MSF map showing correct identification of the rotor core.*

6.10.2 Performance of MSF on double rotor identification

Fig. 6-59 shows the snapshot of the single rotor and 2D MSF map. As seen from Fig 6-59 MSF accurately identified the rotor core areas with better contrast than the periphery with higher MSF at the core better in performance compared to SE, RE and DF. As seen from the power spectrum in Fig 6-6 & 6-7 of the optical electrograms at pixel locations '1' and '2' at the rotor core broader frequency spectrum is seen at the rotor with several frequency components that represents the chaotic nature at the rotor core. However, only a single frequency peak at 8.1 Hz is seen at the rotor periphery in pixel location '3' in Figure 6-5. MSF estimate was 9.4 Hz at the periphery at pixel location '3', 13.1 Hz at the rotor core in pixel location '1' and 16.3 Hz at the rotor core in pixel location '2'. The results demonstrate the robustness of the MSF approach in the frequency domain to accurately identify rotor pivot point better than SE, RE and DF approaches and comparable with MSE, RPDE, kurtosis and IMF approaches.

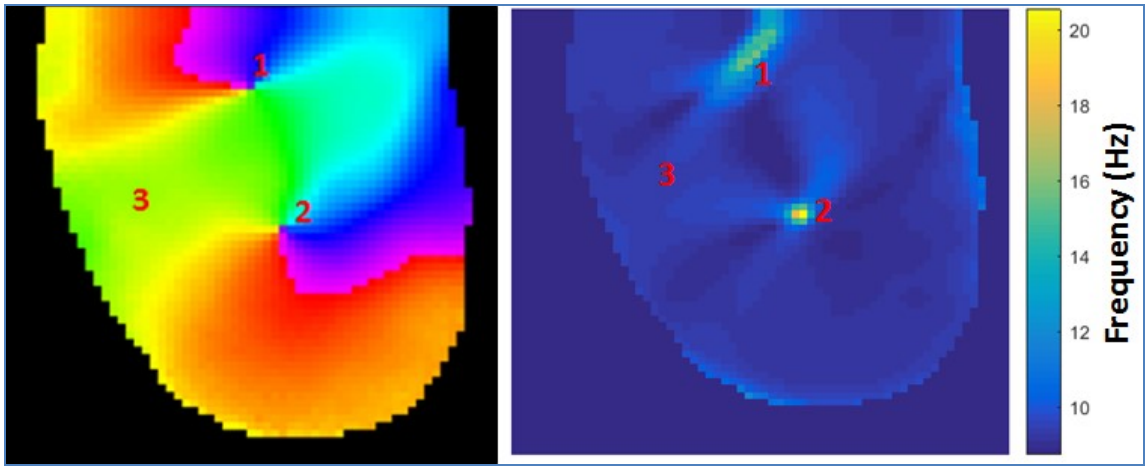

Figure 6-59: Results of MSF approach with double rotor from optical mapping. *(Left) Snapshot of a phase movie showing double rotor with reference pixel locations'1',& '2' at rotor core and '3' at rotor periphery; (Right) Normalized 2D MSF map showing correct identification of the rotor core.*

6.10.3 Performance of MSF approach on meandering rotor identification

6.10.3.1 Performance of MSF on meandering rotor from numerical simulation dataset1

Figure 6-60 shows the snap shot of the voltage distribution movie of the numerically simulated meandering rotor from dataset1 and 2D MSF map. Higher MSF values are seen in the central area similar to the 2D MSE, RPDE, kurtosis and IMF maps implying correct and accurate tracking of the rotor core for this dataset at the reference pixel locations '2' and '3' compared to periphery at '1' inferred from power spectrum in Figs. 6-14, 6-15 & 6-16. This implies superior performance of MSF compared to SE, RE and DF approaches and comparable performance with MSE, RPDE, kurtosis and IMF. MSF estimate at pixel '1' in the periphery was 29.98 Hz, 30.61 Hz at pixel '2' in the pivot point and 32.5 Hz at pixel '3' in the pivot point which enabled robust identification of the rotor core from the periphery in this dataset. The result demonstrate the efficacy of MSF

technique to accurately track meandering rotor based on observations with visual inspections and reference pixel locations for rotor core and periphery.

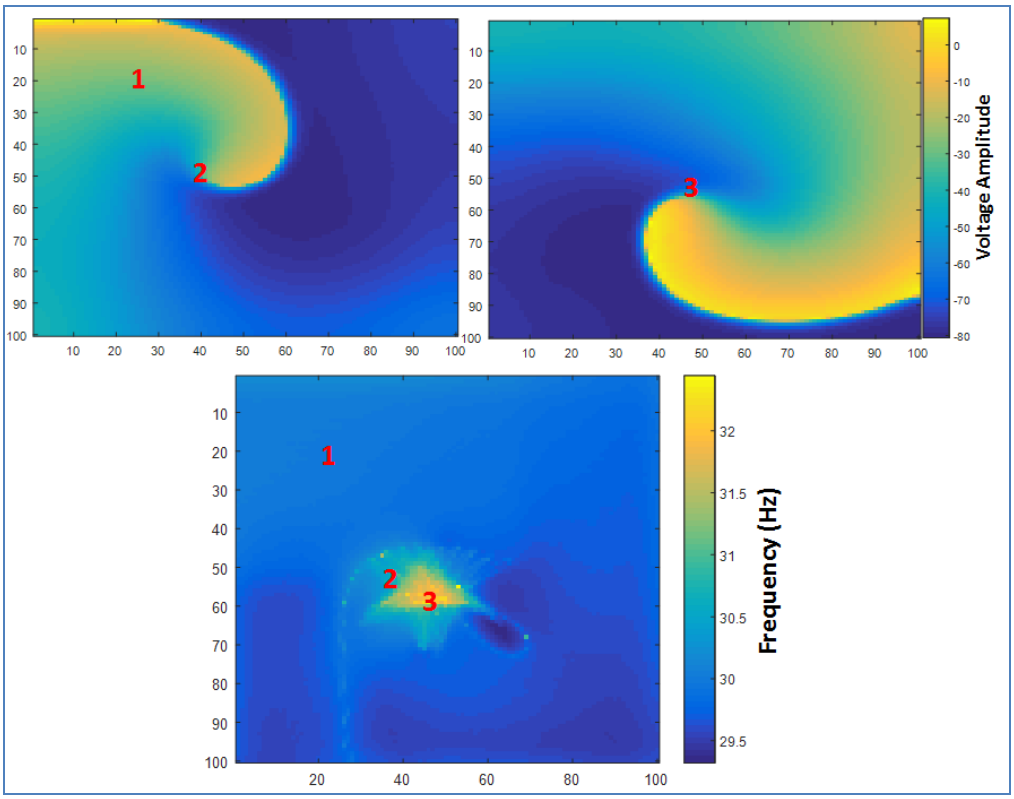

Figure 6-60: Results of MSF approach with numerically simulated meandering rotor dataset1. *(Top-Left) Snapshot of voltage distributions showing single rotor with reference pixel locations'1' at rotor periphery and '2' at rotor core. (Top-Right) shows rotor core at pixel location '3'at the time of snapshot; (Bottom) shows normalized 2D MSF map showing correct identification of the rotor core.*

6.10.3.2 Performance of MSF on meandering rotor from numerical simulation dataset2

Figure 6-61 shows the snap shot of the voltage distribution movie of the numerically simulated meandering rotor from dataset2 and 2D RPDE map. Higher MSF values are seen along the trajectories similar to the 2D MSE map (Fig 6-39) implying correct and accurate tracking of the rotor core for this dataset at the reference pixel locations '2' and

'3' compared to periphery at '1' inferred from power spectrum in Figs. 6-18 to 6-20. This implies superior performance of MSF compared to SE, RE, and DF approaches and similar performance compared with MSE which tracked the meandering rotor better with visual inspections. MSF performance was relatively better compared to RPDE, kurtosis and IMF. MSF estimate at pixel '1' in the periphery was 8.1 Hz, 9.2 Hz at pixel '2' in the pivot point and 8.9 Hz at pixel '3' in the pivot point which enabled robust identification of the rotor core from the periphery in this dataset.

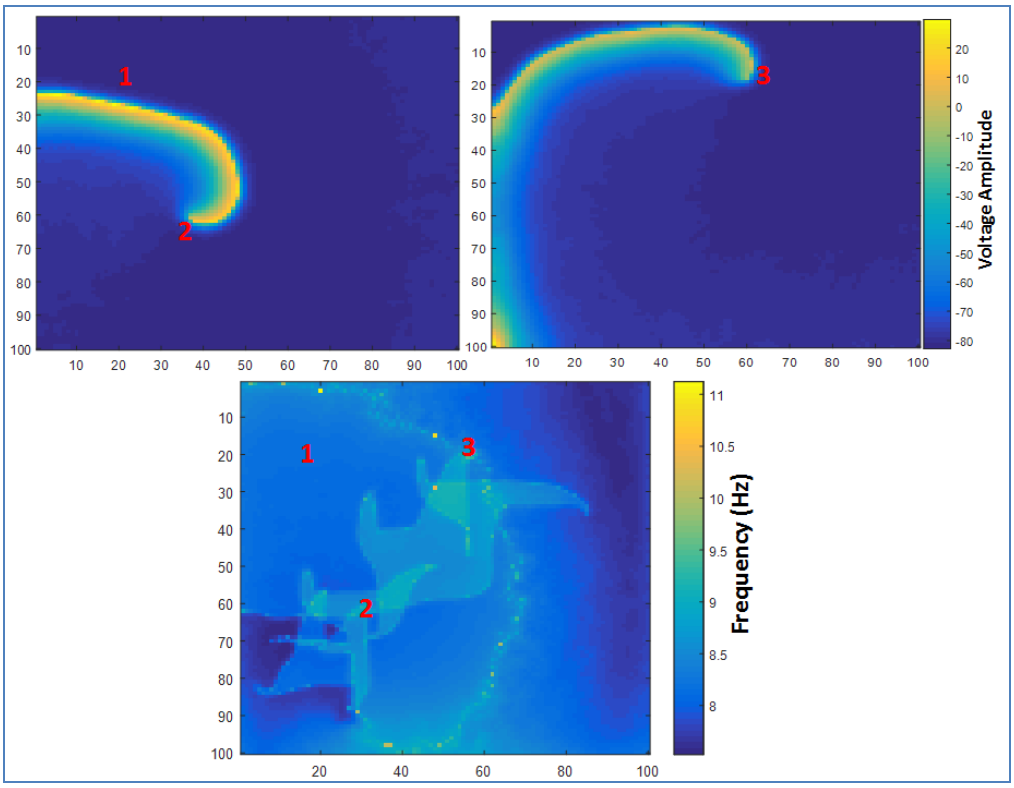

Figure 6-61: Results of MSF approach with numerically simulated meandering rotor dataset2. *(Top-Left) 2D Voltage distributions showing single rotor with reference pixel locations'1' at rotor periphery and '2' at rotor core at the time of snapshot; (Top-Right) shows rotor core at pixel location '3'at the time of snapshot.; (Bottom) shows normalized 2D MSF map.*

The result demonstrate the efficacy of MSF technique to accurately track meandering rotor based on observations with visual inspections and reference pixel locations for rotor core and periphery.

6.10.3.3 Performance of MSF on meandering rotor from optical mapping

Figure 6-62 shows the snap shot of the phase movie of the meandering rotor and 2D MSF map.

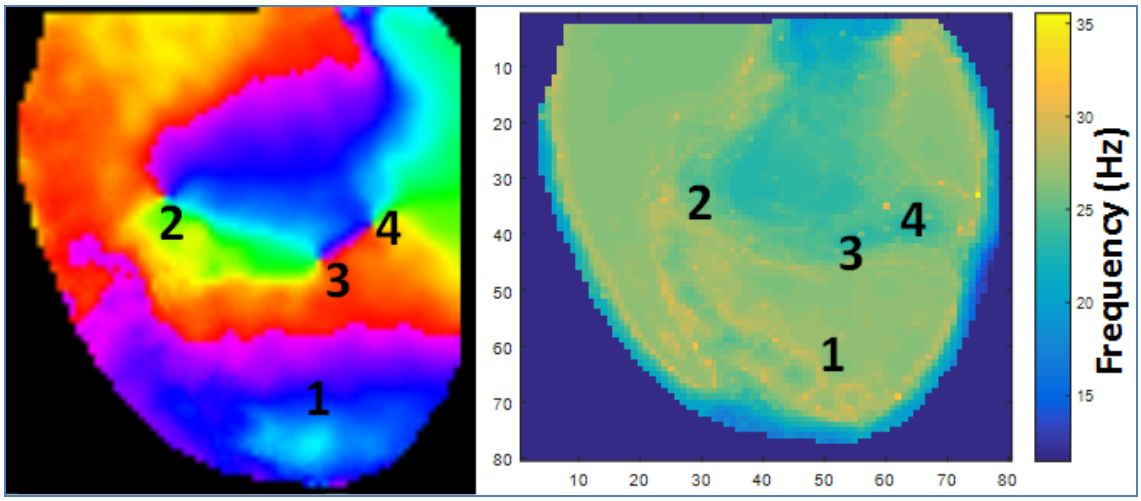

Figure 6-62: Results of MSF approach with meandering rotor from optical mapping. *(Left) Snapshot of a phase movie showing several meandering rotors with reference pixel locations '1' at the rotor periphery, '2', '3' and '4' at rotor cores; (Right) Normalized 2D MSF map.*

2D MSF map shows higher MSF regions along a specific trajectory similar to the 2D MSE map shown in Figure 6-40 which correlates with the trajectories observed from several meandering rotors. The MSF values at pixel locations '1', '2', '3' and '4' were comparable at 25.6 Hz implying the complex nature of the several meandering rotors that contributes to several frequencies inferred from power spectrum in Figs. 6-9 to 6-12. However, the trajectory pattern is similar to MSE, RPDE, kurtosis and IMF maps that

show a patch of low MSF region comparable to these maps indicating the absence of rotor core in this location which can be visually confirmed with the phase movie. This illustrates the robustness of MSF approach that captures the complexity in the frequency domain while other approaches are in the temporal domain measuring similar complexity.

6.11 Discussion

In this thesis, variety of signal processing techniques in time domain (MSE, RPDE, kurtosis and EMD) and frequency domain (MSF) to accurately identify rotor pivot points were developed and validated with optical mapping data with known pivot point locations using ventricular arrhythmia model in an *ex vivo* rabbit heart as well as numerically simulated meandering rotor data. Several types of datasets such as single, double and meandering rotors were tested with each novel approach to demonstrate their efficacy and robustness for tracking the pivot point. Major outcomes of this thesis, is the validation through successful demonstration of these approaches to accurately identify the pivot point in single and double rotors whose exact pivot point locations are obtained for reference using singularity analysis with the phase images. Tracking of pivot point in meandering rotors (numerical simulation and optical data) using these novel approaches were visually compared which also demonstrated reasonable success. The author successfully achieved the objectives of this section of the thesis, by validating the novel approaches through variety of rotor datasets.

This thesis used optical mapping of complex arrhythmias such as ventricular fibrillation (VF) and ventricular tachycardia to visualize rotors. The pivot points of single and double rotors were easily located using singularity analysis from phase mapping that

provided an excellent platform to test and validate the novel approaches developed in this thesis for rotor pivot point identification. All five approaches demonstrated their efficacy and robustness in accurately identifying the rotor core with better contrast from periphery compared with SE which had low contrast and suffered limitation with short time series analysis. Several complex meandering datasets were also used that challenged these approaches to track the pivot points. Visual inspection of the phase and voltage movies was used to gain insights into the ability of these approaches to reasonably track the meandering rotors. While all the approaches demonstrated reasonable success qualitatively, MSE and MSF approaches performed superiorly mainly from qualitative judgment. More rigorous analysis with quantitative accuracy tracking is required to validate these findings.

SE and RE approach identified rotor core regions with lower values compared to the periphery in single, double and meandering numerical rotor dataset1. No specific inferences were possible to make on the pivot point trajectory for the optical mapping meandering rotor data and meandering numerical rotor dataset2. DF approach showed uniform DF throughout the rotor regions for single, double and meandering rotor dataset. No specific inferences were possible to make on the pivot point trajectories which is consistent with the literature.

MSE, RPDE, kurtosis, IMF and MSF approaches robustly identified rotor core regions with higher values compared to the periphery in single, double and meandering rotors. Specifically, MSE and MSF were able to track the trajectories of meandering rotors in both optical and numerical data that matches visual inspection which opens new avenues

of research to track meandering rotors. IMF complexity specifically demonstrated a broader region of rotor core region capturing the intrinsic chaotic nature of the adjacent pixels that may also contribute to the cause and maintenance of the arrhythmia.

A major point of interest to note in this thesis is that there are differences in the disease etiology for VF/VT compared to AF and the validation of these novel approaches were performed only on optical mapping data from ventricular arrhythmias although it supports the existence of rotors in the myocardium. While, it can be realized that creating rotors with AF model is more complex, optical mapping data from these ventricular arrhythmia models were deemed reasonable for validation efforts of these novel approaches to identify rotor pivot point for the purposes of this thesis.

6.12 Conclusion

This chapter focused on rigorous testing and validation effort of the novel approaches developed and discussed in Chapter 3 for rotor pivot point identification. The results demonstrated the efficacy and robustness of MSE, RPDE, kurtosis, EMD and MSF approaches compared with SE, RE and DF approaches on variety of rotor datasets. The author achieved the objectives of this section of thesis through the successful demonstration of the validation of the newly developed quantitative electrogram analysis methods. The results suggest the potential of these approaches for accurate rotor pivot point identification using intracardiac electrogram analysis provided rotor presence can be ensured. Custom MATLAB programs were written for the validation efforts for testing each of these novel approaches based on the algorithm described in Chapter 3.

CHAPTER 7: FEASIBILITY OF OBTAINING PATIENT SPECIFIC 3D MAPS USING CONVENTIONAL CATHETER MAPPING SYSTEM

7.1 Introduction

This chapter focuses on translation efforts of the novel quantitative approaches developed in Chapter 3 to demonstrate the feasibility of obtaining patient specific 3D maps that can assist with intraprocedural guidance during catheter ablation. Intracardiac electrograms from two persistent AF patients in Mayo Clinic, Rochester, MN were used for demonstrating the feasibility of obtaining 3D maps for visualization purposes which may be used to identify active sites throughout the atria but not necessarily the presence of rotors. A brief description of the IRB approvals, the clinical environment in the cardiac catheterization lab where ablations are performed on the AF patients, intracardiac electrogram collection, followed by the description of the AF datasets and the processing steps to obtain patient specific 3D maps for each of the novel approaches which were implemented using custom MATLAB program. Specific electrograms, namely a regular electrogram and electrogram from a high CFAE region are labelled for reference for the second AF dataset and their amplitude histogram and spectrum are provided for referencing during the performance discussion of each of the novel approaches.

This chapter is organized as follows. First patient specific 3D maps from SE, RE and DF approaches are presented for comparison purposes in this thesis. For each of the novel approach such as MSE, RPDE, Kurtosis, EMD and MSF the patient specific 3D maps are presented and discussed separately in each subsection. Comparison of computational times for each approach is provided and compared with computing times from optical

mapping data. Finally, limitations of each of the approach are provided with possible recommendations to overcome them followed by a general discussion of the chapter results.

7.2 Intracardiac electrogram data collection and analysis

The fifth specific aim of this thesis is "*To assess the feasibility of using current catheter mapping system to generate patient specific 3D maps by implementing the novel approaches for rotor mapping using bipolar intra-atrial electrograms from human Atrial Fibrillation patients to guide catheter ablation".* To accomplish this task, collaboration with cardiac electrophysiologists in the cardiac catheterization laboratory in the department of cardiovascular medicine, Mayo Clinic was established to gain access to AF datasets and obtain clinical guidance for the purposes of this thesis. Three expert cardiac electrophysiologists namely Dr.Paul A. Friedman, Dr.Mulpuru K. Siva and Dr.Suraj Kapa courteously agreed to collaborate on this project and all of them have immense eperience in ths field performing consultation and several invasive procedures such as ablation for AF and other arrhythmias. Their extensive research experience studying various AF mechanisms especially the rotor waves at active arrhythmogenic substrates and potnetial interest in the develpoment of new rotor mapping techniques resulted in our successful collaboration for this PhD thesis research and for long-term research and development in this field.

Drs. Mulpuru and Kapa during their work performing ablation procedure for paroxysmal and persistent AF patients created a database which consists of clinical bipolar intracardiac electrograms from patients who underwent electroanatomical

mapping for AF ablation procedure. These sets of AF data in this database offers excellent source of data for this PhD thesis in testing and validating the novel approaches for electrogram analysis developed in this thesis. However, an initial effort of extracting electrograms from the saved database revealed extremely sparse data set which was deemed not sufficient for generating a reasonable 3D map in the LA and RA regions for identifying active substrates that may cause and maintain AF. This motivated prospective collection of data from paroxysmal and persistent AF patients with more electrograms that will add at least 45 minutes of more clinical time which requires approval from the Institutional Review Board (IRB) in Mayo Clinic, Rochester and University of Minnesota. The following sections will describe the environment, patients' and the electrograms that were obtained for this thesis to demonstrate the feasibility of obtaining 3D maps using the novel approaches developed in this thesis using current catheter mapping systems which can be inferred with the currently available LAT and CFAE maps.

7.2.1 Institutional review board approval

Institutional Review Board (IRB) Approval is required to conduct research that involves human subjects and since this is a collaborative project between University of Minnesota and Mayo Clinic, a combined approval was necessary in order to collect data from both paroxysmal (n=40) and persistent (n=40) AF patients for using it in this thesis. Appropriate IRB forms were filled in both the institutions with the research proposal description highlighting the data collection and analysis procedures using the novel approaches developed in this thesis. Data collection proceeded after IRB approval. IRB

research proposal and consent forms from Mayo Clinic and University of Minnesota are included in APPENDIX G.

7.2.2 Clinical setting of AF patients

The patients who will satisfy the inclusion criteria are adults > 18 years with symptomatic AF (both paroxysmal and persistent and both initial and repeat procedures) presenting for ablation based on indications in ACC/AHA/HRS consensus statement for catheter ablation of AF. All patients had their anti-arrhythmic drugs stopped for more than 5 half-lives before the procedure except for amiodarone. Informed consent was obtained from the patient after detailed discussion of the study objectives, methodology etc. Left atrial (LA) thrombus was ruled out by transesophageal echocardiography. All patients underwent pre-procedural CT/MR imaging to delineate the anatomy. Multipolar catheter is placed in the coronary sinus (2-5-2mm spacing decapolar, Biosense Webster, CA). Heparin (100mg/kg) was bolused and a continuous infusion was maintained to maintain an activated clotting time of 290 seconds. Transseptal puncture is performed for left atrial aces. A circular multipolar catheter (Lasso, Biosense Webster, CA) was used to map the PV. LA and right atrial (RA) geometry are created using 3.5 mm tip irrigated ablation catheter (Thermacool, Biosense Webster, CA) and Carto 3 mapping system (Biosense Webster, CA.). Multiple points were taken to create geometry with a fill threshold of 20 with uniform distribution across both chambers.

It is now common to use PentaRay® NAV (Biosense Webster, Inc., a Johnson & Johnson company) catheter shown in Figure 7-1. It has 4 electrodes per arm for a total of 20 electrodes which therefore can capture 20 electrograms during a given mapping time.

One of the main advantages with this mapping catheter is the atraumatic splaying of all five spines against the endocardial surface, providing a high-density map from its 1-mm electrodes covering a surface diameter of 3.5 cm. For the purposes of this research, the electrophysiologist is recommended to use this catheter to obtain more electrograms in a given time.

Figure 7-1: Photograph of a pentarray NAV catheter (Biosense Webster, Inc., a Johnson & Johnson company)

7.2.3 AF data collection and storage

The electrophysiology study was performed in the Cardiac Catheterization Laboratory, in the Division of Cardiovascular Diseases in Mayo Clinic. The patients had transesophageal evaluation to exclude atrial thrombus before the procedure. Electrophysiological study was performed in the post absorptive state under general anesthesia. The LA was accessed transseptally, and a single bolus of 100 IU/kg heparin was administered and repeated to maintain activated clotting time above 190 sec. AF data

were collected from patients presenting either persistent or paroxysmal AF prior to ablation. In persistent case, the electrograms were collected during AF and for paroxysmal patients AF is induced by pacing rapidly in the atrium. In both cases, electrograms were collected after 10 minutes of stable AF.

Electro-anatomic mapping (CARTO, Biosense-Webster) was performed prior to AF ablation. The CARTO mapping system has a sensor position accuracy of 0.8 mm and 5°. With the Thermacool SF catheter, the 3D geometry of the chamber was reconstructed in real time, and at each point, the system records the 12-lead ECG and bipolar electrograms sampled at 977 Hz and low pass filtered at 30 to 500 Hz, thus allowing the electrophysiological information to be color coded and superimposed on the anatomic map. Evenly distributed points were recorded using a fill threshold of 20 mm throughout the RA, LA, and CS. At each point, 5-15 s electrograms as shown in Figure 7-2, together with the surface ECG, were acquired.

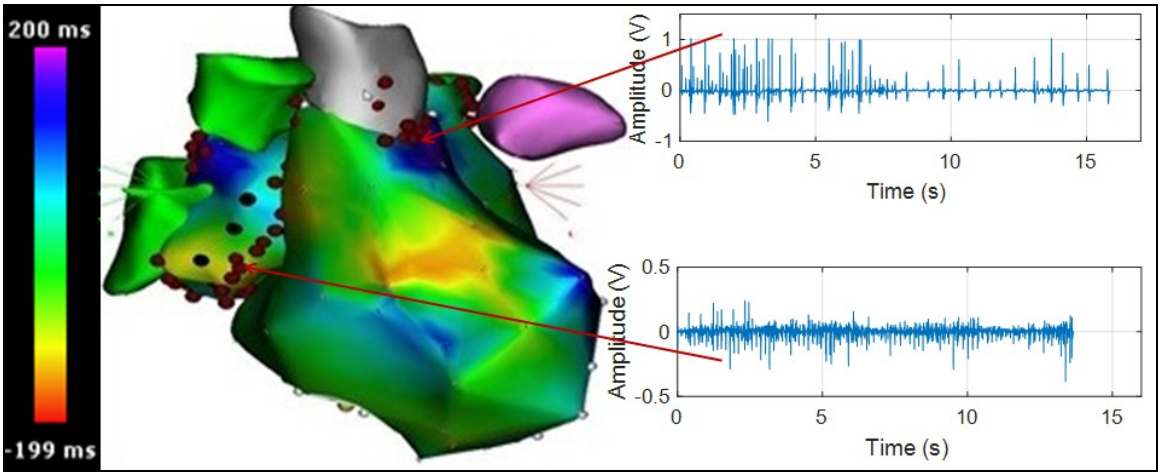

Figure 7-2: Sample intracardiac electrograms from the carto points superimposed on a LAT map using the CARTO System. *Red dots indicate the carto points from where the electrograms were obtained.*

Endocardial contact during point acquisition was facilitated by fluoroscopic visualization of catheter motion, the distance to geometry signaled by the catheter icon on the CARTO system, and confirmed in a subset with intracardiac echocardiography. Due to the challenge of adding extra clinical time to obtain reasonable number of electrograms in the LA and RA, AF patient recruitment and data collection was extremely challenging along with the busy schedules of the cardiac electrophysiologists involved in this work. As a result only two persistent AF patient dataset was obtained after the IRB approval was obtained in the time course of this thesis. The following section discusses the two patients, data extraction and processing steps involved to obtain the 3D maps for visualization to make inferences.

7.2.3.1 Persistent AF patient Case # 1

Dr.Mulpuru obtained informed consent from a 65 year old male persistent AF patient who failed several antiarrhythmic drugs treatment to participate in this research. The clinical setting of the procedure is similar to the description in section 7.2.2. Dr.Mulpuru was able to obtain a complete right and left atrial map during AF using the PentaRay® NAV catheter and the data collection process was performed as described in section 7.2.3. While the mapping data was collected and stored in the database, a challenge existed in the export of the data for offline analysis. As a result, manual extraction of the bipolar electrograms was performed from 57 carto points on the RA, 229 carto points on the LA and 24 carto points on the SVC totaling 310 time domain signal for analysis. Electrogram was obtained in .txt format and processed offline in MATLAB.

Since this was the first AF patient data attempted, only SE was applied to this data during the initial stages of this thesis while other novel approaches were under development to generate 3D SE map for this dataset for feasibility assessment in this thesis. The calculated SE values from MATLAB were re-annotated back exactly to the carto points from where the electrograms came from using the GE Prucka system. This was accomplished manually which involved at least 2 individuals and was a time consuming process. The annotated SE data was then superimposed on the anatomical map to obtain the full 3D SE distribution in the atria by interpolation between the CARTO points for visualization and color coded to represent the range of SE values. The estimated SE values were multiplied by a factor of 10 for display purposes. The CARTO software also allows 3D viewing of this 3D entropy map for easy visualization and interpretation to identify potential active sites that may cause and maintain AF. Although, this process was extremely cumbersome the author was successful in generating a 3D SE map. The CARTO system interpolated the SE values between the sparse CARTO points in the atrial space from the locations of which the electrograms were obtained to achieve a smooth 3D SE map.

7.2.3.2 Persistent AF patient Case # 2

Dr.Kapa obtained informed consent from a 64 year old woman with persistent symptomatic atrial fibrillation presented for ablation after failing antiarrhythmic drugs including dofetilide. She was brought to the cardiac catheterization electrophysiology lab in the fasting state for the ablation procedure. Dr.Kapa was able to obtain a complete right and left atrial map during AF using the PentaRay® NAV catheter.

During ablation, full pulmonary vein isolation was completed with wide area circumferential ablation around both sets of pulmonary veins depicted in Figure 7-3 showing the lesion sets delivered to the patient. A cavotricuspid isthmus (CTI) line was also done given a clinical history of CTI-dependent flutter. The ablation procedure with PVI successfully terminated the AF and the patient was maintained on dofetilide for 3 months post ablation per standard of care post-ablation and then this was discontinued. Over 9 months follow-up since discontinuing dofetilide, she had one paroxysm of symptomatic AF in the setting of receiving anesthesia for orthopedic surgery but otherwise no known recurrence. The study data was stored in Clinic's protected database and the entire study was exported in .xml format for offline analysis following the IRB guidelines, instead of manual extraction performed with patient in Case #1.

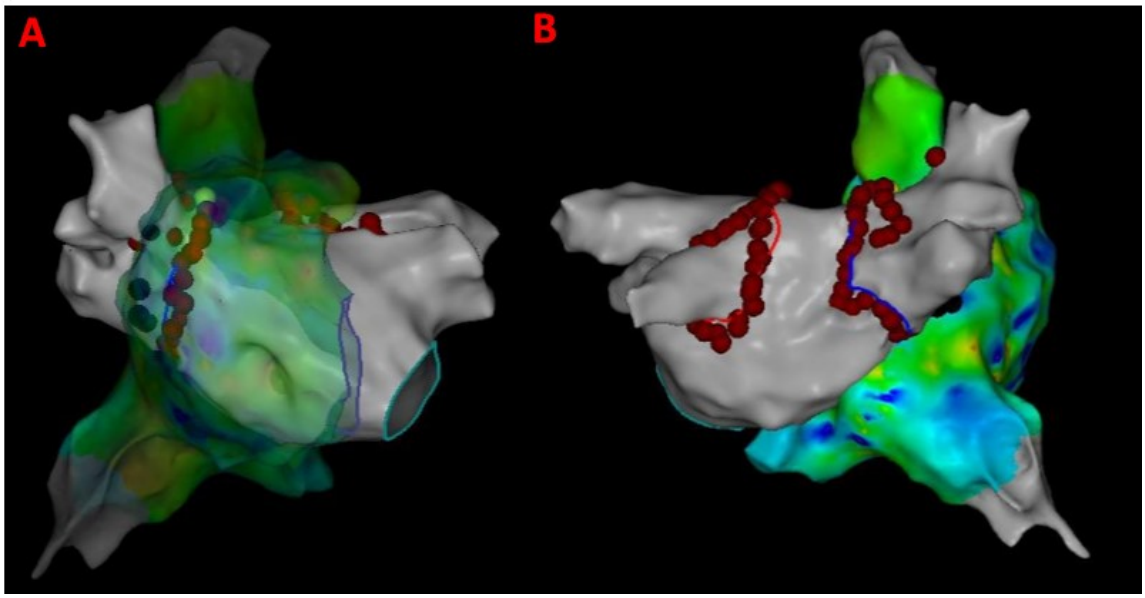

Figure 7-3: Lesion sets delivered to the persistent AF patient. *(A) Antero-Posterior view with RA transparent; (B) Postero-Anterior view; Red dots indicate the lesion points where RF energy was delivered for PVI.*

The data export only allowed 2.5 s of electrogram data and with a sampling rate of approximately 1000 Hz, time series data with 2500 sample points for each electrogram were available for analysis with the novel approaches developed in this thesis. A total of 1055 electrograms were obtained from this patient with 642 electrograms in the LA and 413 electrograms in the RA. The export data also contained the electroanatomic mapping information, catheter coordinates, the locations from which the electrogram were obtained etc. which are useful for recreating the 3D geometry to generate patient-specific 3D maps with offline analysis.

The electrograms were processed as before with all the novel quantitative approaches including SE, RE and DF to obtain eight different 3D maps for inferences and to compare the results from each approach. Propriety MATLAB software from Karlsruhe Institute of Technology, Karlsruhe, Germany was used for visualization purposes to obtain the 3D maps. LAT maps were obtained from the CARTO system shown in Figure 7-4 for comparing the results from the novel approaches developed in this thesis. Bluish to purple regions indicate low activation times that may correspond to chaotic active sites. Greenish to yellow regions represent higher activation times that may correspond to normal atrial activity. As seen from Figure 7-4, late activity can be seen near right atrial appendage (RAA), around right sided pulmonary veins and anterior regions of the inferior vena cava (IVC) indicating potential areas of active AF sites. The electrograms obtained from these regions are expected to portray abnormal atrial activation which can be captured by the novel quantitative electrogram analysis approaches developed in this thesis for comparison with LAT map to make inferences.

Also, CFAE points were obtained from the CARTO system and superimposed on the LAT map to give insights about atrial electrogram fractionation for comparison with the results from novel 3D maps shown in Figure 7-5.

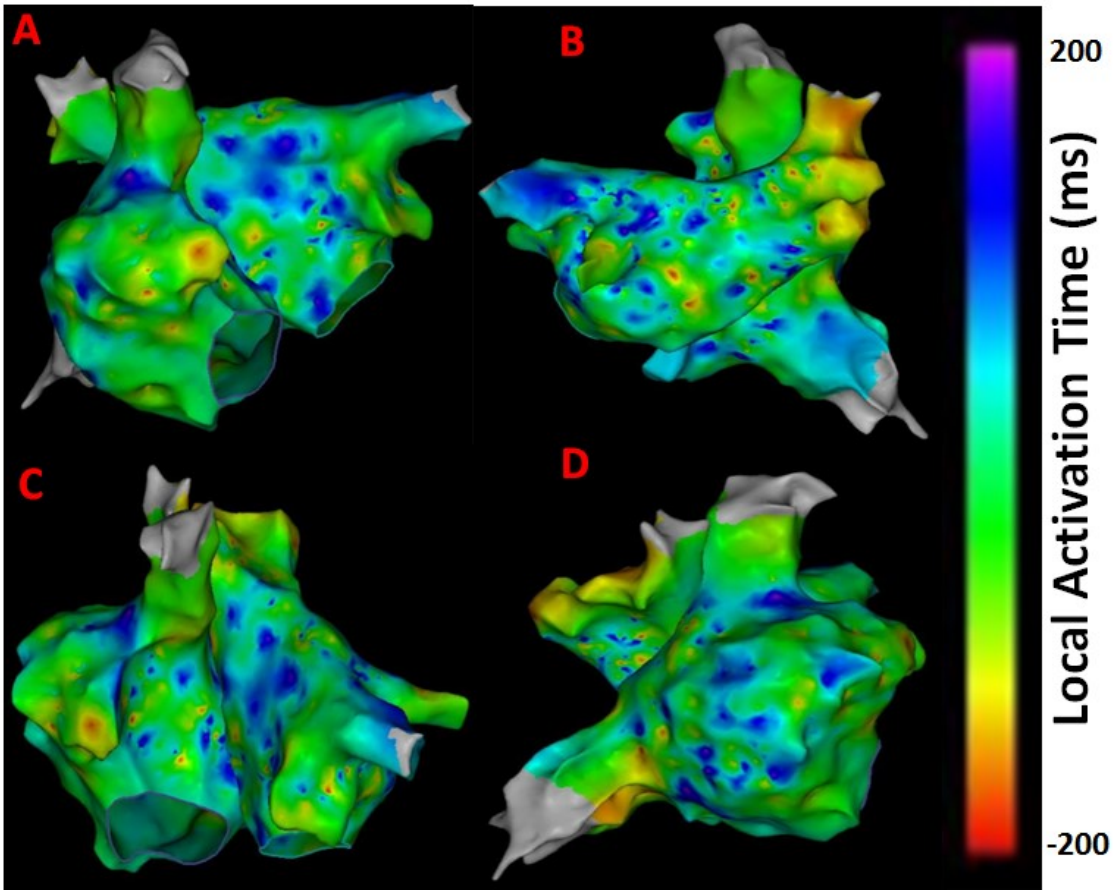

Figure 7-4: LAT maps from the persistent AF patient. *(A) Antero-Posterior view; (B) Postero-Anterior view; (C) Left Anterior Oblique (LAO) view; (D) Right Anterior Oblique (RAO) view*

The CFAE points are defined with a minimum number peaks of 5 and a maximum of 8 in the CARTO system. The red dots in Fig.7-5 have interval confidence level (ICL) > 8 and the blue dots fit within the 5-8 peak range showing several CFAE positive electrograms throughout LA and RA. In specific, high CFAE regions are seen near RA-LA septum, below left superior pulmonary vein (LSPV) and posterior region of the right

sided wide area circumferential ablation (WACA) region have higher CFAE scores indicting the possibility of AF active sites.

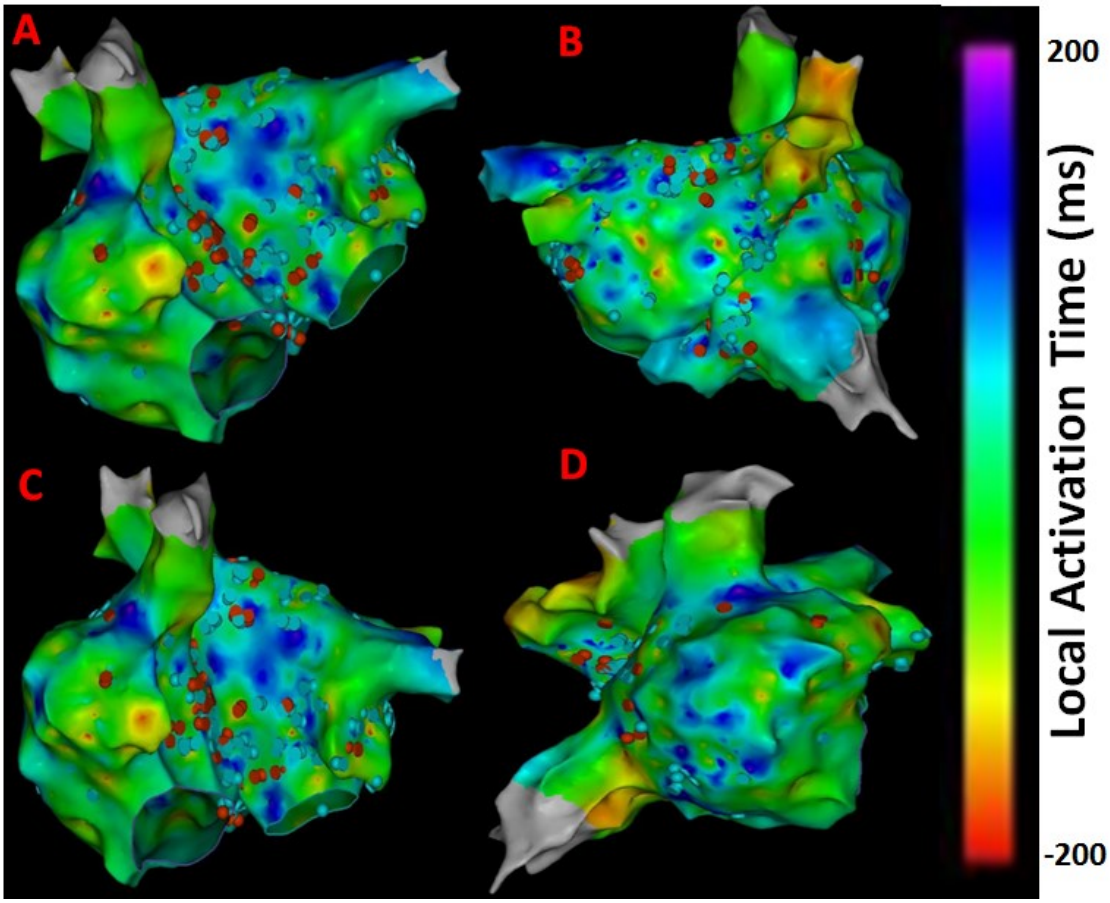

Figure 7-5: CFAE points superimposed on LAT maps from the persistent AF patient. *(A) Antero-Posterior view; (B) Postero-Anterior view; (C) Left Anterior Oblique (LAO) view; (D) Right Anterior Oblique (RAO) view. Red dots have >8 peaks, blue dots fit within the 5-8 peak range. Electrograms having interval confidence level (ICL) score ≥ 5 were considered CFAE positive by CARTO.*

As evident from Figures 7-4 and 7-5 there are several non-overlapping regions of low activation and high CAFÉ scores and vice versa which often provides clinical challenges in identifying true activation sites and therefore provides little guidance for the ablation procedure due to the known limitations of these two techniques. However, information

from these maps can be used in conjunction from the results with the novel approaches since AF active sites have lower LAT and higher CFAE score, which can be used for comparison for the purposes of this thesis. Figure 3-46 shows sample intracardiac electrograms from the persistent AF patient. A normal electrogram from high LAT area is shown in the top-right panel in Fig. 7-6 and a chaotic electrogram is shown in the bottom-right panel in Fig. 7-6 with a high CFAE score indicated by the red dot.

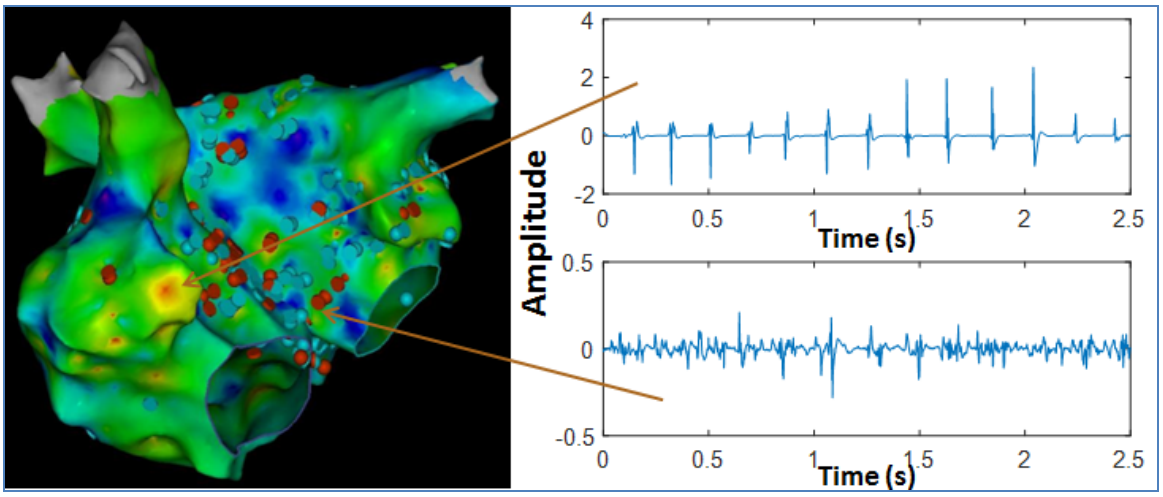

Figure 7-6: Sample intracardiac electrograms on a LAT map using the CARTO System. *(Left) shows LAT map with superimposed CFAE points in Antero-posterior view. (Top-Right) shows a normal intracardiac electrogram with normal activation; (Bottom-Right) shows irregular electrogram with high CFAE score.*

Figures 7-7 & 7-8 show the amplitude histogram and normalized power spectrum of the normal electrogram and chaotic electrogram respectively. As seen from Fig. 7-7 normal intra-atrial electrogram has regular activation pattern resulting in the amplitude histogram and the power spectrum shows less chaotic frequency characteristics. As seen from Fig. 7-8 intra-atrial electrogram from CFAE high spot, has irregular activation pattern resulting in the corresponding amplitude histogram and the power spectrum shows chaotic frequency characteristics.

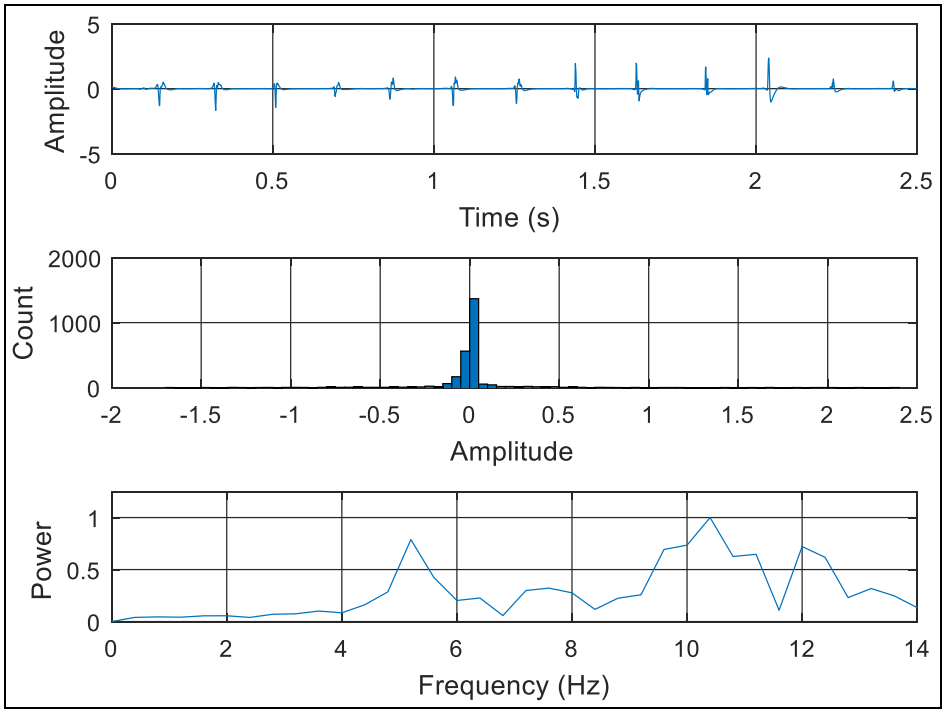

Figure 7-7: Regular electrogram from AF patient2. *(Top) - Voltage distribution. (Middle) - Amplitude histogram; (Bottom) - Normalized power spectrum*

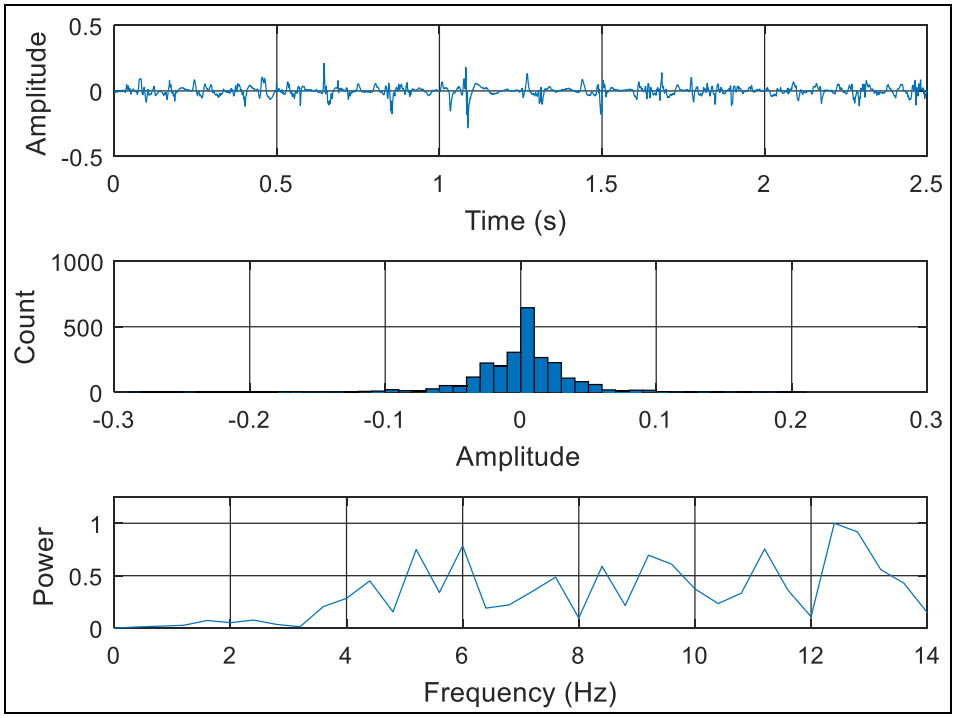

Figure 7-8: Fractionated electrogram from AF patient2. *(Top) - Voltage distribution. (Middle) - Amplitude histogram; (Bottom) - Normalized power spectrum*

The novel approaches developed in this thesis will explore these temporal and frequency characteristics to identify potential active sites that may cause and maintain AF. Consolidated MATLAB program to implement the novel approaches for analyzing intracardiac electrogram data from persistent AF patient was achieved using *'Novel_Approaches_IEGM_Analysis.m'* included in APPENDIX H. 3D visualizations of the novel approaches were realized using custom MATLAB program *'Plot_3D_Maps_IEGM.m'* included in APPENDIX I.

7.3 Patient specific 3D SE Maps

This section presents the results from the two persistent AF patient obtained in this thesis for feasibility analysis in generating patient-specific 3D SE map.

7.3.1 Intracardiac electrogram analysis from AF patient1

Figure 7-9 shows the 3D SE map that was manually obtained by superimposing the calculated SE values on the electroanatomic map at the exact electrogram locations. Higher region of SE is noted at the base of the right atrial appendage (see area with the bluish pink color), which could indicate the presence of active AF causing sites, which is outside the PV area. All other areas have lower SE values (see green and yellow color). Although a causal relationship cannot be established, it can be inferred that for persistent AF patients the active triggers that cause AF may arise from outside PV regions explaining why conventional ablation strategies targeting PV area could fail. This is consistent with literature that for persistent AF patient's rotor waves exists outside PV area in both atria. Although, the 3D SE map shows higher entropy regions which potentially could be an active AF site, it doesn't however indicate the exact pivot point of

the rotors which is the desired ablation point to terminate the rotor wave and hence AF. Therefore, cross reference with conventionally available LAT and CFAE amps and analysis from other novel approaches may be required for drawing important clinical conclusions about AF active sites with respect to rotor identification to locate the exact ablation points.

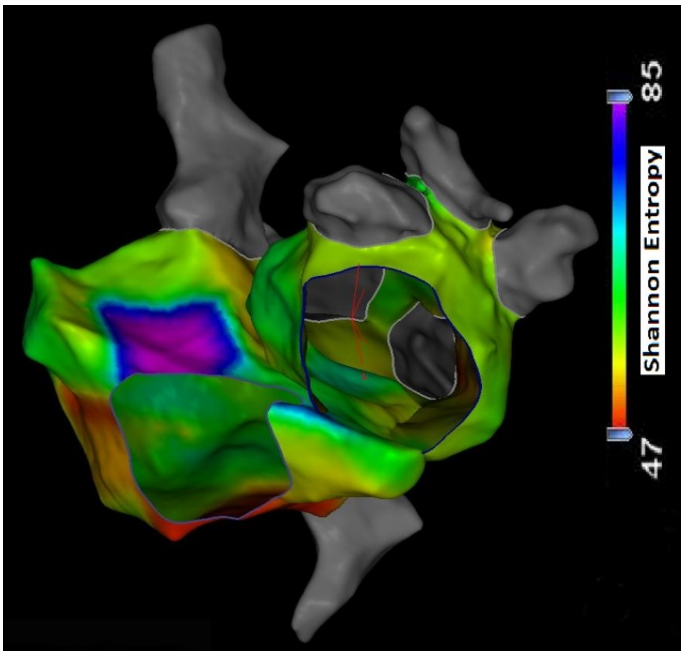

Figure 7-9: 3D SE map from persistent AF patient # 1 in LAO view. *Higher regions of SE are observed at the base of right atrial appendage. Note that for visualization purposes, SE was multiplied by 10.*

This result is a successful demonstration for performing offline electrogram analysis to generate 3D maps using the current catheter based CARTO system. Although, the process involved was manual such as offline MATLAB processing to compute SE, re-annotation on the corresponding carto points and finally superimposing them on anatomical map this approach has shown the feasibility of using SE for visualizing the active sites without the need for new or additional hardware. However, this approach has practical limitations to

offer near real-time guidance for catheter ablation due to manual interventions needed to generate patient-specific 3D maps which motivated the author in explore a more practical way of data export, analysis and 3D map generation discussed in the following section.

7.3.2 Intracardiac electrogram analysis from AF patient2

Figure 7-10 shows the patient-specific 3D SE map in four different views obtained from MATLAB processing without any manual intervention such as described in the previous section.

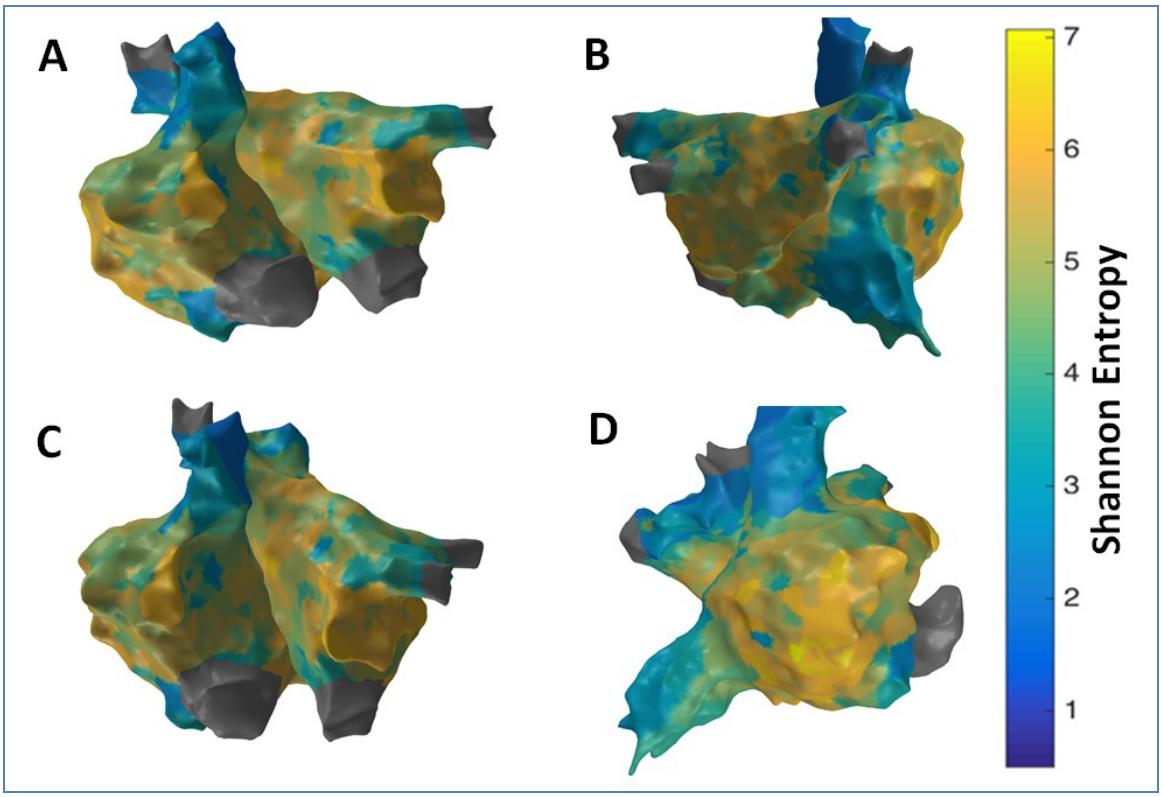

Figure 7-10: 3D SE map from persistent AF patient # 2*. (A) Antero-Posterior view; (B) Postero-Anterior view; (C) Left Anterior Oblique (LAO) view; (D) Right Anterior Oblique (RAO) view.*

Higher SE regions are seen at the RAA and the lateral wall seems to have the highest value indicating the possibility of active sites in these regions. However, no specific

conclusions can be made on rotor identification. There is some correlation with the LAT map with low activity near RAA where higher SE is seen. However, comparison with CFAE map implies no significant overlap of high fractionation areas with higher SE regions. However, the result is a successful demonstration for the feasibility of using current catheter mapping system to obtain 3D maps with automatic processing using custom software. The results also demonstrate the potential for obtaining near real-time 3D maps that can aid cardiac electrophysiologist in clinical guidance during catheter ablation.

7.4 Patient specific 3D RE Maps

7.4.1 Intracardiac electrogram analysis from AF patient2

Figure 7-11 shows the patient-specific 3D RE map in four different views. Similar to the 3D SE map, higher RE regions are seen at the RAA, lateral wall and right side of the roof seems to have the highest RE value indicating the possibility of active sites in these regions. No specific clinical information can be derived especially on rotor identification other than the possibility of visualizing some potential active sites in those regions which are outside the PV regions with higher RE which is expected for a persistent AF patient.

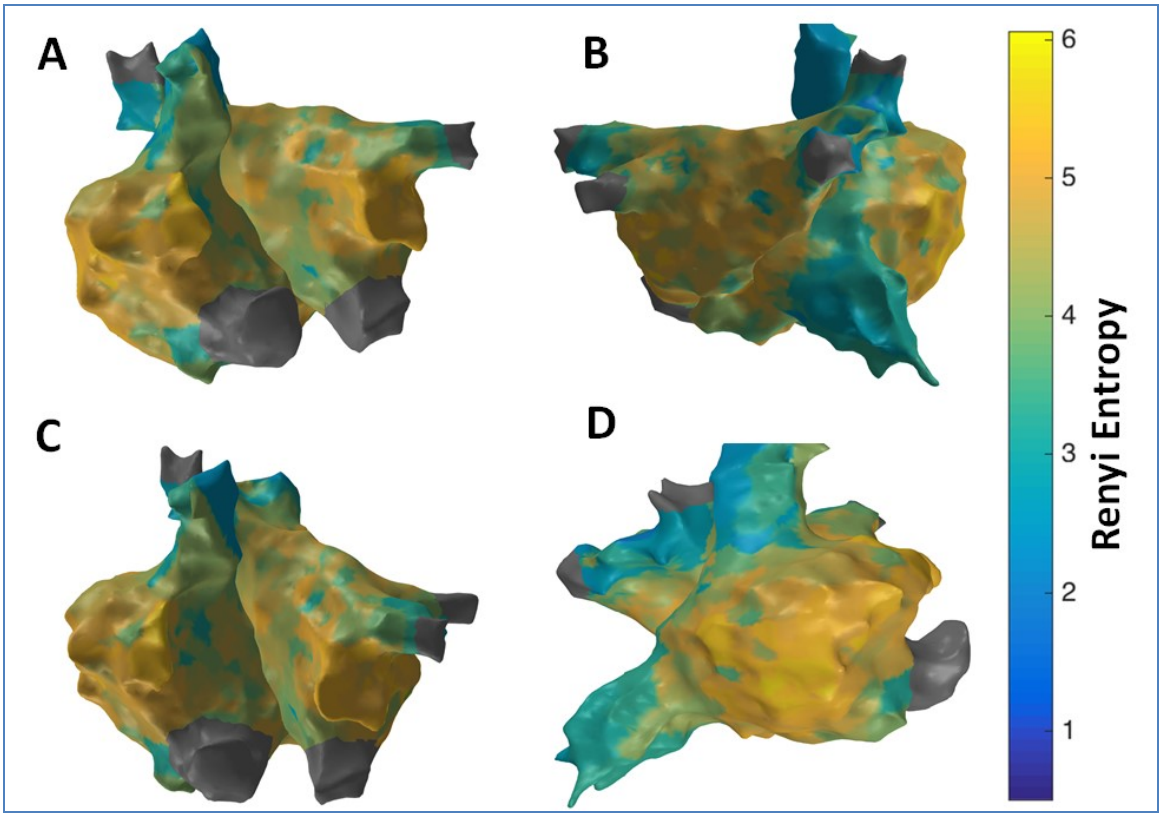

Figure 7-11: 3D RE map from persistent AF patient # 2*. (A) Antero-Posterior view; (B) Postero-Anterior view; (C) Left Anterior Oblique (LAO) view; (D) Right Anterior Oblique (RAO) view.*

7.5 Patient specific 3D DF maps

7.5.1 Intracardiac electrogram analysis from AF patient2

Figure 7-12 shows the patient-specific 3D DF map in four different views. More or less uniform DF region is observed with few focal areas of high and low DF in particular high DF region observed in lateral part of RA. Figures 7-7 & 7-8 bottom panel's shows the power spectrum at the reference regular electrogram region with a peak at 10.1 Hz and chaotic region with a peak at 14.8 Hz. Similar to the 3D SE and RE maps, no specific clinical information can be inferred due to mostly uniform DF regions being observed.

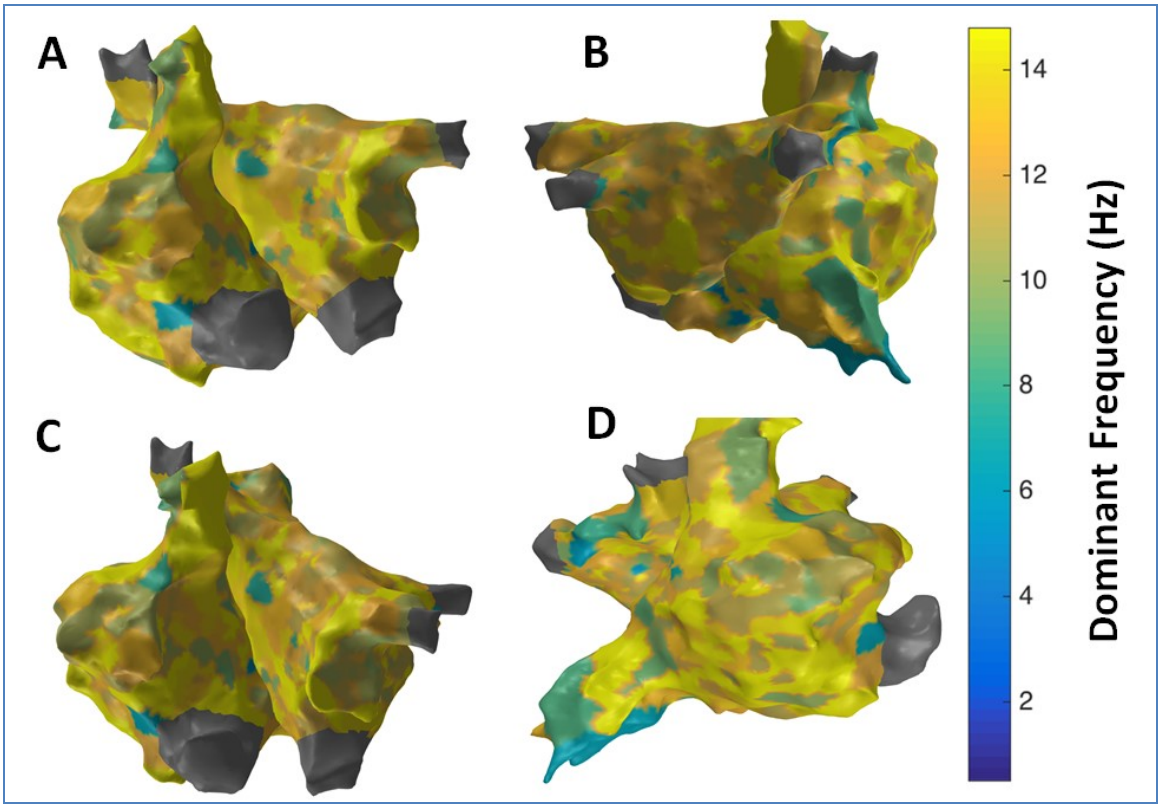

Figure 7-12: 3D DF map from persistent AF patient # 2*. (A) Antero-Posterior view; (B) Postero-Anterior view; (C) Left Anterior Oblique (LAO) view; (D) Right Anterior Oblique (RAO) view.*

7.6 Patient specific 3D MSE maps

7.6.1 Intracardiac electrogram analysis from AF patient2

Figure 7-13 shows the patient-specific 3D MSE map with τ =3 in four different views. MSE approach suggests more localized areas of higher MSE particularly in the region of the septum near the right sided pulmonary veins, posterior aspect of the right veins and posterior wall. The right sided septum, due to far field LA signals, however may reflect a false positive. The high density of MSE in the area of the right veins suggests a high possibility of active site. Although, MSE reveals several focal regions of potentially active sites, no specific clinical information can be derived especially on rotor

identification. Overlapping high CFAE, late activation regions and high MSE can be observed with the 3D MSE around the RA LA septum and right sided PV regions.

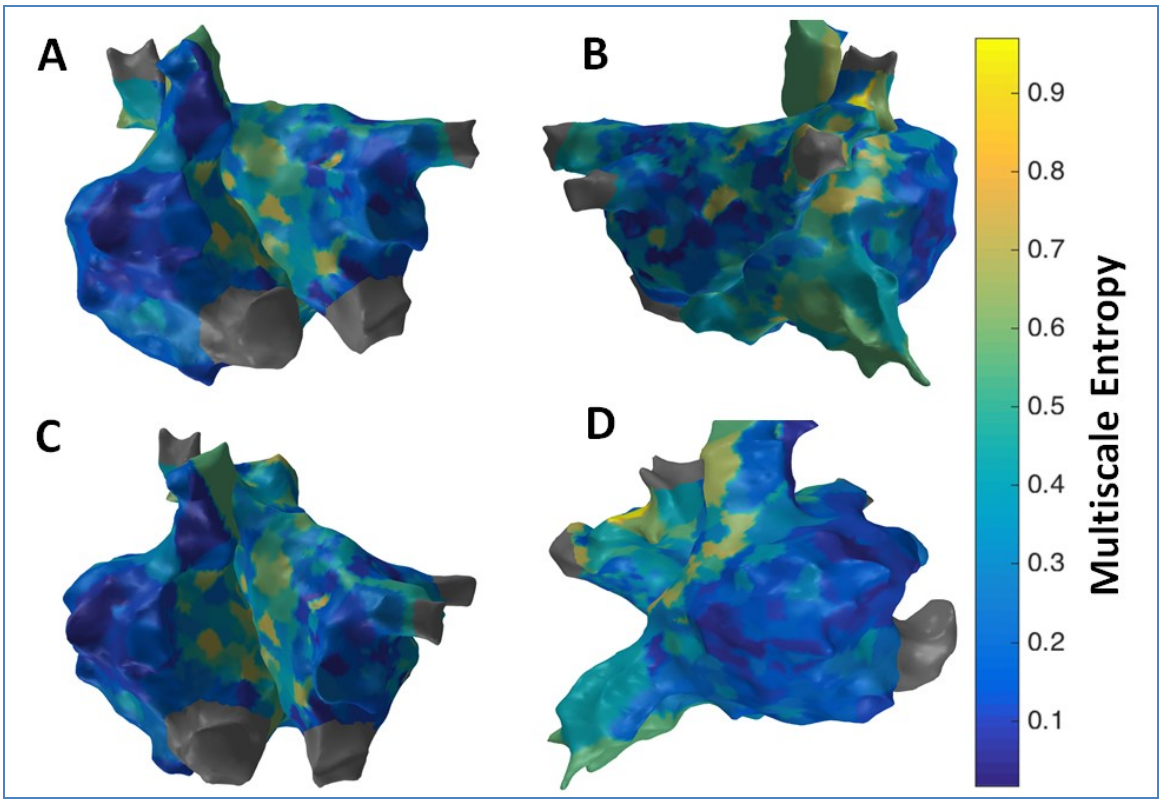

Figure 7-13: 3D MSE map from persistent AF patient # 2*. (A) Antero-Posterior view; (B) Postero-Anterior view; (C) Left Anterior Oblique (LAO) view; (D) Right Anterior Oblique (RAO) view.*

7.7 Patient specific 3D RPDE maps

7.7.1 Intracardiac electrogram analysis from AF patient2

Figure 7-14 shows the patient-specific 3D RPDE map in four different views. RPDE approach suggests more localized areas of higher RPDE particularly in the region of the septum near the right sided pulmonary veins, superior vena cava (SVC), lateral RA and anterior region of inferior vena cava (IVC). Similar to the results from 3D MSE map, 3D RPDE map shows focal areas at the right sided septum, and around SVC and IVC regions

suggesting potentially active sites. Overlapping high CFAE, late activation regions and high RPDE can be observed with the 3D RPDE map around the RA LA septum and right sided PV regions. However, no specific clinical information can be derived especially on rotor identification or confirm the presence of rotors themselves.

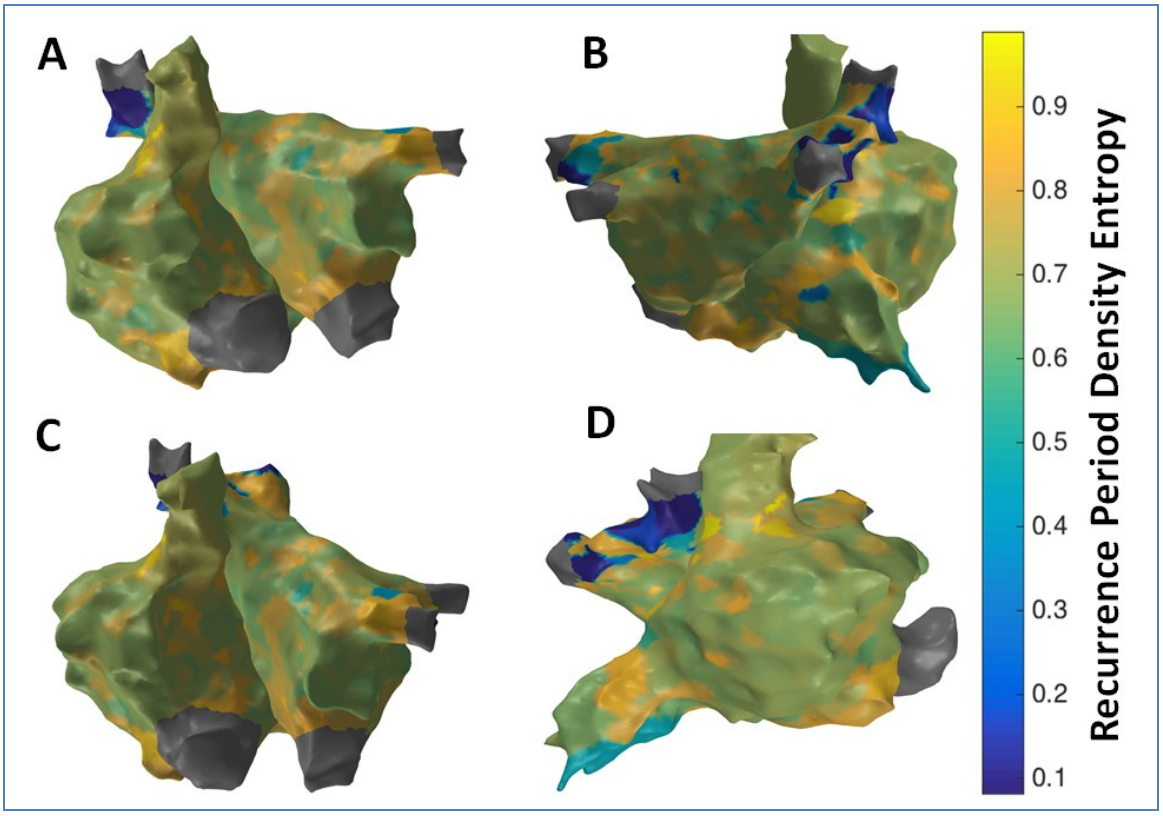

Figure 7-14: 3D RPDE map from persistent AF patient # 2*. (A) Antero-Posterior view; (B) Postero-Anterior view; (C) Left Anterior Oblique (LAO) view; (D) Right Anterior Oblique (RAO) view*

7.8 Patient specific 3D kurtosis maps

7.8.1 Intracardiac electrogram analysis from AF patient2

Figure 7-15 shows the patient-specific 3D kurtosis map in four different views. Kurtosis approach suggests more localized areas of higher kurtosis particularly at anterior regions of IVC, SVC, right sided septum and right sided pulmonary veins.

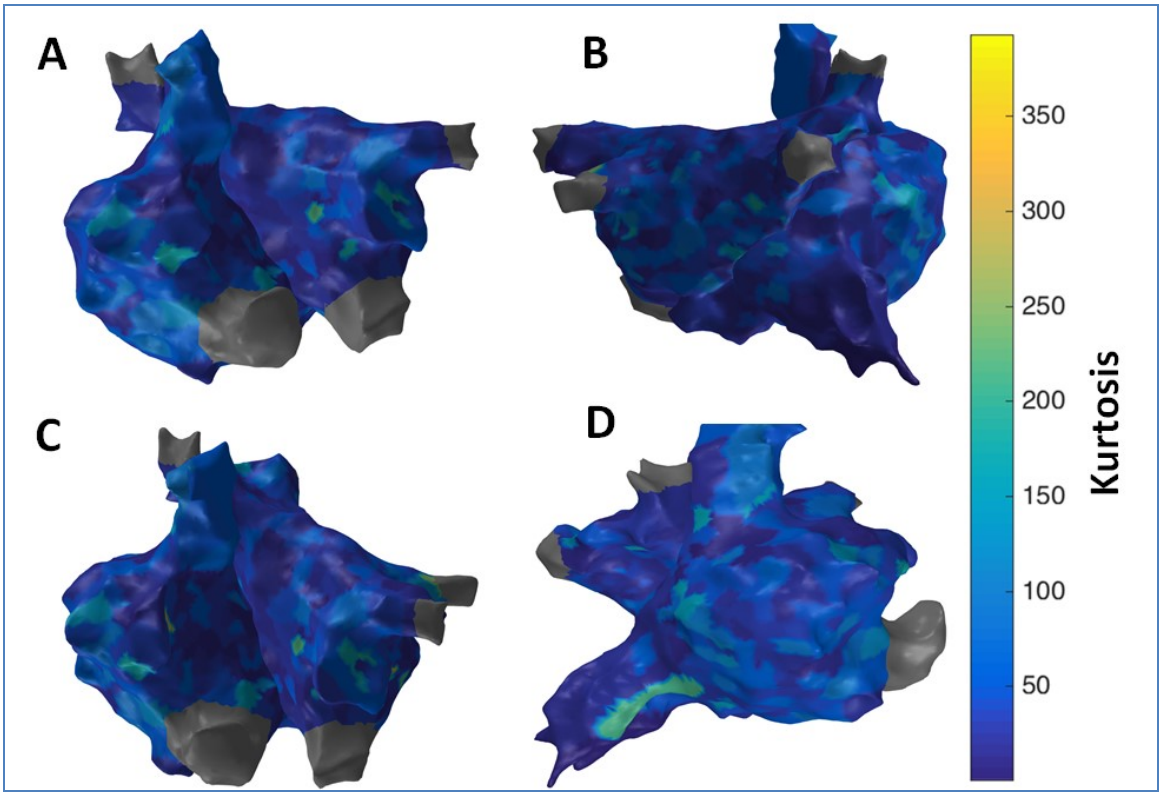

Figure 7-15: 3D kurtosis map from persistent AF patient # 2*. (A) Antero-Posterior view; (B) Postero-Anterior view; (C) Left Anterior Oblique (LAO) view; (D) Right Anterior Oblique (RAO) view*

The focal regions with high kurtosis seen from Fig 4-50 suggest potentially active sites. Overlapping high CFAE, late activation regions and high kurtosis can also be observed with the 3D kurtosis map around the RA LA septum and right sided PV regions. However, no specific clinical information can be derived especially on rotor identification or confirm the presence of rotors themselves.

7.9 Patient specific 3D IMF maps

7.9.1 Intracardiac electrogram analysis from AF patient2

Figures 7-16 and 7-17 shows the EMD of the regular and high CFAE electrograms shown in Figs 7-2 and 7-3.

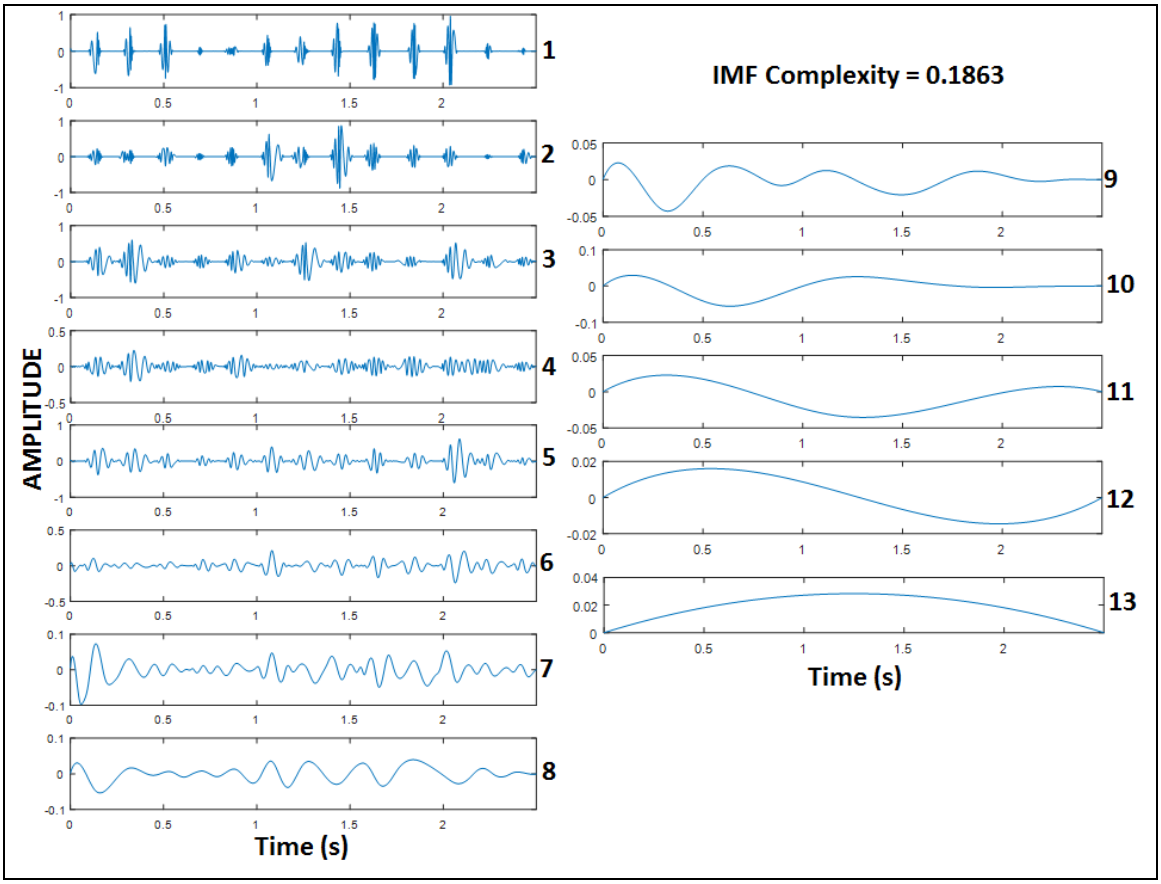

Figure 7-16: Intrinsic mode functions for the regular electrogram from a persistent AF patient. *The electrogram was decomposed into 13 IMF's and the IMF complexity was estimated to be 0.1863.*

As seen from Fig 7-16 13 IMF's were required to decompose the regular electrogram. The IMF complexity was estimated to be 0.1863 for this electrogram using the 2nd, 3rd and 4th IMFs only. Fig. 7-17 shows that only 11 IMF's were required to decompose the high CFAE electrogram. However, IMF complexity was estimated to be 0.3892 for this electrogram using the 2nd, 3rd and 4th IMFs only. This result is interesting, because although fewer IMFs were required to describe the high CFAE electrogram, the IMF complexity was higher than that of the regular electrogram.

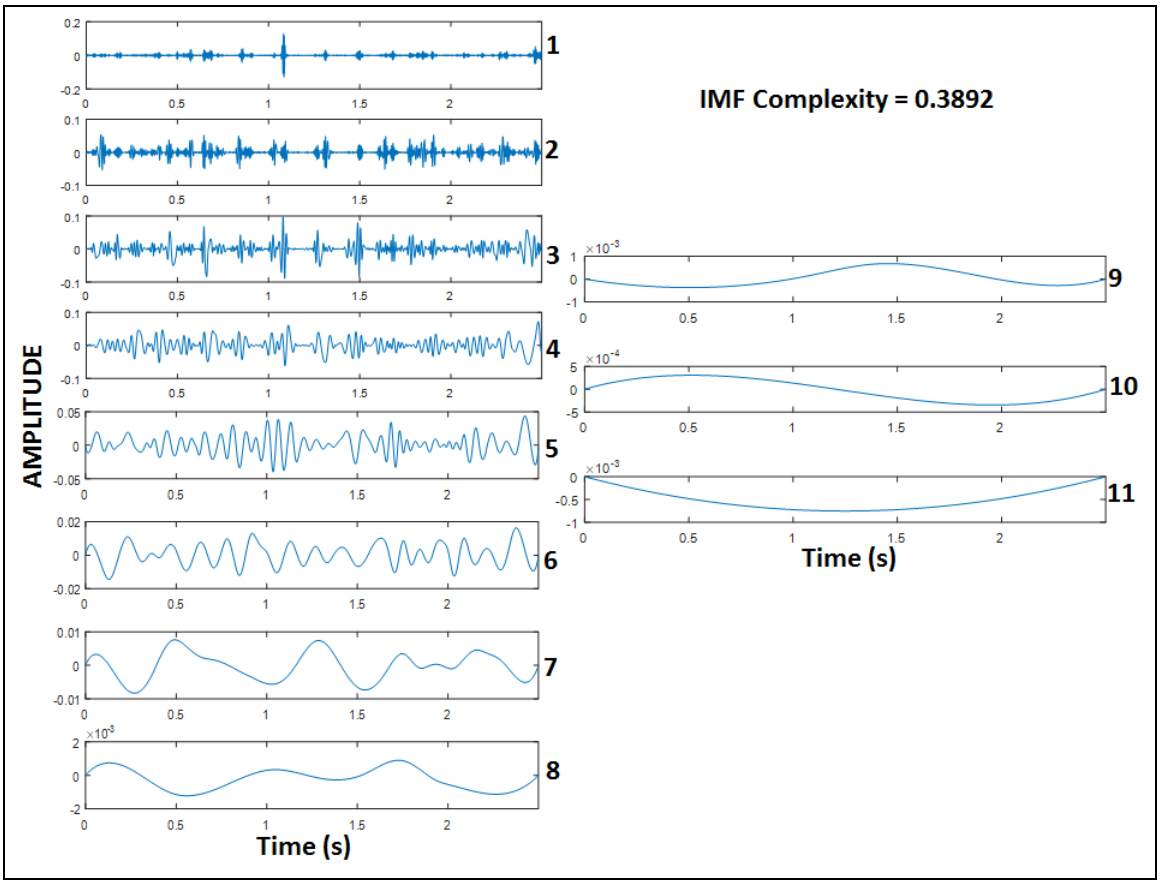

Figure 7-17: Intrinsic mode functions for the high CFAE electrogram from a persistent AF patient. *The electrogram was decomposed into 11 IMF's and the IMF complexity was estimated to be 0.3892.*

A possible, reason for this result is that, the first 4 IMF's of the high CFAE electrogram were much more complex than the first four IMFs of the regular electrogram as evident from figures 7-16 and 7-17 resulting in higher IMF complexity of the high CFAE electrogram. Figure 7-18 shows the patient-specific 3D IMF complexity map in four different views. IMF complexity using EMD approach suggests more localized areas of higher complexity particularly in the region of the septum near the right sided pulmonary veins, and anterior regions of SVC and IVC. Similar to the results from 3D MSE (Fig 7-13) and 3D RPDE (Fig 7-14) map, 3D IMF complexity map in Fig 7-18

shows focal areas at the right sided septum, and around SVC and IVC regions suggesting potentially active sites. Overlapping high CFAE, late activation regions and high IMF complexity can be observed with the 3D IMF complexity map around the RA LA septum and right sided PV regions. However, no specific clinical information can be derived especially on rotor identification or confirm the presence of rotors themselves.

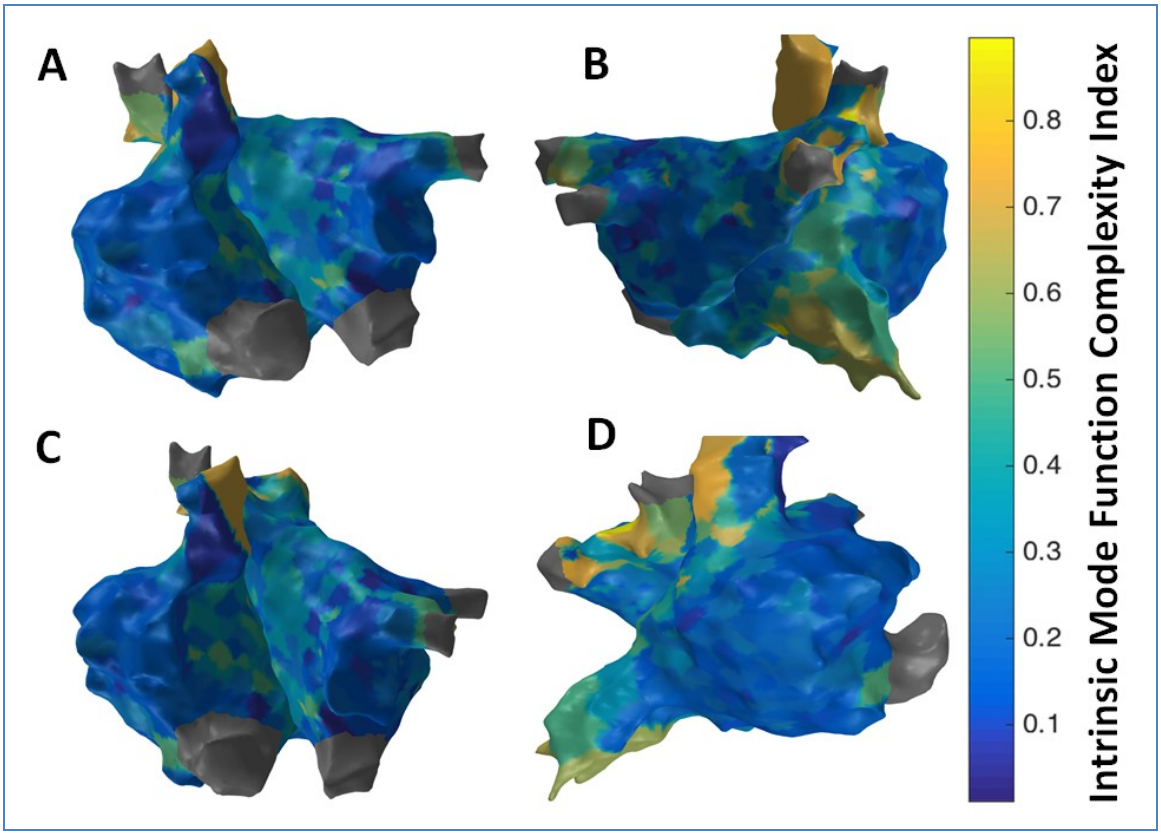

Figure 7-18: 3D IMF map from persistent AF patient # 2*. (A) Antero-Posterior view; (B) Postero-Anterior view; (C) Left Anterior Oblique (LAO) view; (D) Right Anterior Oblique (RAO) view.*

7.10 Patient specific 3D MSF maps

7.10.1 Intracardiac electrogram analysis from AF patient2

Figure 7-19 shows the patient-specific 3D MSF map in four different views.

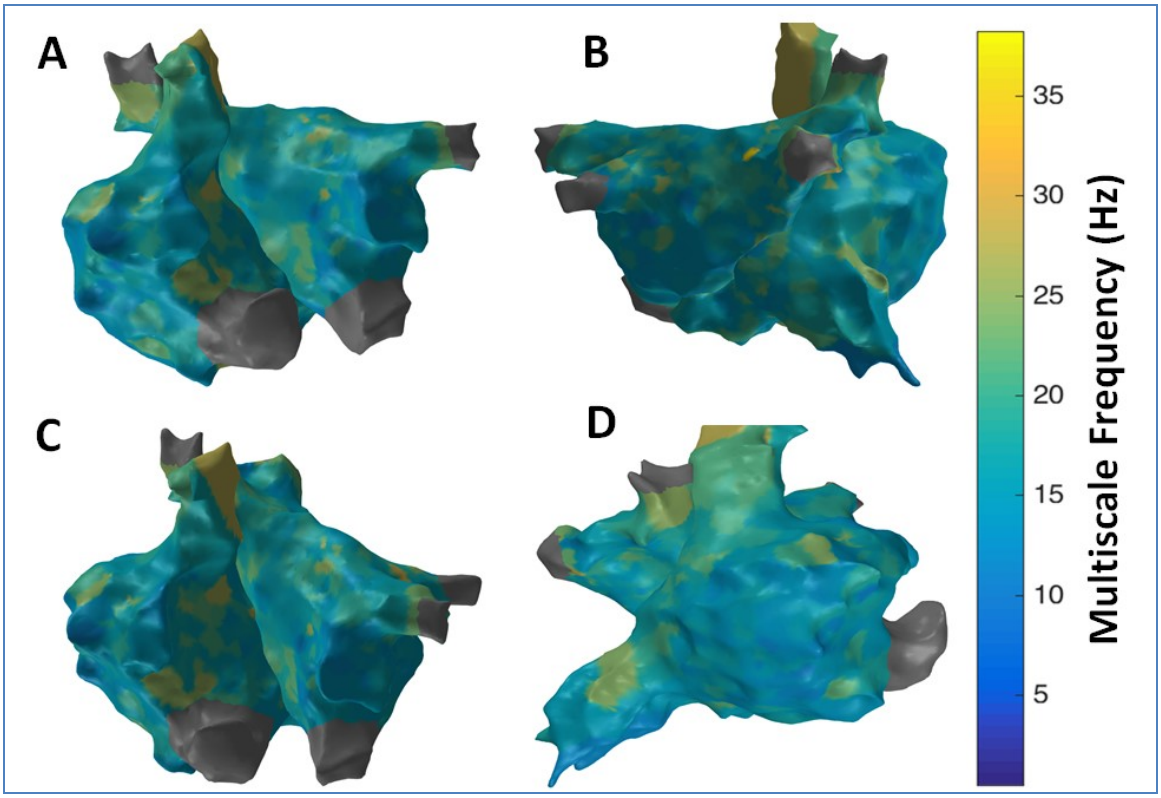

Figure 7-19: 3D MSF map from persistent AF patient # 2*. (A) Antero-Posterior view; (B) Postero-Anterior view; (C) Left Anterior Oblique (LAO) view; (D) Right Anterior Oblique (RAO) view.*

MSF approach suggests more localized areas of higher MSF particularly in the region of the septum near the right sided pulmonary veins, superior vena cava (SVC), lateral RA and anterior region of inferior vena cava (IVC). Bottom panels of Figs. 7-7 and 7-8 shows the power spectrum of electrogram at a CFAE low and CFAE high region that demonstrates the presence of various frequencies at the CFAE high region, which should have higher MSF compared to the CFAE low region. Similar to the results from 3D MSE (Fig 7-13) and 3D RPDE (Fig 7-14) and, 3D IMF complexity (Fig 7-18) maps, 3D MSF map in Figure 7-19 shows focal areas at the right sided septum, and around SVC and IVC regions suggesting potentially active sites. Overlapping high CFAE, late activation

regions and high MSF can be observed with the 3D MSF map around the RA LA septum and right sided PV regions. However, no specific clinical information can be derived especially on rotor identification or confirm the presence of rotors themselves.

7.11 Analysis and comparison of computational times for various approaches

Novel temporal and frequency domain approaches were developed in this thesis and the results demonstrate their efficacy and robustness to accurately identify rotor core regions compared to periphery. Since these approaches exploit different temporal and frequency characteristics of the time series signal their computational power can vary significantly. Therefore, it is important to perform computation time analysis to ensure that these approaches can provide reliable and robust 3D maps in near-real time as the electrogram are acquired in a clinical setting.

To perform the computational analysis two sets of data were chosen: (i) optical mapping data from the double rotor data at pixel location '2' with TS length of 5995 and (ii) intracardiac electrogram from high CFAE point with TS length of 2500. The intracardiac electrogram was approximately twice the length of the optical data analyzed in this section. The analysis was performed on a desktop workstation with Intel ® Core™ i7-6000 CPU @ 3.41 GHz, 16 GB RAM on a 64-bit Windows operating system. Table 4-1 tabulates the key feature for each of the approaches used in this thesis and the computing time for both the datasets.

As seen from Table 7-1, the computing times for SE, RE, DF and kurtosis takes merely less than a fraction of second irrespective of the time series length. MSF took only 0.45 s for both data regardless of their differences in the TS lengths.

Table 7-1: Computational times for different electrogram analysis approaches

Approach	**Key feature of the approach**	**Optical Mapping Data Computing Time (s) TS length = 5995**	**Intracardiac Electrogram Data Computing Time (s) TS length = 2500**
SE	Uncertainty of data in linear space	0.05	0.04
RE	Uncertainty of data in linear space	0.06	0.05
DF	Peak Frequency	0.04	0.03
MSE (τ=1)	Repetitiveness in linear space	1.45	0.85
MSE (τ=2)		1.84	1.21
MSE (τ=3)		2.01	1.48
RPDE	Repetitiveness in phase space	1.61	1.42
Kurtosis	Peakedness of PDF	0.01	0.01
EMD	Complexity of IMF's	3.01	2.33
MSF	Average instantaneous frequency	0.45	0.45

Computing times for MSE approach increased slightly with increase in scale factors from τ=1, 2 and 3 for both datasets with slightly higher values for the optical data due to its higher TS length. The optimal choice for scale factor i.e. τ =3 took 2.01 s for the optical data and 1.48 s for the electrogram. This implies that for at least 1000 spatial points in a clinical setting when processed separately it takes about 25 minutes to compute MSE. However, in a real-setting parallel processing can be employed with supercomputing capabilities which will reduce these times to more reasonable times to obtain 3D maps for near real time guidance. RPDE for both data sets took over a second while EMD approach took the largest amount of time 2-3 s due to the complexity

involved in decomposing the signal first and then performing entropy calculations for 3 IMF's to obtain the final IMF complexity index.

7.12 Limitations of Novel Electrogram analysis approaches

In this thesis four novel time domain based electrogram analysis methods were proposed and implemented such as MSE, RPDE, kurtosis and IMF complexity using EMD and one frequency domain approach namely MSF. The results from rigorous noise testing (Chapter 4) and analysis with several optical and electrogram data (Chapter 6) demonstrated robustness with noise and accurately estimated rotor pivot point with better contrast compared to the periphery. Following section discusses the limitation of each of the approaches while considering translation efforts for intracardiac electrogram processing to obtain patient specific 3D maps.

Limitation of the MSE approach

A limitation of the MSE technique is the need to select a correct choice of the time scale factor 'τ'. Since the nearest neighbor moving averaging is employed, large time scales will cause excessive smoothing of the data which may lead to loss of some complexity information. Therefore, caution should be used in the appropriate choice of scaling factor. The results from this study suggest that a scale factor of $\tau = 3$ may be a reasonable starting point for many applications, but clinical validation is needed.

Limitation of the RPDE approach

RPDE is a robust method to quantify repetitiveness in the phase space. However, a challenge exists in choosing the right size for the dimension 'M' and time delay 'τ' for the given time series data for analysis. Improper choice could lead to invalid or 'Not a

Number – NaN‘ estimates if the mapping from linear space to phase space for the chosen dimension and time delay is invalid based on the nature of the time series data. The results from this study suggest that a time delay factor of $\tau = 2$ and “M=3’ for dimension may be a reasonable starting point for many applications, but clinical validation is needed.

Limitation of kurtosis approach

Kurtosis measures the ‘peakedness’ of the PDF of the time series. Flickering or strong perturbations while acquiring the time series data can make the data to reach more extreme values close to a transition. Such effects can lead to a rise in the kurtosis of a time series prior to the transition and the distribution may become ‘leptokurtic’ wherein the tails of the time series distribution become flatter due to the increased presence of rare values in the time series. This might cause ambiguity in the kurtosis estimation. Manual inspection of the data might be necessary if virtual increase in kurtosis is observed to reduce ambiguity.

Limitation of the EMD approach

A limitation with EMD approach is the requirement to satisfy the conditions needed for robust decomposition of the time series data discussed in Chapter 3. If the time series does not meet these requirements, calculating the envelopes from the extrema becomes impossible resulting in failure to decompose and IMF complexity cannot be estimated. Additionally, the stoppage criteria used for the sifting process should be robust enough so that convergence is achieved in a reasonable amount of time.

Limitation of the MSF approach

The MSF estimates in this thesis were computed as the simple average of the outputs from the 8 filter banks that are separated by a bandwidth 'B' of $2\sqrt{2}$, and one octave apart. However, many non-stationary signals such as ECG and electrograms can vary significantly with its frequency contents with time which implies that a simple average of the filter bank outputs may under estimate or overestimate the final MSF used for analysis. This might cause ambiguity and lead to inaccurate discrimination between the rotor core and periphery if the time series is changing significantly with its frequency content over time. Therefore, performing weighted average instead of simple average can reduce this ambiguity if some *a priori* knowledge of the changing frequency contents is possible to obtain. Also, designing and implementing adaptive filter banks can provide more robust MSF estimates for complex non-stationary time series such as ECG and intracardiac electrogram.

7.13 Discussion

The feasibility of using conventional catheter mapping system to generated patient-specific 3D maps was demonstrated that can potentially provide near-real time clinical guidance during ablation in clinical setting, thereby achieving the objectives of this section of the thesis. Patient specific 3D maps were obtained for a persistent AF patient by processing the electrograms obtained from a pentarray catheter with sequential acquisition using the novel approaches developed in this thesis. The optical mapping data used in this thesis was depolarization data obtained using voltage-sensitive dyes in isolated ex-vivo rabbit heart model of ventricular arrhythmia. Since intracardiac

electrograms also represent depolarization data measured from the electrodes, the novel signal processing techniques developed in this thesis that was validated using optical mapping depolarization data is translatable for quantitative intracardiac electrogram analysis. However, confirming the existence of rotors in human AF is extremely challenging although several group have demonstrated with their custom methods, there are no known reliable methods, and therefore rotor pivot point identification as suitable ablation targets to terminate AF becomes an open question, which needs several clinical studies to reliably demonstrate the presence of rotors in first place.

The results from the 3D maps from the novel approaches revealed several focal regions of high complexity in the 3D MSE, RPDE, IMF and MSF maps. These maps demonstrated the possibility of active sites at RA LA septum, right sided pulmonary veins and anterior regions of SVC and IVC with high complexity from these various time domain and frequency domain techniques. However, no clinical inferences could be made on rotor identification or even the presence of rotors. Nevertheless, these 3D maps demonstrated the fact that active sites were present outside the PV region for a persistent AF patient which is consistent with the literature. The results also suggest the necessity to use a comprehensive 3D map that takes into account information from these various techniques that can possibly provide a faithful focal region of interest that may be an active site. Validation with several AF patient datasets is required to make clinical inference son the pattern of complexity regions in these patients to assess whether or not rotors could be present and if rotor pivot points were identified using these techniques.

A major limitation of using these novel approaches validated with optical mapping data is that optical data from the animal model is high resolution uniform data and mostly noise free. Intracardiac mapping is achieved with sequential mapping that acquires sparse data throughout the atria with very low resolution and contaminated with various noises such as baseline wander noise, VFF and other high frequency noise. In this thesis, bipolar electrograms were used which is relatively free from VFF noise compared to unipolar electrograms. However, slight degree of VFF contamination is always possible depending on the spatial location of the mapping catheter. No preprocessing was performed in the intracardiac electrograms to obtain the 3D maps, which might have affected the results to slight extent if indeed VFF noise was present in some of the processed electrograms. Therefore, future work should include VFF noise removal approaches to reduce ambiguity from VFF noise contamination. Nevertheless, these novel approaches offers promise in providing new avenues for electrogram analysis for possible rotor localization with more controlled animal and human studies. These improved methods can further be validated to demonstrate whether or not ablation at these rotor pivot points in humans can essentially terminate AF permanently which can create a paradigm shift in the clinical management of patients with AF.

7.14 Conclusions

This chapter has demonstrated the feasibility of generating patient specific 3D maps using conventional catheter mapping system. Several focal areas of active sites were implied in a persistent AF patient though these different 3D maps, however no clinical inferences could be made. Also, the results with focal regions of higher complexity do

not imply the presence of rotor pivot points or the presence of rotors themselves. Rigorous testing with several clinical datasets from both paroxysmal and persistent AF patients is required for validation of these results that may provide new insights into rotor identification using these novel approaches. The results confirm that the author successfully achieved the overall objectives of this thesis work, which was to develop novel quantitative electrogram analysis methods for rotor identification that is translatable for analyzing clinical electrogram to generate patient specific 3D maps that can potentially provide near-real time clinical guidance for AF ablation.

CHAPTER 8: CONCLUSIONS AND RECOMMENDATIONS FOR FUTURE WORK

This thesis aimed to develop and validate novel quantitative electrogram analysis techniques that will accurately identify rotor pivot points as suitable targets for ablation to terminate AF. The thesis attempted to provide new avenues for rotor mapping to further advance catheter ablation procedure to successfully terminate AF and other arrhythmias. The objectives were achieved using digital signal processing (DSP) and time series analysis techniques demonstrating feasibility to obtain patient specific 3D maps.

In this work, the author developed several time domain based techniques and a frequency domain based technique in exploiting various temporal and electrical characteristics of the electrograms enabling precise identification of the rotor pivot points. This chapter presents the overall conclusions of the work presented in this thesis. It also provides the author's recommendations for future work in the field to address several challenges in translating novel techniques in processing intracardiac electrograms for real-time visualization of 3D maps that can provide invaluable insights to the electrophysiologist to make inferences and guide catheter ablation to terminate AF and other complex arrhythmias.

8.1 Conclusions

In this work the author successfully developed several novel quantitative electrogram analysis techniques using DSP and time series analysis methods for rotor pivot point identification using MATLAB software. Specifically, the author exploited specific characteristic of the electrogram for each novel technique which is significantly different

at the rotor pivot points compared to the periphery which enabled these techniques for precise identification of the rotor pivot point.

The limitations of the signal processing techniques in conventionally used mapping approaches such as LAT, DF, CFAE and phase mapping motivate novel quantitative approaches in this thesis work. Symbolic dynamics approach with Shannon Entropy and Renyi Entropy to capture the complexity by quantifying the regularity and repetitiveness of the time series data to identify the rotor pivot yielded results that were opposite to what was expected with SE and RE showing lower values at the rotor core compared to the periphery, although enabling its identification. This motivated the author to investigate the reasons behind the unexpected results which led to an important finding that SE and RE are limited for complexity analysis for long time series data. The electrograms and optical mapping data used in this thesis were short time series data only up to 3.5 s which challenged SE and RE approaches.

The MSE technique with nearest-neighbor moving average kernel was developed to overcome the limitations of SE and RE in capturing the complexity by quantifying the regularity and repetitiveness of the new time series data. The results with white, pink and brown noise, simulated sinusoidal and flat baseline ECG signal demonstrated the efficacy of the MSE technique in capturing the complexity better than SE. MSE robustly discriminated NSR and AF on a single lead ECG. The robustness of MSE technique in rotor pivot point identification was demonstrated from the results of MSE in accurately identifying rotor pivot points in single and double rotor optical data. MSE also successfully tracked the rotor pivot point of meandering rotor in both simulated and

optical mapping data. The results indicate that a scale factor $\tau = 3$ is a reasonable choice to ensure reliable identification without excessive smoothing of the data. 3D MSE map for a persistent AF patient indicated potential active sites in the left atrial regions.

Recurrence period density entropy was developed to capture the complexity of the time series data by quantifying the periodicity, or repetitiveness of a signal in phase space unlike MSE approach which can also demonstrate robustness with short time series data. The efficacy of RPDE approach was demonstrated by the results in single, double and meandering rotors performing better than SE and RE approach. The time delay factor and the embedding dimension 'M' for the RPDE approach should be carefully chosen to ensure accurate results in complexity quantification. 3D RPDE map showed higher RPDE values in the regions similar to MSE approach with little less contrast with the surrounding regions.

Kurtosis is the 4^{th} central moment that quantifies the 'peaknedness' of time series data which was investigated as a statistical approach to quantify the complexity of the electrogram time series data for rotor pivot point identification. Precise identification of rotor pivot points was demonstrated with kurtosis for the single and double rotor. For the optical mapping meandering rotor data kurtosis map showed similar tracking patterns like MSE. However, results from the numerically simulated meandering rotor were inconclusive. 3D kurtosis maps showed higher kurtosis regions slightly different than the other techniques. Kurtosis is highly sensitive to noise and the results could vary significantly in the presence of various noise sources in a clinical setting.

The complexity index of the 2nd, 3rd and 4th intrinsic mode functions of the electrogram time series data was quantified using EMD for accurate rotor pivot point identification. The results from single and double rotor demonstrated better contrast with the active rotor pivot zones compared to periphery with a lager region than the other approaches. This may be indicative the EMD quantifies the complexity of the pixels near the rotor core much better than any other approach due to the nature of EMD. 3D IMF map demonstrated active regions similar to that of MSE and MSF maps.

MSF technique captured the chaotic frequency components that distinguished the rotor pivot point and the periphery thus enabling accurate identification. Precise identification of rotor pivot points in single and double rotors demonstrated the efficacy of this approach. MSF robustly discriminated NSR and AF on a single lead ECG without any preprocessing steps. The robustness of MSF technique in rotor pivot point identification was demonstrated from the results of MSE in accurately identifying rotor pivot points in single and double rotor optical data. MSF also successfully tracked the rotor pivot point of meandering rotor in both simulated and optical mapping data similar to MSE results. 3D MSF map for a persistent AF patient indicated potential active sites in the left atrial regions much similar to the 3D MSE map.

The newly developed quantitative electrogram analysis techniques in this thesis work captured the complexity of the time series by quantifying different properties of the data and all of them identified rotor pivot points accurately. The robustness of these different approaches offers the platform for faithful location and ablation of active sites that may cause and maintain AF. The end point of successful ablation is the permanent termination

of AF without affecting the normal myocardium which is the most crucial step for the ablation process and no recurrence of AF.

An important challenge that exists with clinical electrogram analysis for rotor identification is the confirmation of the presence of rotors itself. As evident from the 8 different 3D maps, none of these approaches can confirm the presence of rotors rather illustrate the presence of potential active substrate targets that may cause and maintain AF. Therefore, clinical translation of these novel approaches requires additional work to generate 3D maps which can provide more insights into the organization and localization of rotors for precise location of ablation target points such as the rotor pivot point. On the basis of these inferences, the author makes several recommendations for future work in the following section that will guide through this translation process which has high clinical utility.

8.2 Recommendations for future work

This thesis demonstrated the efficacy and robustness of the several novel quantitative electrogram processing approaches in accurate rotor identification. The 3D maps of a persistent AF patient from these approaches although indicated potential active sites in both the left and right atria outside the PV area, further work is required for successful utility of these approaches for rotor identification in AF and other arrhythmias. Following are the recommendations of the author for successful translation of these novel approaches for clinical utility in the cardiac catheter lab for AF ablation:

(1) Spatial and temporal resolution analysis of newly developed techniques

Intracardiac electrograms are acquired in a sequential fashion with a pentarray electrode system at different temporal points for each spatial location the electrodes were positioned for acquisition. This approach significantly challenges accurate quantification of the spatio-temporal organization of rotors and therefore its precise location in a clinical setting. The newly developed techniques demonstrated robustness in high resolution optical mapping data with known pivot points which is exactly the opposite in the case of intracardiac electrograms which are acquired with low spatial resolution with the uncertainty of the rotor presence. On the basis of this finding, the author recommends a thorough investigation of the influence of spatial and temporal resolution on the accuracy of rotor pivot point identification with all the newly developed approaches. The accuracy of these methods with varying spatial and temporal resolution can be quantified and compared that will further elaborate on the findings of this thesis work. Additionally, since intracardiac electrograms are obtained with sequential approach at varying time points, it results in sparse data. In addition to performing uniform spatial resolution analysis, the techniques should be rigorously tested with sparse data by randomly creating sparse data from optical mapping data with known rotor pivot points, and perform blinded analysis using these novel approaches to compare the results with phase singularity analysis. This approach can yield invaluable information on the performance of each of these techniques that represent the clinical setting of acquiring and processing intracardiac electrogram that can provide suitable directions for clinical translation.

(2) Correlation analysis between the different techniques

Correlation analysis between the different techniques can provide useful insights into organization and localization of these rotors that can guide AF ablation. In particular information from LAT, CFAE, DF and phase mapping from intracardiac electrograms should also be used in combination of these novel approaches to obtain a comprehensive map that can provide accurate representation of the spatio-temporal organization of the rotors thus enabling its precise location. Since DF produces uniform DF regions, DF maps can guide to outline overall rotor zone. It has been established that rotor periphery has low CFAE-mean while rotor core has high CFAE-mean while lower activation time occurs near pivot point and higher activation times near the periphery. Additionally, phase singularity analysis can provide valuable insights into rotor core. This information in conjunction with the results from the newly developed approaches can be correlated to obtain a comprehensive 3D map that will improve identification of pivotal regions of persistent AF in human as a robust estimate of potential AF ablation site on a patient specific manner.

(3) Comparison of electrogram analysis between paroxysmal and persistent AF patients

The author recommends performing a comparative electrogram analysis using these novel approaches between paroxysmal and persistent AF patients to demonstrate the location of active sites with respect to the PV region. Consistent identification of active sites within the PV region for paroxysmal patients and outside PV regions for persistent patient is a validation of previous findings. A comprehensive map based on correlation analysis can help identify precise location of rotor pivot points in the atrial regions to

guide catheter ablation. These results can further justify the rationale for advanced ablation strategies for persistent AF patients in the right and left atrium outside the PV regions to permanently terminate AF and reduce recurrence rates.

(4) Intracardiac electrogram analysis of AF patients before and after ablation

The author recommend performing intracardiac electrogram analysis of AF patients using these novel approaches and also obtain the comprehensive map described in recommendation (2) before and after ablation to demonstrate inefficiency of currently used clinical methods. Conventional lesion sets target active sites only within the PV region even for persistent AF patients. By obtaining electrograms before and after such procedure and comparing their 3D maps will yield invaluable information on the inadequacy of this procedure which will bring a paradigm shift in AF ablation strategies for persistent AF patients. This approach will add more time to the procedure than needed for the conventional mapping, and therefore appropriate IRB approvals and consent from the patient should be acquired prior to the procedure.

(5) Performing ex vivo animal studies with near-real time rotor pivot point identification and ablation

The author recommends performing experiments using *ex vivo* animal models with induced ventricular arrhythmias to optically map the rotors and perform near-real time rotor pivot point identification analysis to obtain 2D maps from these novel approaches. Ablation targeting the identified rotor pivot point locations should be performed in an attempt to terminate the rotor and hence the arrhythmia. Successful ablation using rotor

pivot points identified by these approaches can be a paradigm shift in the clinical diagnosis and treatment of AF and other arrhythmias using these novel approaches.

(6) Investigation of real-time 3D visualization approaches

The 3D maps were generated in this work with offline analysis using custom MATLAB software by superimposing the processed electrograms on the 3D anatomic map at their corresponding spatial locations. The author recommend investigating optimal workflow and processing pipeline to obtain electrograms that can processed in real time during acquisitions to obtain 3D maps in near-real time to be available for the electrophysiologist for making quick observations and inferences for the next course of action for the catheter ablation procedure. The overall goal robust quantitative electrogram analysis techniques are its real-time availability in the clinical setting to guide patient specific catheter ablation. The challenges of 'integration' of these techniques with the commercial catheter mapping system are a major bottleneck which should be explored for an easily adaptable approach.

REFERENCES

[1] Chugh SS, Havmoeller R, Narayanan K, Singh D, Rienstra M, Benjamin EJ, Gillum RF, Kim Y-H, McAnulty JH, Zheng Z-J, Forouzanfar MH, Naghavi M, Mensah GA, Ezzati M & Murray CJL (2014).Worldwide epidemiology of atrial fibrillation: a Global Burden of Disease 2010 Study. *Circulation.* 129, 837–847.

[2] Chen LY, Shen WK. Epidemiology of atrial fibrillation: a current perspective. *Heart Rhythm.* 2007; 4:S1–S6.

[3] Nattel S. (2002) New ideas about atrial fibrillation 50 years on. *Nature* 415: 219-226.

[4] Haissaguerre M, Jais P, Shah DC, Takahashi A, Hocini M, Quiniou G, Garrigue S, Le Mouroux A, Le Metayer P, Clementy J. Spontaneous initiation of atrial fibrillation by ectopic beats originating in the pulmonary veins. *N Engl J Med.* 1998; 339:659–666.

[5] Haissaguerre M, Shah DC, Jais P, Hocini M, Yamane T, Deisenhofer I, Garrigue S, Clementy J. Mapping-guided ablation of pulmonary veins to cure atrial fibrillation. *American Journal of Cardiology.* 2000; 86:9K–19K.

[6] Pandit SV, Jalife J (2013) Rotors and the dynamics of cardiac fibrillation. *Circ Res.* 112: 849-862.

[7] Narayan SM, and Jalife J. "CrossTalk proposal: Rotors have been demonstrated to drive human atrial fibrillation." *The Journal of physiology.* 592, no. 15 (2014): 3163-3166.

[8] Calkins H, Kuck KH, Cappato R, Brugada J, Camm AJ, et al. (2012) 2012 HRS/EHRA/ECAS Expert Consensus Statement on Catheter and Surgical Ablation of Atrial Fibrillation: Recommendations for Patient Selection, Procedural Techniques, Patient Management and Follow-up, Definitions, Endpoints, and Research Trial Design: A report of the Heart Rhythm Society (HRS) Task Force on Catheter and Surgical Ablation of Atrial Fibrillation. Developed in partnership with the European Heart Rhythm Association (EHRA), a registered branch of the European Society of Cardiology (ESC) and the European Cardiac Arrhythmia Society (ECAS); and in collaboration with the American College of Cardiology (ACC), American Heart Association (AHA), the Asia Pacific Heart Rhythm Society (APHRS), and the

Society of Thoracic Surgeons (STS). Endorsed by the governing bodies of the American College of Cardiology Foundation, the American Heart Association, the European Cardiac Arrhythmia Society, the European Heart Rhythm Association, the Society of Thoracic Surgeons, the Asia Pacific Heart Rhythm Society, and the Heart Rhythm Society. *Heart Rhythm.* 9: 632-696.e621.

[9] Oral H, Pappone C, Chugh A, Good E, Bogun F, Pelosi F Jr, Bates ER, Lehmann MH, Vicedomini G, Augello G, Agricola E, Sala S, Santinelli V, Morady F. Circumferential pulmonary-vein ablation for chronic atrial fibrillation. *N Engl J Med.* 2006; 354:934–941. [PubMed: 16510747]

[10] Elayi CS, Di Biase L, Barrett C, Ching CK, al Aly M, et al. (2010) Atrial fibrillation termination as a procedural endpoint during ablation in long-standing persistent atrial fibrillation. *Heart Rhythm*. 7: 1216-1223.

[11] Schmitt C, Ndrepepa G, Weber S, Schmieder S, Weyerbrock S, et al. (2002) Biatrial multisite mapping of atrial premature complexes triggering onset of atrial fibrillation. *Am J Cardiol.* 89: 1381-1387.

[12] Baumert M, Sanders P, Ganesan A. Quantitative-electrogram-based methods for guiding catheter ablation in atrial fibrillation. *Proceedings of the IEEE*. 2016 Feb; 104(2):416-31.

[13] Hurst JW, Schlant, RC, Rackley, CE, Sonnenblick, EH, Wenger, NK (eds.), *The Heart: Arteries and Veins*. McGraw-Hill, New York, 7th ed., 1990, pp.2274-2280.

[14] Texas Heart Institute: Heart Information Center. Accessed January 15, 2017 from http://www.texasheart.org/HIC/Anatomy/systole.cfm

[15] Nerbonne JM, Kass RS. Molecular physiology of cardiac repolarization. *Physiological reviews*. 2005 Oct 1; 85(4):1205-53.

[16] Klabunde R. *Cardiovascular physiology concepts*. Lippincott Williams & Wilkins; 2011 Nov 3.

[17] Macfarlane PW, Lawrie, TDV (eds.), *Comprehensive Electrocardiology: Theory and Practice in Health and Disease*, Pergamon Press, New York., 1st ed., Vol. 1, 2, and 3, 1989, pp. 1785.

[18] Ganesan P, Sterling M, Ladavich S, Ghoraani B. Computer-Aided Clinical Decision Support Systems for Atrial Fibrillation. In *Computer-aided Technologies - Applications in Engineering and Medicine*. March 2017. pp. 91-119. http://dx.doi.org/10.5772/65620

[19] Huff J. *ECG workout: Exercises in arrhythmia interpretation*. Lippincott Williams & Wilkins; 2006.

[20] Widmaier EP, Raff H and Strang KT. *Human Physiology: The Mechanisms of Body Function*. McGraw-Hill, New York, 10th ed., 2006, pp. 397.

[21] Wilson FN, Johnston FD, Macleod AG, Barker PS. Electrocardiograms that represent the potential variations of a single electrode. *American Heart Journal*. 1934 Apr 1; 9(4):447-58.

[22] Ng J, Goldberger JJ. *Practical Signal and Image Processing in Clinical Cardiology*. 2010. Springer London.

[23] Stevenson WG, Soejima K. Recording techniques for clinical electrophysiology. *Journal of cardiovascular electrophysiology*. 2005 Sep 1;16(9):1017-22.

[24] Fuster V, Rydén LE, Cannom DS, Crijns HJ, Curtis AB, Ellenbogen KA, Halperin JL, Le Heuzey JY, Neal KG, Lowe JE, Bertil OS. Guidelines for the management of patients with atrial fibrillation. Executive summary. *Revista española de cardiología*. 2006 Dec; 59(12):1329.

[25] National Collaborating Centre for Chronic Conditions (Great Britain). Atrial fibrillation: national clinical guideline for management in primary and secondary care. 2006. *Royal College of Physicians*.

[26] Crawford T. Left atrial diastolic dysfunction: a new complication after catheter ablation for atrial fibrillation? 2011. *Heart Rhythm.* 8:1372-1373.

[27] Stewart S, Hart CL, Hole DJ, McMurray JJ. A population-based study of the long-term risks associated with atrial fibrillation: 20-year follow-up of the Renfrew/Paisley study. *The American journal of medicine.* 2002 Oct 1; 113(5):359-64.

[28] Camm AJ, Kirchhof P, Lip GY, Schotten U, Savelieva I, Ernst S, Van Gelder IC, Al-Attar N, Hindricks G, Prendergast B, Heidbuchel H. Guidelines for the management of atrial fibrillation. *European heart journal.* 2010 Aug 29:ehq278.

[29] Center for disease Control (CDC) Division for Heart Disease and Stroke Prevention. Atrial Fibrillation Fact Sheet. Accessed January 15, 2017 from https://www.cdc.gov/dhdsp/data_statistics/fact_sheets/fs_atrial_fibrillation.htm

[30] Lip GY, Golding DJ, Nazir M, Beevers DG, Child DL, Fletcher RI. A survey of atrial fibrillation in general practice: the West Birmingham Atrial Fibrillation Project. *Br J Gen Pract.* 1997 May 1;47(418):285-9.

[31] Lloyd-Jones DM, Wang TJ, Leip EP, Larson MG, Levy D, Vasan RS, D'Agostino RB, Massaro JM, Beiser A, Wolf PA, Benjamin EJ. Lifetime risk for development of atrial fibrillation. *Circulation.* 2004 Aug 31; 110(9):1042-6.

[32] Atrial Fibrillation; Symptoms and causes. Accessed January 15, 2017 from http://www.mayoclinic.org/diseases-conditions/atrial-fibrillation/symptoms-causes/dxc-20164936

[33] Winterberg H. Studien u¨ber herzflimmern. I. U ber die wirkung des N. vagus und accelerans auf das Flimmern des Herzens. *Pflugers Arch Physiol.* 1907. 117, 223-256.

[34] Scherf D. Studies on auricular tachycardia caused by aconitine administration. *Proceedings of the Society for Experimental Biology and Medicine*. 1947. 64:233-239.

[35] Moe GK, Abildskov JA. Atrial fibrillation as a self-sustaining arrhythmia independent of focal discharge. *American heart journal.* 1959 Jul 1;58(1):59-70.

[36] Moe GK, Rheinboldt W, Abildskov J (1964) A computer model of atrial fibrillation. *American Heart Journal.* 67: 200-220.

[37] Issa Z, Miller JM, Zipes DP. Clinical Arrhythmology and Electrophysiology: A Companion to Braunwald's Heart Disease: Expert Consult: Online and Print. *Elsevier Health Sciences*; 2012 Apr 24.

[38] Allessie M, Lammers W, Bonke F, and Holen J. *Cardiac Electrophysiology and Arrhythmias*. New York: Grune & Stratton, 1985, ch. Experimental evaluation of Moe's multiple wavelet hypothesis of atrial fibrillation, pp. 265-276.

[39] Cox JL, Canavan TE, Schuessler RB, Cain ME, Lindsay BD, Stone C, Smith PK, Corr PB, Boineau JP. The surgical treatment of atrial fibrillation. II. Intraoperative electrophysiologic mapping and description of the electrophysiologic basis of atrial flutter and atrial fibrillation. *The Journal of thoracic and cardiovascular surgery*. 1991 Mar;101(3):406-26.

[40] Lee S, Sahadevan J, Khrestian CM, Durand DM, Waldo AL (2013) High density mapping of atrial fibrillation during vagal nerve stimulation in the canine heart: restudying the Moe hypothesis. *J Cardiovasc Electrophysiol.* 24: 328-335.

[41] Haissaguerre M, Sanders P, Hocini M, Takahashi Y, Rotter M, et al. (2005a) Catheter Ablation of Long-Lasting Persistent Atrial Fibrillation: Critical Structures for Termination. *Journal of Cardiovascular Electrophysiology.* 16: 1125-1137.

[42] Herweg B, Kowalski M, Steinberg JS (2003) Termination of persistent atrial fibrillation resistant to cardioversion by a single radiofrequency application. Pacing *Clin Electrophysiol.* 26: 1420-1423.

[43] Narayan SM, Krummen DE, Shivkumar K, Clopton P, Rappel W-J, et al. (2012d) Treatment of Atrial Fibrillation by the Ablation of Localized Sources: The Conventional Ablation for Atrial Fibrillation With or Without Focal Impulse and Rotor Modulation (CONFIRM) Trial. *J Am Coll Cardiol*. 60: 628-636.

[44] Tzou WS, Saghy L, Lin D (2011) Termination of persistent atrial fibrillation during left atrial mapping. *J Cardiovasc Electrophysiol.* 22: 1171-1173.

[45] Jalife J, Berenfeld O, Mansour M. Mother rotors and fibrillatory conduction: a mechanism of atrial fibrillation. *Cardiovascular research*. 2002 May 1;54(2):204-16.

[46] Schuessler RB, Grayson TM, Bromberg BI, Cox JL, Boineau JP (1992) Cholinergically mediated tachyarrhythmias induced by a single extrastimulus in the isolated canine right atrium. *Circ Res.* 71: 1254-1267.

[47] Davidenko JM, Pertsov AV, Salomonsz R, Baxter W, Jalife J (1992) Stationary and drifting spiral waves of excitation in isolated cardiac muscle. *Nature.* 355: 349-351.

[48] Veenhuyzen GD, Simpson CS, Abdollah H. MEchanisms of Disease - Atrial Fibrillation. *Canadian Medical Association Journal.* September 28, 2004 vol. 171 no. 7 755-760.

[49] Berenfeld O, Mandapati R, Dixit S, Skanes AC, Chen JA, Mansour M, Jalife J. Spatially Distributed Dominant Excitation Frequencies Reveal Hidden Organization in Atrial Fibrillation in the Langendorff-Perfused Sheep Heart. *Journal of cardiovascular electrophysiology*. 2000 Aug 1; 11(8):869-79.

[50] Chou CC, Chang PC, Wen MS, Lee HL, Chen TC, et al. (2011) Epicardial ablation of rotors suppresses inducibility of acetylcholine-induced atrial fibrillation in left pulmonary vein-left atrium preparations in a beagle heart failure model. *J Am Coll Cardiol.* 58: 158-166.

[51] Wu T-J, Doshi RN, Huang H-LA, Blanche C, Kass RM, et al. (2002) Simultaneous Biatrial Computerized Mapping During Permanent Atrial Fibrillation in Patients with Organic Heart Disease. *J Cardiovasc Electrophysiol.* 13: 571 - 577.

[52] Lazar S, Dixit S, Marchlinski FE, Callans DJ, Gerstenfeld EP (2004) Presence of Left-to-Right Atrial Frequency Gradient in Paroxysmal but Not Persistent Atrial Fibrillation in Humans. *Circulation.* 110: 3181-3186.

[53] Sahadevan J, Ryu K, Peltz L, Khrestian CM, Stewart RW, et al. (2004) Epicardial Mapping of Chronic Atrial Fibrillation in Patients: Preliminary Observations. *Circulation.* 110: 3293-3299.

[54] Sanders P, Berenfeld O, Hocini M, Jais P, Vaidyanathan R, et al. (2005) Spectral analysis identifies sites of high-frequency activity maintaining atrial fibrillation in humans. *Circulation.* 112: 789-797.

[55] Gerstenfeld EP, Sahakian AV, Swiryn S. Evidence for transient linking of atrial excitation during atrial fibrillation in humans. *Circulation.* 1992; 86:375-382.

[56] Dewire J, Calkins H. State-of-the-art and emerging technologies for atrial fibrillation ablation. *Nature Reviews Cardiology.* 2010 Mar 1;7(3):129-38

[57] Atienza F, Almendral J, Jalife J, Zlochiver S, Ploutz-Snyder R, Torrecilla EG, Arenal A, Kalifa J, Fernandez-Aviles F, Berenfeld O. Real-time dominant frequency mapping and ablation of dominant frequency sites in atrial fibrillation with left-to-

right frequency gradients predicts long-term maintenance of sinus rhythm. *Heart Rhythm.* 2009; 6:33-40.

[58] Chen J, Mandapati R, Berenfeld O, Skanes AC, Gray RA, Jalife J. Dynamics of wavelets and their role in atrial fibrillation in the isolated sheep heart. *Cardiovasc Res.* 2000; 48:220-232.

[59] Mansour M, Mandapati R, Berenfeld O, Chen J, Samie FH, Jalife J. Left-to-right gradient of atrial frequencies during acute atrial fibrillation in the isolated sheep heart. *Circulation.* 2001;103: 2631-2636.

[60] Sarmast F, Kolli A, Zaitsev A, Parisian K, Dhamoon AS, Guha PK, Warren M, Anumonwo JMB, Taffet SM, Berenfeld O, Jalife J. Cholinergic atrial fibrillation: I-k,i-ach gradients determine unequal left/right atrial frequencies and rotor dynamics. *Cardiovasc Res.* 2003; 59:863-873.

[61] Guillem MS, Climent AM, Rodrigo M, Fernández-Avilés F, Atienza F, Berenfeld O. Presence and stability of rotors in atrial fibrillation: evidence and therapeutic implications. *Cardiovascular research.* 2016 Jan 19:cvw011.

[62] Jais P, Haissaguerre M, Shah DC, Chouairi S, Gencel L, Hocini M, Clementy J. A focal source of atrial fibrillation treated by discrete radiofrequency ablation. *Circulation*. 1997; 95:572-576

[63] Gray RA, Jalife J, Panfilov AV, Baxter WT, Cabo C, Davidenko JM, Pertsov AM. Mechanisms of cardiac fibrillation. *Science.* 1995; 270:1222-1223

[64] Cabo C, Pertsov AM, Davidenko JM, Baxter WT, Gray RA, Jalife J. Vortex shedding as a precursor of turbulent electrical activity in cardiac muscle. *Biophys J.* 1996; 70:1105-1111.

[65] Iravanian S, Nabutovsky Y, Kong CR, Saha S, Bursac N, Tung L. Functional reentry in cultured monolayers of neonatal rat cardiac cells. *Am J Physiol Heart Circ Physiol.* 2003; 285:H449-456.

[66] Baxter WT, Mironov SF, Zaitsev AV, Jalife J, Pertsov AM. Visualizing excitation waves inside cardiac muscle using transillumination. *Biophys J.* 2001; 80:516-530

[67] Yamazaki M, Filgueiras-Rama D, Berenfeld O, Kalifa J. Ectopic and reentrant activation patterns in the posterior left atrium during stretch-related atrial fibrillation. *Prog Biophys Mol Biol.* 2012; 110:269-277.

[68] Mandapati R, Skanes A, Chen J, Berenfeld O, Jalife J. Stable microreentrant sources as a mechanism of atrial fibrillation in the isolated sheep heart. *Circulation.* 2000; 101:194-199.

[69] Kneller J, Zou R, Vigmond EJ, Wang Z, Leon LJ, Nattel S. Cholinergic atrial fibrillation in a computer model of a two- dimensional sheet of canine atrial cells with realistic ionic properties. *Circ Res*. 2002; 90:E73-E87.

[70] Berenfeld O, Pertsov AM. Dynamics of intramural scroll waves in three-dimensional continuous myocardium with rotational anisotropy. *J Theor Biol.* 1999; 199: 383-394.

[71] Wellner M, Berenfeld O, Jalife J, Pertsov AM. Minimal principle for rotor filaments. *Proc Natl Acad Sci.* 2002; 99:8015-8018.

[72] Cherry EM, Ehrlich JR, Nattel S, Fenton FH. Pulmonary vein reentry--properties and size matter: Insights from a computational analysis. *Heart Rhythm.* 2007; 4:1553-1562.

[73] Calvo CJ, Deo M, Zlochiver S, Millet J, Berenfeld O. Attraction of rotors to the pulmonary veins in paroxysmal atrial fibrillation: A modeling study. *Biophys J.* 2014; 106:1811-1821.

[74] Cha TJ, Ehrlich JR, Zhang L, Chartier D, Leung TK, Nattel S. Atrial tachycardia remodeling of pulmonary vein cardiomyocytes: Comparison with left atrium and potential relation to arrhythmogenesis. *Circulation.* 2005; 111:728-735.

[75] Yamazaki M, Mironov S, Taravant C, Brec J, Vaquero LM, Bandaru K, Avula UM, Honjo H, Kodama I, Berenfeld O, Kalifa J. Heterogeneous atrial wall thickness and stretch promote scroll waves anchoring during atrial fibrillation. *Cardiovasc Res.* 2012; 94:48-57.

[76] Hansen BJ, Zhao J, Csepe TA, Moore BT, Li N, Jayne LA, Kalyanasundaram A, Lim P, Bratasz A, Powell KA, Simonetti OP, Higgins RS, Kilic A, Mohler PJ, Janssen PM, Weiss R, Hummel JD, Fedorov VV. Atrial fibrillation driven by micro-

anatomic intramural re-entry revealed by simultaneous sub-epicardial and sub-endocardial optical mapping in explanted human hearts. *Eur Heart J.* 2015; 36:2390-2401.

[77] Tanaka K, Zlochiver S, Vikstrom KL, Yamazaki M, Moreno J, Klos M, Zaitsev AV, Vaidyanathan R, Auerbach DS, Landas S, Guiraudon G, Jalife J, Berenfeld O, Kalifa J. Spatial distribution of fibrosis governs fibrillation wave dynamics in the posterior left atrium during heart failure. *Circ Res.* 2007; 101:839-847.

[78] Pandit SV, Berenfeld O, Anumonwo J, Zaritski R, Kneller J, Nattel S, Jalife J. Ionic determinants of functional reentry in a 2-d model of human atrial cells during simulated chronic atrial fibrillation. *Biophys J.* 2005.

[79] Samie FH, Mandapati R, Gray RA, Watanabe Y, Zuur C, Beaumont J, Jalife J. A mechanism of transition from ventricular fibrillation to tachycardia: Effect of calcium channel blockade on the dynamics of rotating waves. *Circ Res.* 2000; 86:684-691.

[80] Bollmann A, Sonne K, Esperer HD, Toepffer I, Klein HU. Patients with persistent atrial fibrillation taking oral verapamil exhibit a lower atrial frequency on the ecg. *Ann Noninvasive Electrocardiol*. 2002; 7:92-97.

[81] Filgueiras-Rama D, Martins RP, Mironov S, Yamazaki M, Calvo CJ, Ennis SR, Bandaru K, Noujaim SF, Kalifa J, Berenfeld O, Jalife J. Chloroquine terminates stretch-induced atrial fibrillation more effectively than flecainide in the sheep heart. *Circ Arrhythm Electrophysiol.* 2012; 5:561-570.

[82] Kalifa J, Jalife J, Zaitsev AV, Bagwe S, Warren M, Moreno J, Berenfeld O, Nattel S. Intraatrial pressure increases rate and organization of waves emanating from the superior pulmonary veins during atrial fibrillation. *Circulation.* 2003; 108:668-671.

[83] Schuessler RB, Grayson TM, Bromberg BI, Cox JL, Boineau JP. Cholinergically mediated tachyarrhythmias induced by a single extrastimulus in the isolated canine right atrium. *Circ Res.* 1992; 71:1254-1267.

[84] Ganesan AN, Kuklik P, Lau DH, Brooks AG, Baumert M, Lim WW, Thanigaimani S, Nayyar S, Mahajan R, Kalman JM, Roberts-Thomson KC. Bipolar electrogram shannon entropy at sites of rotational activation: implications for ablation

of atrial fibrillation. *Circulation: Arrhythmia and Electrophysiology*. 2012 Jan 1:CIRCEP-112.

[85] Lin WS, Tai CT, Hsieh MH, Tsai CF, Lin YK, Tsao HM, Huang JL, Yu WC, Yang SP, Ding YA, Chang MS, Chen SA. Catheter ablation of paroxysmal atrial fibrillation initiated by nonpulmonary vein ectopy. *Circulation.* 2003; 107:3176-3183.

[86] Sahadevan J, Ryu K, Peltz L, Khrestian CM, Stewart RW, Markowitz AH, Waldo AL. Epicardial mapping of chronic atrial fibrillation in patients: Preliminary observations. *Circulation*. 2004; 110:3293-3299.

[87] Guillem MS, Climent AM, Castells F, Husser D, Millet J, Arya A, Piorkowski C, Bollmann A. Noninvasive mapping of human atrial fibrillation. *J Cardiovasc Electrophysiol*. 2009; 20:507-513.

[88] Cuculich PS, Wang Y, Lindsay BD, Faddis MN, Schuessler RB, Damiano RJ, Jr., Li L, Rudy Y. Noninvasive characterization of epicardial activation in humans with diverse atrial fibrillation patterns. *Circulation.* 2010; 122:1364-1372.

[89] Haissaguerre M, Hocini M, Shah AJ, Derval N, Sacher F, Jais P, Dubois R. Noninvasive panoramic mapping of human atrial fibrillation mechanisms: A feasibility report. *J Cardiovasc Electrophysiol*. 2013; 24:711-717.

[90] Narayan SM, Krummen DE, Shivkumar K, Clopton P, Rappel WJ, Miller JM. Treatment of atrial fibrillation by the ablation of localized sources: Confirm (conventional ablation for atrial fibrillation with or without focal impulse and rotor modulation) trial. *J Am Coll Cardiol.* 2012; 60:628-636.

[91] Wijffels MC, Kirchhof CJ, Dorland R, Allessie MA. Atrial fibrillation begets atrial fibrillation. *Circulation.* 1995 Oct 1; 92(7):1954-68.

[92] Van Gelder IC, Hagens VE, Bosker HA, Kingma JH, Kamp O, Kingma T, Said SA, Darmanata JI, Timmermans AJ, Tijssen JG, Crijns HJ. A comparison of rate control and rhythm control in patients with recurrent persistent atrial fibrillation. *New England Journal of Medicine*. 2002 Dec 5; 347(23):1834-40.

[93] Wyse DG, Waldo AL, DiMarco JP, Domanski MJ, Rosenberg Y, Schron EB, Kellen JC, Greene HL, Mickel MC, Dalquist JE, Corley SD. Atrial Fibrillation

Follow-up Investigation of Rhythm Management (AFFIRM) Investigators. A comparison of rate control and rhythm control in patients with atrial fibrillation. *N Engl J Med.* 2002 Dec 5; 347(23):1825-33.

[94] Lown B, Amarasingham R, Neuman J. New method for terminating cardiac arrhythmias. Use of synchronized capacitor discharge. *Jama*. 1962 Nov; 182:548-55.

[95] Cox JL, Schuessler RB, Lappas DG, Boineau JP. An 8 1/2-year clinical experience with surgery for atrial fibrillation. *Annals of surgery.* 1996 Sep; 224(3):267.

[96] Cox JL. Cardiac surgery for arrhythmias. *Pacing and clinical electrophysiology.* 2004 Feb 1; 27(2):266-82.

[97] Packer DL, Asirvatham S, Munger TM. Progress in nonpharmacologic therapy of atrial fibrillation. *Journal of cardiovascular electrophysiology.* 2003 Dec 1; 14(s12):S296-309.

[98] Natale A. Atrial fibrillation in 2012: Advances in catheter-ablation treatment of AF. *Nature Reviews Cardiology.* 2013 Feb 1; 10(2):63-4.

[99] Chen YH, Lu ZY, Hou JW, Wang Q, Lin H, Li YG. Cryoablation vs. radiofrequency ablation for treatment of paroxysmal atrial fibrillation: a systematic review and meta-analysis. *Europace.* 2017 Jan 8:euw330.

[100] Bhakta D, Miller JM. Principles of electroanatomic mapping. *Indian Pacing Electrophysiol J.* 2008 Jan;8(1):32-50.

[101] Pappone C, Oreto G, Lamberti F, Vicedomini G, Loricchio ML, Shpun S, Rillo M, Calabro MP, Conversano A, Ben-Haim SA, Cappato R. Catheter ablation of paroxysmal atrial fibrillation using a 3D mapping system. *Circulation.* 1999 Sep 14; 100(11):1203-8.

[102] Pappone C, Rosanio S, Oreto G, Tocchi M, Gugliotta F, Vicedomini G, Salvati A, Dicandia C, Mazzone P, Santinelli V, Gulletta S. Circumferential radiofrequency ablation of pulmonary vein ostia. *Circulation.* 2000 Nov 21; 102(21):2619-28.

[103] Keane D, Ruskin J. Pulmonary vein isolation for atrial fibrillation. *Rev Cardiovasc Med.* 2002; 3(4):167-75.

[104] Hocini M, Nault I, Wright M, Veenhuyzen G, Narayan SM, Jaïs P, Lim KT, Knecht S, Matsuo S, Forclaz A, Miyazaki S. Disparate evolution of right and left atrial rate during ablation of long-lasting persistent atrial fibrillation. *Journal of the American College of Cardiology*. 2010 Mar 9; 55(10):1007-16.

[105] Haïssaguerre M, Sanders P, Hocini M, Hsu LF, Shah DC, Scavée C, Takahashi Y, Rotter M, Pasquié JL, Garrigue S, Clémenty J. Changes in atrial fibrillation cycle length and inducibility during catheter ablation and their relation to outcome. *Circulation.* 2004 Jun 22; 109(24):3007-13.

[106] Ernst S, Ouyang F, Löber F, Antz M, Kuck KH. Catheter-induced linear lesions in theleft atrium in patients with atrial fibrillation: An electroanatomic study. *Journal of the American College of Cardiology.* 2003 Oct 1; 42(7):1271-82.

[107] Nademanee K, McKenzie J, Kosar E, Schwab M, Sunsaneewitayakul B, Vasavakul T, Khunnawat C, Ngarmukos T. A new approach for catheter ablation of atrial fibrillation: mapping of the electrophysiologic substrate. *Journal of the American College of Cardiology.* 2004 Jun 2; 43(11):2044-53.

[108] Hunter RJ, Diab I, Tayebjee M, Richmond L, Sporton S, Earley MJ, Schilling RJ. Characterization of Fractionated Atrial Electrograms Critical for Maintenance of Atrial Fibrillation Clinical Perspective. *Circulation: Arrhythmia and Electrophysiology.* 2011 Oct 1; 4(5):622-9.

[109] Catheter Ablation vs Anti-arrhythmic Drug Therapy for Atrial Fibrillation Trial (CABANA). Accessed March 21 2017 from https://clinicaltrials.gov/ct2/show/NCT00911508

[110] Rosenbaum D, Jalife J, editors. *Optical mapping of cardiac excitation and arrhythmias.* Wiley-Blackwell; 2001 Dec 3

[111] Salama, G., & Choi, B. R. Optical mapping of impulse propagation in the atrioventricular node. In D. S. Rosenbaum & J. Jalife (Eds.), *Optical mapping of cardiac excitation and arrhythmias.* 2001. pp. 177–196). Futura.

[112] Arora R, Das MK, Zipes DP, Wu J. Optical mapping of cardiac arrhythmias. *Indian pacing and electrophysiology journal.* 2003 Oct; 3(4):187.

[113] Gray RA, Pertsov AM, Jalife J. Spatial and temporal organization during cardiac fibrillation. *Nature.* 1998 Mar 5; 392(6671):75-8.

[114] Massé S, Downar E, Chauhan V, Sevaptsidis E, Nanthakumar K. Ventricular fibrillation in myopathic human hearts: mechanistic insights from in vivo global endocardial and epicardial mapping. *American Journal of Physiology-Heart and Circulatory Physiology.* 2007 Jun 1; 292(6):H2589-97.

[115] PhysioNet and PhysioBank. Accessed January 15 2017 from https://physionet.org/users/

[116] Scherlag BJ, Samet P, Helfant RH. His bundle electrogram. *Circulation.* 1972 Sep 1; 46(3):601-13.

[117] Pieper CF, Blue R, Pacifico A. Simultaneously collected monopolar and discrete bipolar electrograms: comparison of activation time detection algorithms. *Pacing and Clinical Electrophysiology.* 1993 Mar 1; 16(3):426-33.

[118] Berenfeld O, Zaitsev AV, Mironov SF, Pertsov AM, Jalife J. Frequency-dependent breakdown of wave propagation into fibrillatory conduction across the pectinate muscle network in the isolated sheep right atrium. *Circulation research.* 2002 Jun 14; 90(11):1173-80.

[119] Elvan A, Linnenbank AC, Misier AR, Delnoy PP, Beukema WP, Jacques MT. Dominant frequency of atrial fibrillation correlates poorly with atrial fibrillation cycle length. *Circulation: Arrhythmia and Electrophysiology.* 2009 Jan 1: CIRCEP-108.

[120] Iyer AN, Gray RA. An experimentalist's approach to accurate localization of phase singularities during reentry. *Annals of biomedical engineering.* 2001 Jan 1; 29(1):47-59.

[121] Cappato R, Calkins H, Chen SA, Davies W, Iesaka Y, Kalman J, Kim YH, Klein G, Natale A, Packer D, Skanes A. Up-dated worldwide survey on the methods, efficacy and safety of catheter ablation for human atrial fibrillation. *Circulation: Arrhythmia and Electrophysiology.* 2009 Jan 1: CIRCEP-109.

[122] Yoshida K, Chugh A, Good E, Crawford T, Myles J, Veerareddy S, Billakanty S, Wong WS, Ebinger M, Pelosi F, Jongnarangsin K. A critical decrease in dominant

frequency and clinical outcome after catheter ablation of persistent atrial fibrillation. *Heart Rhythm.* 2010 Mar 31; 7(3):295-302.

[123] Schilling C. Analysis of Atrial Electrograms. *Karlsruhe transactions on biomedical engineering*. 2012. 17.

[124] Stiles MK, Brooks AG, Kuklik P, John B, Dimitri H, Lau DH, Wilson L, Dhar S, ROBERTS-THOMSON RL, Mackenzie L, Young GD. High-Density Mapping of Atrial Fibrillation in Humans: Relationship Between High-Frequency Activation and Electrogram Fractionation. *Journal of cardiovascular electrophysiology.* 2008 Dec 1; 19(12):1245-53.

[125] Zhao J, Yao Y, Huang W, Shi R, Zhang S, LeGrice IJ, Lever NA, Smaill BH. Novel methods for characterization of paroxysmal atrial fibrillation in human left atria. *The open biomedical engineering journal.* 2013; 7:29.

[126] Faes L, Nollo G, Antolini R, Gaita F, Ravelli F. A method for quantifying atrial fibrillation organization based on wave-morphology similarity. *IEEE Transactions on Biomedical Engineering.* 2002 Dec; 49(12):1504-13.

[127] Shannon CE. A mathematical theory of communication. ACM SIGMOBILE *Mobile Computing and Communications Review.* 2001 Jan 1;5(1):3-55.

[128] Kamath, C. Entropy-Based Algorithm to Detect Life Threatening Cardiac Arrhythmias Using Raw Electrocardiogram Signals. *Middle-East Journal of Scientific Research,* 12 (10): 1403-1412, 2012.

[129] Orozco-Duque A, Ugarte JP, Tobón C, Saiz J, Bustamante J. Approximate entropy can localize rotors, but not ectopic foci during chronic atrial fibrillation: A simulation study. In *Computing in Cardiology Conference (CinC),* 2013 2013 Sep 22 (pp. 903-906). IEEE.

[130] Ugarte JP, Orozco-Duque A, Tobón C, Kremen V, Novak D, Saiz J, Oesterlein T, Schmitt C, Luik A, Bustamante J. Dynamic approximate entropy electroanatomic maps detect rotors in a simulated atrial fibrillation model. *PloS one.* 2014 Dec 9; 9(12):e114577.

[131] Hoekstra B, Diks CG, Allessie MA, Goedb J. Nonlinear analysis of epicardial atrial electrograms of electrically induced atrial fibrillation in man. *Journal of cardiovascular electrophysiology.* 1995 Jun 1; 6(6):419-40.

[132] Corino VD, Sassi R, Mainardi LT, Cerutti S. Signal processing methods for information enhancement in atrial fibrillation: Spectral analysis and non-linear parameters. *Biomedical Signal Processing and Control.* 2006 Oct 31; 1(4):271-81.

[133] Botteron GW, Smith JM. A technique for measurement of the extent of spatial organization of atrial activation during atrial fibrillation in the intact human heart. *IEEE Transactions on Biomedical Engineering.* 1995 Jun; 42(6):579-86.

[134] Lovett EG, Ropella KM. Time-frequency coherence analysis of atrial fibrillation termination during procainamide administration. *Annals of biomedical engineering.* 1997 Nov 1; 25(6):975-84.

[135] Richter U, Faes L, Ravelli F, Sornmo L. Propagation pattern analysis during atrial fibrillation based on sparse modeling. *IEEE Transactions on Biomedical Engineering.* 2012 May; 59(5):1319-28.

[136] Arunachalam, SP., and Brown, LF. Real-time estimation of the ECG-derived respiration (EDR) signal using a new algorithm for baseline wander noise removal. In Engineering in Medicine and Biology Society, 2009. EMBC 2009. *Annual International Conference of the IEEE*, 5681-5684 (2009).

[137] Brown LF and Arunachalam SP. Real-time T-P knot algorithm for baseline wander noise removal from the electrocardiogram. *Biomedical Sciences Instrumentation.* 45, 65-70 (2009).

[138] Brown LF and Arunachalam SP. Real-time estimation of the ecg-derived respiration (edr) signal. *Biomedical Sciences Instrumentation*. 45, 59-64 (2009).

[139] Verma A, Lakkireddy D, Wulffhart Z, Pillarisetti J, Farina D, Beardsall M, Whaley B, Giewercer D, Tsang B, Khaykin Y. Relationship Between Complex Fractionated Electrograms (CFE) and Dominant Frequency (DF) Sites and Prospective Assessment of Adding DF-Guided Ablation to Pulmonary Vein Isolation in Persistent Atrial Fibrillation (AF). *Journal of cardiovascular electrophysiology.* 2011 Dec 1; 22(12):1309-16.

[140] Atienza F, Almendral J, Ormaetxe JM, Moya Á, Martínez-Alday JD, Hernández-Madrid A, Castellanos E, Arribas F, Arias MÁ, Tercedor L, Peinado R. Comparison of radiofrequency catheter ablation of drivers and circumferential pulmonary vein isolation in atrial fibrillation: a noninferiority randomized multicenter RADAR-AF trial. *Journal of the American College of Cardiology.* 2014 Dec 16; 64(23):2455-67.

[141] Oral H, Chugh A, Good E, Wimmer A, Dey S, Gadeela N, Sankaran S, Crawford T, Sarrazin JF, Kuhne M, Chalfoun N. Radiofrequency catheter ablation of chronic atrial fibrillation guided by complex electrograms. *Circulation.* 2007 May 22; 115(20):2606-12.

[142] Oral H, Chugh A, Good E, Crawford T, Sarrazin JF, Kuhne M, Chalfoun N, Wells D, Boonyapisit W, Gadeela N, Sankaran S. Randomized Evaluation of Right Atrial Ablation After Left Atrial Ablation of Complex Fractionated Atrial Electrograms for Long-Lasting Persistent Atrial Fibrillation CLINICAL PERSPECTIVE. *Circulation: Arrhythmia and Electrophysiology.* 2008 Apr 1; 1(1):6-13.

[143] Oral H, Chugh A, Yoshida K, Sarrazin JF, Kuhne M, Crawford T, Chalfoun N, Wells D, Boonyapisit W, Veerareddy S, Billakanty S. A randomized assessment of the incremental role of ablation of complex fractionated atrial electrograms after antral pulmonary vein isolation for long-lasting persistent atrial fibrillation. *Journal of the American College of Cardiology.* 2009 Mar 3; 53(9):782-9.

[144] Verma A, Sanders P, Champagne J, Macle L, Nair GM, Calkins H, Wilber DJ. Selective Complex Fractionated Atrial Electrograms Targeting for Atrial Fibrillation Study (SELECT AF). *Circulation: Arrhythmia and Electrophysiology.* 2014 Feb 1; 7(1):55-62.

[145] Li WJ, Bai YY, Zhang HY, Tang RB, Miao CL, Sang CH, Yin XD, Dong JZ, Ma CS. Additional Ablation of Complex Fractionated Atrial Electrograms After Pulmonary Vein Isolation in Patients With Atrial Fibrillation Clinical Perspective. *Circulation: Arrhythmia and Electrophysiology.* 2011 Apr 1;4 (2):143-8.

[146] Verma A, Jiang CY, Betts TR, Chen J, Deisenhofer I, Mantovan R, Macle L, Morillo CA, Haverkamp W, Weerasooriya R, Albenque JP. Approaches to catheter

ablation for persistent atrial fibrillation. *New England Journal of Medicine.* 2015 May 7; 372(19):1812-22.

[147] Narayan SM, Krummen DE, Enyeart MW, Rappel WJ. Computational mapping identifies localized mechanisms for ablation of atrial fibrillation. *PloS one.* 2012 Sep 26; 7(9):e46034.

[148] Narayan SM, Krummen DE, Clopton P, Shivkumar K, Miller JM. Direct or coincidental elimination of stable rotors or focal sources may explain successful atrial fibrillation ablation: on-treatment analysis of the CONFIRM trial (Conventional ablation for AF with or without focal impulse and rotor modulation). *Journal of the American College of Cardiology.* 2013 Jul 9; 62(2):138-47.

[149] Miller JM, Kowal RC, Swarup V, Daubert JP, Daoud EG, Day JD, Ellenbogen KA, Hummel JD, Baykaner T, Krummen DE, Narayan SM. Initial independent outcomes from focal impulse and rotor modulation ablation for atrial fibrillation: multicenter FIRM registry. *Journal of cardiovascular electrophysiology.* 2014 Sep 1; 25(9):921-9.

[150] Benharash P, Buch E, Frank P, Share M, Tung R, Shivkumar K, Mandapati R. Quantitative analysis of localized sources identified by focal impulse and roter modulation mapping in atrial fibrillation. *Circulation: Arrhythmia and Electrophysiology.* 2015 Apr 14: CIRCEP-115.

[151] Seitz J, Bars C, Théodore G, Beurtheret S, Lellouche N, Bremondy M, Ferracci A, Faure J, Penaranda G, Yamazaki M, Avula UM. AF ablation guided by spatiotemporal electrogram dispersion without pulmonary vein isolation: a wholly patient-tailored approach. *Journal of the American College of Cardiology.* 2017 Jan 24; 69(3):303-21.

[152] Konings KT, Smeets JL, Penn OC, Wellens HJ, Allessie MA. Configuration of unipolar atrial electrograms during electrically induced atrial fibrillation in humans. *Circulation.* 1997; 95:1231–1241.

[153] de Bakker JM, Wittkampf FH. The pathophysiologic basis of fractionated and complex electrograms and the impact of recording techniques on their detection and interpretation. *Circ Arrhythm Electrophysiol.* 2010; 3:204–213.

[154] Ghoraani B, Dalvi R, Gizurarson S, Das M, Ha A, Suszko A, Krishnan S, Chauhan V.S. Localized rotational activation in the left atrium during human atrial fibrillation: Relationship to complex fractionated atrial electrograms and low-voltage zones. *Heart Rhythm.* 2013; 10(12):1830-8.

[155] Lin PF, Lo MT, Tsao J, Chang YC, Lin C, Ho YL. Correlations between the signal complexity of cerebral and cardiac electrical activity: a multiscale entropy analysis. *PloS one.* 2014 Feb 3; 9(2):e87798.

[156] Kolmogorov AN. Entropy per unit time as a metric invariant of automorphism, Dokl. *Russ. Acad. Sci.* 1959; 124:754–755.

[157] Powell GE, Percival IC. Spectral entropy method for distinguishing regular and irregular motion of Hamiltonian systems, *J. Phys. A: Math. Gen.*1979; 12:2053–2071.

[158] Roberts SJ, Penny W, Rezek I. Temporal and spatial complexity measures for electroencephalogram based brain–computer interfacing. *Med. Biol. Eng. Comput.*1999; 37:93–98.

[159] Rosso OA, Blanco S, Yordanova J, Kolev V, Figliola A, Schurmann A, Basar M. Wavelet entropy: a new tool for analysis of short duration brain electrical signals. *J. Neurosci. Methods*. 2001; 105: 65–75.

[160] Bandt C, Pompe B. Permutation entropy: a natural complexity measure for time series. *Phys. Rev. Lett.* 2002; 88.

[161] Pincus S. Approximate entropy (Apen) as a complexity measure, *Chaos.* 1995; 5:110–117.

[162] Richman JS, Moorman JR. Physiological time-series analysis using approximate entropy and sample entropy, *Am. J. Physiol. Heart Circ. Physiol.* 2000; 278: H2039–H2049.

[163] Fogedby HC. On the phase–space approach to complexity, *J. Stat. Phys.*1992; 69 411–425.

[164] Costa M, Goldberger AL, Peng CK., Multiscale entropy analysis of complex physiologic time series, *Phys. Rev. Lett.* 2002; 89: 068102.

[165] Wu S D, Wu C W, Lee KY, Lin SG. Modified multiscale entropy for short-term time series analysis. *Physica A: Statistical Mechanics and its Applications,* 2013; 392(23):5865-5873.

[166] Humeau-Heurtier, A., 2015. The multiscale entropy algorithm and its variants: a review. *Entropy.* 17(5), pp.3110-3123.

[167] Gao, J., Hu, J., Liu, F. and Cao, Y., 2015. Multiscale entropy analysis of biological signals: a fundamental bi-scaling law. *Frontiers in computational neuroscience,* 9, p.64.

[168] Azami, H. and Escudero, J., 2016. Improved multiscale permutation entropy for biomedical signal analysis: Interpretation and application to electroencephalogram recordings. *Biomedical Signal Processing and Control,* 23, pp.28-41.

[169] Zhang, Y., Wei, S., Long, Y. and Liu, C., 2015. Performance analysis of multiscale entropy for the assessment of ECG signal quality. *Journal of Electrical and Computer Engineering*, 2015, p.31.

[170] Little, M., McSharry, P., Moroz, I. and Roberts, S. Stroboscopic method for detecting complex dynamics in disordered speech. *IEEE Trans. Biomed. Eng*, 2006. 1, pp.1-6.

[171] Little, M., McSharry, P., Moroz, I. and Roberts, S. Nonlinear, biophysically-informed speech pathology detection. In 2006 *IEEE International Conference on Acoustics Speech and Signal Processing Proceedings*. 2006, Vol. 2, pp. II-II). IEEE.

[172] Little, M., McSharry, P., Roberts, S., Costello, D.,Moroz. I. Exploiting nonlinear recurrence and fractal scaling properties for voice disorder detection, *BioMedical Engineering OnLine*. 2007, 6:23.

[173] Sharma, L.N., Dandapat, S. and Mahanta, A. Kurtosis based multichannel ECG signal denoising and diagnostic distortion measures. In *TENCON 2009-2009 IEEE Region 10 Conference.* 2009. pp. 1-5. IEEE.

[174] Phlypo, R., Zarzoso, V., Comon, P., D'Asseler, Y. and Lemahieu, I. Extraction of atrial activity from the ECG by spectrally constrained ICA based on kurtosis sign. In *Independent Component Analysis and Signal Separation*. 2007.pp. 641-648. Springer Berlin Heidelberg.

[175] Huang, N. E., Z. Shen, S. R. Long, M. C. Wu, H. H. Shih, Q. Zheng, N.-C. Yen, C. C. Tung, and H. H. Liu. The empirical mode decomposition and the Hilbert spectrum for nonlinear and non-stationary time series analysis. *Proc. R. Soc. London, Ser. A,* 1998, 454, 903–995.

[176] Huang NE. Hilbert-Huang transform and its applications. *World Scientific;* 2014.

[177] Mohebbi, M., & Ghassemian, H. Predicting termination of paroxysmal atrial fibrillation using empirical mode decomposition of the atrial activity and statistical features of the heart rate variability. *Medical & biological engineering & computing,* 2014, 52(5), 415-427.

[178] Salisbury, J. I., & Sun, Y. Assessment of chaotic parameters in nonstationary electrocardiograms by use of empirical mode decomposition. *Annals of biomedical engineering,* 2004, 32(10), 1348-1354.

[179] Wu, Z.H.; Huang, N.E. Ensemble empirical mode decomposition: A noise-assisted data analysis method. *Adv. Adapt. Data Anal.* 2009, 1, 1–41.

[180] Lei, Y.; He, Z.; Zi, Y. Application of the EEMD method to rotor fault diagnosis of rotating machinery. *Mech. Syst. Signal Process.* 2009, 23, 1327–1338.

[181] Hu X, Peng S, Hwang WL. EMD revisited: A new understanding of the envelope and resolving the mode-mixing problem in AM-FM signals. *IEEE Transactions on Signal Processing.* 2012 Mar; 60(3):1075-86.

[182] Knutsson, Hans, Carl-Fredrik Westin, and Gösta Granlund. "Local multiscale frequency and bandwidth estimation." In *Image Processing, 1994. Proceedings. ICIP-94., IEEE International Conference*, vol. 1, pp. 36-40. IEEE, 1994.

[183] Stockwell RG, Mansinha L, Lowe RP. Localization of the complex spectrum: the S transform. *IEEE transactions on signal processing*. 1996 Apr;44(4):998-1001.

[184] Liu G, Fomel S, Chen X. Time-frequency analysis of seismic data using local attributes. *Geophysics.* 2011 Nov;76(6):P23-34.

[185] Clifford, G.D., Azuaje, F. and Mcsharry, P., 2006. ECG statistics, noise, artifacts, and missing data. *Advanced Methods and Tools for ECG Data Analysis*, 6, p.18.

[186] El B'charri, O., Latif, R., Elmansouri, K., Abenaou, A. and Jenkal, W., 2017. ECG signal performance de-noising assessment based on threshold tuning of dual-tree wavelet transform. *Biomedical engineering online,* 16(1), p.26.

[187] Arunachalam SP. A New Real-time Algorithm for Obtaining the ECG-derived Respiration (EDR) Signal from the Electrocardiogram (ECG). *ProQuest*; 2007.

[188] McManus, D.D., Lee, J., Maitas, O., Esa, N., Pidikiti, R., Carlucci, A., Harrington, J., Mick, E. and Chon, K.H., 2013. A novel application for the detection of an irregular pulse using an iPhone 4S in patients with atrial fibrillation. Heart Rhythm, 10(3), pp.315-319.

[189] Holm, M., Pehrson, S., Ingemansson, M., Sörnmo, L., Johansson, R., Sandhall, L., Sunemark, M., Smideberg, B., Olsson, C. and Olsson, S.B., 1998. Non-invasive assessment of the atrial cycle length during atrial fibrillation in man: introducing, validating and illustrating a new ECG method. Cardiovascular Research, 38(1), pp.69-81.

[190] Darbar, D., Jahangir, A., Hammill, S.C. and Gersh, B.J., 2002. P Wave Signal-Averaged Electrocardiography to Identify Risk for Atrial Fibrillation. Pacing and clinical electrophysiology, 25(10), pp.1447-1453.

[191] Bollmann, A., Husser, D., Mainardi, L., Lombardi, F., Langley, P., Murray, A., Rieta, J.J., Millet, J., Olsson, S.B., Stridh, M. and Sörnmo, L., 2006. Analysis of surface electrocardiograms in atrial fibrillation: techniques, research, and clinical applications. Europace, 8(11), pp.911-926.

[192] Patil, M.J., Khadse, B.K. and Suralkar, S.R., Discrimination Between Atrial Fibrillation (AF) & Normal Sinus Rhythm (NSR) Using Linear Parameters. Pratibha: International Journal of Science, Spirituality, Business and Technology (IJSSBT), p.108.

[193] Benjamin EJ, Chen PS, Bild DE, et al. Prevention of atrial fibrillation: Report from a National Heart, Lung, and Blood Institute workshop.Circulation. 2009;119:606-618

[194] Goldberger AL, Amaral LAN, Glass L, Hausdorff JM, Ivanov PCh, Mark RG, Mietus JE, Moody GB, Peng C-K, Stanley HE. PhysioBank, PhysioToolkit, and

PhysioNet: Components of a New Research Resource for Complex Physiologic Signals. *Circulation.* 101(23):e215-e220.

[195] Mironov, S., Jalife, J. & Tolkacheva, E.G. Role of conduction velocity restitution and short-term memory in the development of action potential duration alternans in isolated rabbit hearts. *Circulation*. 118, 17-25 (2008).

[196] Matiukas, A., Pertsov, A.M., Kothari, P., Cram, A. & Tolkacheva, E.G. Optical mapping of electrical heterogeneities in the heart during global ischemia. *Conf Proc IEEE Eng Med Biol Soc.* 1, 6321-6324 (2009).

[197] Zlochiver S, Yamazaki M, Kalifa J, Berenfeld O. Rotor meandering contributes to irregularity in electrograms during atrial fibrillation. *Heart rhythm.* 2008 Jun 30;5(6):846-54.

[198] Pandit SV, Warren M, Mironov S, Tolkacheva EG, Kalifa J, Berenfeld O, Jalife J. Mechanisms underlying the antifibrillatory action of hyperkalemia in Guinea pig hearts. *Biophysical journal.* 2010 May 19; 98(10):2091-101.

APPENDIX A
DISSERTATION OUTCOMES

PEER REVIEWED CONFERENCE PUBLICATIONS

1. **Arunachalam, S.P.,** Mulpuru, S.K., Friedman. P.A., and Tolkacheva, E.G. (2015). Feasibility of visualizing higher regions of Shannon Entropy in Atrial Fibrillation patients. *Proceedings of the 37th Annual International Conference of the IEEE Engineering in Medicine and Biology Society*, 4499-4502. PMID: 26778442.

2. **Arunachalam, S.P.,** Annoni, E.M., Mulpuru, S.K., Friedman. P.A., and Tolkacheva, E.G. (2016). Novel Multiscale Frequency Approach to Identify Rotor Pivot Point. *Journal of Medical Devices*. 10(2), 020948.

3. **Arunachalam, S.P**., Mulpuru, S.K., Friedman. P.A., and Tolkacheva, E.G. (2016). Rotor Pivot Point Identification with Intrinsic Mode Function Complexity Index using Empirical Mode Decomposition. *Proceedings of the 2016 IEEE EMBS International Student Conference (ISC 2016)*. 1-4.

4. **Arunachalam, S.P**., Annoni, E.M., Mulpuru, S.K., Friedman. P.A., and Tolkacheva, E.G. (2016). Kurtosis as a Statistical Approach to Identify Pivot Point of the Rotor. *Proceedings of the 38th Annual International Conference of the IEEE Engineering in Medicine and Biology Society*, 497-500. PMID: 28268379

5. **Arunachalam, S.P**., Annoni, E.M., and Tolkacheva, E.G. (2016). Novel Multiscale Entropy Approach for Rotor Pivot Point Identification. *Proceedings of the 2016 Biomedical Engineering Society (BMES) Annual Meeting*. Minneapolis, Minnesota.

6. **Arunachalam, S.P**., Kapa, S., Mulpuru, S.K., Friedman. P.A., and Tolkacheva, E.G. (2017). Rotor Pivot Point Identification using Recurrence Period Density Entropy. *Biomedical Sciences Instrumentation*.

7. **Arunachalam, S.P.,** Annoni, E.M., Kapa, S., Mulpuru, S.K., Friedman. P.A., and Tolkacheva, E.G. (2017). Robust discrimination of Normal Sinus Rhythm and Atrial Fibrillation on ECG using a multiscale frequency technique. *Journal of Medical Devices*.

PEER REVIEWED JOURNAL SUBMISSIONS

1. Arunachalam, S.P., Kapa, S., Mulpuru, S.K., Friedman. P.A., and Tolkacheva, E.G. (2017). Novel Multiscale Entropy Technique for Short Time Series Analysis: Feasibility Study using Cardiac Signal Analysis. *Journal of Healthcare Engineering.*

2. **Arunachalam, S.P.,** Kapa, S., Mulpuru, S.K., Friedman. P.A., and Tolkacheva, E.G. (2017). Novel Approaches for Quantitative Electrogram Analysis for Intraprocedural Guidance for Catheter Ablation: A Case of a Patient with Persistent Atrial Fibrillation. *Journal of Medical Imaging*.

3. Annoni, E.M., **Arunachalam, S.P.,** Kapa, S., Mulpuru, S.K., Friedman. P.A., and Tolkacheva, E.G. (2017). Novel quantitative analytical approaches for rotor identification and associated implications for mapping. *Heart Rhythm*.

AWARDS

Second Place Poster Award for the poster on "*Novel Entropy Approach to Identify the Core of the Rotors in Atrial Fibrillation*", Institute of Engineering in Medicine, 2nd Annual Meeting, Cardiovascular Engineering Theme. University of Minnesota, Minneapolis, Minnesota - *September 2014*

Second Place Poster Award for the poster on "*Novel Multiscale Frequency Approach to Identify Pivot Point of the Rotor*", Institute of Engineering in Medicine, 4th Annual Meeting, Cardiovascular Engineering Theme. University of Minnesota, Minneapolis, Minnesota - *September 2016*

Contest Chair's Award for overall best written and oral presentation for the paper "Rotor pivot point identification using recurrence period density entropy", 54th Annual Rocky Mountain Bioengineering Symposium, Denver, Colorado – *April 2017*

PATENT APPLICATIONS

Tolkacheva, E.G., **Arunachalam, S.P**., Mulpuru, S.K., and Friedman. P.A. (2016). Graphically Mapping Rotors in a Heart using Shannon Entropy. United States Utility Patent Application Serial Number 15/373,193, filed on December 8, 2016. (University of Minnesota – Office of Technology & Commercialization)

Arunachalam, S.P., and Tolkacheva, E.G. (2017). Graphically Mapping rotors in a Heart. United States Utility Patent Application Serial Number 15/427,349, filed on February 8, 2017. (University of Minnesota – Office of Technology & Commercialization)

Arunachalam, S.P., Suraj Kapa., Mulpuru, S.K., Friedman. P.A. and Tolkacheva, E.G. (2017). Rotor Identification using Recurrence Period Density Entropy. ***Intellectual Property Disclosure Case # 2016-341, Mayo Clinic-Rochester***

APPENDIX B

MATLAB Program for Implementing Multiscale Entropy Technique

"NMSE.m"

```
% Written by Shivaram Poigai Arunachalam
% Subroutine function to calculate Nearest-Neighbor Multi-Scale Entropy
% (NMSE) for the time series data
% data - incoming time series data
% scale - time scale factor chosen to estimate nearest neighbor moving
average
% r - Predefined threshold for template matching chosen to be 20% of
the
% standard deviation of the incoming time series data
% MS_E - Returns the multi-scale entropy value of the time series
% This subroutine uses two functions namely NNMA- Nearest-Neighbor
Moving
% Average and SampEn which computes the sample entropy of the new time
% series data

% Last Modified: Feb 23 2016

function MS_E = NMSE(data, scale)
r = 0.2*std(data);                % Threshold to define matching
template vectors
for i = 1:scale
NT = NNMA(data, i);               % Compute the new time (NT) series
Nearest-Neighbor moving average based on the defined time scale factor
MS_E(i) = SampEn(NT,r,i);         % Compute the Sample Entropy of the
new time series
end


% ---------- END OF PROGRAM ----------------------------------
```

"NNMA.m"

```
% Written by Shivaram Poigai Arunachalam
% Subroutine function to calculate NNMA- Nearest-Neighbor Moving
% Averaged time series based on the desired time scale factor 's'
% data - incoming time series data
% s - time scale factor chosen to estimate nearest neighbor moving
average
% NNMA - Nearest Neighbor Moving Average - procedure

% Last Modified February 23 2016

function data = NNMA(data,s)
N = length(data);             % Estimate the length of the incoming
time series data
for i = 1:N - s               % for loop to compute nearest neighbor
moving average based on the time scale factor
    if i > s                  % check for the presence of backward
neighbor
data(i) = mean(data((i-s):(i + s)));  % compute the average of the
corresponding nearest neighbors
    end
end

% ---------------- END OF PROGRAM ------------------------------------
```

"SampEn.m"

```
% Written by Shivaram Poigai Arunachalam
% Subroutine function to calculate NNMA- Nearest-Neighbor Moving
% Averaged time series based on the desired time scale factor 's'
% data - incoming time series data
% r - Predefined threshold for template matching chosen to be 20% of
the
% standard deviation of the incoming time series data
% delay - time delay between successive time series points to be
considered
% Reference: Wu, S. D., Wu, C. W., Lee, K. Y., & Lin, S. G. (2013).
Modified multiscale entropy for short-term time series analysis.
Physica A: Statistical Mechanics and its Applications, 392(23), 5865-
5873.
% Last Modified February 23 2016
function MS_Entropy = SampEn(data,r,delay)
N = length(data);                          % Find the length of the time
series
Nn = 0;                                    % Initial value for the number
of matched template vectors for dimension 'm'
Nd = 0;                                    % Initial value for the number
of matched template vectors for dimension 'm+1'
for i = 1:N - 3*delay                      % Loop to construct template
vectors in 'm' dimension
for j = i + delay:1:N - 2*delay            % Loop to construct template
vectors in 'm+1' dimension
if abs(data(i)-data(j))<r && abs(data(i + delay)-data(j + delay))<r  %
Calculate the Euclidean distance of the template vectors to be within
the threshold 'r' in 'm' dimension
Nn = Nn + 1;                                                        %
increase the # of matched template vectors by 1 if a matching template
vector is found
if abs(data(i + 2*delay)-data(j + 2*delay))<r                       %
Calculate the Euclidean distance of the template vectors to be within
the threshold 'r' in 'm+1' dimension
Nd = Nd + 1;                                                        %
increase the # of matched template vectors by 1 if a matching template
vector is found
end                  % end of if statement for 'Nd'
end                  % end of if statement for 'Nn'
end                  % end of for statement for 'j loop'
end                  % end of for statement for 'i loop'
MS_Entropy = -log(Nd/Nn);                   % Calculate the Sample
entropy as the ratio of matched template vectors in 'm+1' dimension to
'm' dimension

% --------------- END OF PROGRAM ----------------------------------
```

APPENDIX C

MATLAB Program to Compute Recurrence Period Density Entropy

"rpde.m "

```
% Performs fast recurrence period density entropy (RPDE) analysis on an
input signal to
% obtain an estimate of the H_norm value.
%
% Useage:
% [H_norm, rpd] = rpde(x, m, tau)
% [H_norm, rpd] = rpde(x, m, tau, epsilon)
% [H_norm, rpd] = rpde(x, m, tau, epsilon, T_max)
% Inputs
%    x       - input signal: must be a row vector
%    m       - embedding dimension
%    tau     - embedding time delay
% Optional inputs
%    epsilon - recurrence neighborhood radius
%              (If not specified, then a suitable value is chosen
automatically)
%    T_max   - maximum recurrence time
%              (If not specified, then all recurrence times are
returned)
% Outputs:
%    H_norm  - Estimated RPDE value
%    rpd     - Estimated recurrence period density
%
% (c) 2007 Max Little. If you use this code, please cite:
% Exploiting Nonlinear Recurrence and Fractal Scaling Properties for
Voice Disorder Detection
% M. Little, P. McSharry, S. Roberts, D. Costello, I. Moroz (2007),
% BioMedical Engineering OnLine 2007, 6:23
% Date Modified: FEB 20, 2017
% Modified By SHIVARAM POIGAI ARUNACHALAM



function [H_norm, rpd] = rpde(x, m, tau, epsilon, T_max)

if ((nargin < 3) || (nargin > 5))
    help rpde;

    return;

end

if (nargin < 4)
    epsilon = 0.12;
end
```

```
if (nargin < 5)
    T_max = -1;
end

rpd = close_ret(x, m, tau, epsilon); % Compute RPDE using close_ret.c

if (T_max > -1)
    rpd = rpd(1:T_max);
end

rpd = rpd/sum(rpd);

N = length(rpd);
H = 0;

for j = 1:N
   H = H - rpd(j) * logz(rpd(j));
end
H_norm = H/log(N); % Compute normalized RPDE



% FUNCTIONS

function y = logz(x)
if (x > 0)
   y = log(x);
else
   y = 0;
end

% ************* END OF PROGRAM ************************
```

C Program to Compute Recurrence Period Density

"close_ret.c"

```
/* Close returns code by M. Little (c) 2006 */
#include <math.h>
#include <stdlib.h>
#include <stdio.h>
#include "mex.h"
#include "matrix.h"
/* Real variable type */
#define  REAL        double

/* Input parameters */

#define  X_IN        prhs[0]
#define  EMBEDDIM_IN prhs[1]
#define  EMBEDDEL_IN prhs[2]
#define  ETA_IN      prhs[3]

/* Output parameters */

#define  CRS_OUT     plhs[0]

/* function definition */
#define  SYNTAX      "close_returns = close_ret(x, embed_dim, embed_delay, eta)"

/* Create embedded version of given sequence */

static void embedSeries
(
```

```
  unsigned long embedDims,      /* Number of dimensions to embed */
  unsigned long embedDelay,     /* The embedding delay */
  unsigned long embedElements,  /* Number of embedded points in embedded sequence
*/
  REAL          *x,             /* Input sequence */
  REAL          *y              /* (populated) Embedded output sequence */
)
{
  unsigned int i, d, inputDelay;

  for (d = 0; d < embedDims; d ++)
  {
    inputDelay = (embedDims - d - 1) * embedDelay;
    for (i = 0; i < embedElements; i ++)
    {
      y[i * embedDims + d] = x[i + inputDelay];
    }
  }
}
/* Search for first close returns in the embedded sequence */
static void findCloseReturns
(
  REAL          *x,             /* Embedded input sequence */
  REAL          eta,            /* Close return distance */
  unsigned long  embedElements,    /* Number of embedded points */
  unsigned long  embedDims,        /* Number of embedding dimensions */
  unsigned int   *closeRets        /* Close return time histogram */
)
{
  REAL  eta2 = eta * eta;
```

```
REAL  diff, dist2;
unsigned long  i, j, d, timeDiff, etaFlag;
for (i = 0; i < embedElements; i ++)
{
  closeRets[i] = 0;
}
for (i = 0; i < embedElements; i ++)
{
  j = i + 1;
  etaFlag = 0;
  while ((j < embedElements) && !etaFlag)
  {
    dist2 = 0.0f;
    for (d = 0; d < embedDims; d ++)
    {
      diff   = x[i * embedDims + d] - x[j * embedDims + d];
      dist2 += diff * diff;
    }
    if (dist2 > eta2)
    {
      etaFlag = 1;
    }

    j ++;
  }
  etaFlag = 0;
  while ((j < embedElements) && !etaFlag)
  {
    dist2 = 0.0f;
    for (d = 0; d < embedDims; d ++)
```

```
        {
          diff   = x[i * embedDims + d] - x[j * embedDims + d];
          dist2 += diff * diff;
        }
        if (dist2 <= eta2)
        {
          timeDiff = j - i;
          closeRets[timeDiff] ++;
          etaFlag = 1;
        }
        j ++;
      }
    }
}
/* Main entry point */
/* lhs - output parameters */
/* rhs - input parameters */
void mexFunction(
    int         nlhs,          /* number of expected outputs */
    mxArray     *plhs[],       /* array of pointers to output arguments */
    int         nrhs,          /* number of inputs */
#if !defined(V4_COMPAT)
    const mxArray *prhs[]      /* array of pointers to input arguments */
#else
    mxArray *prhs[]        /* array of pointers to input arguments */
#endif
)
{
  long          rows, columns, vectorElements, embedElements, i;
  unsigned long  embedDims, embedDelay;
```

```
REAL          etaIn;
  REAL          *CRSOut;         /* Output vector of close return counts */
REAL          *sequenceIn;     /* Input vector */
unsigned long  *closeRets;      /* Close return counts */
REAL          *embedSequence;   /* Embedded input vector */
/* Check for proper number of arguments */
if ((nrhs != 4) || (nlhs != 1))
{
  mexErrMsgTxt("Incorrect number of parameters.\nSyntax: "SYNTAX);
}
/* Checks on input sequence vector */
rows          = mxGetM(X_IN);
columns       = mxGetN(X_IN);
vectorElements = columns * rows;
if (columns != 1)
{
  mexErrMsgTxt("Input sequence must be a row vector.");
}
if (!mxIsDouble(X_IN) || mxIsComplex(X_IN))
{
  mexErrMsgTxt("Input sequence must be floating-point real.");
}
sequenceIn = mxGetPr(X_IN);

/* Checks on close return distance */
if (!mxIsDouble(ETA_IN) || mxIsComplex(ETA_IN))
{
  mexErrMsgTxt("Close return distance eta must be floating-point real.");
}
etaIn = *mxGetPr(ETA_IN);
```

```
  /* Checks on embedding dimension */
  if (!mxIsNumeric(EMBEDDIM_IN) || mxIsComplex(EMBEDDIM_IN))
  {
    mexErrMsgTxt("Embedding dimension must be an integer.");
  }
  embedDims = (unsigned long)*mxGetPr(EMBEDDIM_IN);
  /* Checks on embedding delay */
  if (!mxIsNumeric(EMBEDDEL_IN) || mxIsComplex(EMBEDDEL_IN))
  {
    mexErrMsgTxt("Embedding delay must be an integer.");
  }
  embedDelay = (unsigned long)*mxGetPr(EMBEDDEL_IN);

  /* Create embedded version of input sequence */
  embedElements = vectorElements - ((embedDims - 1) * embedDelay);
  embedSequence = (REAL *)mxCalloc(embedElements * embedDims, sizeof(REAL));
  embedSeries(embedDims, embedDelay, embedElements, sequenceIn,
embedSequence);

  /* Find close returns */
  closeRets = (unsigned long *)mxCalloc(embedElements, sizeof(unsigned long));
  findCloseReturns(embedSequence, etaIn, embedElements, embedDims, closeRets);

  /* Create output vectors, get pointer access */
  CRS_OUT = mxCreateDoubleMatrix(embedElements, 1, mxREAL);
  CRSOut  = mxGetPr(CRS_OUT);
  for (i = 0; i < embedElements; i ++)
  {
    CRSOut[i] = closeRets[i];
```

```
  }
  /* Release allocated memory. */
  mxFree(embedSequence);
  mxFree(closeRets);

  return;
}
/*          END OF PROGRAM     */
```

APPENDIX D

MATLAB Program for Empirical Mode Decomposition

"emd.m"

```
function imf = emd(x)

% This MATLAB program computes the intrinsic mode functions (IMF) of
the
% input time series 'x' using Empirical Mode Decomposition (Hilbert-
Huang Transform)
% Reference:
% Huang, N. E., Z. Shen, S. R. Long, M. C. Wu, H. H. Shih, Q. Zheng,
N.-C. Yen,
% C. C. Tung, and H. H. Liu, 1998: The empirical mode decomposition and
the
% Hilbert spectrum for nonlinear and non-stationary time series
analysis. Proc.
% R. Soc. London, Ser. A, 454, 903-995.
% MATLAB Code Adapted from MATHWORKS CENTRAL
% Date Modified: FEB 20, 2017
% Modified by: SHIVARAM POIGAI ARUNACHALAM

x   = transpose(x(:));
imf = [];
while ~ismonotonic(x)  % Check for monotonic function
   x1 = x;
   sd = Inf;
   while (sd > 0.1) || ~isimf(x1)
      s1 = getspline(x1);
      s2 = -getspline(-x1);
      x2 = x1-(s1+s2)/2;

      sd = sum((x1-x2).^2)/sum(x1.^2);
      x1 = x2;
   end

   imf{end+1} = x1;
   x          = x-x1;

end
imf{end+1} = x;        % Compute IMF's

% FUNCTIONS

function u = ismonotonic(x)

u1 = length(findpeaks(x))*length(findpeaks(-x));
if u1 > 0, u = 0;
else      u = 1; end
```

```
function u = isimf(x)

N  = length(x);
u1 = sum(x(1:N-1).*x(2:N) < 0);
u2 = length(findpeaks(x))+length(findpeaks(-x));
if abs(u1-u2) > 1, u = 0;
else               u = 1; end

function s = getspline(x)

N = length(x);
p = findpeaks(x);
s = spline([0 p N+1],[0 x(p) 0],1:N);

function n = findpeaks(x)

n    = find(diff(diff(x) > 0) < 0);
u    = find(x(n+1) > x(n));
n(u) = n(u)+1;

% *************** END OF PROGRAM ****************************
```

"MMSE.m"

```
% Adapted from:
% Reference: Wu, S. D., Wu, C. W., Lee, K. Y., & Lin, S. G. (2013).
Modified multiscale
% entropy for short-term time series analysis. Physica A: Statistical
Mechanics and
% its Applications, 392(23), 5865-5873.
% Modified by Shivaram Poigai Arunachalam
% Subroutine function to calculate Modified Multi-Scale Entropy
% (MMSE) for the time series data
% data - incoming time series data
% scale - time scale factor chosen to estimate forward moving average
% r - Predefined threshold for template matching chosen to be 20% of
the
% standard deviation of the incoming time series data
% E - Returns the multi-scale entropy value of the time series
% This subroutine uses two functions namely movingaverage.m and
% SampEn.m which computes the sample entropy of the new time
% series data

% Last Modified: Feb 23 2016

function E = MMSE(data, scale)
r = 0.2*std(data);   % Threshold to define matching template vectors
for i = 1:scale
buf = movingaverage(data, i); % Compute the new time (NT) series with
forward moving average based on the defined time scale factor
E(i) = SampEn(buf,r,i);       % Compute the Sample Entropy of the new
time series
end

% --------------  END OF PROGRAM ------------------------------
```

"movingaverage.m"

```
% Adapted from:
% Reference: Wu, S. D., Wu, C. W., Lee, K. Y., & Lin, S. G. (2013).
Modified multiscale
% entropy for short-term time series analysis. Physica A: Statistical
Mechanics and
% its Applications, 392(23), 5865-5873.
% Modified by Shivaram Poigai Arunachalam
% Subroutine function to calculate forward moving average value of time
% series based on the desired time scale factor's'
% data - incoming time series data
% s - time scale factor chosen to estimate forward moving average
values

% Last Modified Feb 23 2016

function data = movingaverage(data,s)
N = length(data);        % Estimate the length of the incoming time
series data
for i = 1:N - s + 1      % for loop to compute forward moving average
based on the time scale factor
data(i) = mean(data(i:i + s - 1)); % Compute moving average
end                       % End of main loop

% ------------------ END OF PROGRAM ----------------------------------
--
```

APPENDIX E

MATLAB Program to estimate multiscale frequency (MSF) index

"FrequencyEstimation_1D.m "

```
function [FE_w, FE_Hz, DF] = FrequencyEstimation_1D(signal_1D, T)

%% Local Multiscale Frequency and Bandwidth Estimation
%  Reference: Knutsson, H., Westin, C.-F., and Granlund, G., 1994,
"Local Multiscale Frequency and
%  Bandwidth Estimation," IEEE International Conference on Image
Processing (ICIP-94), IEEE,
%  Vol. 1, pp. 36-40.

% Written by Elizabeth M. Annoni
% Modified By Shivaram Poigai Arunachalam
% This program computes the multiscale frequency (MSF) index for the
input
% time series using eight log-Gabor filters
% The MSF index is computed as the average of the frequency estimation

% Last Modified Feb 20, 2017

% clear all
% clc
% close all

Fs = 1/T;              % Compute the Sampling Frequency
L = length(signal_1D); % Estimate the length of the input signal
t = (0:L-1)*T;         % Establish time points for plotting


y = signal_1D;
% y = signal_1D - 1i*hilbert(signal_1D);
% figure
% plot(t,y);
% title('Pixel Signal');

NFFT = 2^nextpow2(L);      % Estimate the nearest 2 power for FFT
computation
Y = fft(y,NFFT);           % Compute Fast Fourier Transform (FFT)
f = Fs*linspace(0,1,NFFT); % Establish frequency bins for plotting

fin = 2*pi*f;              % Convert to Hz from rad

% figure
% plot(f,abs(Y));
% title('Pixel Spectrum');

% %% Find Dominant Frequency
```

```
% ind = find(abs(Y(1,1:end/2)) == max(abs(Y(1,2:end/2))));
% DF = f(ind(1));
%
% %% Remove Harmonics
% y = double(y);
% if (DF ~= 0)
%     maxFreq = 50;
%     fsample = 1/T;
%     q = 10;
%     % Remove 1st harmonic
%     df1 = DF*2;
%     if (df1 < maxFreq)
%         %notch filter centered at df1
%         w0 = df1/(fsample/2);
%         bw = w0/q;
%         [b1,a1] = iirnotch(w0,bw,q);
%         y1 = filter(b1,a1,y);
%         y = y1;
%     end
%     % Remove 2nd harmonic
%     df2 = DF*3;
%     if (df2 < maxFreq)
%         %notch filter centered at df2
%         w0 = df2/(fsample/2);
%         bw = w0/q;
%         [b2,a2] = iirnotch(w0,bw,q);
%         y2 = filter(b2,a2,y);
%         y = y2;
%     end
%     % Remove 3rd harmonic
%     df3 = DF*4;
%     if (df3 < maxFreq)
%         %notch filter centered at df3
%         w0 = df3/(fsample/2);
%         bw = w0/q;
%         [b3,a3] = iirnotch(w0,bw,q);
%         y3 = filter(b3,a3,y);
%         y = y3;
%     end
%
% end

%Y = fft(y,NFFT);

%% Apply log-Gabor filters to input signal

p0 = pi;                    % Value of p0
N = 8;                      % Number of log-Gabor filters = 8
pis = [];
for i = 1:N
    pi_i = 2^i * p0;
    pis = [pis, pi_i];
end
% pis = [pi/128, pi/64, pi/32, pi/16, pi/8, pi/4, pi/2, pi];
```

```
% This Section designs the filters similar to Knutsson et al.

filtSigTime = [];
for i  = 1:length(pis)
    B = 2*sqrt(2);
    Cb = 4/(B^2 * log(2));
    R2_i = exp(-Cb*log(fin/pis(i)).^2);
    filtSig_i = (Y').*R2_i;
    filtSigTime_i = ifft(filtSig_i);
    filtSigTime = [filtSigTime; filtSigTime_i];
end

 %% Multiscale Frequency Estimation

removeEdge = 0;
%removeEdge = 50;
for j = removeEdge+1:length(signal_1D)-removeEdge
    numTemp = 0;
    for m = 1:7
        numTemp = numTemp + ((2^(m+0.5))*(filtSigTime(m+1,j)));
    end
    denTemp = 0;
    for m = 1:7
        denTemp = denTemp + (filtSigTime(m,j));
    end

    rho(j) = p0 * (1/denTemp) * numTemp;
end

% See how smoothing affects output
% figure
% plot(abs(rho));
% hold on
% plot(smooth(abs(rho),10));
% plot(smooth(abs(rho),50));
% plot(smooth(abs(rho),100));
% legend('Original','Smooth:10','Smooth:50', 'Smooth: 100');

 % figure
% plot(abs(rho)/(2*pi));
%
% avgFE_w = mean(abs(rho));
% avgFE_Hz = mean(abs(rho))/(2*pi);

% switching output from single averaged map to a FE movie
FE_w = abs(rho);          % MSF in radians
FE_Hz = abs(rho)/(2*pi);  % MSF in Hertz

end  % End of Main Loop

% ************** END OF PROGRAM ************************************
```

APPENDIX F

MATLAB Program for Optical Mapping Rotor Data Analysis using Novel Approaches

"Novel_Approaches_Optical_Data_Analysis.m"

```
% MATLAB Program to extract the pixel data from Optical .var data
format
% and collect the time series data through each pixels for the 1998
time
% frames. The following analysis are performed
% (1) Dominant Frequency (DF) estimate in Hz
% (2) Shannon Entropy (SE) at each pixel locations
% (3) Renyi Entropy (RE) at each pixel locations
% (4) Multi-Scale Entropy (MSE)
% (5) Kurtosis (Kt)
% (6) Multi-Scale Frequency (MSF)
% (7) Reccurrence Period Density Entropy (RPDE)
% (8) Intrinsic Mode Function (IMF) Complexity Index
% The results are compared with each other to get a consensus regarding
the
% behavior especially at the known pivotal regions
% Written by Shivaram Poigai Arunachalam
% This program is adapted to analyze figure-of-8 and meandering rotor
% Last Modified: February 20 2017

clear all
close all
clc

%
**********************************************************************
%                     OBTAIN RAW OPTICAL DATA
%
**********************************************************************

load('spiral_flt_masked.mat');          % load the spiral data
d = SpiralFltMasked;                    % spiral data variable
c=24;                                   % index to point the end of
header
L = 1998;                               % Number of frames
F = zeros(1998,64,64);                  % Define 3D array to pull out
frame data
I = zeros(64,64,1998);                  % Define 3D array to pull out
time series intensity data through each pixel across frames

%**********************************************************************
***
%                       OBTAIN FRAME DATA
```

```
%*********************************************************************
***
% The following for loop pulls out individual frame data from the
single
% long 1D matrix

for k = 1:1998
for i = 1:64
    for j = 1:64
        F(k,i,j) = d(c+j,1);
    end
    c=c+64;
end
end

% End of loop to obtain frames data

% The following section plots few frames for visualization

% F1 = reshape(F(1,:,:),64,64);figure(1),image(F1)
% F2 = reshape(F(2,:,:),64,64);figure(2),image(F2)
% F3 = reshape(F(3,:,:),64,64);figure(3),image(F3)
% F4 = reshape(F(4,:,:),64,64);figure(4),image(F4)
% F5 = reshape(F(5,:,:),64,64);figure(5),image(F5)

%*********************************************************************
***
%             OBTAIN TIME SERIES INTENSITY DATA across FRAMES
%*********************************************************************
***
% The following for loop pulls out times series data at each pixel
across
% different frames (1998)

for i = 1:64
    for j = 1:64
        for k = 1:1998
        I(i,j,k) = F(k,i,j);
        end
    end
end

% End of loop to obtain times series data

ShE=zeros(64,64);           % 2D array to store Shannon Entropy values
RnE=zeros(64,64);           % 2D array to store Renyi Entropy values
DmF=zeros(64,64);           % 2D array to store Dominant Frequency
values
Kt =zeros(64,64);           % 2D array to store Kurtosis values
MSE=zeros(64,64);           % 2D array to store Multi-Scale Entropy
values
MSF=zeros(64,64);           % 2D array to store Multi-Scale Frequency
values
```

```
RPDE=zeros(64,64);          % 2D array to store RPDE values
IMF = zeros(64,64);         % 2D array to store IMF values

% x_loc = input(' Please enter the x coordinate (1:64):');
% y_loc = input(' Please enter the y coordinate (1:64):');

for ii = 1:64
    for jj = 1:64

%g=squeeze(I(x_loc,y_loc,:));

g=squeeze(I(ii,jj,:));

%*************************************************************************
***
%              ENTROPY CALCULATIONS FROM RAW DATA
%*************************************************************************
***
mx = max(g);            % Maximum intensity value of the optical
intensity
mi = min(g);            % Minimum intensity value of the optical
intensity
bin = mi:1:mx;          % Create amplitude bins with 1 unit intensity
difference for bin size
h = hist(g,bin);        % Create histogram data using specified bin
size

% figure(6), plot(h);     % Plot the histogram
% xlabel(' Bin Number ');
% ylabel(' Frequency ');
% title(sprintf(' Intensity Histogram of the optical data at pixel
location [%d,%d]  ',x_loc,y_loc));

l = length(h);          % Calculate the size of histogram matrix
P = zeros(1,l);         % Create array for probability density function
S = zeros(1,l);         % Create array to be used for Shannon Entropy
calculations
N = zeros(1,l);         % Create array to be used for Shannon Entropy
calculations
R = zeros(1,l);         % Create array to be used for Renyi Entropy
calculations
alpha = 0.25;           % Specify alpha value for Renyi Entropy
calculations

%-------------------------------------------------------------------------
---
%              Estimate Shannon and Renyi Entropy
%-------------------------------------------------------------------------
---

% The following loop calculates the intermediary terms used in Shannon
and
```

```
% Renyi entropy

for i = 1:l
    P(i) = h(i)/L;              % Probability that a given sample falls
within a particular amplitude bin
    S(i) = P(i)*log2(P(i));     % Shannon Entropy Term
        N(i) = S(i);
     if isnan(N(i))             % Check for NAN and replace it with 0
        N(i) = 0;
     end
    R(i) = P(i)^alpha;          % Renyi Entropy term
end

SE = -1*sum(N);                 % Calculate Shannon Entropy
RE = log(sum(R))*(1/(1-alpha)); % Calculate Renyi Entropy

% sprintf(' The Shannon Entropy SE = %2.4f and Renyi Entropy RE = %2.4f
', SE, RE) % Display Shannon and Renyi Entropy
% z = axis;
% Obtain the current axis values
% text(z(2)/1.6,z(4)/1.6,sprintf('Shannon Entropy = %2.4f ', SE));
% Display Shannon Entropy in the plot window
% text(z(2)/1.6,z(4)/1.6 + z(4)/10,sprintf('Renyi Entropy = %2.4f
',RE)); grid;   % Display Renyi Entropy in the plot window

ShE(ii,jj)=SE;          % Assign Shannon Entropy value to the current
pixel location
RnE(ii,jj)=RE;          % Assign Renyi Entropy value to the current
pixel location

% ***********************END oF SE AND RE SECTION
**********************
%*********************************************************************
***
%            Recurrence Period Density Entropy CALCULATIONS FROM RAW
DATA
%*********************************************************************
***
% This section of the program computes RPDE from the raw optical data
%---------------------------------------------------------------------
---

[H_norm, rpd] = rpde(double(g),3,2); % Compute RPDE

RPDE(ii,jj) = H_norm;

% ********************END oF RPDE SECTION
*******************************

%---------------------------------------------------------------------
---
%              Estimate Dominant Frequency
```

```
%-------------------------------------------------------------------------
---

Fs=600;                                 % Frame rate, which is the sampling
rate in Hz
Ts = 1/Fs;                              % Sampling period in seconds
Y = fft(g)/L;                           % Compute the Fast Fourier
Transform
t = (0:L-1)*(1/Fs);                     % Define time vector for plotting
based on Sampling Rate
f = Fs/2*linspace(0,1,L/2+1);           % Define the corresponding
frequency vector for plotting
A1 = max(2*abs(Y(1:L/2+1)));            % Max value for plotting
A2 = (2*abs(Y(1:L/2+1)))/A1;            % Normalized power spectrum
A2(1)=0;                                % make the dc value to zero to find
dominant frequency peak
A = [f' A2];                            % make frequency amplitude array
[DF,v] = max(A);                        % find max frequency and its
location

% Plotting on the same window for reference

% figure(7), subplot(211), plot(t,g); grid; % Plot the raw optical data
time series
% xlabel('TIme (s) ');
% ylabel(' Intensity Values ');
% title(sprintf(' Plot of the Raw Time series optical data at pixel
location [%d,%d]  ',x_loc,y_loc));
% subplot(212), plot(f,(2*abs(Y(1:L/2+1)))/A1); % Plot the spectrum to
locate dominant frequency
% title(sprintf('Amplitude Spectrum of optical data at pixel location
[%d,%d] ',x_loc,y_loc));
% xlabel('Frequency (Hz)')
% ylabel('Normalized |Y(f)|')
% grid; axis([ 0 50 0 1]);
% sprintf(' The Dominant Frequency DF = %2.4f (Hz)', f(v(2)))
%
% if f(v(2)) < 8
% DmF(ii,jj)=f(v(2));
% end
%
% if f(v(2)) > 8
% DmF(ii,jj)= 7.85;  % at least 3 pixels near the rotor core shows
higher energy at the first harmonic of the DF for the dingle rotor data
only, which is inconsistent. I am forcing them to the nominal DF
% end

DmF(ii,jj)=f(v(2));      % Get the dominant frequency - Frequency which
has the highest energy

%----------------- END OF DOMINANT FREQUENCY SECTION  -----------------
---
```

```
%*************************************************************************
***
%            Multi-Scale Frequency CALCULATIONS FROM RAW DATA
%*************************************************************************
***
% This section of the program computes MSF from the raw optical data
%-------------------------------------------------------------------------
---

[FE_w, FE_Hz] = FrequencyEstimation_1D(g, Ts);
 msf = mean(FE_Hz); % Compute multiscale frequency index
 MSF(ii,jj) = msf;  % Assign MSF to the array for corresponding pixel
location

% ******************END OF MULTISCALE FREQUENCY SECTION
******************

%-------------------------------------------------------------------------
---
%               Estimate Kurtosis
%-------------------------------------------------------------------------
---


Kt(ii,jj) = kurtosis(g);      % Estimate the 4th central moment using
MATLAB's in-built function 'kurtosis'


%----------------- END OF KURTOSIS SECTION ---------------------------
--

%-------------------------------------------------------------------------
---
%               Estimate Multi-Scale Entropy
%-------------------------------------------------------------------------
---

E = NMSE(g,2);           % Estimate multi-scale entropy with scale
factor = 3
MSE(ii,jj) = max(E);     % Get the maximum value

%---------------------- END OF MSE SECTION ---------------------------
--

%*************************************************************************
***
%     Intrinsic Mode Function Complexity Index CALCULATIONS FROM RAW
DATA
%*************************************************************************
***
% This section of the program computes IMF from the raw optical data
```

```
%-------------------------------------------------------------------------
---

if max(g) > 0
E = emd(double(g));     % Perform EMD to estimate IMFs
s = size(E);            % Get the number of IMFs for this time series
data
s2 = s(2);
im = zeros(s2,1);

% Compute Complexity of the 2nd IMF

for ee = 2

    TEMP1  = E(1,ee);
    TEMP2  = TEMP1{1,1};
mse2 = MMSE(TEMP2, 2);          % compute IMF complexity with entropy
mse2 = max(max(mse2));
%clear TEMP1 TEMP2
end

% Compute Complexity of the 3rd IMF
for ee = 3

    TEMP1  = E(1,ee);
    TEMP2  = TEMP1{1,1};
mse3 = MMSE(TEMP2, 2);          % compute IMF complexity with entropy
mse3 = max(max(mse3));
%clear TEMP1 TEMP2
end

% Compute Complexity of the 4th IMF
for ee = 4

    TEMP1  = E(1,ee);
    TEMP2  = TEMP1{1,1};
mse4 = MMSE(TEMP2, 2);         % Compute IMF complexity with entropy
mse4 = max(max(mse4));
%clear TEMP1 TEMP2
end

imf = (mse2+mse3+mse4)/3; % Compute IMF complexity as the average (2,3
& 4)

IMF(ii,jj) = imf; % Assign the IMF complexity to the array for
corresponding pixel

end      % End of while loop
    end  % End of the MAIN loop (jj)
end      % End of the MAIN loop (ii)

max_SE=max(max(ShE));     % Find the maximum SE value
```

```
ShE = ShE/max_SE;          % Normalize the SE map using the max SE value

max_RE=max(max(RnE));      % Find the maximum RE value
RnE = RnE/max_RE;          % Normalize the RE map using the max RE value

max_Kt=max(max(Kt));       % Find the maximum Kt value
Kt = Kt/max_Kt;            % Normalize the Kt map using the max Kt value

max_MSE=max(max(MSE));     % Find the maximum MSE value
MSE = MSE/max_MSE;         % Normalize the MSE map using the max MSE
value

max_RPDE=max(max(RPDE)); % Find the maximum MSE value
RPDE = RPDE/max_RPDE;      % Normalize the MSE map using the max MSE
value

max_IMF=max(max(IMF));   % Find the maximum IMF value
IMF = IMF/max_IMF;         % Normalize the IMF map using the max MSE value

figure(1),imagesc(ShE), colorbar, title(' Normalized 2D Shannon Entropy
Map');      % Plot the Normalized 2D Shannon Entropy map
figure(2),imagesc(RnE), colorbar, title(' Normalized 2D Renyi Entropy
Map');        % Plot the Normalized 2D Renyi Entropy map
figure(3),imagesc(DmF), colorbar, title('  2D Dominant Frequency Map');
% Plot the 2D Dominant Frequency map
figure(4),imagesc(Kt),  colorbar, title(' Normalized 2D Kurtosis Map')
% Plot the Normalized 2D Kurtosis map
figure(5),imagesc(MSE), colorbar; title(' Normalized 2D MSE Map:Scale
Factor = 3 ')% Plot the Normalized 2D Multi-Scale Entropy map
figure(6),imagesc(MSF),  colorbar, title(' 2D MSF Map ')
% Plot the 2D Multi-Scale Frequency map
figure(7),imagesc(RPDE),colorbar, title(' Normalized 2D RPDE Map ')
% Plot the 2D RPDE map
figure(8),imagesc(IMF),colorbar, title(' Normalized 2D IMF Map ')
% Plot the 2D IMF map

%******************** END OF PROGRAM *********************************
```

APPENDIX G

Institutional Review Board (IRB) Documents – Mayo Clinic & University of Minnesota

MAYO CLINIC

HIPAA Authorization to Use and Disclose Protected Health Information

Name and Clinic Number

Approval Date: **August 25, 2016**
Not to be used after: **August 24, 2017**

Study Title: Analysis of Atrial Fibrillation (AF) and Ventricular Fibrillation (VF) electrograms to calculate entropy to identify pivotal regions during fibrillation.

IRB#: 14-003210

Principal Investigator: Dr. Siva K Mulpuru and Colleagues

During this research, information about your health will be collected. Under Federal law called the Privacy Rule, health information is private. However, there are exceptions to this rule, and you should know who may be able to see, use and share your health information for research and why they may need to do so. Information about you and your health cannot be used in this research study without your written permission. If you sign this form, it will provide that permission. You will be given a copy of this form.

Health information may be collected about you from:

- Past, present and future medical records.
- Research procedures, including research office visits, tests, interviews and questionnaires.

This information will be used and/or given to others to:

- Do the research.
- Report the results.
- See if the research was done correctly.

If the results of this study are made public, information that identifies you will not be used.

Your health information may be used or shared with:

- Mayo Clinic research staff involved in this study.

Your health information may also be shared with:

- The Mayo Clinic Institutional Review Board that oversees the research.
- Other Mayo Clinic physicians involved in your clinical care.
- Researchers involved in this study at other institutions.
- Federal and State agencies (such as the Food and Drug Administration, the Department of Health and Human Services, the National Institutes of Health and other United States agencies) or government agencies in other countries that oversee or review research.
- The sponsor(s) of this study and the people or groups it hires to help perform this research.
- A group that oversees the data (study information) and safety of this research.

MAYO CLINIC

HIPAA Authorization to Use and Disclose Protected Health Information

Name and Clinic Number

Approval Date: August 25, 2016
Not to be used after: August 24, 2017

Protection of your health information after it has been shared with others:

Mayo Clinic asks anyone who receives your health information from us to protect your privacy; however, once your information is shared outside Mayo Clinic, we cannot promise that it will remain private and it may no longer be protected by the Privacy Rule.

Your Privacy Rights

You do not have to sign this form, but if you do not, you cannot take part in this research study. Your decision won't change the access to medical care or any other benefits you get at Mayo Clinic now or in the future.

If you cancel your permission to use or share your health information, your participation in this study will end and no more information about you will be collected; however, information already collected about you in the study may continue to be used.

You can cancel your permission to use or share your health information at any time by sending a letter to the address below:

Mayo Clinic
Office for Human Research Protection
ATTN: Notice of Revocation of Authorization
200 1st Street SW
Rochester, MN 55905

Alternatively, you may cancel your permission by emailing the Mayo Clinic Research Subject Advocate at: researchsubjectadvocate@mayo.edu

Please be sure to include in your letter or email:

- The name of the Principal Investigator,
- The study IRB number and /or study name, and
- Your contact information.

Your permission lasts until the end of this study, unless you cancel it. Because research is an ongoing process, we cannot give you an exact date when the study will end.

Your signature documents your permission to use your protected health information for this research.

	/ /	: AM/PM
Printed Name	Date	Time

_____
Signature

MAYO CLINIC

IRB Minimal Risk Protocol Template

Note: If this study establishes a human specimen repository (biobank) for research purposes, do not use this template. Use the Mayo Clinic Human Specimen Repository Protocol Template found on the IRB home page under Forms and Procedures at http://intranet.mayo.edu/charlie/irb/

First-time Use: Use this template to describe your study for a new IRB submission.

1. Complete the questions that apply to your study.
2. Save an electronic copy of this protocol for future revisions.
3. When completing your IRBe application, you will be asked to upload this template to the protocol section.

Modification: To modify this template after your study has been approved:

1. Open your study in IRBe. Click on the study 'Documents' tab and select the most recent version of the protocol. Save it to your files.
2. Open the saved document and activate "Track Changes".
3. Revise the protocol template to reflect the modification points, save the template to your files
4. Create an IRBe Modification for the study and upload the revised protocol template.

General Study Information

Principal Investigator: Mulpuru K. Siva

Study Title: Analysis of Atrial Fibrillation (AF) and Ventricular Fibrillation (VF) electrograms to calculate entropy to identify pivotal regions during fibrillation.

Protocol version number and date: Version 1 4/18/2014

Purpose

Hypothesis: Shannon and/or Renyi entropy can be used to predict the location of the core of the rotor outside of pulmonary during persistent AF

Aims, purpose, or objectives: In this study, we aim to develop a new technique based on entropy estimation that can identify pivotal (self-sustaining) regions of chaotic rhythms like human AF. We will enhance the analysis by providing a spatial correlation between the new and already existing techniques at different atrial locations to reconstruct waveform propagation and identify structural disruptions, as sites of substrate abnormality to identify the core of rotors that causes AF.

Background (*Include relevant experience, gaps in current knowledge, preliminary data, etc.*):

Atrial Fibrillation (AF) or irregular activation of the atria is one of the most common cardiac arrhythmia and is one of the leading sources of health care expenditure in the United States. AF serves as an adverse prognostic marker and is associated with increased rates of the death stroke and heart failure events. Several mechanisms of AF have been described so far, with the most accepted mechanism being the complex interplay between various triggers that induce arrhythmia via reentry or triggered activity, and myocardial substrates that maintain them. Recent animal research shows that AF may also be maintained by rapid localized sources (rotors). The recent development of patient-specific computational mapping has revealed that the substrates for human AF are not necessarily 'random', but also comprised of stable electrical rotors and focal sources at diverse locations within either atrium.

Maintenance of sinus rhythm with anti-arrhythmic drugs and cardioversions is associated with increased quality of life in patients with symptomatic AF. However, efficacy of anti-arrhythmic drugs is only marginal in maintenance of sinus rhythm. For the past years, there is a rise in popularity of catheter ablation, which is an invasive non-pharmacological therapy that aims to restore normal sinus rhythm in the atria by eliminating triggers that maintain AF. Although more successful, recurrence rates are high, particularly in patients with persistent or long-standing AF. In these patients, AF is mostly maintained by the rotors that are located outside of pulmonary veins (PV) region. A major challenge in these patients is accurate identification of the arrhythmogenic substrates, so that ablative therapy can be successfully applied. Current processing methods that are used to identify AF vulnerable regions include analysis of the dominant frequency (DF), complex fractionated electrograms (CFAE), phase analysis and local activation maps. All these techniques are based on temporal analysis of electrograms from different spatial locations of atria. However, the high frequency of recurrence of arrhythmias in patients with persistent AF after PV isolation and linear ablation, show that these current techniques of AF analysis are not adequate to predict critical areas of AF maintenance. As a result, none of the currently available commercial mapping systems can predict the rotor location outside of PV in patients with persistent AF.

Subject Information – charts, records, images, or specimens are considered 'subjects'

Target accrual: *Proposed number of subjects to be included in your study at your site. "Subjects" may include Mayo Clinic charts, records, or specimens, **and/or** charts, records, or specimens received at Mayo Clinic from external sources for collaborating analysis by the investigator under this IRB application*:

Subject population: 40 patients

Inclusion Criteria: Patients presenting either persistent or paroxysmal AF

Exclusion Criteria:

Will a Certificate of Confidentiality be obtained? *If yes, provide an explanation.*

MAYO CLINIC

Study Design

Methods: *Describe, in detail, the research activities that will be conducted under this protocol*:
Electrograms are normally collected during AF/VF ablation and creation of LA geometry. These digitized and deidentified electrograms from ICDs and recording systems will be imported for offline analysis in MATLAB to compute dominant frequency and entropy to identify pivotal regions of the rotor. Across different patients the ability of the new method will be evaluated to correlate with peak dominant frequency.

Resources: *Describe the available resources to conduct the research (personnel, time, facilities, mentor commitment, etc.)*: Mulpuru Siva and Colleagues will assist in obtaining the EGM from recording systems and ICD's and serve as mentors for Shivaram Poigai Arunachalam who will conduct the EGM analysis using digital signal processing in MATLAB.

Check all that apply. If none apply, leave blank:

☐ This is a multisite study involving Mayo Clinic and non-Mayo Clinic sites.
When checked, describe the research procedures/activities being conducted **only** at Mayo Clinic:

X☐ Mayo Clinic staff will be engaged in research activity at a non-Mayo Clinic site. *When checked, provide the location and a detailed description of the Mayo Clinic research staff involvement.*
Shivaram Poigai Arunachalam is a PhD candidate at the University of Minnesota, School of Bioengineering. He will have access to the **deidentified data** for signal processing. He is currently an engineer here at the Mayo Clinic. He will receive mentoring from Alena Talkachova, Associate Professor of Biomedical engineering at the University of Minnesota to develop tools for signal processing.

The data from our recording systems (Pruka, GE) will be exported in a de-identified format without any patient identifiers on an encrypted USB drive. The patients will be numerically labelled as subjects 1-40 and only the principal investigator will have access to the key that links subject numbers to the actual patient identifiers. Shivaram and Dr. Talkachova will not have access to this key.

☐ This study is to establish and/or maintain an ongoing database or registry for research purposes only.

☐ The research involves contact or interaction with subjects, for example, surveys, questionnaires, observation, blood draw.

☐ The study involves audiotaping or videotaping

Blood Collection

MAYO CLINIC

If this study involves prospective blood collection by finger, heel, ear stick or venipuncture, complete the following:

☐ **From healthy, non pregnant, adult subjects who weigh at least 110 pounds**. For a minimal risk application, the amount of blood drawn from these subjects may not exceed 550ml in an 8 week period and collection may not occur more frequently than 2 times per week.

Volume per blood draw: _____ml

Frequency of blood draw (e.g. single draw, time(s) per week, per year, etc.) _____

☐ **From other adults and children considering age, weight, and health of subject.** For a minimal risk application, the amount of blood drawn from these subjects may not exceed the lesser of 50 ml or 3 ml per kg in an 8 week period, and collection may not occur more frequently than 2 times per week.

Volume per blood draw: _____ml

Frequency of blood draw (e.g. single draw, time(s) per week, per year, etc.)_____

Review of Chart, Images, Specimens

Provide the date range for collection of data and/or specimens that will be included in your research dataset. (*Example: 01/01/2000 to 12/31/2012*)

Date range: prospective data collection

Check all that apply:

☐ This study involves only data and/or specimens that exist at the time this application is submitted to the IRB (IRB submission date). No data or specimens will be collected beyond this date.

X☐ This study involves only data and/or specimens that will be collected after submission to the IRB.

The study involves data and/or specimens that exist at the time of submission to the IRB **and** data and/or specimens that will be collected after submission to the IRB, for example a study that includes collection of existing data and prospective collection of specimens.

☐ Data and/or specimens used in this study are collected under another IRB protocol. *When checked, provide the IRB number(s) from which the research material will be obtained and check the box below to attest that subjects have provided consent for future use of their data and/or specimens, as described in this protocol.*

IRB Number(s):

MAYO CLINIC

□Subjects have provided consent for use of their data and/or specimens, as described in this protocol.

☐ Other data sources will be utilized in this study. When checked, provide all data sources:

Data Confidentiality, HIPAA Subject Identifiers

Review the list of subject identifiers below and, if applicable, check the box next to each subject identifier being recorded at the time you are collecting/abstracting data/specimens for use in this study.

Subject Identifiers: Individually identifiable information, including demographic data, that identifies the individual or for which there is reasonable basis to believe it can be used to identify the individual. NOTE: Identifiers apply to subjects enrolled in your study and to the subject's relatives, household members, employers, etc.

Internal refers to subject identifiers that will be included in the dataset maintained by the study team. **External** refers to subject identifiers that will be shared with persons outside of the immediate study team, for example, sent to an external collaborator or shared with a national registry.

SUBJECT IDENTIFIERS **Check all that apply**	INTERNAL IDENTIFIER	EXTERNAL IDENTIFIER
Name	X	
Social Security number		
Medical record/patient registration number, lab accession, specimen or radiologic image number	X	
Study number, subject ID, or any other unique identifying number, characteristic or code that can be used to link the identity of the subject to the data	X	
Dates: All elements of dates [month, day, and year] directly related to an individual. Their birth date, date of death, date of diagnosis, etc. **Note:** Recording a year only is not a unique identifier.		
Medical device identifiers and serial numbers		
Biometric identifiers, including finger and voice prints, full face photographic images and any comparable images		
Web Universal Resource Locators (URLs), Internet Protocol (IP) address numbers, email address		
Street address, city, county, precinct, zip code, and their equivalent geocodes		
Phone or fax numbers		
Account, member, certificate or professional license numbers, health		

beneficiary numbers		
Vehicle identifiers and serial numbers, including license plate numbers		
If None of the above identifiers will be recorded or maintained in the dataset and/or sent outside of the study team, please check "None".	None	☒ None

Statistical Information

Note: Power analyses and study endpoints are not needed for a pilot or feasibility studies.

☐ No statistical information.

Statistical Considerations

Power Statement:

Correlation coefficients will be used to compare dominant frequency and entropy measurements from electrograms. Each patient will have more than 100 electrograms recorded and will give us enough statistical power to correlate these methods.

Data Analysis Plan: The time series AF electrogram data will be analyzed using MATLAB for computing dominant frequency and entropy (Shannon and Renyi).

Endpoints - correlation at the core of the rotor.
Primary: We hypothesize that the entropy estimations will be higher at the points where the dominant frequency exists thereby identifying the rotor pivot points that can be potential target ablation sites for AF.

Secondary: N/A

CONSENT FORM

Analysis of Atrial Fibrillation (AF) and Ventricular Fibrillation (VF) electrograms to calculate entropy to identify pivotal regions during fibrillation

You are invited to participate in a research study about understanding the mechanism of atrial or ventricular fibrillation in humans as you are having an ablation/device procedure. We ask that you read this form and ask any questions you may have before agreeing to be in the study.

This study is being conducted by *Mr.Poigai Arunachalam Shivaram M.S. M.P.H. Department of Biomedical Engineering, University of Minnesota Minneapolis, MN, Dr.Alena G. Talkachova Ph.D., Depart of Biomedical Engineering, University of Minnesota Minneapolis, MN, Dr. Mulpuru K. Siva, Division of Cardiovascular Diseases, Mayo Clinic, Rochester, MN and Dr.Paul A. Friedman Division of Cardiovascular Diseases, Mayo Clinic, Rochester, MN.*

Study Purpose

The purpose of the study is to develop a new technique based on entropy estimation that can identify pivotal (self-sustaining) regions of chaotic rhythms for human AF.

Study Procedures

If you agree to participate you will be asked to give permission for analysis of electrograms obtained during the ablation/device procedure. The electrograms will not have any identifying information and are routinely obtained on all patients undergoing ablation/ device procedures.

Risks of Study Participation

The risks of this research study are minimal, which means that we do not believe that they will be any different than what you would experience at a routine clinical ablation. All data used for analysis at the University of Minnesota will be de-identified to minimize the risk.

Benefits of Study Participation

This study will not make your health better. It is for the benefit of advancing science and understanding the mechanisms of fibrillation.

Alternatives to Study Participation

Please understand that your participation is voluntary and you have the right to withdraw your consent or discontinue participation at any time without penalty.

Study Costs/Compensation

The principal investigator of this study is paid to cover the costs of conducting the research.

Research Related Injury

There are no potential research related injuries anticipated for this study.

Confidentiality

The records of this study will be kept private. In any publications or presentations, we will not include any information that will make it possible to identify you as a subject. Study data will be encrypted according to current University policy for protection of confidentiality.

Protected Health Information (PHI)

Your PHI created or received for the purposes of this study is protected under the federal regulation known as HIPAA. Refer to the attached HIPAA authorization for details concerning the use of this information.

Voluntary Nature of the Study

Please understand that your participation is voluntary and you have the right to withdraw your consent or discontinue participation at any time without penalty.

Specifically, your current or future medical care at the Mayo Clinic will not be jeopardized if you choose not to participate.

Contacts and Questions

If you have any questions about this research study you can contact Dr.Mulpuru K. Siva at 507-255-4152 If you have any concerns, complaints, or general questions about research or your rights as a participant, please contact University of Minnesota Institutional Review Board to speak to someone independent of the research team at 612-626-5654.

You will be given a copy of this form to keep for your records.

Statement of Consent

I have read the above information. I have asked questions and have received answers. I consent to participate in the study.

Signature of Subject_____

Date_____

Signature of Person Obtaining Consent_____

Date_____

APPENDIX H

MATLAB Program for IEGM Analysis using Novel Approaches

"Novel_Approaches_IEGM_Analysis.m"

```
% MATLAB program for Intracardiac Electrogram (IEGM) Analysis
% The purpose of this program is analyze the raw IEGM data during AF
% using Shannon entropy, Renyi entropy, Multiscale Entropy, Recurrence
% Period Density Entropy, Kurtosis, Empirical Mode Decomposition,
% Dominant Frequency Analysis and Multiscale Frequency.

% Written by Shivaram Poigai Arunachalam; Advisor: Dr.Alena Talkachova
% First Code: Sep 30 2013;
% Last Modified Feb 20 2017

clear all
close all
clc
clear all

%*************************************************************************
***
%              RAW INTRACARDIAC ELECTROGRAM DATA INPUT
%*************************************************************************
***
% This section of the program INPUTS AND PLOTS the raw IEGM obtained
from
% the GE Prucka System with sampling rate of Fs=977 Hz
%-------------------------------------------------------------------------
---

format long
% fname = input(' Enter the File name ', 's');
% C=load(fname);              % Load the IEGM data
% %y=interp(y,5);             % Sampling Rate is increased for better
spectral resolution
% Fs =(977);                  % Sampling Rate
% % L=length(y);              % Length of the data vector


h  = load('CARTO_import_map1_LA-1.mat');  % Load IEGM data from Left
Atrium
%h1 = load('CARTO_import_map2_2-RA.mat'); % Load IEGM data from Right
Atrium
C = h.DxData.data.rovTrace;
%C1 = h1.DxData.data.rovTrace;
Fs = 1000;                                % Sampling Rate

% Allocate arrays for storing processed data for each approach

S_E   = zeros(642,1);       % Array for Shannon Entropy
R_E   = zeros(642,1);       % Array for Renyi Entropy
D_F   = zeros(642,1);       % Array for Dominant Frequency
```

```
MS_E  = zeros(642,1);       % Array for Multiscale Entropy
MS_F  = zeros(642,1);       % Array for Multiscale Frequency
KT    = zeros(642,1);       % Array for Kurtosis
RPDE  = zeros(642,1);       % Array for Recurrence Period Density
Entropy
IMF   = zeros(642,1);       % Array for Intrinsic Mode Function
Complexity

% ********* Main Loop to process each IEGM time series data
************

for j = 1:642       % Loop through all IEGM data

y = C(:,j);
L=length(y);        % Compute length of the time series
t = (0:L-1)*(1/Fs); % Define time vector for plotting based on Sampling
Rate

% figure(1), plot(t,y); grid; % Plot the raw IEGM
% xlabel('Time (s) ');
% ylabel(' Amplitude (mV) ');
% title(sprintf(' Plot of the Raw Intracardiac Electrogram (IEGM) from
%s data',fname));


%*********************************************************************
***
%              ENTROPY CALCULATIONS FROM RAW DATA
%*********************************************************************
***
% This section of the program INPUTS AND PLOTS the raw IEGM obtained
from
% the GE Prucka System with sampling rate of Fs=977 Hz
%---------------------------------------------------------------------
---

mx = max(y);            % Maximum amplitude value of the intracardiac
electrogram
mi = min(y);            % Minimum amplitude value of the intracardiac
electrogram
bin = mi:.001:mx;       % Create amplitude bins with 0.001 mV bin size
h = hist(y,bin);        % Create histogram data using specified bin
size
figure(2), plot(h);     % Plot the histogram
xlabel(' Bin Number ');
ylabel(' Frequency ');
%title(' Amplitude Histogram with bin size = 0.001 mV '); grid;
%title(sprintf(' Amplitude Histogram for %s data ',fname));grid;
l = length(h);          % Calculate the size of histogram matrix
P = zeros(1,l);         % Create array for probability density function
S = zeros(1,l);         % Create array to be used for Shannon Entropy
calculations
N = zeros(1,l);         % Create array to be used for Shannon Entropy
calculations
```

```
R = zeros(1,l);          % Create array to be used for Renyi Entropy
calculations
alpha = 0.25;            % Specify alpha value for Renyi Entropy
calculations

%-------------------------------------------------------------------
---
%              Estimate Shannon and Renyi Entropy
%-------------------------------------------------------------------
---

% The following loop calculates the intermediary terms used in Shannon
and
% Renyi entropy

for i = 1:l
    P(i) = h(i)/L;               % Probability that a given sample falls
within a particular amplitude bin
    S(i) = P(i)*log2(P(i));      % Shannon Entropy Term
        N(i) = S(i);
     if isnan(N(i))              % Check for NAN and replace it with 0
        N(i) = 0;
     end
    R(i) = P(i)^alpha;           % Renyi Entropy term
end

SE = -1*sum(N);                  % Calculate Shannon Entropy
RE = log(sum(R))*(1/(1-alpha)); % Calculate Renyi Entropy

%*******************************************************************
***
%              KURTOSIS CALCULATIONS FROM RAW DATA
%*******************************************************************
***
% This section of the program computes kurtosis from the raw IEGM
obtained from
% the GE Prucka System with sampling rate of Fs = 1000 Hz
%-------------------------------------------------------------------
---

Kt = kurtosis(y);  % Compute Kurtosis

%
*********************************************************************

%*******************************************************************
***
%            Multi-Scale Entropy CALCULATIONS FROM RAW DATA
%*******************************************************************
***
% This section of the program computes MSE from the raw IEGM obtained
from
% the GE Prucka System with sampling rate of Fs = 1000 Hz
%-------------------------------------------------------------------
---
```

```
MSE = NMSE(y,3);           % Estimate multi-scale entropy with scale
factor = 3
MSE = max(max(MSE));

%
**********************************************************************

%**********************************************************************
***
%              DOMINANT FREQUENCY CALCULATIONS FROM RAW DATA
%**********************************************************************
***
% This section of the program computes the DF from the raw IEGM
obtained from
% the GE Prucka System with sampling rate of Fs = 1000 Hz
%----------------------------------------------------------------------
---

Y = fft(y)/L;                    % Compute the Fast Fourier Transform
f = Fs/2*linspace(0,1,L/2+1);    % Define the corresponding frequency
vector for plotting
A1 = max(2*abs(Y(1:L/2+1)));     % Max value for plotting
A1x = (2*abs(Y(1:L/2+1)))/A1;
A1x(1)=0;
A1X = [f' A1x];
%for i = 1:15
min_freq = 5; max_freq = 15;
%DF_boy = A1X(f<15,:);
%[df,v] = max(A1X(f<15));            % find max frequency and its
location
[df,v] = max(A1X(f<15,2));
% [df1,v1] = max(A1X(5<f,2));
% DF = max(f(v),f(v1));
DF = f(v);

% figure(3),plot(f,(2*abs(Y(1:L/2+1)))/A1);% Plot the spectrum to
locate dominant frequency
% title(sprintf('Single-Sided Amplitude Spectrum of IEGM from %s data
',fname));
% xlabel('Frequency (Hz)')
% ylabel('|Y(f)|')
% grid
% axis([ 0 250 0 1]);

%
**********************************************************************

%**********************************************************************
***
%            Multi-Scale Frequency CALCULATIONS FROM RAW DATA
%**********************************************************************
***
% This section of the program computes MSF from the raw IEGM obtained
from
```

```
% the GE Prucka System with sampling rate of Fs = 1000 Hz
%-------------------------------------------------------------------------
---

[FE_w, FE_Hz] = FrequencyEstimation_1D(y, 0.001);
 MSF = mean(FE_Hz); % Compute multiscale frequency index

%
**************************************************************************

%**************************************************************************
***
%            Recurrence Period Density Entropy CALCULATIONS FROM RAW
DATA
%**************************************************************************
***
% This section of the program computes RPDE from the raw IEGM obtained
from
% the GE Prucka System with sampling rate of Fs = 1000 Hz
%-------------------------------------------------------------------------
---

[H_norm, rpd] = rpde(double(y),3,2); % Compute RPDE

%
**************************************************************************

%**************************************************************************
***
%     Intrinsic Mode Function Complexity Index CALCULATIONS FROM RAW
DATA
%**************************************************************************
***
% This section of the program computes IMF from the raw IEGM obtained
from
% the GE Prucka System with sampling rate of Fs = 1000 Hz
%-------------------------------------------------------------------------
---

if max(y) > 0
E = emd(double(y));    % Perform EMD to estimate IMFs
s = size(E);           % Get the number of IMFs for this time series
data
s2 = s(2);
im = zeros(s2,1);

% Compute Complexity of the 2nd IMF

for ii = 2

    TEMP1  = E(1,ii);
    TEMP2  = TEMP1{1,1};
mse2 = MMSE(TEMP2, 2);         % Compute IMF complexity with entropy
mse2 = max(max(mse2));
%clear TEMP1 TEMP2
```

```
end

% Compute Complexity of the 3rd IMF
for ii = 3

    TEMP1  = E(1,ii);
    TEMP2  = TEMP1{1,1};
mse3 = MMSE(TEMP2, 2);          % Compute IMF complexity with entropy
mse3 = max(max(mse3));
%clear TEMP1 TEMP2
end

% Compute Complexity of the 4th IMF
for ii = 4

    TEMP1  = E(1,ii);
    TEMP2  = TEMP1{1,1};
mse4 = MMSE(TEMP2, 2);         % Compute IMF complexity with entropy
mse4 = max(max(mse4));
%clear TEMP1 TEMP2
end

imf = (mse2+mse3+mse4)/3; % Compute IMF complexity as the average (2,3
& 4)

end

%
**********************************************************************

sprintf(' The Shannon Entropy SE = %2.4f and Renyi Entropy RE = %2.4f
', SE, RE); % Display Shannon and Renyi Entropy
z = axis;
% Obtain the current axis values
text(z(2)/1.6,z(4)/1.6,sprintf('Shannon Entropy = %2.4f ', SE));
% Display Shannon Entropy in the plot window
text(z(2)/1.6,z(4)/1.6 + z(4)/10,sprintf('Renyi Entropy = %2.4f
',RE));          % Display Renyi Entropy in the plot window
text(z(2)/1.6,z(4)/1.6 + z(4)/20,sprintf('Kurtosis = %2.4f  ',Kt));
text(z(2)/1.6,z(4)/1.8,sprintf('Multi-Scale Entropy = %2.4f  ',MSE));
text(z(2)/1.6,z(4)/2,sprintf('Multi-Scale Frequency = %2.4f  ',MSF));
text(z(2)/1.6,z(4)/2.25,sprintf('Dominant Frequency = %2.4f  ',DF));
text(z(2)/1.6,z(4)/2.5,sprintf('RPD Entropy = %2.4f  ',H_norm));
text(z(2)/1.6,z(4)/2.75,sprintf('IMF Complexity = %2.4f  ',imf));

S_E(j,1)  = SE;     % Assign corresponding SE values to the array
R_E(j,1)  = RE;     % Assign corresponding RE values to the array
D_F(j,1)  = DF;     % Assign corresponding DF values to the array
MS_E(j,1) = MSE;    % Assign corresponding MSE values to the array
MS_F(j,1) = MSF;    % Assign corresponding MSF values to the array
KT(j,1)   = Kt;     % Assign corresponding Kurtosis values to the array
RPDE(j,1) = H_norm; % Assign corresponding RPDE values to the array
IMF(j,1)  = imf;    % Assign corresponding IMF values to the array

% figure(3),
```

```
% subplot(211),plot(t,y); grid; % Plot the raw IEGM
% xlabel('Time (s) ');
% ylabel(' Amplitude (mV) ');
% title(sprintf(' Plot of the Raw Intracardiac Electrogram (IEGM) from
%s data',fname));
% subplot(212), plot(h);     % Plot the histogram
% xlabel(' Bin Number ');
% ylabel(' Frequency ');
% %title(' Amplitude Histogram with bin size = 0.001 mV '); grid;
% title(sprintf(' Amplitude Histogram for %s data ',fname));grid;
% %sprintf(' The Shannon Entropy SE = %2.4f and Renyi Entropy RE =
%2.4f ', SE, RE) % Display Shannon and Renyi Entropy
% z = axis;
% Obtain the current axis values
% text(z(2)/1.6,z(4)/1.6,sprintf('Shannon Entropy = %2.4f ', SE));
% Display Shannon Entropy in the plot window

% Plotting on the same window for reference

% figure(4), subplot(211), plot(t,y); grid; % Plot the raw IEGM
% xlabel('Time (s) ');
% ylabel(' Amplitude (V) ');
% title(sprintf(' Plot of the Raw Intracardiac Electrogram (IEGM) from
%s data ',fname));
% subplot(212), plot(f,A1x); % Plot the spectrum to locate dominant
frequency
% title(sprintf('Single-Sided Amplitude Spectrum of IEGM from %s data
',fname));
% xlabel('Frequency (Hz)')
% ylabel('Normalized |Y(f)|')
% grid; axis([ 0 25 0 1]);

% Check for not-a-number (NAN) values for each approach - example
below:

%  for i  = 1:642
%      x = isnan(RPDE(i));
%      if x == 0
%          RPDE(i) = RPDE(i);
%      else
%          RPDE(i) = min(RPDE(:));
%      end
%  end


end         % End of the main loop

% **********************   END OF PROGRAM **********************
```

APPENDIX I

MATLAB Program to obtain 3D MAPS for Visualization from NOVEL ELECTROGRAM ANALYSIS

"Plot_3D_Maps_IEGM.m"

```
% ------------------------------------------------------
%
%    MATLAB script to obtain 3D MAPS from NOVEL ELECTROGRAM ANALYSIS
%    Ver. 1.2.0
%
%    Created:       Tobias Oesterlein        (21.02.2017)
%    Last modified: Tobias Oesterlein        (21.02.2017)
%
%    Institute of Biomedical Engineering (IBT)
%    Karlsruhe Institute of Technology (KIT)
%
%    http://www.ibt.kit.edu
%
%    Copyright 2000-2017 - All rights reserved.
%    USER: SHIVARAM POIGAI ARUNACHALAM
% ------------------------------------------------------
%

% clear memory

close all
clear
clc




%% setup folder structure

% initialize path variables
setPathVariables;

%addpath(genpath(fullfile(gitpath,'common','file_input_output','Rhythmi
a')))
addpath(genpath(fullfile(gitpath,'common','file_input_output','vtk')))
addpath(genpath(fullfile(gitpath,'projects','EGMDataProcessing','Electr
odesProcessing')))
%addpath(genpath(fullfile(gitpath,'projects','EGMDataProcessing','Filte
ringAndProcessing')))
addpath(genpath(fullfile(gitpath,'projects','EGMDataProcessing','geomet
ricalOperations')))
addpath(genpath(fullfile(gitpath,'projects','EGMDataProcessing','interp
olation')))
```

```
addpath(genpath(fullfile(gitpath,'projects','EGMDataProcessing','plotti
ngEGMs')))
addpath(genpath(fullfile(gitpath,'projects','FastMarchingMATLAB')))
%addpath((fullfile(gitpath,'projects','IBT_ECG_Toolbox','ECG_Processing
')))
%addpath((fullfile(gitpath,'projects','IBT_ECG_Toolbox','Filtering')))
addpath((fullfile(gitpath,'thirdparty','geom3d','geom3d')))
addpath((fullfile(gitpath,'thirdparty','geom3d','meshes3d')))
addpath(fullfile(KaPAVIEpath))
clear KaPAVIEpath
clear gitpath
clear SVNpath
clear clinicalDatapath


%% load data

% imported EGMs and anatomy
LAimport=load('CARTO_import_map1_LA-1.mat');
LAresult=load('LA_IEGM_Analysis.mat');
RAimport=load('CARTO_import_map2_2-RA.mat');
RAresult=load('RA_IEGM_Analysis.mat');

% match both anatomies
% f=ValveGeo(2).xyz;
% b=TMPbv.ValveGeo.xyz;
% mapInd=find(ismember(f,b,'rows'));
% ValveGeo(2).xyz=ValveGeo(2).xyz(mapInd,:);
% ValveGeo(2).normals=ValveGeo(2).normals(mapInd,:);
% ValveGeo(2).Faces=TMPbv.ValveGeo.Faces;
% ValveGeo(2).vertOrgInd=ValveGeo(2).vertOrgInd(mapInd);


%% Rearrange data for processing

% geometry model
GeoModelGroups(2)=LAimport.GeoModelGroups(2);
GeoModelGroups(1)=RAimport.GeoModelGroups(1);

% valve model
ValveGeo(2)=LAimport.ValveGeo(2);
ValveGeo(1)=RAimport.ValveGeo(1);

% Ana
Ana=RAimport.Ana;

% Props
Props.processingMode='exact';

% EGM positions
AMaps_data(1).surfPtxyz=RAimport.DxData.data.surfPtxyz;
AMaps_data(2).surfPtxyz=LAimport.DxData.data.surfPtxyz;

% EGM data
```

```
AMaps_data(1).rovTrace=RAimport.DxData.data.rovTrace;
AMaps_data(2).rovTrace=LAimport.DxData.data.rovTrace;

% Manually set the amplitude so that later recordings are taken
AMaps_sigFeat(1).maxBipolAmpGood=1:size(AMaps_data(1).rovTrace,2);
AMaps_sigFeat(2).maxBipolAmpGood=1:size(AMaps_data(2).rovTrace,2);

% analysis results
AMaps_sigFeat(1).D_F  =RAresult.D_F;
AMaps_sigFeat(1).IMF  =RAresult.IMF;
AMaps_sigFeat(1).KT   =RAresult.KT;
AMaps_sigFeat(1).MS_E =RAresult.MS_E;
AMaps_sigFeat(1).MS_F =RAresult.MS_F;
AMaps_sigFeat(1).RPDE =RAresult.RPDE;
AMaps_sigFeat(1).R_E  =RAresult.R_E;
AMaps_sigFeat(1).S_E  =RAresult.S_E;

AMaps_sigFeat(2).D_F  =LAresult.D_F;
AMaps_sigFeat(2).IMF  =LAresult.IMF;
AMaps_sigFeat(2).KT   =LAresult.KT;
AMaps_sigFeat(2).MS_E =LAresult.MS_E;
AMaps_sigFeat(2).MS_F =LAresult.MS_F;
AMaps_sigFeat(2).RPDE =LAresult.RPDE;
AMaps_sigFeat(2).R_E  =LAresult.R_E;
AMaps_sigFeat(2).S_E  =LAresult.S_E;


%% get surface projection and coverage maps

fprintf('Generating coverage map ... \n')


% define interpolation radius
radius_green=5;     % radius of green [mm]
radius_yellow=10;     % radius of yellow [mm]
radius=[radius_green radius_yellow];

for nAtrium=1:2

    if ~GeoModelGroups(nAtrium).exists
        continue
    end

    % get electrode positions near surface according to preprocessing
    elecPos=AMaps_data(nAtrium).surfPtxyz;

    % get vertices closest to elec positions

AMaps_sigFeat(nAtrium).elecValveGeoInd=getElecSurfaceVertex(ValveGeo(nA
trium),elecPos);

end

parfor nAtriumP=1:2
```

```
    if ~GeoModelGroups(nAtriumP).exists
        continue
    end

    % generate Coverage Map with coloring according to electrodes
distance
    if strcmp(Props.processingMode,'exact')

CoverageMapTmp{nAtriumP}=getGeoCoverage(ValveGeo(nAtriumP),AMaps_sigFea
t(nAtriumP).elecValveGeoInd,radius,'exact');
    else

CoverageMapTmp{nAtriumP}=getGeoCoverage(ValveGeo(nAtriumP),AMaps_sigFea
t(nAtriumP).elecValveGeoInd,radius,'fastest');
    end
end

% copy data for parallel usage
clear('CoverageMap')
for nAtrium=1:2
    if ~GeoModelGroups(nAtrium).exists
        continue
    end
    CoverageMap(nAtrium)=CoverageMapTmp{nAtrium};
end
if ~GeoModelGroups(2).exists
    CoverageMap(2).name=[];
end
clear('CoverageMapTmp')

parfor nAtriumP=1:2

    if ~GeoModelGroups(nAtriumP).exists
        continue
    end

    % add the geometry information about the good covering Geo to
Coverage Map

CoverageMapGeoTmp{nAtriumP}=getCoveredGeometry(ValveGeo(nAtriumP),Cover
ageMap(nAtriumP).yellowverticesind);
end

% copy data for parallel usage
clear('CoverageMapGeo')
for nAtrium=1:2
    if ~GeoModelGroups(nAtrium).exists
        continue
    end
    CoverageMapGeo(nAtrium)=CoverageMapGeoTmp{nAtrium};
end
if ~GeoModelGroups(2).exists
    CoverageMapGeo(2).xyz=[];
end
```

```
clear('CoverageMapGeoTmp')

% compute surface area after CoverageMap has been generated
for nAtrium=1:2

    if ~GeoModelGroups(nAtrium).exists
        continue
    end

    % get total surface areaa in cm^2

CoverageMap(nAtrium).surfaceAreaTotalValveGeo=trimeshSurfaceArea(ValveG
eo(nAtrium).xyz/10,ValveGeo(nAtrium).Faces);

CoverageMap(nAtrium).surfaceAreaCoveredValveGeo=trimeshSurfaceArea(Cove
rageMapGeo(nAtrium).xyz/10,CoverageMapGeo(nAtrium).Faces);

end



% generate plot of coverage
%data_struct(1).vertices=[GeoModelGroups(1).xyz;
GeoModelGroups(2).xyz];
%data_struct(1).faces=[GeoModelGroups(1).Faces;
Ana.numNodesRADxGeo+GeoModelGroups(2).Faces];
clear data_struct
data_struct(1).vertices=[GeoModelGroups(1).xyz; GeoModelGroups(2).xyz];
data_struct(1).faces=[GeoModelGroups(1).Faces;
Ana.numNodesRADxGeo+GeoModelGroups(2).Faces];
data_struct(1).data=repmat([0.5 0.5
0.5],size(data_struct(1).vertices,1),1);
data_struct(2).vertices=[ValveGeo(1).xyz; ValveGeo(2).xyz];
data_struct(2).faces=[ValveGeo(1).Faces;
Ana.numNodesRAValveGeo+ValveGeo(2).Faces];
data_struct(2).data=[CoverageMap(1).data;CoverageMap(2).data];
fh=figure;
plotGeometryWithData(fh,data_struct,[],[],[]);
hold on
%remainingPtsInds=vertcat([AMaps_data(1).pointIDinRecInfo;
AMaps_data(2).pointIDinRecInfo]);
if GeoModelGroups(1).exists
    plot3(AMaps_data(1).surfPtxyz(1,:),AMaps_data(1).surfPtxyz(2,:),...
        AMaps_data(1).surfPtxyz(3,:),'.r','MarkerSize',10)
end
if GeoModelGroups(2).exists
    plot3(AMaps_data(2).surfPtxyz(1,:),AMaps_data(2).surfPtxyz(2,:),...
        AMaps_data(2).surfPtxyz(3,:),'.g','MarkerSize',10)
end
title('Coverage Map')
set(gca,'FontSize',14)
set(gcf,'Color','w')
set(gca,'Box','off','XColor','w','YColor','w','ZColor','w')

clear('radius_green','radius_yellow','radius','remainingPtsInds','elecP
os',...
```

```
    'data_struct','nAtrium','fh')

fprintf(' ... completed\n\n')


%% Generate interpolation matrix

fprintf('Generating interpolation matrix ... \n')

% define threshold for low amplitude signals being scar
Ana.minAmpThreshold=0.04;

% find entries to remove
for nAtrium=1:2

    if ~GeoModelGroups(nAtrium).exists
        continue
    end

    % find all signals, which are projected onto the same location
    sigToDelete=[];
    for nSig=1:size(AMaps_sigFeat(nAtrium).elecValveGeoInd,1)
        % get all entries for this vertex

currentVertex=find(AMaps_sigFeat(nAtrium).elecValveGeoInd==AMaps_sigFea
t(nAtrium).elecValveGeoInd(nSig));
        if length(currentVertex)>1
            % use amplitude to reject some of the signals

[val,ind]=max(AMaps_sigFeat(nAtrium).maxBipolAmpGood(currentVertex));
            sigToDelete=[sigToDelete;...
                [currentVertex(1:ind-1); currentVertex(ind+1:end)]];
        end

    end
    sigToDelete=unique(sigToDelete);

    % remove signals
    indicesOfAtrium=sigToDelete;
    %selectedAtriumForPoints(indicesOfAtrium(sigToDelete{nAtrium}))=[];
    AMaps_sigFeat(nAtrium).elecValveGeoInd(indicesOfAtrium)=[];
    AMaps_sigFeat(nAtrium).maxBipolAmpGood(indicesOfAtrium)=[];
    AMaps_sigFeat(nAtrium).D_F(indicesOfAtrium)=[];
    AMaps_sigFeat(nAtrium).IMF(indicesOfAtrium)=[];
    AMaps_sigFeat(nAtrium).KT(indicesOfAtrium)=[];
    AMaps_sigFeat(nAtrium).MS_E(indicesOfAtrium)=[];
    AMaps_sigFeat(nAtrium).MS_F(indicesOfAtrium)=[];
    AMaps_sigFeat(nAtrium).RPDE(indicesOfAtrium)=[];
    AMaps_sigFeat(nAtrium).R_E(indicesOfAtrium)=[];
    AMaps_sigFeat(nAtrium).S_E(indicesOfAtrium)=[];
    AMaps_data(nAtrium).surfPtxyz(:,indicesOfAtrium)=[];
    AMaps_data(nAtrium).rovTrace(:,indicesOfAtrium)=[];

    % define surface normals for the electrodes
```

```
%AMaps_sigFeat(nAtrium).elec_geoNormal=GeoModelGroups(nAtrium).normals(
...
    %    AtrialCatheters(nAtrium).elec_geoind,:);

    % get low voltage signals

AMaps_sigFeat(nAtrium).lowVoltageSignals=(AMaps_sigFeat(nAtrium).maxBip
olAmpGood<Ana.minAmpThreshold);

end

for nAtriumP=1:2

    if ~GeoModelGroups(nAtriumP).exists
        continue
    end

    % generate NNvol interpolation matrix for fast performance
    AMaps_interpMats(nAtriumP).NNvol_interp_matrix =
generateNearestNeighborVolumeInterpolationMatrix(ValveGeo(nAtriumP),...
        AMaps_sigFeat(nAtriumP).elecValveGeoInd);

    % generate interpolation matrix for precise interpolation
    if strcmp(Props.processingMode,'exact')

[AMaps_interpMats(nAtriumP).interp_matrix_minLaPlacian,AMaps_interpMats
(nAtriumP).interp_matrix_linearLaPlacian] = ...

generateLaplacianInterpolationMatrix(ValveGeo(nAtriumP),AMaps_sigFeat(n
AtriumP).elecValveGeoInd);
    end
end
if ~GeoModelGroups(2).exists
    AMaps_interpMats(2).NNvol_interp_matrix=[];
end

for nAtrium=1:2

    if ~GeoModelGroups(nAtrium).exists
        continue
    end

    % compute projection matrix from Elecs to Surface Area

CoverageMap(nAtrium).surfaceAreaByElectrodes=computeSurfaceAreaByElectr
odes(ValveGeo(nAtrium).xyz/10, ...
        ValveGeo(nAtrium).Faces,
AMaps_interpMats(nAtrium).NNvol_interp_matrix,
CoverageMapGeo(nAtrium).UNCOVEREDverticesOrgInd);

    % compute total surface area covered by electrodes (slighly bigger
than covered area due to boundary including)
```

```
CoverageMap(nAtrium).surfaceAreaByElectrodesTotal=sum(CoverageMap(nAtri
um).surfaceAreaByElectrodes);

end

clear('sigToDelete','currentVertex','val','ind','indicesOfAtrium')

% generate plot of NN interpolation
clear data_struct
data_struct(1).vertices=[GeoModelGroups(1).xyz; GeoModelGroups(2).xyz];
data_struct(1).faces=[GeoModelGroups(1).Faces;
Ana.numNodesRADxGeo+GeoModelGroups(2).Faces];
data_struct(1).data=repmat([0.5 0.5
0.5],size(data_struct(1).vertices,1),1);
data_struct(2).vertices=[ValveGeo(1).xyz; ValveGeo(2).xyz];
data_struct(2).faces=[ValveGeo(1).Faces;
Ana.numNodesRAValveGeo+ValveGeo(2).Faces];
[row1,~]=find(AMaps_interpMats(1).NNvol_interp_matrix');
[row2,~]=find(AMaps_interpMats(2).NNvol_interp_matrix');
dataraw=[row1;size(AMaps_interpMats(1).NNvol_interp_matrix,2)+row2];
permutationInds=randperm(size(AMaps_interpMats(1).NNvol_interp_matrix,2
)+...
    size(AMaps_interpMats(2).NNvol_interp_matrix,2));
data_struct(2).data=permutationInds(dataraw)';
figure
patch('Vertices',data_struct(1).vertices,'Faces',data_struct(1).faces,.
..
    'FaceColor','interp','FaceVertexCData',data_struct(1).data,...
    'EdgeColor','none','CDataMapping','scaled','FaceAlpha',1);
hold on
patch('Vertices',data_struct(2).vertices,'Faces',data_struct(2).faces,.
..
    'FaceColor','interp','FaceVertexCData',data_struct(2).data,...
    'EdgeColor','none','CDataMapping','scaled','FaceAlpha',1);
title('NN interpolation areas')
set(gca,'FontSize',14)
set(gcf,'Color','w')
set(gca,'Box','off','XColor','w','YColor','w','ZColor','w')
hold on
%remainingPtsInds=vertcat([AMaps_data(1).pointIDinRecInfo;
AMaps_data(2).pointIDinRecInfo]);
if ~isempty(AMaps_data(1).surfPtxyz)
    plot3(AMaps_data(1).surfPtxyz(1,:),AMaps_data(1).surfPtxyz(2,:),...
        AMaps_data(1).surfPtxyz(3,:),'.r','MarkerSize',10)
end
if ~isempty(AMaps_data(2).surfPtxyz)
    plot3(AMaps_data(2).surfPtxyz(1,:),AMaps_data(2).surfPtxyz(2,:),...
        AMaps_data(2).surfPtxyz(3,:),'.g','MarkerSize',10)
end
colormap('hsv')    % clinical use of LAT: early red, late blue
% set initial view settings
view(3); daspect([1 1 1]); axis tight
camlight;  camlight(-80,-10); lighting phong; %flat gouraud phong none
```

```
material([0.4 0.4 0.2 10 0.8]) % sets the ambient/diffuse/specular
strength, specular exponent, and specular color reflectance of the
objects.
set(gca, 'ZTick',zeros(1,0), 'YTick',zeros(1,0), 'XTick',zeros(1,0));

clear('row1','row2','dataraw','permutationInds','remainingPtsInds',...
    'nAtrium','nAtriumP','nSig')

fprintf(' ... completed\n\n')



%% interpolate maps based on this method

fprintf('Generating maps ... \n')

for nAtrium=1:2

    if ~GeoModelGroups(nAtrium).exists
        continue
    end

    AMaps_maps(nAtrium).D_F =
interpolateDataOnSurfaceNearestNeighborVolume(...

AMaps_sigFeat(nAtrium).D_F,AMaps_interpMats(nAtrium).NNvol_interp_matri
x);
    AMaps_maps(nAtrium).IMF =
interpolateDataOnSurfaceNearestNeighborVolume(...

AMaps_sigFeat(nAtrium).IMF,AMaps_interpMats(nAtrium).NNvol_interp_matri
x);
    AMaps_maps(nAtrium).KT =
interpolateDataOnSurfaceNearestNeighborVolume(...

AMaps_sigFeat(nAtrium).KT,AMaps_interpMats(nAtrium).NNvol_interp_matrix
);

    AMaps_maps(nAtrium).MS_E =
interpolateDataOnSurfaceNearestNeighborVolume(...

AMaps_sigFeat(nAtrium).MS_E,AMaps_interpMats(nAtrium).NNvol_interp_matr
ix);
    AMaps_maps(nAtrium).MS_F =
interpolateDataOnSurfaceNearestNeighborVolume(...

AMaps_sigFeat(nAtrium).MS_F,AMaps_interpMats(nAtrium).NNvol_interp_matr
ix);
    AMaps_maps(nAtrium).RPDE =
interpolateDataOnSurfaceNearestNeighborVolume(...

AMaps_sigFeat(nAtrium).RPDE,AMaps_interpMats(nAtrium).NNvol_interp_matr
ix);
```

```
    AMaps_maps(nAtrium).R_E =
interpolateDataOnSurfaceNearestNeighborVolume(...

AMaps_sigFeat(nAtrium).R_E,AMaps_interpMats(nAtrium).NNvol_interp_matri
x);
    AMaps_maps(nAtrium).S_E =
interpolateDataOnSurfaceNearestNeighborVolume(...

AMaps_sigFeat(nAtrium).S_E,AMaps_interpMats(nAtrium).NNvol_interp_matri
x);
end
if ~GeoModelGroups(2).exists
    AMaps_maps(2).R_E=[];
end

clear('nAtrium')

fprintf(' ... completed\n\n')



%% Initialize view

viewSet(1).name='AP';
viewSet(1).CameraPosition  = [126.21 730.47 749.14];
viewSet(1).CameraTarget    = [-28.157 53.044 110.48];
viewSet(1).CameraUpVector  = [-0.44958 0.66485 -0.59654];
viewSet(1).CameraViewAngle = 7.9051;

viewSet(2).name='RAO';
viewSet(2).CameraPosition  = [-778.02 -26.508 677.93];
viewSet(2).CameraTarget    = [-28.157 53.044 110.48];
viewSet(2).CameraUpVector  = [-0.28709 0.92478 -0.24973];
viewSet(2).CameraViewAngle = 7.9051;

viewSet(3).name='LAO';
viewSet(3).CameraPosition  = [261.11 902.44 402.84];
viewSet(3).CameraTarget    = [-28.157 53.044 110.48];
viewSet(3).CameraUpVector  = [-0.68264 0.43467 -0.58743];
viewSet(3).CameraViewAngle = 7.9051;

viewSet(4).name='PA';
viewSet(4).CameraPosition  = [-384.06 -311.99 -683.69];
viewSet(4).CameraTarget    = [-28.157 53.044 110.48];
viewSet(4).CameraUpVector  = [-0.44778 0.87151 -0.19991];
viewSet(4).CameraViewAngle = 7.9051;



%% Plot maps

%
listFields=fields(AMaps_maps);
for nFields=1:length(listFields)
```

```
    % compile data
    currentField=listFields{nFields};
    saveNamePrefix=fullfile('figures',['AnalysisResultPlot_'
currentField]);
    dataraw=[AMaps_maps(1).(currentField);
AMaps_maps(2).(currentField)];

    % generate plot

    fh=figure;
    clear data_struct
    data_struct(1).vertices=[GeoModelGroups(1).xyz;
GeoModelGroups(2).xyz];
    data_struct(1).faces=[GeoModelGroups(1).Faces;
Ana.numNodesRADxGeo+GeoModelGroups(2).Faces];
    data_struct(1).data=repmat([0.5 0.5
0.5],size(data_struct(1).vertices,1),1);

patch('Vertices',data_struct(1).vertices,'Faces',data_struct(1).faces,.
..
        'FaceColor','interp','FaceVertexCData',data_struct(1).data,...
        'EdgeColor','none','CDataMapping','scaled','FaceAlpha',1);
    hold on;

    data_struct(2).vertices=[ValveGeo(1).xyz; ValveGeo(2).xyz];
    data_struct(2).faces=[ValveGeo(1).Faces;
Ana.numNodesRAValveGeo+ValveGeo(2).Faces];
    data_struct(2).data=dataraw;

patch('Vertices',data_struct(2).vertices,'Faces',data_struct(2).faces,.
..
        'FaceColor','interp','FaceVertexCData',data_struct(2).data,...
        'EdgeColor','none','CDataMapping','scaled','FaceAlpha',1);

    set(gca,'FontSize',14)
    title(currentField,'Interpreter','none')
    % load('clinicalColormaps','NavX_LAT_cmap')
    % colormap(NavX_LAT_cmap);
    c=colorbar;
    c.Label.String=currentField;
    c.Label.Interpreter='none';

    % set initial view settings
    view(3); daspect([1 1 1]); axis tight
    camlight;  camlight(-80,-10); lighting phong; %flat gouraud phong
none
    material([0.4 0.4 0.2 10 0.8]) % sets the ambient/diffuse/specular
strength, specular exponent, and specular color reflectance of the
objects.
    set(gca, 'ZTick',zeros(1,0), 'YTick',zeros(1,0),
'XTick',zeros(1,0));
    set(gcf,'Color','w')
    set(gca,'Box','off','XColor','w','YColor','w','ZColor','w')

    set(gca,'CameraPosition',viewSet(1).CameraPosition);
    set(gca,'CameraUpVector',viewSet(1).CameraUpVector);
```

```
    set(gca,'CameraUpVector',viewSet(1).CameraUpVector);
    set(gca,'CameraViewAngle',viewSet(1).CameraViewAngle);

    % save fig file
    saveas(fh,[saveNamePrefix],'fig');

    % save images
    for nView=1:4
        set(gca,'CameraPosition',viewSet(nView).CameraPosition);
        set(gca,'CameraUpVector',viewSet(nView).CameraUpVector);
        set(gca,'CameraUpVector',viewSet(nView).CameraUpVector);
        set(gca,'CameraViewAngle',viewSet(nView).CameraViewAngle);

        saveas(fh,[saveNamePrefix '_' viewSet(nView).name],'png');

    end
end

% ************** END of PROGRAM *****************
```